University of Strathclyde
Department of Electronic and Electrical Engineering

Modular Multilevel Converter Designs for Medium-Voltage Machine Drives

by

Mohamed Said Diab
B.Sc., M.Sc.

A thesis presented in fulfilment of the requirements for the degree of Doctor of Philosophy

2019

This thesis is the result of the author's original research. It has been composed by the author and has not been previously submitted for examination which has led to the award of any degree.

Signed: *Mohamed Diab* Date: 18/04/2019

Acknowledgements

I would like to express my appreciation to my supervisors Prof. Barry Williams and Dr Derrick Holliday for their useful comments and remarks throughout the learning process of this PhD thesis.

My deepest thankfulness goes to Dr Grain Adam who provided me with assistance and valuable discussion during my research period.

Besides my supervisors and academic mentors, I would like to express my sincere appreciation to Dr Ahmed Abbas for his guidance, continuous support, sharing ideas, and help since the early stages of my graduate research up to the PhD.

I also would like to thank Dr Ahmed Massoud, Dr Shehab Ahmed, and Dr Ayman Abdel-Khalik for their valuable technical contributions, contribution to the funding of this research, and for their important role in my research career.

Thanks to colleagues and staff at PEDEC group. On a personal level, Dr Ahmed Darwish, Dr Azmy Gowaid, and Dr Mohamed Atef. I extend my thanks to them and the rest of the team for assistance, useful discussions, and the encouraging atmosphere.

Abstract

Various industry sectors are now adopting high-power applications that involve power electronics on a large scale. This increases the power level requirement of the adjustable-speed drives utilized in such applications to scores of megawatts, triggering the need for high-power driving at the medium-voltage (MV) level. Thus, this thesis addresses the modular multilevel converter (MMC) as a promising topology for MV machine drives. A special focus is given to the variable-speed operation of MMC-fed three-phase machines, where the MMC experiences a serious challenge when operating at low frequencies. The MMC's unique operation principles imply its floating submodule (SM) capacitors experience voltage fluctuation at the fundamental operating frequency. At lower operating frequencies, MMC capacitor voltage fluctuations can reach extreme levels, inversely proportional to the operating frequency, where increasing the SM capacitance for voltage ripple compensation is not viable. In this context, this thesis proposes an approach for SM capacitor voltage ripple compensation, which employs magnetic chain links involving dual half-bridges (DHBs) to interface the SMs, for ripple power decoupling. The approach is able to transfer the ripple power of one SM to another in a bidirectional fashion, countering the energy fluctuation. This allows for an even capacitive energy distribution across MMC SMs, independent of the operating frequency, resulting in a significant reduction in SM capacitance. A class of different DHB modules allocations relevant to the MMC SMs is investigated.

Also, this thesis addresses MMC application for multiphase machine drives, where reduced topological designs derived from the standard MMC are presented for six-phase machine drives. The topologies are enhanced to realize a more-economic six-phase machine drive without any performance compromise.

Analytical investigations are derived for the different approaches presented in this thesis, while necessary control algorithms are analyzed. The viability of proposed concepts and approaches are substantiated through both simulation and experimentation.

Acronyms

AC	Alternating Current
ACC	Active Cross Connected
APOD	Alternative Phase Opposition Disposition
CD	Carrier Disposition
CHB	Cascaded H-Bridge
CM	Common Mode
DAB	Dual Active Bridge
DC	Direct Current
DFB	Dual Full Bridge
DFOC	Direct Field Orientated Control
DHB	Dual Half Bridge
DM	Differential Mode
DTC	Direct Torque Control
FACTS	Flexible Alternating Current Transmission System
FB	Full Bridge
FC	Flying Capacitor
GTO	Gate Turn Off
HB	Half Bridge
HF	High Frequency
HPF	High Pass Filter
HVDC	High Voltage Direct Current
H9A-MMC	Hybrid Nine-Arm Modular Multilevel Converter
IFOC	Indirect Field Orientated Control
IGBT	Insulated Gate Bipolar Transistor
IGCT	Integrated Gate Commutated Thyristor
KCL	Kirchhoff's Current Law
LPF	Low Pass Filter
MMC	Modular Multilevel Converter
MV	Medium Voltage
NLC	Nearest Level Control
NPC	Neutral Point Clamped
PD	Phase Disposition
PI	Proportional Integral
PLL	Phase Locked Loop
POD	Phase Opposition Disposition
PR	Proportional Resonant
PSC	Phase Shifted Carrier
PWM	Pulse Width Modulation
Q2L	Quasi Two-Level

SHE	Selective Harmonic Elimination
SM	Sub-Module
SPWM	Sinusoidal Pulse Width Modulation
STATCOM	Static Synchronous Compensator
SVM	Space Vector Modulation
THD	Total Harmonic Distortion
VOC	Voltage Oriented Control
VSI	Voltage Source Inverter
ZCS	Zero Current Switching
ZVS	Zero Voltage Switching
8A-MMC	Eight-Arm Modular Multilevel Converter
9A-MMC	Nine-Arm Modular Multilevel Converter
12A-MMC	Twelve-Arm Modular Multilevel Converter

List of Symbols

C	SM capacitance
C_f	Resonant filter capacitance
D	Converter duty cycle
f_c	Carrier frequency
f_h	High frequency
f_o	Fundamental output frequency
i_C	Capacitor current
i_{circ}	Circulating current
i_d	d-axis current component
I_{dc}	DC-link current
i_{dg}	*d*-axis grid current component
i_{ds}, i_{ds1}, i_{ds2}	*d*-axis stator current component
i_{d2f}	Double-frequency *d*-axis current component
i_h/ I_h	High-frequency current
i_L	Lower-arm current
i_M	Middle-arm current
I_o	Output current magnitude
i_q	*q*-axis current component
i_{qg}	*q*-axis grid current component
i_{qs}, i_{qs1}, i_{qs2}	*q*-axis stator current component
i_{q2f}	Double-frequency *q*-axis current component
i_s	Stator current
i_T/I_T	Transformer current
i_U	Upper-arm current
K	Number of FB-SMs per arm
K_h	Modulation margin utilization coefficient for HF injection
K_T	Torque constant
k_1, k_2	Tuning parameters of PR controller
L_{arm}, L	Arm inductance
L_f	Resonant filter inductance
L_g	Grid inductance
L_m	Transformer magnetizing inductance
L_p	Transformer primary-side leakage inductance
L_s	Transformer secondary-side leakage inductance
L_T	Transformer leakage inductance
m_1, m_2	Modulation signals of DHB converter
M	Modulation index

n	Number of SMs inserted in the power path
N	Number of SMs per arm
N_r	Rotor speed
N_R	Number of redundant SMs per arm
n_T	Transformer turns ratio
p_{cm}	Common-mode power component
P_{DHB}	DHB converter power
p_{dm}	Differential-mode power component
P_g	Grid active power
p_L	Lower-arm power
P_{SM}	SM decoupled power
p_U	Upper-arm power
Q_g	Grid reactive power
T_d	Dwell time of Q2L operation mode
T_e	Electromagnetic torque
V_c	Nominal SM capacitor voltage
v_{CE}	IGBT collector-to-emitter voltage
v_{cm}	Common-mode voltage
V_{cp}	DHB primary-side capacitor voltage
V_{cs}	DHB secondary-side capacitor voltage
v_d	*d*-axis voltage component
V_{dc}	DC-link voltage
$V_{dc\ avg}$	Average DC voltage
v_{dg}	*d*-axis grid voltage component
v_{ds}	*d*-axis stator voltage component
V_g	Grid voltage magnitude
v_{GE}	IGBT gate-to-emitter voltage
V_h /v_h	High-frequency voltage
v_L	Lower-arm voltage
v_M	Middle-arm voltage
V_o	Output voltage magnitude
V_{o_D}	Dual MMC output voltage magnitude
v_p	Transformer primary-side voltage
v_q	*q*-axis voltage component
v_{qg}	*q*-axis grid voltage component
v_{qs}	*q*-axis stator voltage component
v_s	Transformer primary-side voltage
v_U	Upper-arm voltage
w_{cm}	Common-mode energy component
w_{dm}	Differential-mode energy component

w_L	Lower-arm energy
w_U	Upper-arm energy
δ	Phase-angle difference for power flow
Δv_{c_U}	Upper-arm SM capacitor voltage ripple
Δv_{c_L}	Lower-arm SM capacitor voltage ripple
$\Delta V_{c\,cm}$	Peak-to-peak CM SM capacitor voltage ripple
$\Delta V_{c\,dm}$	Peak-to-peak DM SM capacitor voltage ripple
ΔW	Peak-to-peak energy variation
$\Delta V_{c\,DHB}$	Peak-to-peak capacitor voltage ripple with DHB balancing
$\theta_a, \theta_b, \theta_c$	Phase angles of ac output voltage
θ_f	Rotor flux angle
θ_g	Grid voltage angle
θ_r	Rotor position angle
θ_{sl}	Slip angle
σ	Space-orientation angle of six-phase machines
φ	Power factor angle
ψ_r	Rotor flux
ψ_{dr}	d-axis rotor flux component
ψ_{qr}	q-axis rotor flux component
ω	Angular frequency
ω_h	Angular high frequency

Subscripts

U	Upper arm
M	Middle arm
L	Lower arm
g	Grid
s	Stator
r	Rotor
max	Maximum value
min	Minimum value

Superscripts

$*$	Reference value

Contents

Chapter 1

Introduction

Over time, medium-voltage (MV) drives have found widespread applications in various industry sectors such as ship propulsion, oil and gas, production plants, and process industries. These applications adopt electrically-driven machines in multiple forms of fans, compressors, pumps, extruders, and rolling mills. The machines are fed via power electronic converters at a power level ranging from hundreds of kilowatts to scores of megawatts, at the MV level of 2.3–13.8 kV [1]. Table 1.1 shows various MV drive applications along with the respective power ranges, where the power level reaches 100 MW for oil and gas applications. Nonetheless, market description of MV drives shows that the majority of installed MV drives are in the power range of 1–4 MW with a voltage level of 3.3–6.6 kV [2]. At such high ratings, the MV converter topology choice plays a key role for both the feasibility and reliability of the drive system, where many technical challenges should be considered.

Table 1.1: Industry applications of MV drives [1]

Industry sector	Application	Power range
Chemical and cement	extruders, pumps, compressors, blowers, cement mills, fans, mixers, and presses	0.5−4 MW
Marine	propulsion drives, booster-generators, thrusters, winders, and dredge pumps	2−20 MW
Water	pumps and blowers	0.5−40 MW
Mining	ore mills, mine hoists, conveyor belts, pumps, crushers, blowers, compressors, and excavators	2−15 MW
Metal	hot and cold rolling mill, sectional steel mill, and blast furnace converter	2−25 MW
Oil and gas	turbo compressors, reciprocating compressors, and centrifugal pumps	1−100 MW

1.1 Overview of High-Power MV Converters

The development of MV machine drives started in the mid-1980s using the timely prevailing 4.5 kV gate turn off (GTO) thyristors [3], while scored a technical leap in the 1990s with the advent of high-power insulated-gate bipolar transistors (IGBTs) and integrated gate commutated thyristors (IGCTs) [4], [5]. MV converters in megawatt power level are not considered standard interface circuits, but part of the drive or energy conversion system. This returns to the different performance characteristics implied by the adopted applications, where the power converter circuit must fit such characteristics. Further, there are technical requirements and challenges for MV drives that differ in many aspects from those of the low-voltage ($\leq$ 600 V) drives. They are described as power quality requirements at the line-side rectifier, challenges associated with the motor-side converter design, and switching devices constraints. Since the scope of this thesis is directed to MV drive converters, the focus will be given to motor-side converter challenges.

1.1.1 Motor-Side Converter Challenges

A. dv/dt and wave reflections

Depending on both the converter dc-link voltage and the switching speed of the employed semiconductor devices, high dv/dt can arise at the rising and falling edges of the converter output voltage. This can cause a premature failure of the motor winding insulation due to partial discharge, in addition to shaft bearing failure due to induced rotor shaft voltages through stray capacitances between the stator and rotor. High dv/dt also causes electromagnetic emission in cables connecting both the converter and motor, adversely affecting any nearby sensitive electronic equipment. Further, high dv/dt may cause voltage doubling effect at the rising and falling edges of the converter voltage due to wave reflections in long connection cables exceeding a certain limit. This returns to the mismatch between the wave impedance of the cable and the impedances at its converter and motor ends, which can double the voltage on the motor terminals at each switching transient [2].

B. Common-mode voltage stress:

Normally, the switching action of any converter circuit generates common-mode (CM) voltages that are described as zero-sequence voltages superimposed with switching noise. The CM voltage appears differentially across the motor neutral point and the grounding point, where it can increasingly affect the motor line-to-ground voltage, leading to a premature failure of the motor winding insulation system. The CM voltage is often ignored in low-voltage drives due to their conservative insulation system design. However, in MV drives, the CM voltage should be properly mitigated to avoid costly replacement of the damaged motor in addition to the loss of production [6].

C. Motor de-rating

High-power converters often generate a large amount of current and voltage harmonics that cause an increased power loss in the motor winding and its magnetic core. If not mitigated, the motor is de-rated and cannot operate at its full capacity [2].

D. Use of converter output filter

For MV converters adopting capacitive filter at their output stage, there is a possibility of creating *LC* resonant circuit between the filter capacitor and the motor winding inductance. The resonant mode of the *LC* circuit may be excited by the harmonic voltages or currents produced by the converter [2]. Although the motor winding resistances may offer some damping (which implies losses), this concern should be addressed when designing the MV converter.

1.1.2 Motor-Side Converter Configurations

Several power converter topologies have been established to fulfil the motor-side requirements economically and efficiently. A structural overview of the main MV drive topologies is presented in Fig. 1.1 [7]. Among them, voltage-source inverters (VSIs) are the dominant topologies for MV drive applications due to their versatility, simple integration in various application environments, and evolution with continuous advancement in semiconductor technology. The two-level converter is

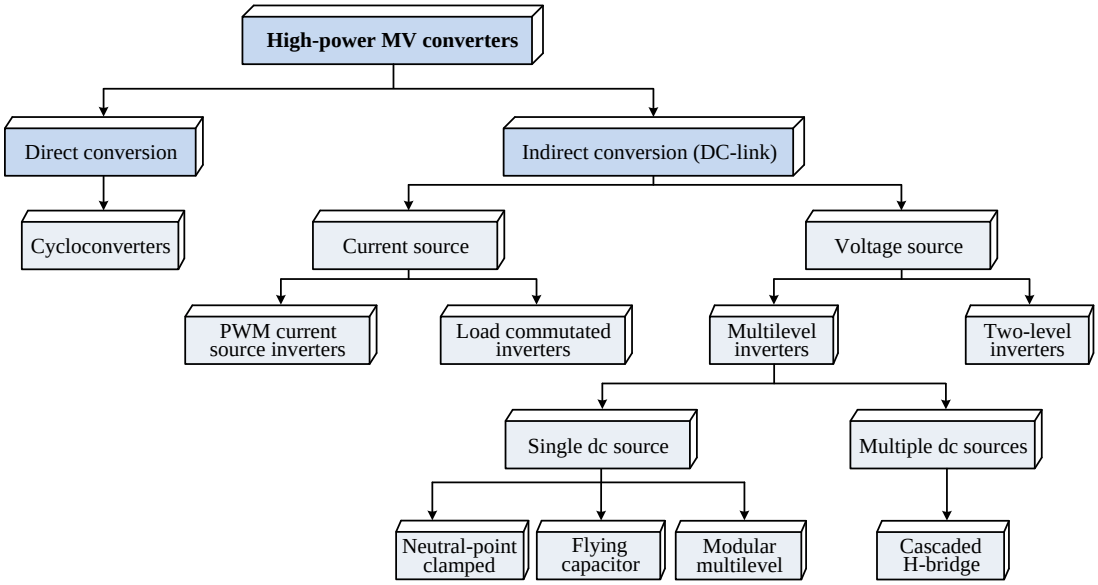

Fig. 1.1 Overview of MV drive topologies.

the most common VSI topology that has been adopted in many diversified applications. However, the maximum voltage blocking capability in addition to the current capacity of the currently available MV IGBT devices practically limits the maximum attainable power of the two-level converter to the lower end of the high-power range. Although the nominal power of the two-level converter can be increased by adopting series- and parallel-connected IGBTs, a lot of concerns arise pertinent to the balance of both the voltage and current sharing between the connected devices. Also, it is commonly preferred to increase the motor voltage rather than the motor current, which results in enhanced drive efficiency. Higher voltage is achieved by series connection of switching devices, which requires snubber circuits to ensure balanced voltage sharing between the devices. The additional balancing circuits result in power losses and subsequent power de-rating. Thus, in high-power applications, multilevel VSIs are gaining most attraction, being a prominent solution that delivers high-power using mature medium-power semiconductor technology, with notable advantages compared with traditional two-level VSIs [8]. These advantages are fundamentally focused on output voltage quality improvements in addition to the ease of nominal power scalability. The basic idea of multilevel converters is to connect several devices in series while clamping the voltages between the respective devices. Depending on the voltage clamping

technique, many multilevel converter topologies have evolved. The state-of-the-art multilevel converter topologies are the neutral-point-clamped (NPC), flying-capacitors (FC), and cascaded H-bridge (CHB) converters [9]. These three converter topologies have emerged as standard products for industrial MV drives, however with some limitations pertinent to the limited number of voltage levels due to capacitor voltage balancing issues for both the NPC and FC converters, and the necessity of providing a large number of isolated power supplies for the CHB converter. The restrictions of the state-of-the-art multilevel converters triggered the need for a new multilevel converter topology that can be flexibly scaled for a wider range of voltage and output power. Thus, the modular multilevel converter (MMC) was developed in 2002 as a promising contender for medium- to high-voltage high-power applications, outperforming its counterparts [10]. Being in the multilevel category, the MMC inherits the advantages of the state-of-the-art multilevel converter topologies, while solely enjoying the features of modularity, scalability, redundancy, and reliability. Through extensive research during the past decade, the MMC has been considered a proven technology where it is now utilized in high-voltage direct current (HVDC) transmission systems as a standard commercialized converter interface [11], while is recently drawing the research interest as the next generation machine-drive technology [12].

1.1.3 Industrial MV Drives

Being the most convenient converter topologies matching the motor-side requirements, multilevel VSIs have been adopted and marketed as MV drive products by major drive manufacturers, as overviewed in Table 1.2 [2], [7]. As itemized, the NPC converter receives most of market attention, where three-level NPC has been widely used in several MV drive applications and is considered one of the most commonly applied topologies being able to double the maximum attainable output power with a doubled dc-link voltage, compared with the two-level VSI. The NPC is characterized by a relatively small dc-link capacitance, simple power circuit topology, low component count, and straightforward protection and modulation schemes. Although it scores the highest converter efficiency among the available

Table 1.2: Market overview of industrial multilevel-converter-based MV drives

Topology	Type	Manufacturer	Power	Semiconductor
3L-NPC	ACS1000	ABB	0.3−5 MVA	IGCT
	ACS6000	ABB	3−36 MVA	
	Sinamics SM150	Siemens	5−28 MVA	
	Sinamics GM150	Siemens	0.6−10.1 MVA	IGBT
	MV7000	GE	3−21 MVA	
	Dura-Bilt5i MV	TMEIC GE	7.5 MVA	
	VDM7000	Alstom	7−9.5 MVA	GTO
5L-NPC	ACS5000	ABB	1.7−24 MVA	IGCT
4L-FC	VDM6000	Alstom	0.5−9 MVA	IGBT
CHB	Perfect Harmony GH180	Siemens	0.3−24 MVA	IGBT
	HIVECOL-HVI	Hitachi	0.3−16.7 MVA	
	PowerFlex 6000	Rockwell Automation	2.2−11 MVA	
MMC	M2L 3000	Benshaw	0.2−7.5 MVA	IGBT
	Sinamics SM120 CM	Siemens	4−13.3 MVA	IGBT/IGCT
	Perfect Harmony GH150	Siemens	4−47 MVA	IGBT/IGCT

industrial solutions, it requires a large *LC* output filter to drive standard motors. The five-level version of the NPC receives a little market interest due to capacitor voltage balancing concerns associated with increasing the NPC number of voltage levels. The FC converter was not found competitive and has been rarely developed by MV drives manufacturers due to challenges in both balancing and pre-charging of its employed capacitors. Also, the stored energy of the capacitors is increased by a factor of 10 and 20 for both the three-level and four-level versions of the FC converter compared to their NPC counterparts, respectively. The CHB converter found market importance due to its modular cell structure, where both the voltage and power levels can be easily scaled. The main shortcoming of the CHB converter topology that impedes its wider market adoption is its requirement for isolated power supplies as a dc-link for each cell. This can be realized using multi-winding phase-shifted transformers, which increases CHB converter cost and complexity. The

absence of a common dc-link voltage is an additional concern of the CHB converter topology. The MMC, which was originally developed for HVDC applications, is the latest multilevel converter topology to put a toe in the MV drives market. The MMC inherits the operating principle of the CHB converter, however without the need for isolated dc power supplies. Instead, the MMC is directly connected to a common dc-link voltage, employing a series connection of submodules (SMs) each clamped to a flying dc capacitor functioning as an energy buffer. The main MMC advantage is its unlimited extendibility to any voltage/power level. That is how Siemens developed the Perfect Harmony GH150 MV drive rated at 47 MVA and 11 kV output voltage [13].

1.2 Motivation and Objectives

Generally, electronically-controlled adjustable-speed operation of a machine drive reflects on both the drive system and the power source, where it eliminates the necessity for expensive mechanical components for speed control, increases machine longevity, and reduces energy losses, power line disturbances, and the risk of machine damage during both start up and stop. Only 3% of currently installed MV machines are controlled by adjustable-speed drives [2]. Consequently, there is a significant scope for introducing efficient adjustable-speed drives in industrial applications.

MMC application as a controlled MV drive faces serious challenges pertinent to its unique operating principles. Due to their floating nature, MMC SM capacitors are directly exposed to load current circulation, resulting in voltage fluctuations at the fundamental operating frequency. At lower frequencies, the voltage fluctuations increase, reaching extreme levels at near zero frequencies. MMC low frequency operation becomes even harder with constant torque loads, where SM capacitor voltage variation further increases due to the increased load current. This precludes the MMC from MV applications with constant Volt/Hertz control, that is, constant torque loads; limiting its utilization to a narrow band of quadratic-torque loads such as pumps, fans, and compressors [14]. This gives a margin for extra control effort to limit SM capacitor voltage fluctuation at low operating frequencies. Therefore, the

main objective of this thesis is to address MMC full-load low frequency operation for MV adjustable-speed drive applications.

Also, the thesis focuses on MMC application in multiphase machine drives, where a reduction in the machine per-phase current can be achieved, compared to traditional three-phase machines. This reduces the current capacity of the employed semiconductor devices and allows for further increase in the machine nominal power level. Although the standard structure of the MMC phase leg can be directly extended to synthesize any number of phases, the increased number of employed switching devices, reactive elements, and measuring transducers complicates the drive system and increases both size and cost. Therefore, this thesis targets developing reduced MMC structures to power multiphase machines in an economical way.

1.3 Thesis Contributions

Thesis contributions are summarized as follows:

- Identifying a set of desirable features in candidate MV power electronic converters for high-power machine drives.
- Reviewing state-of-the-art MMC configurations and control methods for MV high-power adjustable-speed drive applications.
- Proposing an MMC power decoupling approach for SM capacitor voltage ripple compensation as a comprehensive solution for MMC low-frequency operation, independent of the operating frequency and loading condition.
- Analysing the power decoupling approach in detail and elaborates its application to three-phase machines with both open-end and closed-end stator windings.
- Presenting several implementations of the power decoupling approach, while undertaking assessments to quantify the pros and cons.
- Proposing MMC configurations with topological reduction for six-phase machine drive applications.
- Providing conclusions as well as recommendations for future extension of the research undertaken in this thesis.

Chapter 2

General Aspects of the Modular Multilevel Converter

This chapter presents the preparation for the subsequent chapters by detailing the MMC operating principle, modulation techniques, and control algorithms, in addition to a brief discussion of its applications. Also, it highlights the main challenges of MMC-fed variable-speed drives, where simulation results are provided to assess MMC performance at different operating frequencies.

2.1 Introduction to Multilevel Converters

The wide spread of the numerous industrial applications employing high-power apparatus implies the MV grid to be inevitably utilized as the main power source [1]. For an MV grid, it is troublesome to connect only one power semiconductor device for direct interface. Thus, the multilevel converter structure has been introduced as a prominent alternative for high-power and MV operating conditions. The invention of the multilevel concept was patented in 1975 [15]. The term multilevel began with the three-level converter [16]. Thereafter, several multilevel converter topologies have been developed [17]–[24]. The elementary concept of a multilevel converter to achieve higher power is to use a series of switching devices with several lower-voltage dc sources to perform the power conversion by synthesizing a staircase voltage waveform at the output. Capacitors, batteries, and renewable energy sources can be adopted as the multiple dc voltage sources. Proper commutation of the switching devices aggregates these multiple dc sources in order to achieve high voltage at the output. Nonetheless, the nominal voltage of the switching devices depends only on the rating of the dc voltage sources to which they are clamped.

2.1.1 Pros and Cons of Multilevel Converters

A multilevel converter has several advantages over a conventional two-level converter that uses high switching-frequency pulse width modulation (PWM). The attractive features of a multilevel converter can be highlighted as bulleted below.

- **Staircase waveform quality**: Multilevel converter is capable of producing a staircase output voltage with minimum total harmonic distortion (THD), which in turn contributes to substantial reduction of bulky passive filters used for harmonic compensation in two-level converters. Also, it reduces the dv/dt stresses, reducing the electromagnetic compatibility problems.
- **CM voltage**: Multilevel converter produces lower CM voltage, reducing the stress across the bearing of multilevel converter-fed motors. CM voltage can be further eliminated by using advanced modulation strategies [25].
- **Input current**: Multilevel converter draws a continuous input current with low distortion.
- **Switching frequency**: Multilevel converter can support lower switching frequencies, resulting in overall lower switching losses and higher efficiency.
- **Reliability:** Multilevel converter reliability is enhanced, since operation is ensured under component failure at a reduced power level.

Notwithstanding, multilevel converters have minor shortcomings; most significantly is the large number of required semiconductor devices. Although this does not yield a significant capital cost increase since lower-voltage devices are used, the operational cost is increased due to the converter cooling requirements. Additionally, an increased number of gate drive circuits and more elaborate mechanical layout are required.

2.1.2 Review of Multilevel Converter Topologies

Various multilevel converter topologies have been intensively investigated during the last two decades, where some of them have been proven to be beneficial contenders. Among them, the NPC, FC, and CHB converters are the most common multilevel converter configurations to be reported in the literature with a wide scope of applications. They have been successfully implemented in various medium- to high-

voltage applications. Such applications are STATCOM [26], FACTS [27], HVDC [28], utility interface for renewable energy systems [29], and MV machine drives [30]. However, the state-of-the-art multilevel converters are experiencing shortcomings pertinent to their voltage level extendibility, where capacitor voltage balancing concerns are aroused when increasing the number of voltage levels of both the NPC and FC converters. Whereas, the prime necessity of providing isolated dc sources for the CHB converter restricts its wide utilization. A remarkable advance in the cascaded bridge converters design was scored in 2002 by Marquardt and Lesnicar, yielding to the MMC topology [10]. Through the past decade, the MMC has snatched the attention in both MV and HV market based on its outstanding merits that enable it to outperform its counterparts. Since the focus of this thesis is given to the MMC topology, the next section presents a detailed description of the MMC structure, operation principle, and modulation techniques.

2.2 Modular Multilevel Converter

The MMC preserves the features of cascaded converter topologies, without the need for isolated dc sources and complicated phase-shifting transformers. Thus, MMCs can reach any operating voltage from the MV level (2.3–13.8 kV) to the HV level (33–400 kV) and power rating of 0.226–1000 MW [31].

2.2.1 MMC Structure

The MMC structure is based on series connection of identical SMs, where the SM is the basic building block which lies behind the MMC modularity feature. Since three-phase systems are the most common, a circuit diagram for a three-phase MMC feeding an induction machine is shown in Fig. 2.1. It consists of three phase legs each comprising two arms; namely upper and lower arms. Both arms are connected in series between the dc terminals through arm inductors L_{arm}, while the ac terminal is realized as the intermediary node between the two arms. The arm inductor serves as a current limiter to suppress the circulating current due to the voltage mismatch between the total voltages of the phase legs and the dc-link voltage. Each arm is formed by

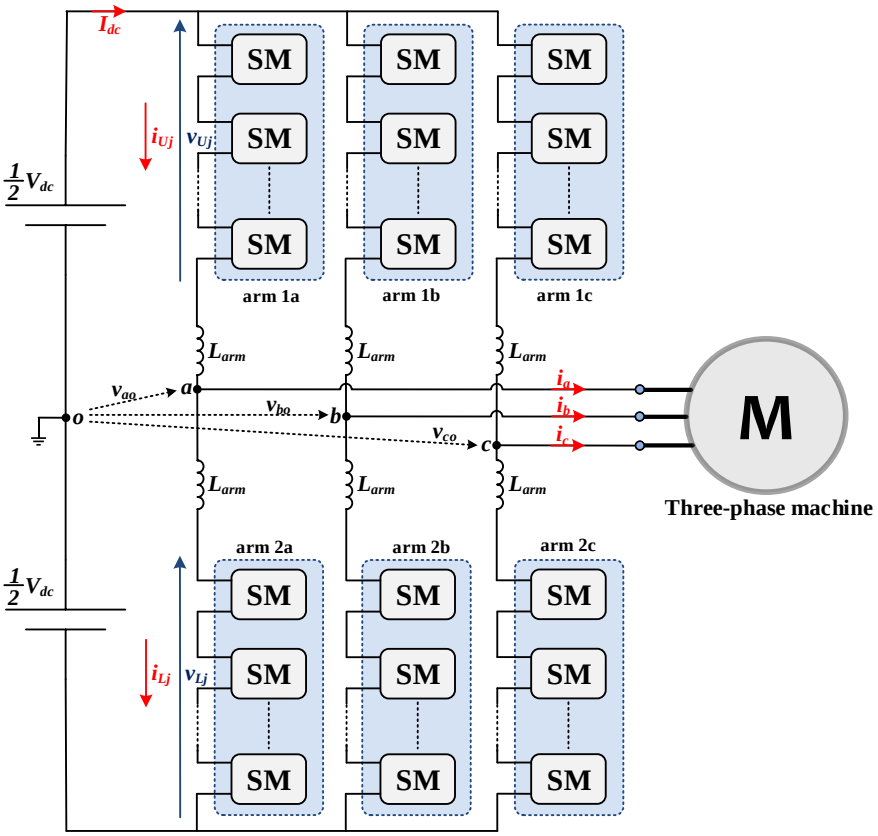

Fig. 2.1 Circuit diagram of a standard MMC topology feeding a three-phase machine.

N series connected SMs, where the number N varies from less than ten up to several hundreds, depending on the application voltage requirements. The SM is a two-terminal circuit incorporating a local capacitor of an equivalent capacitance C and a nominal voltage V_c, acting as an energy buffer to realize the dc voltage source by which the multilevel voltage waveform is synthesized. Each arm is designed to block the full dc-link voltage V_{dc}, yielding the nominal voltage of each SM capacitor $V_c = V_{dc}/N$. The SM can be implemented through several configurations, although the half-bridge (HF) and full-bridge (FB) configurations are the most common. HB-SMs can generate two voltage states (0 and $+V_c$), with the commutations of two switching devices, as shown in Fig. 2.2a. Whereas, FB-SMs, shown in Fig 2.2b, can generate three voltage states (0, $+V_c$, and $-V_c$), however with a doubled number of employed switching devices, as compared to HB-SMs.

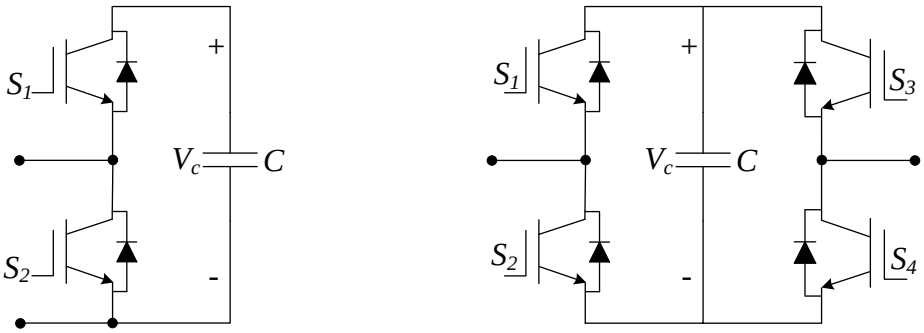

Fig. 2.2 Configurations of MMC SMs using: (a) HB-SMs and (b) FB-SMs.

2.2.2 MMC Modulation Techniques

Depending on the switching state of each individual SM, the corresponding local capacitor can be series inserted in the power path or bypassed. Proper insertion/bypass of SMs is achieved by adopting a suitable modulation technique, such as the sinusoidal pulse-width modulation (SPWM), space vector modulation (SVM), selective harmonic elimination (SHE), and nearest-level control (NLC) [8]. Both the SVM and SHE significantly increase the implementation complexity as the number of voltage levels increases. Oppositely, the NLC is much easier to implement, where it generates a staircase waveform at the output stage with a reduced switching frequency, however with considerable harmonic content, particularly at a lower number of voltage levels. Therefore, the discussion in this chapter will be based on utilization of carrier-based SPWM, being the most convenient approach in terms of implementation simplicity and reduced harmonic content in the output voltage.

The SPWM technique uses either phase-shifted carriers (PSC) or carrier disposition (CD) approaches. The PSC-SPWM is utilized to control each MMC SM separately, where it employs a carrier signal for each SM, thus N carriers for each arm. The carrier signals have the same carrier frequency f_c, however shifted by $2\pi/N$ to achieve harmonic cancellation, as shown in Fig. 2.3. Nonetheless, the PSC-SPWM technique significantly increases the switching frequency per individual SM, where the latter is switched with the carrier frequency. Therefore, the overall switching frequency of each MMC phase-leg is $2Nf_c$, resulting in increased switching losses.

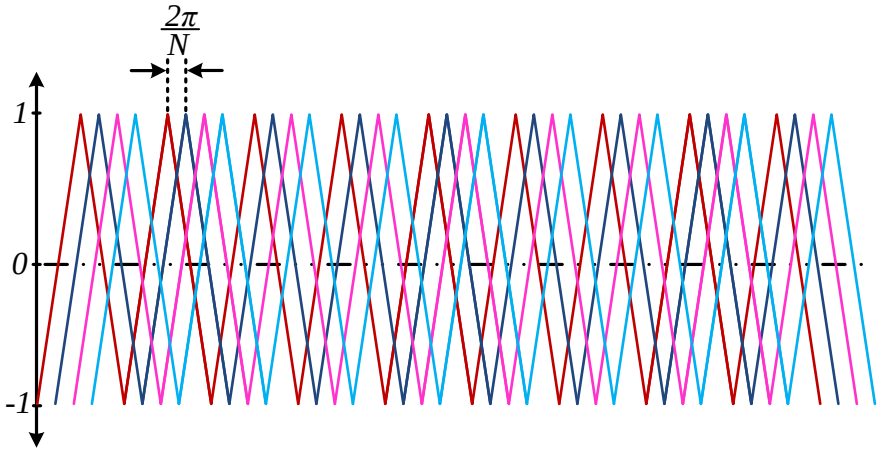

Fig. 2.3 PSC approach for MMC modulation.

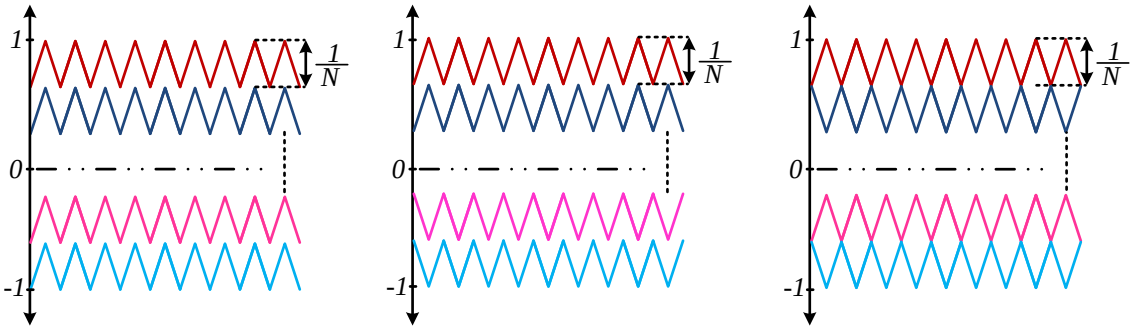

Fig. 2.4 Multi-carrier PWM technique using: (a) PD, (b) POD, and (c) APOD.

On the other hand, the CD-SPWM technique effectively reduces the overall switching frequency of each MMC phase-leg by $1/N$, compared to the PSC-SPWM. The CD approach employs N carrier signals with the same carrier frequency, however symmetrically displaced by $1/N$ offset. Three carrier arrangements are commonly adopted in CD-SPWM:

- **Phase disposition (PD):** where all carrier signals are in phase.
- **Phase opposition disposition (POD):** where carriers above the zero reference are in phase but shifted by 180° from those carriers below the zero reference.
- **Alternative phase opposition disposition (APOD):** where each carrier band is shifted by 180° from the adjacent carrier.

The main differences between the CD arrangements are graphically depicted in Fig 2.4. Among them, the PD carriers' arrangement is recommended as it produces an output voltage with a better harmonic distribution and reduced switching frequency per semiconductor device. Thus, the PD-SPWM technique will be adopted in this thesis as the basic MMC modulation technique.

2.2.3 Voltage Balancing of SM capacitors

By comparing the reference sinusoidal signal with vertically shifted carriers of the CD approach, the number of SM capacitors to be inserted in the power path n, is determined. The specific n SM capacitors are decided such that a charge balance across all SM capacitors is maintained. That is, the SM capacitors of both the upper and lower arms are always measured and sorted in ascending or descending order. When the arm current charges the capacitors, the switch combination that inserts SMs with the lowest capacitor voltages while bypassing those with the highest voltages is selected. When the arm current discharges the capacitors, the switch combination that inserts SMs with the highest capacitor voltages while bypasses those with the lowest voltages is selected. In this way, the voltages of MMC SM capacitors are maintained within a limited band of voltage fluctuation around the nominal value.

2.2.4 MMC Mathematical Analysis

Referring to Fig. 2.1, the output voltage of a general MMC phase-leg is denoted by v_{jo}, where o is a virtual ground located at the dc-link mid-point. The machine current is denoted by i_j, where $j \in \{a, b, c\}$. Both the output voltage and machine current are generally expressed as:

$$\begin{cases} v_{jo} = V_o \cos(\omega t + \theta_j) \\ i_j = I_o \cos(\omega t + \theta_j - \varphi) \end{cases} \tag{2.1}$$

where V_o and I_o are the voltage and current amplitudes, respectively, ω is the output angular frequency, θ_j is the phase angle of the output voltage ($\theta_a = 0°$, $\theta_b = 120°$, and $\theta_c = 240°$), and φ is the machine power-factor angle. The magnitude of the ac

phase voltage is defined by the modulation index M and the voltage of the input source V_{dc}, as follows.

$$V_o = \frac{1}{2} M\, V_{dc} \tag{2.2}$$

The MMC arm voltages in addition to the arm currents are given by (2.3) and (2.4), respectively, with the subscripts 'U' and 'L' referring to the corresponding 'upper' and 'lower' arm. Both arms within the same phase-leg are controlled in a complementary manner such that the voltage between the dc poles of the MMC is V_{dc}, as elaborated by (2.3).

$$\begin{cases} v_{Uj} = \frac{1}{2} V_{dc} - v_{jo} \\ v_{Lj} = \frac{1}{2} V_{dc} + v_{jo} \end{cases} \tag{2.3}$$

$$\begin{cases} i_{Uj} = i_{circ\,j} + \frac{1}{2} i_j \\ i_{Lj} = i_{circ\,j} - \frac{1}{2} i_j \end{cases} \tag{2.4}$$

where $i_{circ\,j}$ is the circulating current of the phase-leg j, passing through the dc loops comprising the dc side and each converter leg, and is calculated as:

$$i_{circ\,j} = \frac{1}{2}(i_{Uj} + i_{Lj}) \tag{2.5}$$

The circulating currents are mainly caused by the differences of the SM capacitor voltages in the upper and lower arms of the three converter legs that are connected in parallel on a common dc bus. The circulating current is fundamentally formed by a dc component associated with the active power transfer between the converter and the dc side, in addition to a series of low-order harmonics due to the SM capacitor voltage fluctuations when attempting to maintain the voltage balance between the dc side and the converter legs. For a standard MMC, the circulating current experiences only even-order harmonics, where the odd harmonics appear anti-phase in the capacitor voltage fluctuation of both the upper- and lower-arm SMs due to the out-of-phase modulation of each arm. Since the circulating currents flow internally among the three converter legs, they do not affect the waveforms of the converter output voltage nor the current. However, they increase the conduction losses of semiconductor devices, which

reduces the efficiency of the converter and threatens the safe-operation of both the semiconductors and capacitors. Even-order harmonics contained by circulating current can be suppressed through several techniques. Accordingly, the circulating current is considered as a dc component which is calculated through a lossless power balance between the dc input and ac output as shown in (2.6), where I_{dc} is the MMC dc input current.

$$i_{circ\ j} = \frac{I_{dc}}{3} = \frac{MI_o \cos\varphi}{4} \tag{2.6}$$

2.2.5 Circulating Current Control

Generally, the circulating current harmonics can be attenuated by increasing the arm inductance, however at the expense of increased voltage drop, inductor size, and reactive power requirement [32]. Alternatively, various control methods to entirely eliminate circulating current harmonics can be utilized as introduced in the literature, using proportional integral (PI) control [33], proportional resonant (PR) control [34], and a parallel resonant filter [35]. A brief explanation for each harmonic suppression methodology is given as follows.

A. PI controller-based suppression method

This harmonics suppression method can be only implemented for three-phase MMC systems, where the circulating current dominantly pulsates in a negative sequence at twice the fundamental frequency. The control method is schematically represented in Fig. 2.5, where the circulating currents are transformed from three rotating components in the stationary frame into two dc components (dq components) in the double line-frequency negative-sequence rotational reference frame (i_{d2f} and i_{q2f}). The reference value of both d and q components of the circulating current are set to zero, while the error between the reference and the actual values of both orthogonal components are fed into conventional PI controllers. With cross coupling compensation, the control signals can be obtained from the PI controllers in the dq frame, where they are inversely transformed to obtain the three-phase reference values of the voltage unbalance. These reference values are utilized as correction signals for MMC modulation. Tuning of PI controller parameters is independent of the MMC operating frequency, where many tuning methods can be utilized as discussed in [36].

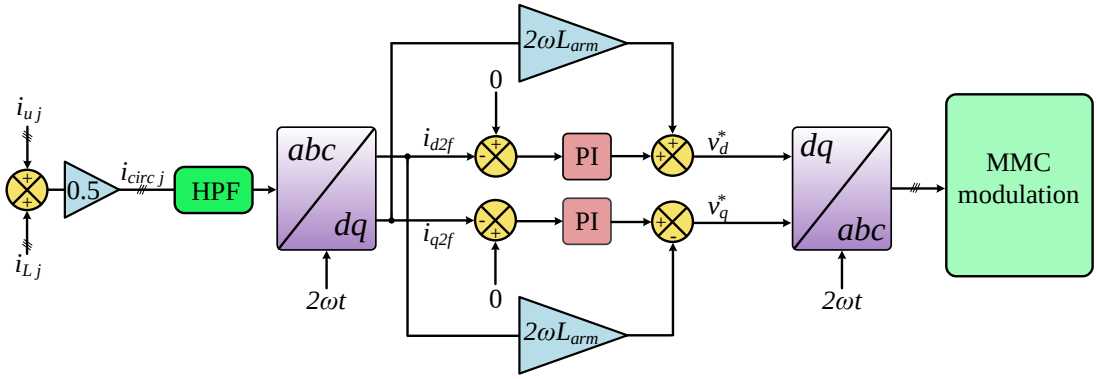

Fig. 2.5 Block diagram of circulating current control using PI controllers.

B. PR controller-based suppression method

This is a simple suppression method implemented in the stationary frame without any harmonic extraction algorithm, that is, can be applied to any number of MMC phases. The controller consists of paralleled resonant regulators, where the resonant frequency is ideally set at $2\omega, 4\omega, 6\omega$, etc., since even-order harmonics exist in the circulating current. However, not all even-order harmonic resonant controllers are essential since the harmonic current amplitude inversely decreases as the order increases. Thus, only the second- and fourth-order harmonic resonant controllers are necessary, as schematically presented in Fig. 2.6, where k_1 and k_2 are tuning parameters of both PR controllers. Since the reference circulating current is set to zero, the dc component of the circulating current may be slightly affected especially if the bandwidth of the PR controllers is not narrow. The reference output signal obtained from the paralleled PR controllers is used as a correction signal for MMC modulation.

It should be noted that when the PR controller suppression method is used with variable frequency scenarios of the MMC drive, adaptive tuning for the parameters k_1 and k_2 should be used [37].

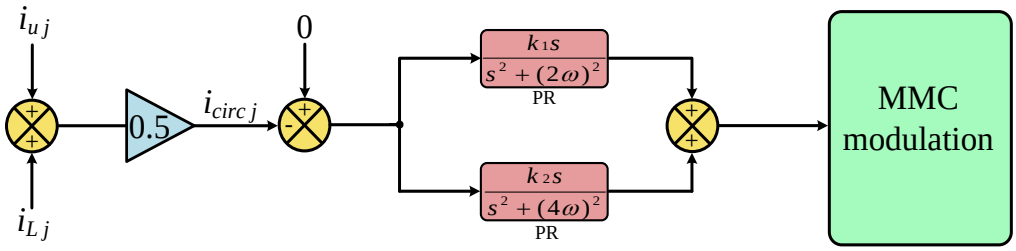

Fig. 2.6 Block diagram of circulating current control using PR controllers.

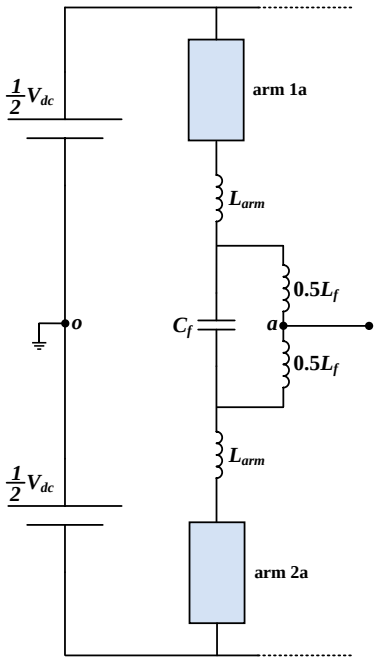

Fig. 2.7 An MMC phase-leg with a parallel resonant filter for circulating current control.

C. Parallel-resonant filter

Being the most dominant even-order harmonic in the circulating current, the second-order harmonic can be entirely eliminated by employing a hardware parallel-resonant filter in each MMC phase leg, as shown in Fig. 2.7. The resonant filter is comprised of a capacitor connected in parallel with a split-inductor. The MMC ac terminal is maintained from the split-inductor mid-point. Both the inductance (L_f) and capacitance (C_f) requirement of the resonant filter are calculated according to (2.7).

$$\sqrt{L_f C_f} = \frac{1}{2\omega} \tag{2.7}$$

A major shortcoming of this approach is that the resonant filter is not adaptive to block the second frequency harmonic when the MMC is operating at variable frequencies. Therefore, it is not suitable for variable-speed operation of MMC-fed machine drives.

2.2.6 MMC Applications

MMCs have been commercialized in several standard and customized products for medium- to high-voltage high-power applications. MMC industrial applications are

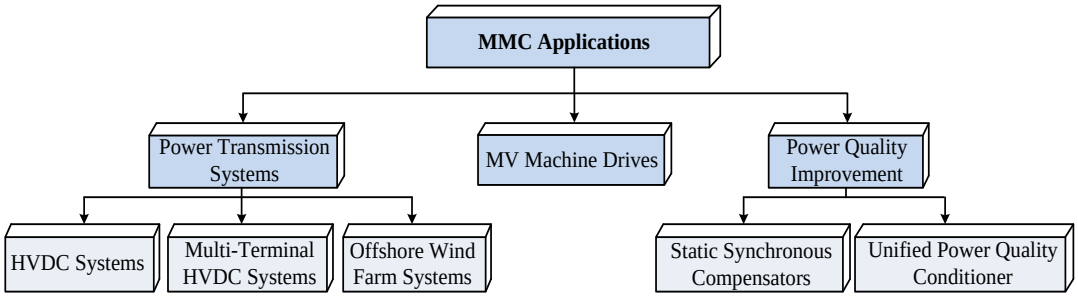

Fig. 2.8 MMC Applications.

generally itemized as power transmission systems, machine drives, and power quality improvement, as detailed in Fig. 2.8. Since the scope of this thesis is the MMC-fed MV machine drives, this MMC application will be investigated in the next section.

2.3 MMC Application for MV Machine Drives

MMCs have been an attractive solution for MV machine drive applications due to their modular structure, ease of voltage scalability, single dc-link system, and operation with standard machines without output filters. MMC-based machine drive systems are commercially available with an operating voltage range of 2.3–11 kV [13], [38], [39]. These systems are available with either a passive or an active front-end converter (ac–dc converter) at the grid side, and an MMC at the motor side. The typical system configuration of the MMC-based motor drive and its control schemes are presented in the following subsections.

2.3.1 System Configuration

In machine drive applications, power conversion is generally realized through two cascaded stages. The first stage employs an ac–dc converter (rectifier system) which converts both the fixed voltage and frequency of the ac grid supply into a dc voltage. In the second stage, the dc voltage is converted into a variable-voltage and variable-frequency ac supply at the motor terminals using a dc–ac converter (inverter system). In MMC-based motor drives, the MMC is configured as the dc–ac converter, while the ac–dc conversion stage can be implemented in two possible configurations. The first configuration adopts a diode bridge converter as a rectifier, where either 12-, 18-, or 24-pulse diode bridge rectifiers can be employed using a phase-shifting transformer,

as shown in Fig. 2.9a. Although the passive rectifier system eliminates the low-order harmonics in the line current and also improves the power quality at the grid side, the grid power factor cannot be controlled. The second configuration applies a back-to-back MMC-based topology, as shown in Fig. 2.9b, where it is suitable for regenerative applications and allows for grid power factor control. Both the transmission line and transformer leakage inductances act as a grid filter, minimizing the switching frequency harmonics and improving the grid current quality.

In the back-to-back configuration of MMC-based motor drive system, the grid-side MMC is used to regulate the dc-link voltage and to improve the grid power factor (reactive power control). These objectives can be achieved using a voltage-oriented control (VOC) scheme [40], [41]. Whereas, the motor-side MMC is used to match the drive requirements such as speed/torque and flux. To fulfil these objectives, several

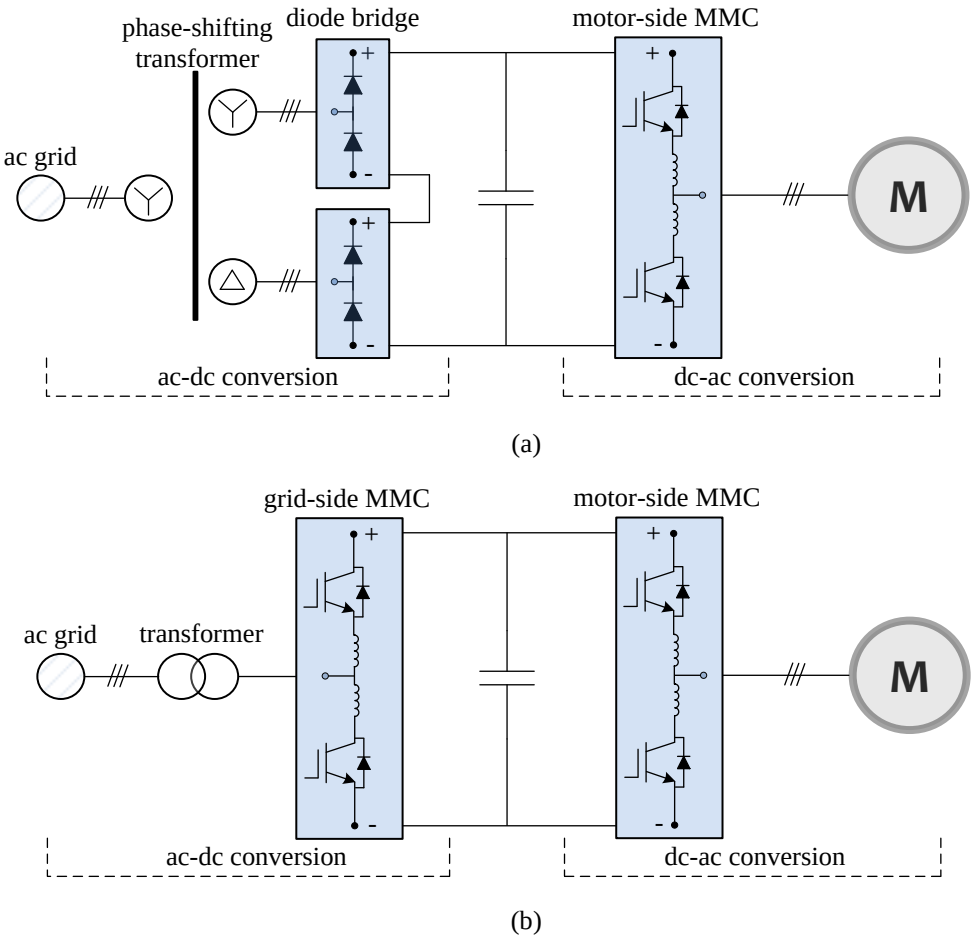

Fig. 2.9 MMC-based motor drive system using: (a) a 12-pulse passive rectifier and (b) an MMC-based active rectifier.

control methods, such as direct field-orientated control (DFOC), indirect field-orientated control (IFOC), and direct torque control (DTC), are discussed in the literature [42], [43]. These control methods are well established and used in commercial motor drive systems. In the following subsection, the VOC scheme for grid-side MMC and the IFOC scheme for motor-side MMC are discussed.

2.3.2 Control Schemes

A. VOC of grid-side MMC

VOC is a common control scheme for grid-tied converters, which offers decoupled control of active and reactive power. For the grid-side MMC, the VOC is fundamentally designed to control the dc-link voltage and the grid reactive power, generating the necessary three-phase modulation signals v^*_{abc} that are used along with any of the previously discussed carrier-based SPWM approaches to generate the SM gating signals. The VOC scheme is implemented based on transformation between the abc stationary frame and the dq synchronous frame. Thus, the grid voltage is measured and its angle θ_g is obtained using the phase-locked loop (PLL) [44]. The grid voltage angle is used in the abc- to dq-frame transformation where three-phase time-varying signals become dc components and easier to control using PI regulators. Both the three-phase grid voltages and currents ($v_{g,abc}$ and $i_{g,abc}$) are measured and transformed into the dq frame. The grid active and reactive powers in the dq frame are defined as P_g and Q_g, respectively, and are calculated as:

$$P_g = 1.5\,(v_{dg}\,i_{dg} + v_{qg}\,i_{qg}) \tag{2.8a}$$

$$Q_g = 1.5\,(v_{qg}\,i_{dg} - v_{dg}\,i_{qg}) \tag{2.8b}$$

where v_{dg} and v_{qg} are d- and q-axis grid voltage components, respectively, while i_{dg} and i_{qg} are d- and q-axis grid current components, respectively. From (2.8), both the active and reactive grid power depend on i_{dg} and i_{qg}, which increases the controller complexity and affects converter dynamic performance. The controller design can be simplified by aligning the grid voltage vector V_g along with the d axis of the dq synchronous reference frame, which is referred to as ‘voltage orientation’.

Accordingly, v_{qg} becomes zero, while v_{dg} has a constant value equal of $|V_g|$, where the active and reactive grid power components are rewritten as:

$$P_g = 1.5\, v_{dg}\, i_{dg} \tag{2.9a}$$

$$Q_g = -1.5\, v_{dg}\, i_{qg} \tag{2.9b}$$

Referring to (2.9), the VOC allows for a decoupled control of P_g and Q_g by controlling i_{dg} and i_{qg}, respectively. The control block diagram of the VOC along with the grid-side MMC circuit diagram are shown in Fig. 2.10. The control consists of two inner current control loops for the control of the d- and q-axis grid current components, and a single outer voltage control loop for dc-link voltage control.

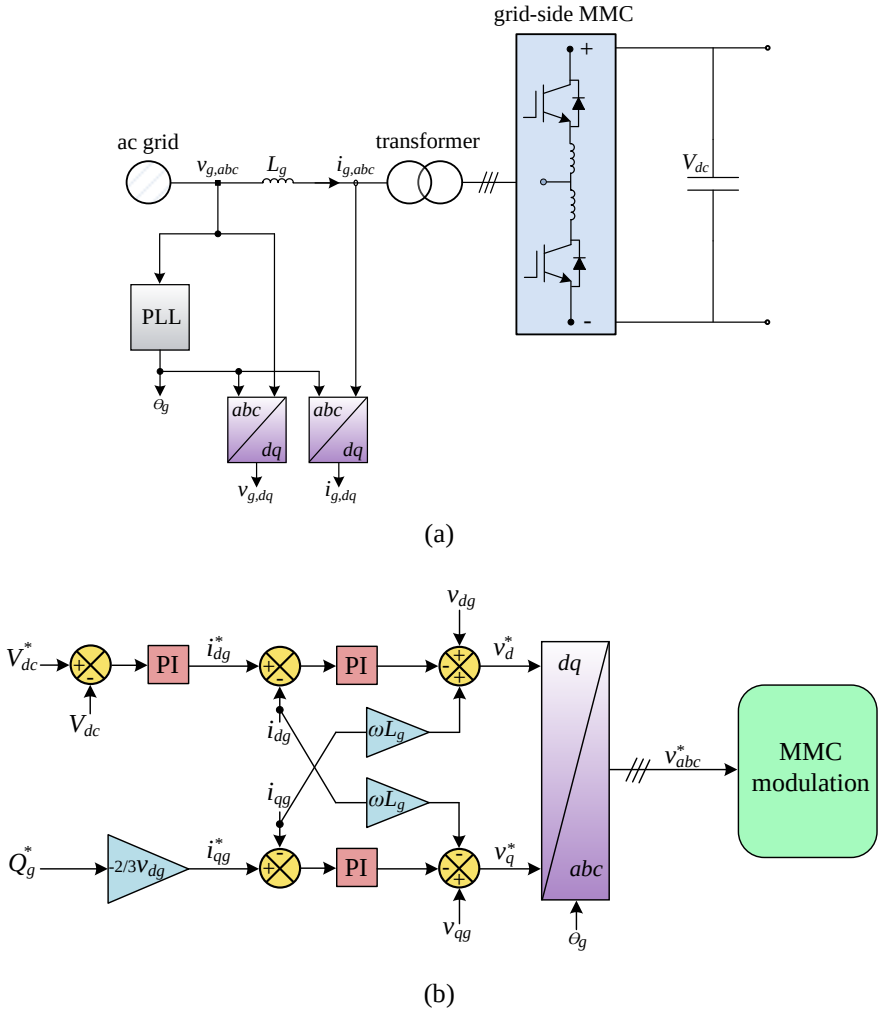

Fig. 2.10 Control of grid-side MMC; (a) circuit diagram and (b) VOC block diagram.

From (2.9), the q-axis reference current component i^*_{qg} is:

$$i^*_{qg} = \frac{{Q_g}^*}{-1.5\, v_{dg}} \tag{2.10}$$

where ${Q_g}^*$ is the reference grid reactive power which is set to zero for unity power factor operation, a negative value for leading power factor operation, or a positive value for lagging power factor operation. The d-axis current reference i^*_{dg} represents the active power of the system, and is obtained from the dc-link voltage PI regulator.

To decouple the d- and q-axis current controllers, the induced voltages across the grid inductance L_g due to the transformation from abc to dq frame are added to the control loops. The induced voltages are obtained from the state-space model of the grid-side equivalent circuit [45].

B. IFOC of motor-side MMC

The IFOC scheme is used to control both the motor speed and rotor flux, where the scheme is implemented in the rotor flux reference frame. The field orientation concept is similar to the voltage orientation in the control of grid connected systems. Typically, field orientation can be classified into stator flux, air-gap flux, and rotor flux orientations. Among them, the rotor flux orientation is simple and easy to implement for motor drives [42].

The electromagnetic torque developed by the motor drive system is a function of both the d- and q-axis rotor flux components ψ_{dr} and ψ_{qr}, respectively, and is given as:

$$T_e = K_T\, (\psi_{dr}\, i_{qs} - \psi_{qr}\, i_{ds}) \tag{2.11}$$

where K_T is the torque constant which depends on the number of motor poles and both the magnetizing and rotor inductances, while i_{ds} and i_{qs} are the d- and q-axis stator current components, respectively. Decoupled control of the rotor flux and electromagnetic torque can be achieved by aligning the rotor flux vector ψ_r along with the d axis of the synchronous dq frame. The process of rotor flux vector alignment with the d axis is referred to as 'field orientation'. As a result, the q-axis rotor flux

component becomes zero, while the d-axis component equals ψ_r. Accordingly, the electromagnetic torque is rewritten as:

$$T_e = K_T \, \psi_r \, i_{qs} \tag{2.12}$$

The stator current vector i_s can be resolved into two orthogonal current components. The d-axis current component i_{ds} is the flux-producing component, whereas the q-axis current component i_{qs} is the torque-producing one. In field orientation, the rotor flux is maintained constant at its rated value. That is, i_{ds} becomes constant and equal to its rated value, while i_{qs} is independently controlled to match the required torque demand.

In field orientation, determining the rotor flux vector position θ_f is a key issue, where several methods can be adopted. If θ_f is determined through the measured stator voltages and stator currents, then the method is referred to as DFOC. If the rotor flux vector position is indirectly obtained as a function of the measured rotor position angle θ_r and the calculated slip angle θ_{sl} as shown in (2.13), the control is termed IFOC.

$$\theta_f = \theta_r + \theta_{sl} \tag{2.13}$$

In this thesis, the IFOC approach is considered for the MMC-based motor drive system with the control block diagram shown in Fig. 2.11. IFOC uses a cascaded control structure consisting of outer rotor flux and speed control loops, and inner current control loops. In rotor flux control, the reference rotor flux ψ^*_r is generated with respect to the reference rotor speed N^*_r. When operating below the rated speed, the reference rotor flux is maintained at its rated value. Whereas, operating above the rated speed implies the reference rotor flux be reduced such that the motor is operating in flux weakening region. The reference rotor flux is compared with the estimated rotor flux ψ_r, and their difference is minimized using a PI controller providing the reference d-axis stator current component i^*_{ds}. The speed control loop minimizes the error between the reference and actual speed, providing the reference electromagnetic torque T^*_e, which is divided by the torque constant K_T to obtain the reference q-axis stator current component i^*_{qs}. The feedback dq stator current components i_{ds} and

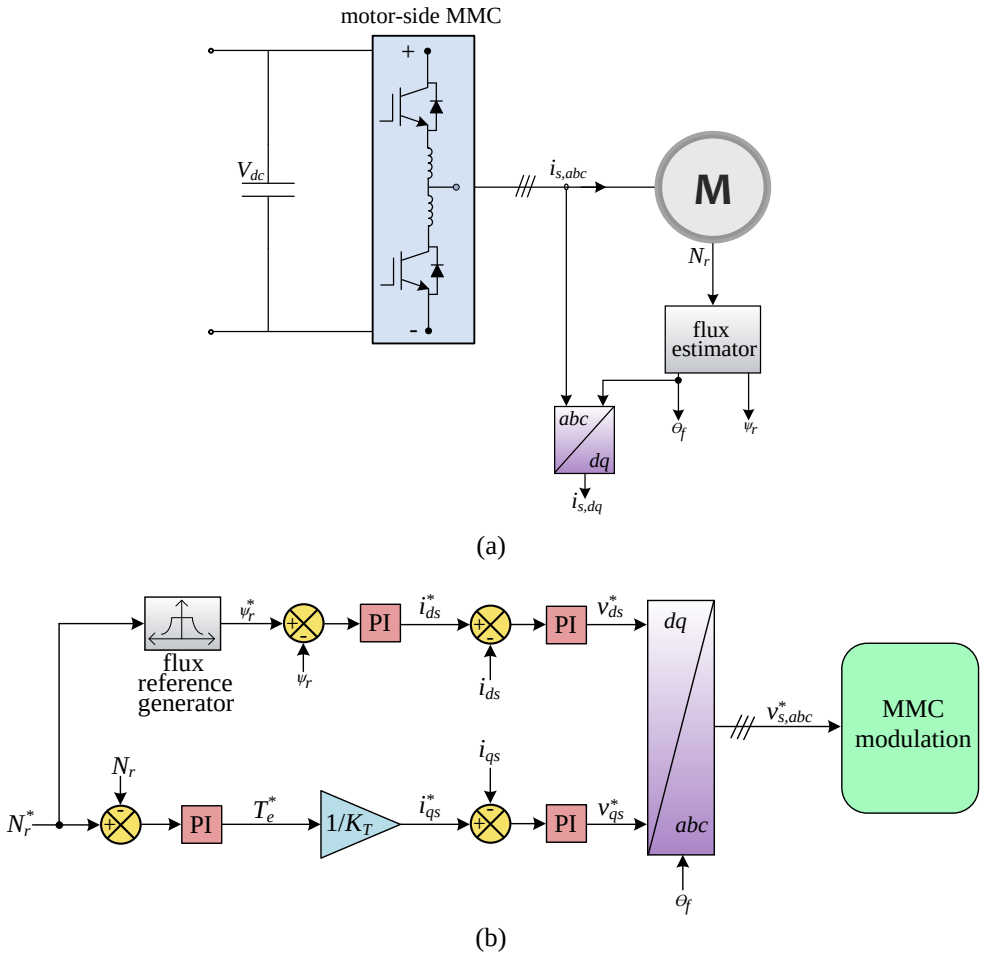

Fig. 2.11 Control of motor-side MMC; (a) circuit diagram and (b) IFOC block diagram.

i_{qs} are obtained by transforming the measured three-phase stator currents $i_{s,abc}$ in abc frame to the rotor flux synchronous dq frame. The feedback currents are compared with their references, and corresponding errors are fed to PI controllers to generate the reference stator voltages $v^*{}_{ds}$ and $v^*{}_{qs}$ in the dq frame. The dq voltages are transformed back to the abc frame, providing the reference three-phase stator voltages $v^*{}_{s,abc}$ that are used with the PWM to generate the MMC gating signals.

2.3.3 Challenges

Although the MMC has been already adopted in the industry as an MV machine drive, serious challenges impede its operation at low frequencies for variable-speed drive applications. The MMC unique operation principles imply its floating SM capacitors experience voltage fluctuation at the fundamental operating frequency. Thus, the SM

capacitance is designed fairly large to keep the capacitor voltage ripple within prescribed tolerances. At lower operating frequencies, the MMC performance is not rigid, where capacitor voltage fluctuations can reach high levels, inversely proportional to the operating frequency, that could threaten the safety of switching devices and adversely affect MMC reliability and normal operation. The increase of SM capacitance for voltage ripple compensation can be a reasonable solution, however up to some extent of reduced frequency range, although this increases both converter size and stored energy. Nonetheless, at near zero frequency, the SM capacitor voltage undergoes a unidirectional change with extreme voltage ripple, where increasing the SM capacitance is no longer viable. With this significant challenge, the MMC is not suitable to drive a machine at a constant torque while Volt/Hertz control is applied, which precludes it from many applications with variable-frequency scenarios where operation from standstill at rated current/torque and continuous low-speed operation are required. Thus, MMC-fed machine drive applications are currently constrained to a narrow range of quadratic-torque loads such as fans, pumps, and compressors [14], [46].

2.3.4 Simulation Results

To highlight the MMC challenge at low frequency operation, this subsection provides simulation results to investigate MMC performance at different operating frequencies using a 10 MW MATLAB/SIMULINK model. The MMC is fed from a 25 kV dc link voltage and is assumed to generate 13.8 kV line-to-line, that is, the modulation index is set to 0.904 at a rated frequency of 50 Hz. The MMC feeds a three-phase star-connected passive load comprising a resistor connected in series with an inductor (*RL* load). The simulation parameters are listed in Table 2.1.

It should be noted that since the ultimate scope of the simulation study is to investigate the steady state performance of the MMC at different operating frequencies, passive *RL* load can be fairly used rather than a real machine to assess the SM capacitor voltage variation. The reason is that simulating machines with available simulation tools at the megawatt power level is extremely slow due to the high inertia of the machine. However, sample simulation results for the MMC feeding real machines will be presented in Chapter 4 to assess the MMC dynamic performance.

A. Performance at rated frequency

Fig. 2.12 shows the fundamental waveforms at 10 MW steady-state operation of a conventional MMC at both the rated output current and frequency. The line voltages are shown to traverse between 17 voltage levels, while the load currents have a high quality sinusoidal profile. The upper- and lower-arm currents are controlled to suppress both the second- and fourth-order harmonic components, using the PR-based regulation method, to provide a near-constant circulating current as assumed in the mathematical analysis. The recorded peak arm current is 510 A, while the average circulating current is 135 A. The capacitor voltage ripple alternates at the fundamental frequency with $\pm$7.8%, while the SM capacitance is 2 mF. The input current has switching harmonics, with an average value of 0.4 kA.

Table 2.1: Parameters for conventional MMC simulation

Number of SMs per arm (N)	10
Rated active power	10 MW
Input dc voltage (V_{dc})	25 kV
Nominal SM capacitor voltage (V_c)	2.5 kV
Rated line voltage	13.8 kV
Rated current magnitude (I_o)	655 A
Fundamental output frequency (f_o)	50 Hz
Carrier frequency (f_c)	2 kHz
Arm inductance (L_{arm})	2 mH
SM capacitance (C)	2 mF
Load resistance	$15.5\times\frac{f_o}{50}\ \Omega$
Load inductance	24 mH

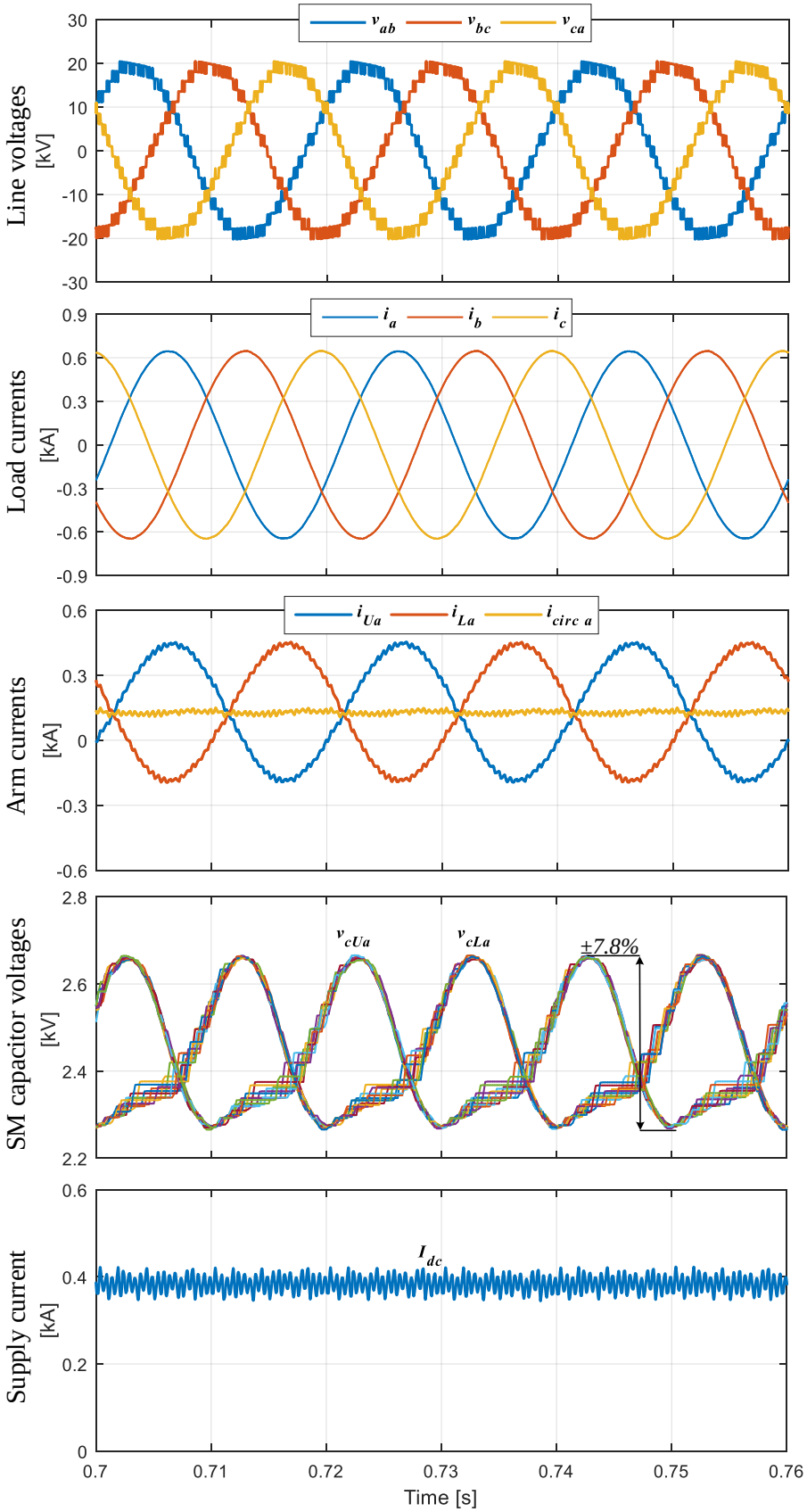

Fig. 2.12 Simulation waveforms for a steady-state operation of a conventional MMC at 50 Hz.

B. Performance at reduced frequencies

Figs. 2.13–2.15 assess the performance of the conventional MMC when operating at low frequencies, according to a Volt/Hertz control scheme, where the results are obtained for continuous operation at 10, 5, and 1 Hz, respectively. In this simulation study, the output voltage is reduced in accordance with the operating frequency reduction, while the load resistance is varied linearly with the operating frequency to maintain the output current constant at the rated value, at all frequencies, to emulate the constant torque characteristic of variable-speed motors. To compensate the increased SM capacitor voltage ripple, the SM capacitance is increased to 10 mF. Also, the arm inductance is set to 5 mH to limit the inrush current at the reduced frequencies. Although the number of voltage levels is reduced as a consequence of the operating frequency reduction, the output currents are high-quality sinusoidal waveforms at rated value, at all different frequencies. The arm currents are controlled to suppress the dominant even harmonics. The SM capacitor voltage ripple is ±8.24% at 10 Hz (see Fig. 2.13), while it is almost doubled to ±15.82% when the frequency is halved (see Fig. 2.14). At 1 Hz, the SM capacitors experience a significant increase in voltage fluctuation, where the voltage ripple is extreme as ±79.11% (see Fig. 2.15), adversely affecting the arm current control, where clear distortion appears in both the upper- and lower-arm currents.

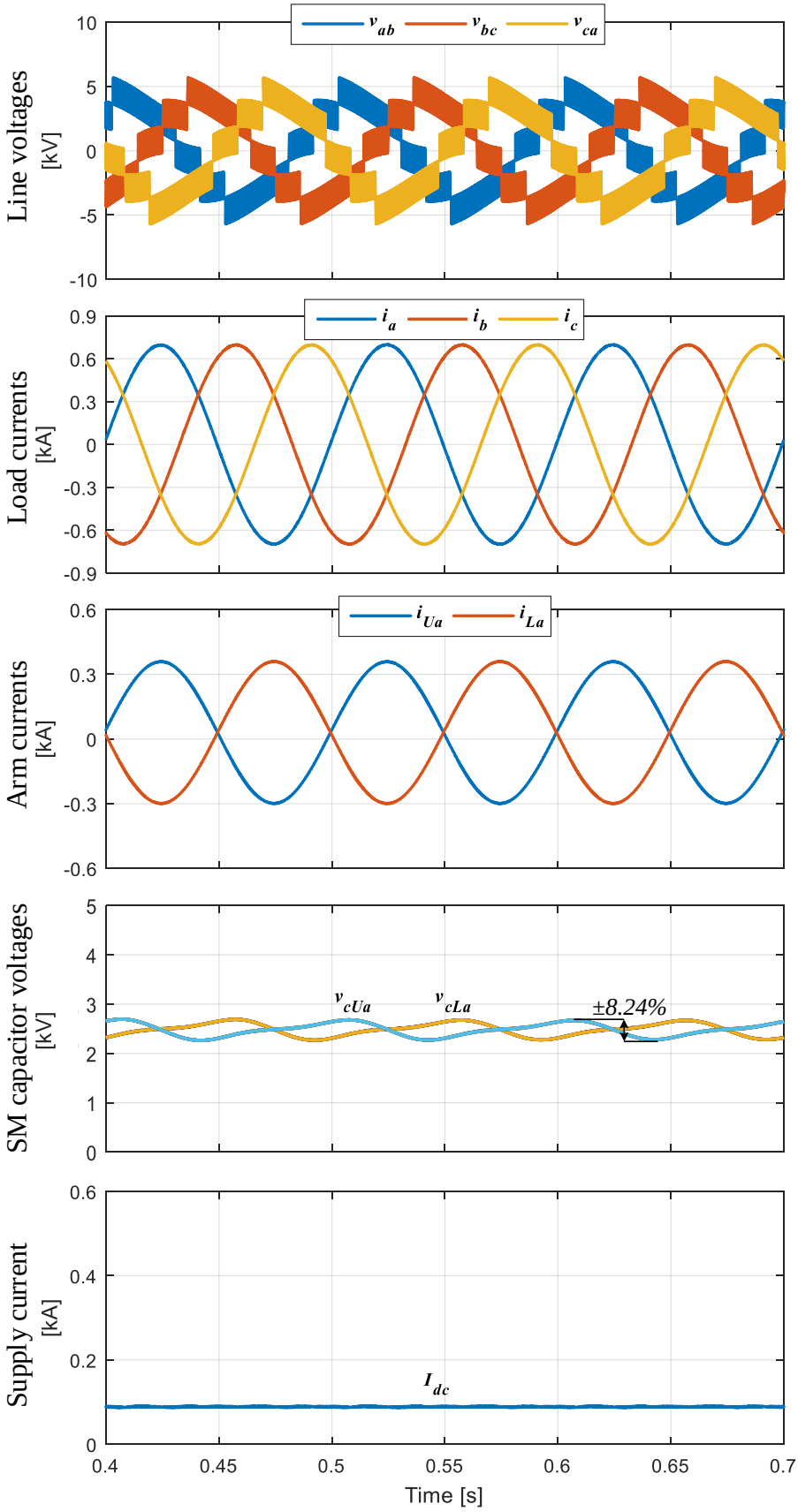

Fig. 2.13 Simulation waveforms for a steady-state operation of a conventional MMC at 10 Hz.

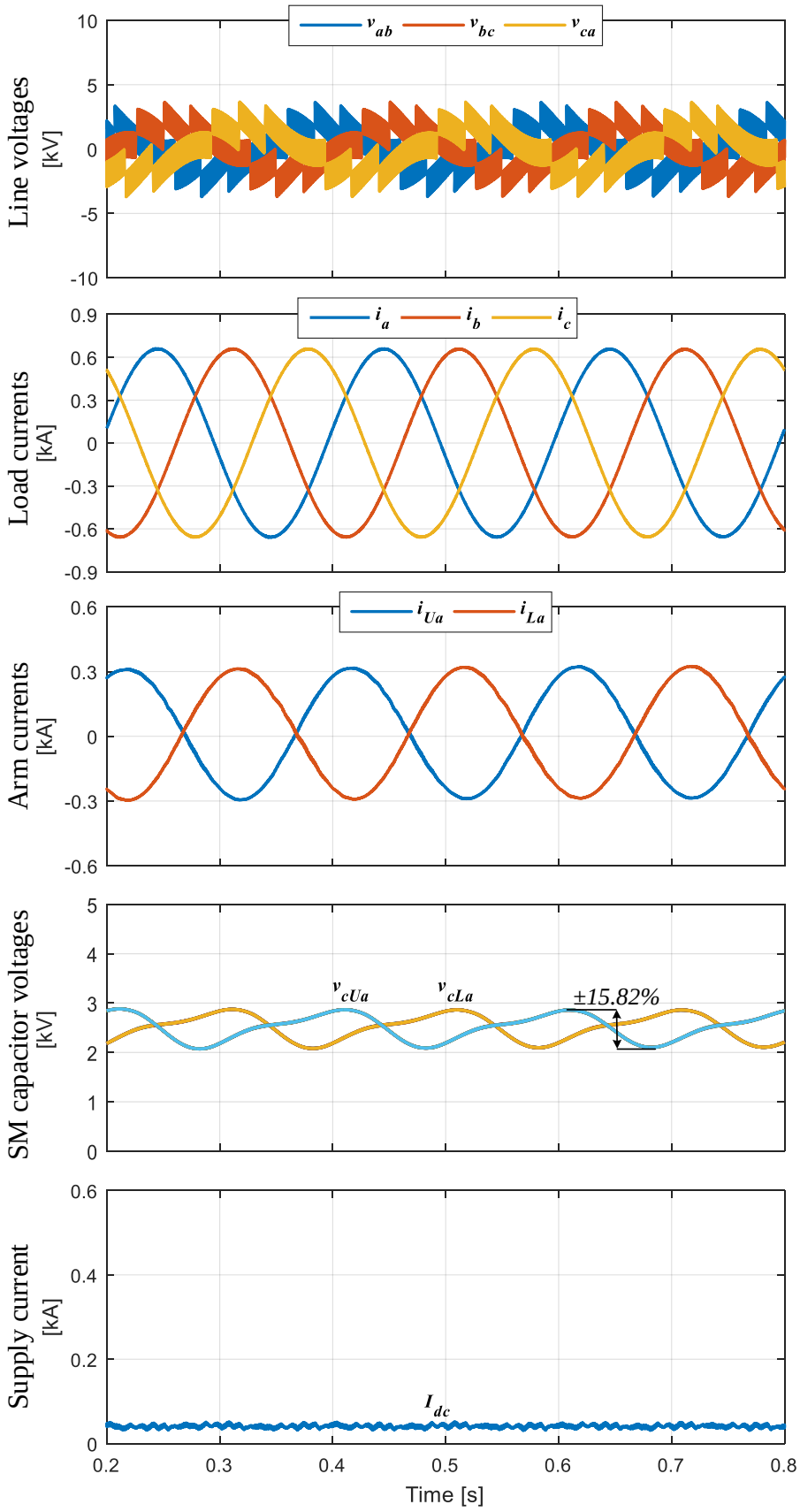

Fig. 2.14 Simulation waveforms for a steady-state operation of a conventional MMC at 5 Hz.

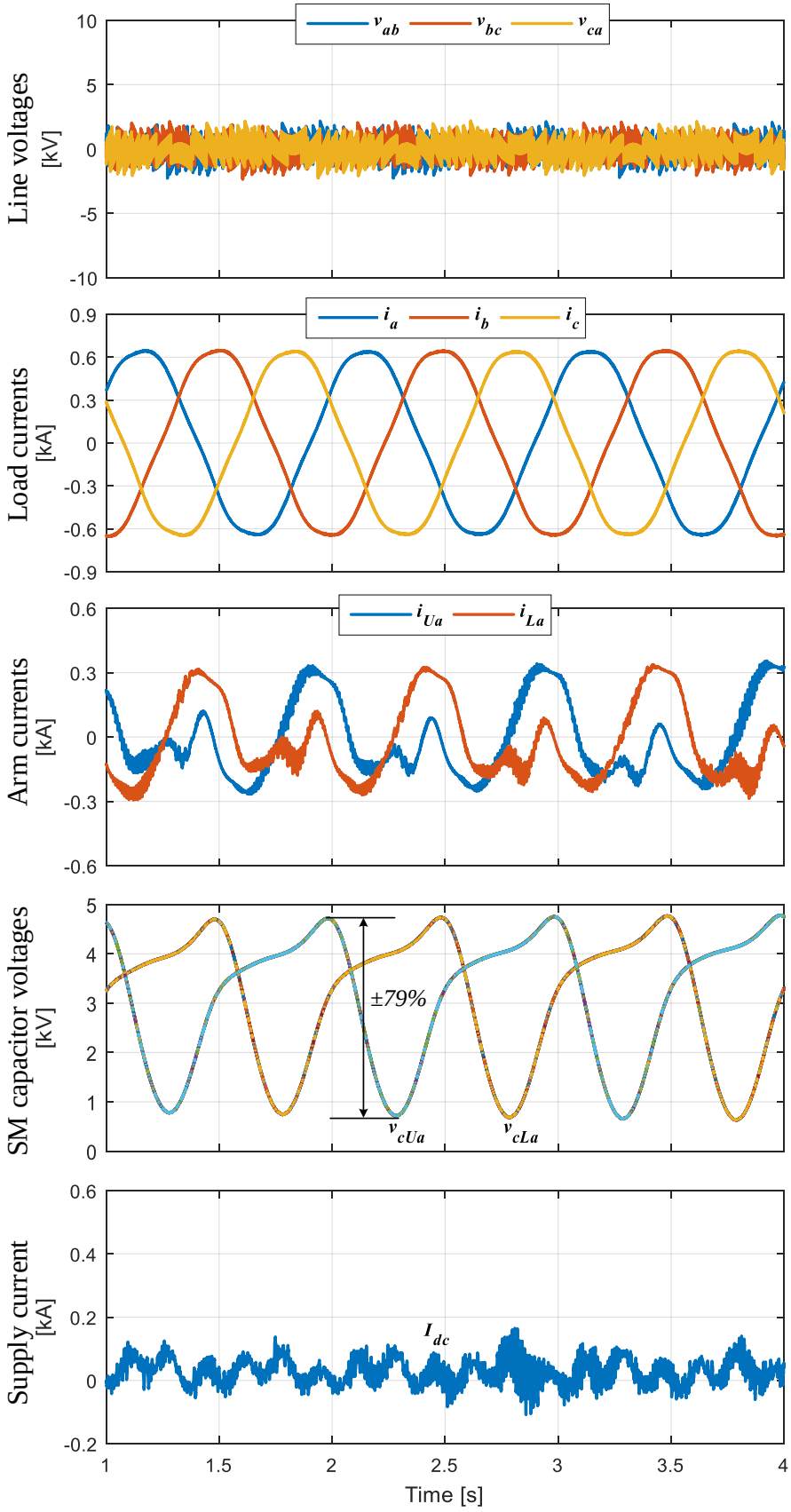

Fig. 2.15 Simulation waveforms for a steady-state operation of a conventional MMC at 1 Hz.

2.4 Summary

In this chapter, an overview of MMC fundamentals has been presented, and its applications have been highlighted with focus on MV machine drives application. The MMC is a proven technology for medium- to high-voltage high-power applications, where it has been adopted in various industry sectors. MMC application for MV machine drives has been standardized for constant-speed applications, however, the variable-speed application experiences serious challenge pertinent to SM capacitor voltage fluctuation at low operating frequencies. At reduced frequencies, the positive and negative periods of arm currents are extensively long, yielding an excessive SM capacitor voltage ripple. Increasing the SM capacitance to mitigate this voltage ripple is not a practical solution due to the associated cost and size of the MMC system. Several approaches have been introduced in the literature to extend MMC operation to reduced frequency range, while preserving its reliability and efficiency. These approaches will be discussed in Chapter 3.

Chapter 3

Literature Review of MMC-Based Machine Drives

This chapter reviews the main approaches in the literature for variable-speed operation of MMC-based machine drives. The approaches are fundamentally proposed to enhance the SM capacitor voltage ripple profile when the MMC is operating at low frequencies. The state-of-the-art approaches for MMC low-frequency operation are classified and discussed, while their pros and cons are enumerated.

3.1 Overview of MMC Approaches for Low Frequency Operation

Several approaches have been proposed in the literature to restrain the inherent problem of wide voltage fluctuations across the MMC floating capacitors at low operating frequencies. The approaches can be categorized according to their operating principle into:

1) Creating a new high-frequency (HF) ripple power to cancel the fundamental-frequency ripple power by injecting HF voltage and current into the MMC arms.
2) Changing the MMC operation mode to alleviate the sources of ripple power.

Under these two categories, various solutions have been introduced based on proposing software algorithms and applying modifications to the basic MMC structure. Most of the reported approaches are able to satisfactorily suppress SM capacitor voltage-ripple at low operating frequencies, however with unavoidable limitations or compromises. These approaches are qualitatively investigated in the next sections to quantify their gains and shortcomings.

3.2 High-Frequency Injection Methods

According to the ripple power analysis established in Section 3.1, the DM ripple power component lies behind the excessive SM capacitor voltage ripple. Thus, if HF voltage and current signals coexist in an MMC arm, they create HF ripple power that can be used to counterbalance the main pulsating power [14]. Although the established HF power stands as a new power component introduced to the MMC system, its associated voltage ripple is negligible since corresponding SM capacitor impedance is small at the injection frequency. With MMC operation enjoying two degrees of freedom, represented in the CM phase voltage v_{cm} and the circulating current i_{circ}, the HF signals can be deliberately injected into the MMC arms by controlling the waveform of both v_{cm} and i_{circ}, without affecting neither the output voltage nor current. That is, an HF voltage, v_h, is added to the converter output phase voltage and an HF CM current, i_h, is added to the circulating current, yielding new arm voltages and currents as shown in (3.1) and (3.2), respectively. A control block diagram elaborating the HF injection scheme is presented in Fig. 3.1, while the idealized waveforms for both the injected HF CM current and the resultant arm current are shown in Fig. 3.2.

$$\begin{cases} v_{Uj} = \frac{1}{2}V_{dc} - v_{jo} - v_h \\ v_{Lj} = \frac{1}{2}V_{dc} + v_{jo} + v_h \end{cases} \tag{3.1}$$

$$\begin{cases} i_{Uj} = i_{circ\,j} + \frac{1}{2}i_j + i_h \\ i_{Lj} = i_{circ\,j} - \frac{1}{2}i_j + i_h \end{cases} \tag{3.2}$$

Multiplying (3.1) and (3.2) yields the arm power comprised of a new CM and DM components generally written as:

$$p_{cm} = \frac{1}{2}V_{dc}\, i_h - \frac{1}{2}v_h\, i_j \tag{3.3a}$$

$$p_{dm} = \frac{V_{dc}\, i_j}{4}\left(1 - \left(\frac{2\, v_{jo}}{V_{dc}}\right)^2\right) - v_h\, i_h - v_{jo}\, i_h - v_h\, i_j \tag{3.3b}$$

where both terms in the CM power are HF components, resulting in negligible SM capacitor voltage ripple. Whereas, the third and fourth terms of the DM power are HF components, while the second term is the product of the HF injected signals, and is

used to counterbalance the first term which represents the fundamental-frequency ripple power.

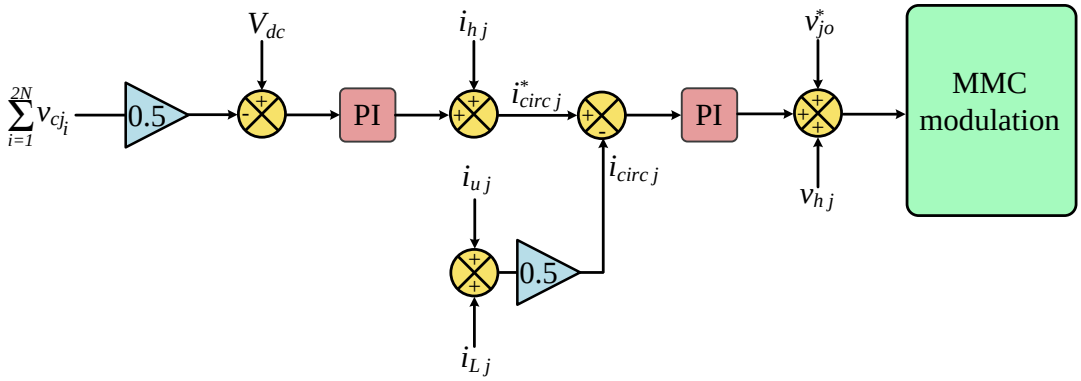

Fig. 3.1 Control block diagram of HF injection method.

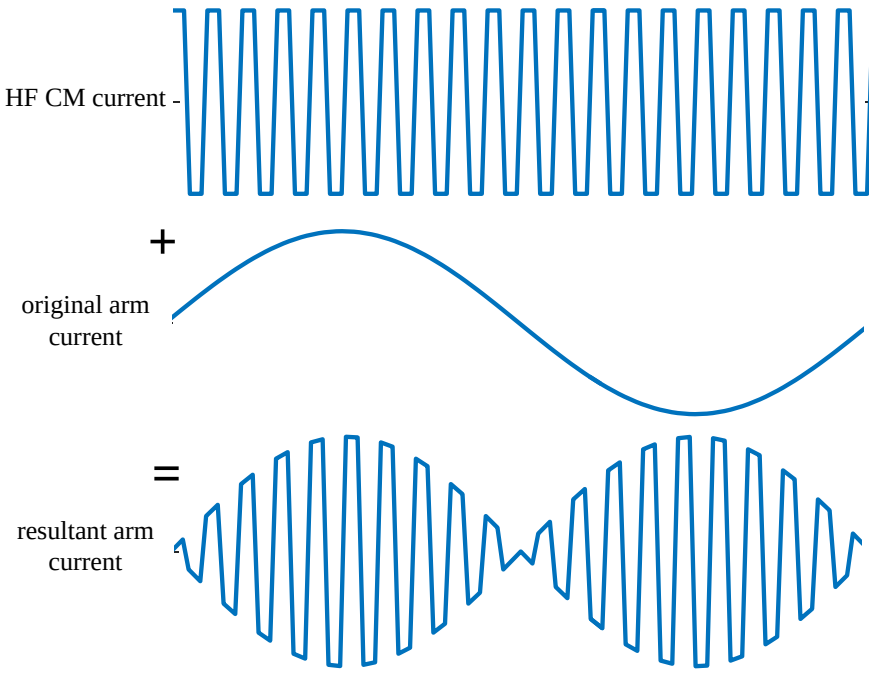

Fig. 3.2 Idealized waveforms of HF injection method using quasi-square CM current waveform.

3.2.1 Sinusoidal HF Injection

In this method, the injected voltage and current are defined as sinusoidal signals, as:

$$\begin{cases} v_h = V_h \sin(\omega_h t) \\ i_h = I_h \sin(\omega_h t) \end{cases} \tag{3.4}$$

where V_h and I_h are the magnitudes of the injected HF voltage and current, respectively, and are defined according to (3.4), while ω_h is the angular frequency of the injected signals.

$$V_h I_h = \frac{V_{dc} i_j}{2} \left(1 - \left(\frac{2 v_{jo}}{V_{dc}}\right)^2\right) \tag{3.5}$$

Substituting (3.4) and (3.5) in (3.3b) yields the DM power as:

$$p_{dm} = \frac{V_{dc} i_j}{4} \left(1 - \left(\frac{2 v_{jo}}{V_{dc}}\right)^2\right) \cos(2\omega_h t) - v_{jo} i_h - v_h i_j \tag{3.6}$$

where the DM arm power is entirely comprised of HF components. That is, the HF injection approach exploits MMC degrees of freedom to redistribute the power between the upper and lower arms, where injected signals produce HF power exchange between the arms. This allows the SM capacitors to be charged and discharged more frequently such that their voltage ripple is attenuated [12], [14], [47]–[50].

It should be noted that larger injected current results in higher power loss across MMC switching devices. Referring to (3.5), reducing the injected CM current magnitude necessitates increasing the injected voltage. Nonetheless, the injected voltage is bounded by MMC modulation index, where to avoid over-modulation, the peak injected voltage is:

$$V_h = \left(\frac{1-M}{2K_h}\right) V_{dc} \tag{3.7}$$

where K_h is a coefficient representing the modulation margin utilization, and is usually assigned between 1.05 and 1.2. Setting K_h to unity means the MMC is at the verge of over-modulation after inserting an HF voltage into the arm voltages. Accordingly, the peak injected CM current is:

$$I_h = \frac{K_h\, i_j}{1-M}\left(1 - M\cos^2(\omega t + \theta_j)\right) \tag{3.8}$$

Although the HF voltage injection is directly realized through MMC modulation, CM current injection implies tracking control (as shown in Fig. 3.1), imposing limitations on the bandwidth of the current control loop. To achieve good controllability of the injected current, the choice of ω_h must be less than $1/10$ the MMC switching frequency. Whereas, to satisfactorily mitigate the SM capacitor voltage ripple at low-operating frequencies, ω_h is recommended to be at least 4–10 times the mid-range operating frequency [51]. That is, for a 50 Hz rated frequency, the injected signals are maintained at 100–250 Hz.

Although the HF injection method is theoretically able to entirely suppress MMC arm ripple power, it experiences the following significant shortcomings:

- The CM voltage introduced at the motor terminals results in insulation and bearing current problems that harm the motor and shorten its lifetime [52].
- The injected CM current remarkably increases the MMC arm currents. This increases the current stress of the switching devices, and consequently the power loss, which necessitates oversizing the current capacity of the switching devices with higher cooling requirements.
- The injected CM current can be unacceptably high in the intermediate-speed range (when the modulation index is high), where it can be as high as three times the nominal current [12]. Therefore, full ripple power suppression is usually adopted only in the low-speed range, while it has to be either dropped or tapered off at higher speeds.
- HF injection method is more convenient with quadratic-torque loads, where both the load torque and current are relatively small at low to medium speeds, that is, necessary injected current peak can be bearable. In contrast, constant-torque loads imply constant current within the whole speed range, where the injection approach will not be so effective.
- A conflict in coordinating the intentionally injected signals control and the basic MMC control loops (such as output current control and capacitor voltage balancing control) may arise, causing stability problems during transient conditions.

Several improved injection approaches have been adopted to ultimately alleviate both the introduced CM voltage and current stress of the switching devices. These approaches are subsequently discussed.

3.2.2 Improved Injection Methods with Reduced Current Stress

To reduce the injected CM current peak, the HF injected waveforms are reshaped from a sinusoidal waveform into third-order harmonic injected sinusoidal waveform [53] and both square and quasi-square waveforms [46], [54]–[56]. Common to all modified waveforms, the fundamental component of the injected voltage is attempted to be boosted, without causing over-modulation. Equations describing the injected HF voltage using third-harmonic injected sinusoidal and square waveform are given by (3.9) and (3.10), respectively.

$$v_h = \left(\frac{1-M}{2K_h}\right) V_{dc} \left(\sin(\omega_h t) + \tfrac{1}{6}\sin(3\omega_h t)\right) \tag{3.9}$$

$$v_h = \begin{cases} \left(\frac{1-M}{2K_h}\right) V_{dc} & (0 < t \leq \frac{1}{2f_h}) \\ -\left(\frac{1-M}{2K_h}\right) V_{dc} & (\frac{1}{2f_h} < t \leq \frac{1}{f_h}) \end{cases} \tag{3.10}$$

In [53] and [57], several combinations of injected waveforms were adopted for assessment. Compared to the sinusoidal injection method, injecting a square-wave voltage and a sinusoidal CM current associated with third harmonic achieves a 33.8% reduction in the peak injected current. A further improvement to reduce the peak injected current up to 50% is achieved by adopting a square waveform for both the injected voltage and current signals. However, square-wave signals are not applicable in practical implementation, where a square-wave circulating current induces a large voltage across the arm inductors at the rising and falling transitions, which imposes serious control disturbances. Moreover, the square-wave HF voltage results in high dv/dt CM voltage at the motor terminals, threatening the lifespan of motor bearing. Thus, the quasi-square (trapezoidal) wave injection is a more practical alternative.

3.2.3 Improved Injection Methods for Full Speed Range

Since traditional HF injection methods are not practically suitable for a medium- to high-speed range of constant-torque loads, a flexible control scheme to reduce the average SM capacitor voltage at the intermediate speed range has been proposed in [12], [58], and [59]. At motor speeds in the range of 0.3–1 p.u., the HF injection scheme is dropped, while the SM capacitor voltage is varied in accordance to the motor speed by regulating both the dc and ac components of the PWM reference signal. This allows increasing the SM capacitor voltage-ripple as the motor speed decreases, where a larger capacitor-voltage ripple can be tolerated without exceeding maximum capacitor voltage limits. At speeds lower than 0.3 p.u., the traditional HF injection method is adopted to suppress the low frequency ripple power. One shortcoming of this modified HF injection approach is the high computational burden required to determine the optimal average SM capacitor voltage.

Another approach for a constant-ripple range of SM capacitor voltage for the entire speed range is suggested in [60]. In this approach, an improved circulating current injection method is proposed, which does not completely eliminate the capacitor voltage ripple, but maintains it bounded within reasonable definable values. Unlike the traditional injection method (where the injected current magnitude increases with operating frequency increase for full ripple-power compensation), the improved injection method finds a more appropriate way to utilize the injected HF current component by allowing the SM capacitors to buffer a portion of the power variation. As a result, the injected current magnitude can be reduced, yielding lower MMC power losses and reduced semiconductor current rating.

3.2.4 Improved Injection Methods with Reduced CM Voltage

To alleviate the CM voltage associated with the HF injection method, a family of modified MMC structures have been proposed in [61]–[64], employing physical power transfer channels between the MMC arms for power redistribution.

A. Vertical power transfer channels

In [61] and [62], each MMC arm is divided into two sub-arms while their conjunction nodes are drawn out to connect the middle taps of each pair of upper and lower arms

through a cross-connected branch. The branch has been realized through either N HB-SMs or a flying capacitor, yielding an active cross-connected MMC (ACC-MMC) and a flying capacitor MMC (FC-MMC), as shown in Figs. 3.3a and 3.3b, respectively.

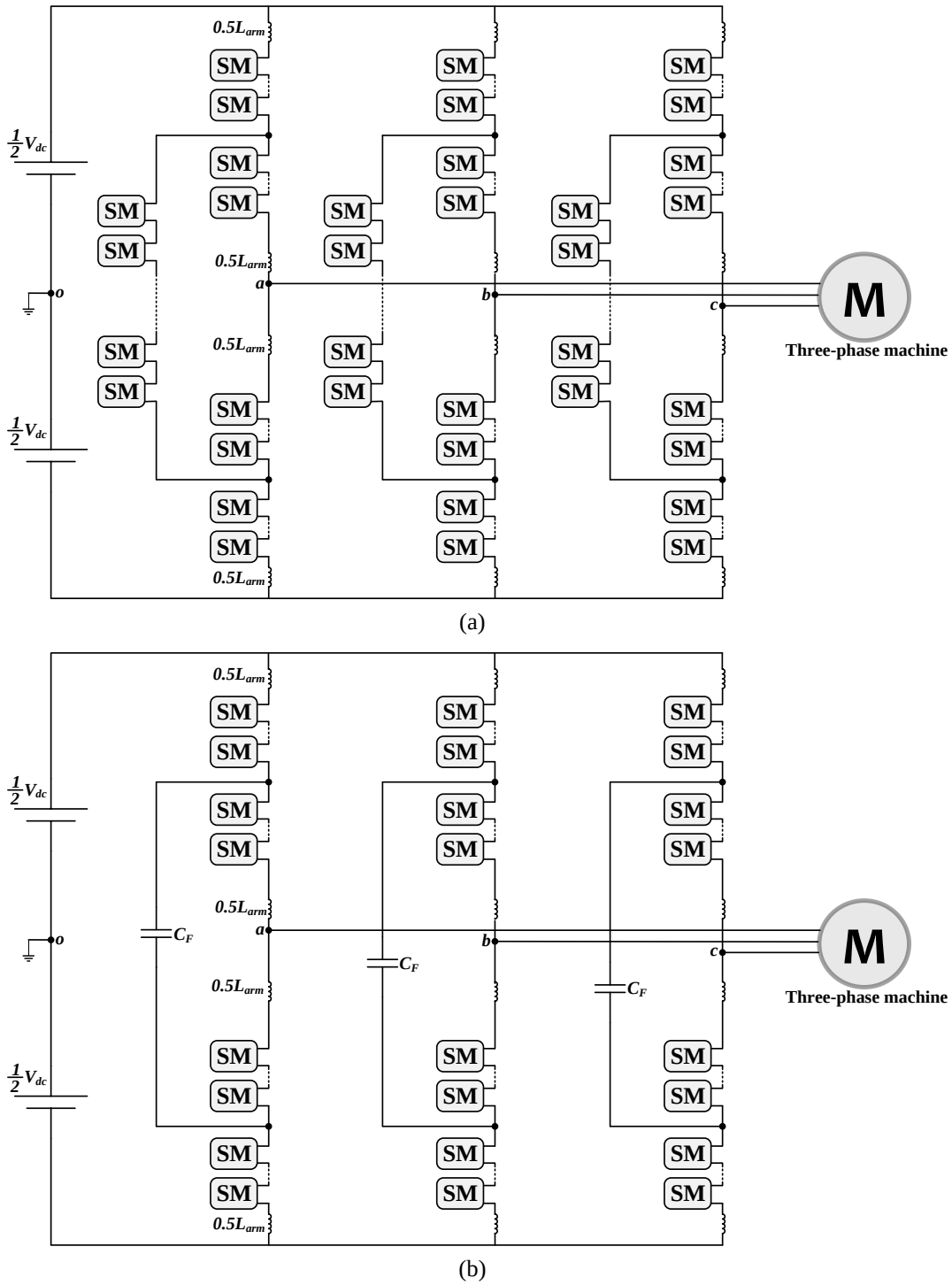

Fig. 3.3 Modified MMC configurations with vertical power transfer channel; (a) ACC-MMC and (b) FC-MMC.

The modified MMC configurations are operated under the HF injection method, where an HF voltage is intentionally introduced into the sub-arms to create one degree of freedom to redistribute the power between the upper and lower arms. The injected voltage amplitude is complementary to the output phase-voltage magnitude for full voltage margin utilization. In each arm, the HF voltages across the sub-arms are inversely arranged to cancel their effect on the dc and ac sides and to avoid a CM voltage at the machine terminals. This is elaborated in the equivalent circuit of one phase-leg of the modified configurations, as in Fig. 3.4a and 3.4b for the ACC-MMC and FC-MMC, respectively. An HF current i_h is excited by the differential voltage component in the cross-connected branch to interact with the HF voltage in the arms to redistribute the power between the upper and lower arms. When the MMC is required to operate in a low-frequency condition, each pair of MMC arms experiences unbalanced power. If the power in the upper arm is higher than that of the lower arm, an HF current flows through the cross-connected branch to maintain the upper-arm capacitors charged and the lower-arm capacitors discharged. In contrast, when the upper arm power is less than that of the lower arm, the HF current flows in a reverse direction. Referring to Fig. 3.4, the pulsating power can be transferred between U_1 and L_2 and between U_2 and L_1. Since the CM voltage at the ac terminals does not contain the HF component, the injected HF voltage is shaped as a square wave to reduce the current stress.

Both the ACC-MMC and FC-MMC inherit the same ripple power suppression performance as the traditional HF injection methods, however without inducing additional CM voltage at the machine terminals. Notwithstanding, both modified MMC configurations employ additional hardware. For each phase-leg, the ACC-MMC adopts an extra N HB-SMs, while the FC-MMC assembles a cross-connected capacitor. The FC rated voltage is half the dc-link voltage, which may limit the overall voltage rating of the FC-MMC to the medium range [65]. Also, the cross-connected FC in each phase-leg needs a pre-charging, whereas the oscillation between the cross-connected FC and the arm inductors must be mitigated during the pre-charging process to avoid a negative FC voltage, especially if a polarized capacitor is utilized. Common to both the ACC-MMC and FC-MMC, the number of SMs per arm must be even, such that the arm can be equally split into a top half and a bottom half.

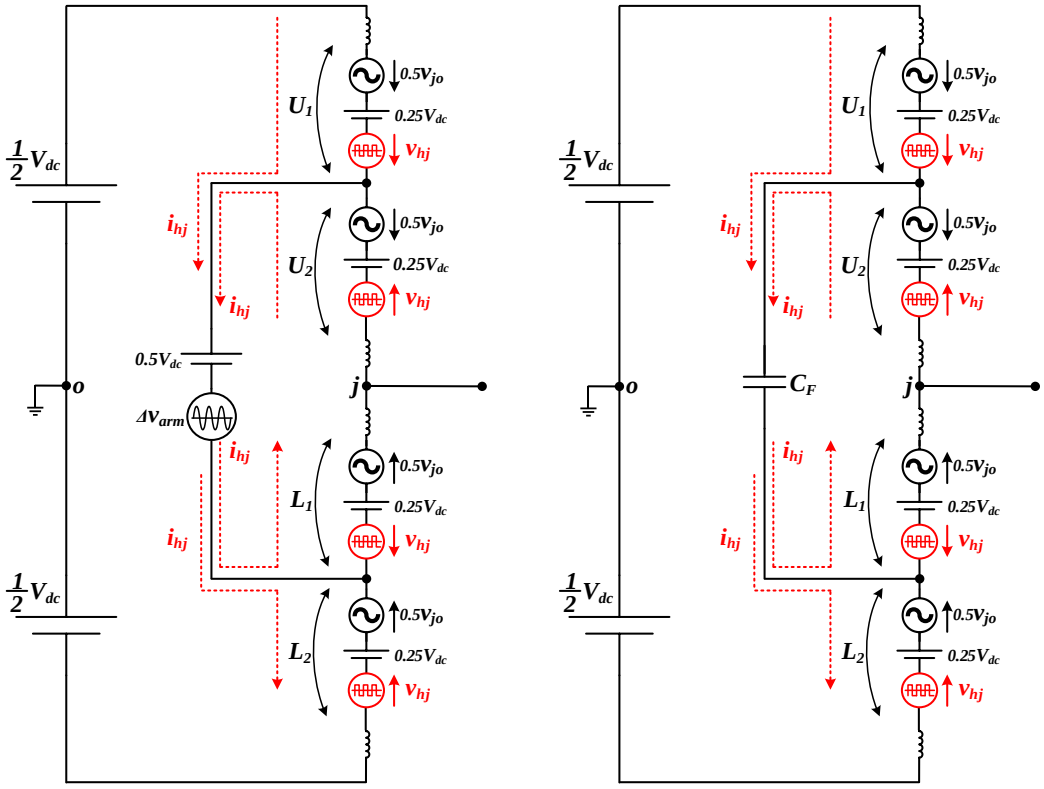

Fig. 3.4 Per-phase equivalent circuit of: (a) ACC-MMC and (b) FC-MMC.

B. Horizontal power transfer channels

In [63] and [64], the power transfer channels are realized by series connected FB-SMs assembled in either star or delta channels, yielding a star-channel and delta-channel MMC, as shown in Figs. 3.5a and 3.5b, respectively. Common to both configurations, each arm is divided into two halves, with cross connection of each set of three adjacent arms at their middle tap nodes through two sets of star-/delta-channel branches. The HF injection method is applied, where an HF voltage is inserted into the sub-arms in a reverse order such that the net added CM voltage sums to zero. Since the power fluctuations among the three phases are shifted by 120° due to the phase displacement of the three-phase fundamental components, HF currents with 120° phase shift are used to redistribute the power among the three-phase legs through the two channel sets in the upper and lower arms. The vector sum of each three HF currents in the two sets of star-/delta-channel branches is zero. The two sets of channel branches transmit the power from high-power arm to low-power ones by producing HF current i_h, as

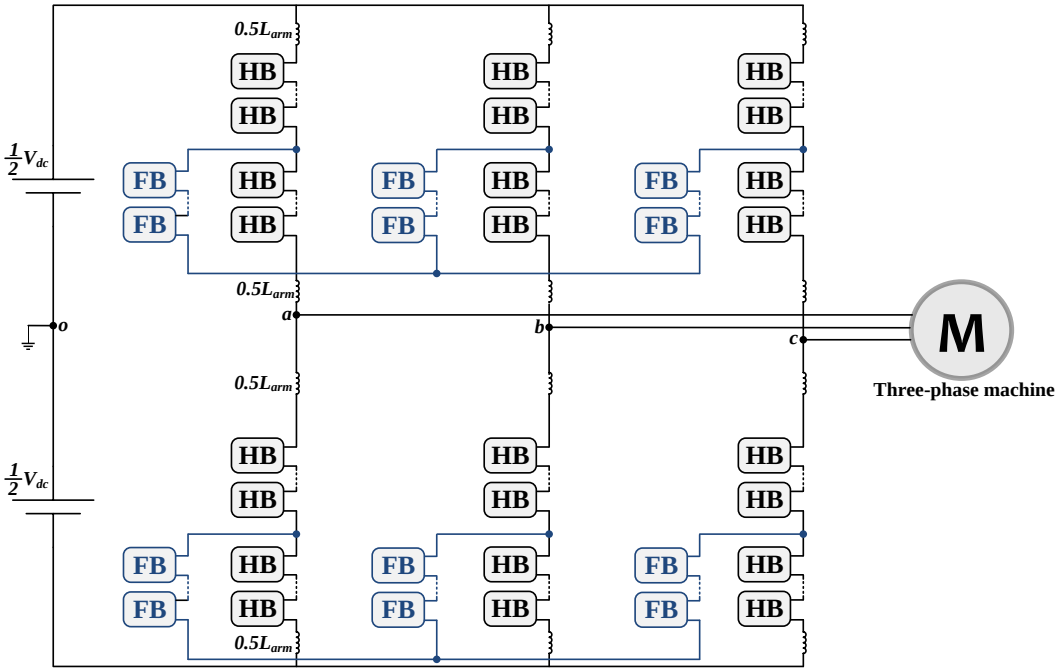

(a)

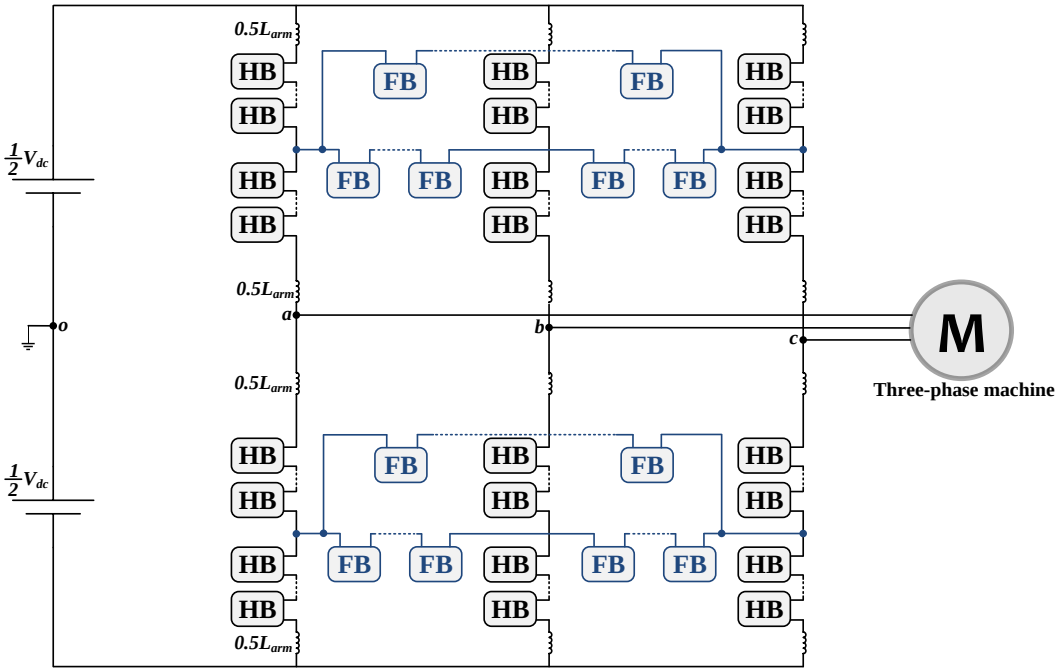

(b)

Fig. 3.5 Modified MMC configurations with horizontal power transfer channel: (a) star-channel MMC and (b) delta-channel MMC.

shown in the equivalent circuits in Fig. 3.6a and 3.6b for the star-channel and delta-channel MMCs, respectively. When the upper-arm power of phase a is larger than that of the other two upper arms, the lower-arm power of phase a is less than the other lower arms. Thus, the upper channel branch pumps power from the upper arm of phase

a by inducing HF current, transmitting the power to the other two upper arms. The lower channel branch conducts the reverse action because of the opposite power fluctuations. The rebalanced power amongst the three-phase legs leads to minimized SM capacitor voltage fluctuations. Meanwhile, the HF voltages do not appear at the ac terminals due to the automatic cancellation in the two halves of each arm.

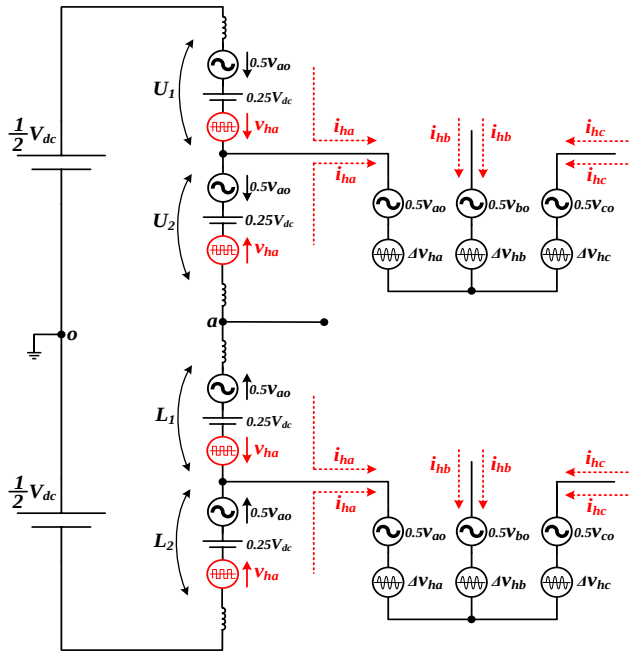

(a)

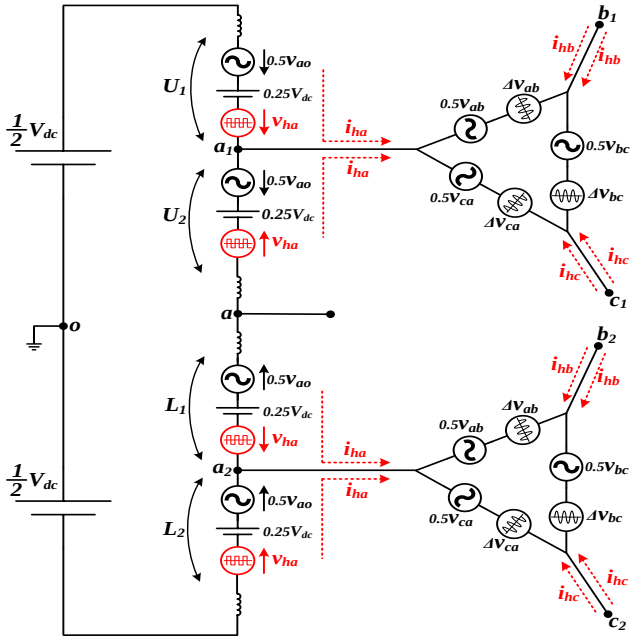

(b)

Fig. 3.6 Per-phase equivalent circuit of: (a) star-channel MMC and (b) delta-channel MMC.

Similar to the ACC-MMC and FC-MMC, both the star- and delta-channel MMCs are able to adopt HF injection methods to suppress MMC ripple power at low-operating frequencies without introducing additional CM voltage at the ac terminals, however with extra hardware. The added hardware is a series connection of FB-SMs, for a bipolar voltage requirement, assembled in either three-phase star or delta channels. The number of FB-SMs is determined based on the MMC voltage rating. That is, each branch of the star channel is synthesized by $0.25N$ FB-SMs, while each delta channel branch comprises $0.25\sqrt{3}N$ FB-SMs. Also, both the star- and delta-channel MMCs necessitate the number of SMs per arm be even, to maintain access to the arm middle tap node. Compared to the ACC-MMC, both the star- and delta-channel MMCs employ a lower number of SMs in the added power transfer channel. Nonetheless, the incorporation of FB-SMs in the power transfer channel keeps the number of extra required IGBTs in the star-channel MMC equal to that of the ACC-MMC, while the number of extra IGBTs in the delta-channel MMC is 73% higher than that employed by the ACC-MMC.

3.2.5 Injection Methods with FB-SMs

In [66], the HF injection method is applied to an MMC with FB-SMs. This results in 75% and 66% reduction in the voltage and current stresses of FB switching devices, respectively, compared to that of HB-SMs under HF injection at the same power rating. This returns to the possibility of reducing the dc-link voltage, which stands as a major culprit behind the fundamental-frequency ripple power, when operating with FB-SMs while enabling the negative-voltage state. This allows the MMC to operate in a voltage-boost mode with over-modulation. Although FB-MMC doubles the number of switching devices, the total device cost is close to the HB-MMC since the rated voltage of switching devices in FB-SMs is half that of the HB-SMs. Further, the FB-MMC has extra benefits such as the dc fault ride-through capability.

3.3 Modified Operation-Mode Methods

The inherent MMC ripple power can be attenuated by changing the MMC mode of operation, reducing the sources that are fundamentally responsible for large power fluctuation. Consequently, the SM capacitors can withstand reduced voltage ripple without adopting any suppression method.

3.3.1 MMC with Variable Average Dc Voltage

A constant ratio between the dc-link voltage and operating frequency (V_{dc}/ω) yields a constant capacitive energy fluctuation in MMC arms. In this context, several approaches have been proposed to reduce the average dc-link voltage across the MMC phase-legs at low operating frequencies. A hybrid MMC topology adopting a chopper circuit at the dc-link side has been proposed in [67] to reduce the average dc voltage delivered to the MMC. The chopper circuit is realized through a series switch, S_s, connected between MMC phase-legs and the dc-link voltage, as shown in Fig. 3.7. The switch function is to connect or disconnected the MMC circuit to/from the dc-link voltage. The switch can be realized via a series array of either IGBTs or thyristors, while an RC snubber circuit is connected in parallel with the MMC for switching harmonics filtering.

Referring to Fig. 3.7, the hybrid MMC topology operates the switch S_s with a duty cycle D, resulting in an alternating voltage across the MMC circuit as shown in Fig. 3.8. The average voltage $V_{dc\,avg}$ across the MMC circuit is given by:

$$V_{dc\,avg} = DV_{dc} + (1 - D)MV_{dc} \tag{3.21}$$

The reduction in the average voltage supplying the MMC reduces the dc component in the arm voltage, resulting in lower SM capacitor voltage ripple. The duty cycle must be properly selected to achieve a balance between the dc and ac powers. For constant-torque loads, the duty cycle is equal to the modulation index ($D = M$). At low operating frequencies, the average dc voltage across the MMC circuit cannot be lowered to near zero. Thus, SM capacitor voltage ripple increases at extremely low speeds, calling for larger SM capacitance. That is why a method to decrease the

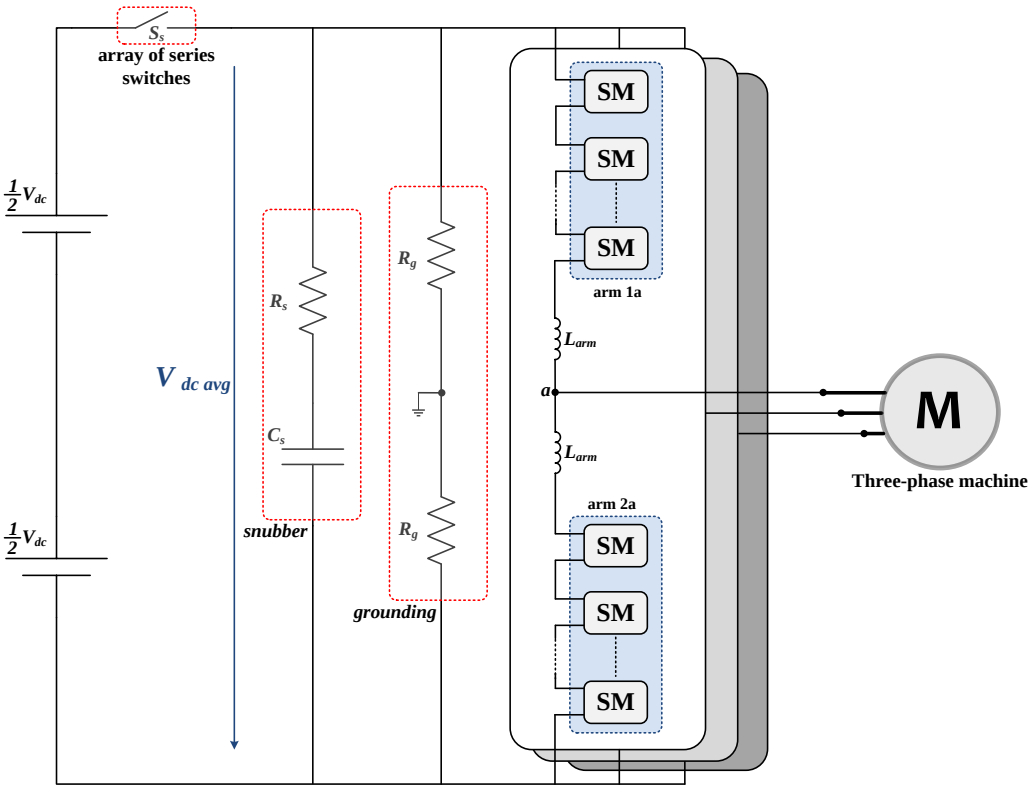

Fig. 3.7 Hybrid MMC with series switch.

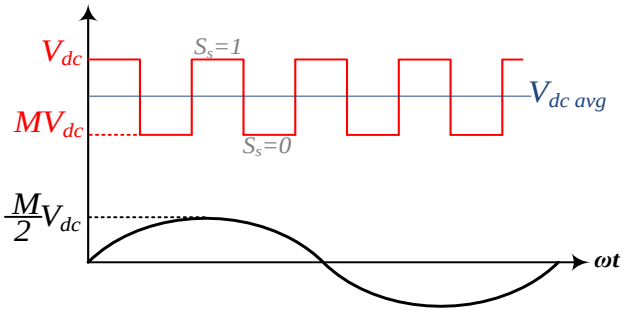

Fig. 3.8 Sketch map of ac output voltage and reduced average dc voltage of the hybrid MMC.

average SM capacitor voltage of the hybrid MMC is presented in [68] to efficiently drive the machine at extremely low speeds without significantly increasing the SM capacitance, where the nominal SM capacitor voltage is reduced such that a larger voltage ripple can be tolerated.

Since the input switch S_s blocks the full dc-link voltage, an array of series connected switches is needed, which raises concerns with complicated voltage-sharing circuits. As an alternative, the dc-link voltage can be maintained variable using a combination of thyristors and diode rectifiers, as shown in Fig. 3.9 [69]. This approach achieves

step regulation of the dc-link voltage according to the motor speed, where the average dc voltage across the MMC circuit can be reduced to 25% of the full dc-link voltage, resulting in a 75% reduction in the corresponding SM capacitor voltage ripple at 0.25 p.u. speed.

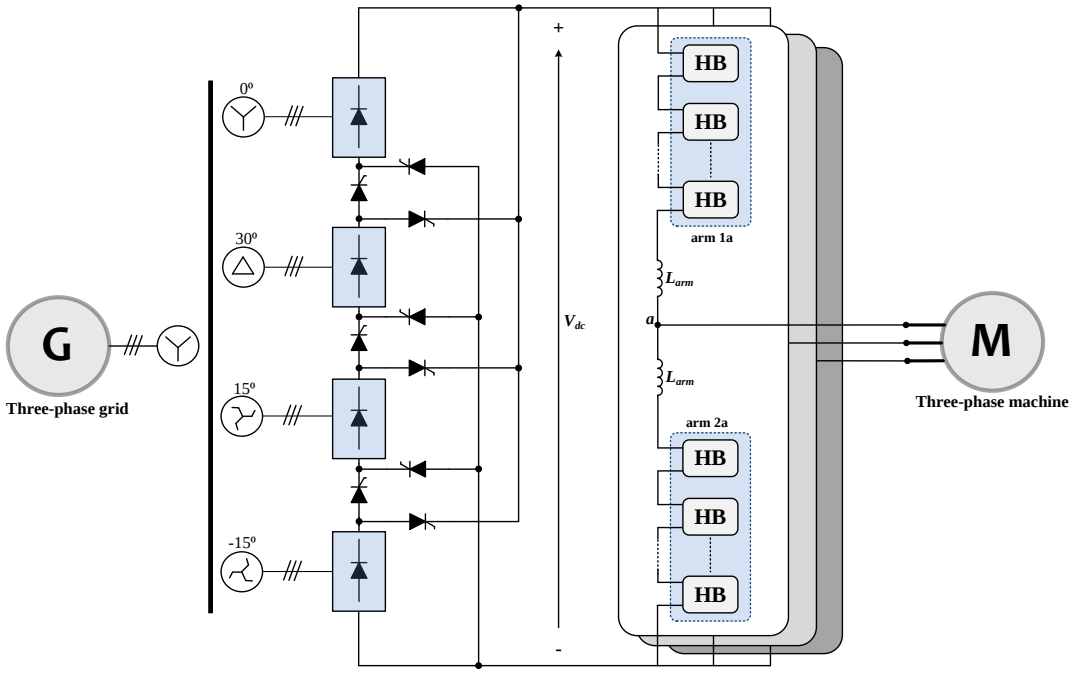

Fig. 3.9 MMC configuration supplied from a combination of thyristors and diode rectifier.

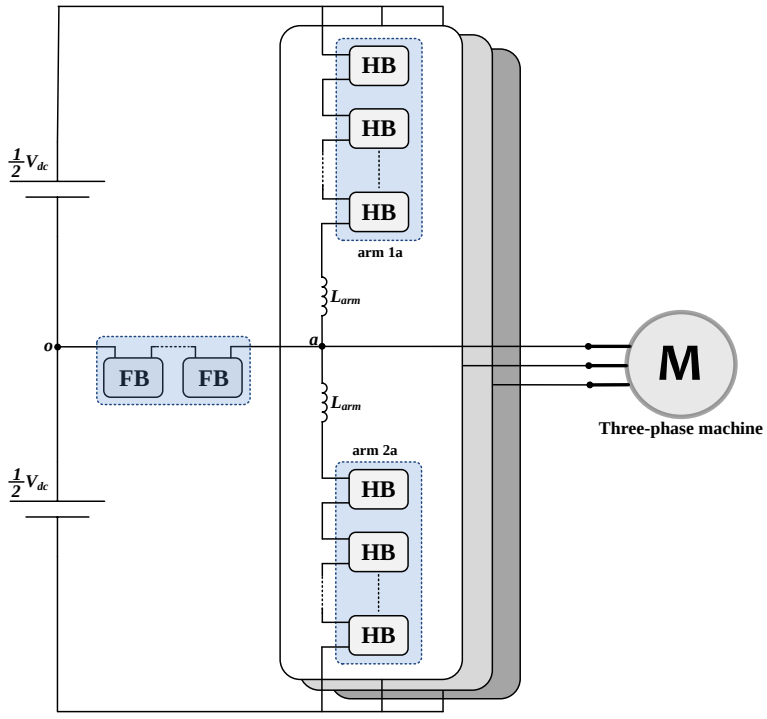

Fig. 3.10 T-type MMC.

A similar approach is presented in [70], where a T-type MMC employs $0.5N$ FB-SMs between the midpoint of the dc-link voltage and the midpoint of each phase-leg, as shown in Fig. 3.10. When the output voltage (frequency) is lower than 0.5 p.u., either the upper or lower arm is used together with the FB arm to realize half the dc-link voltage as the main supply. Accordingly, both the dc and ac components in the arm voltage are reduced by 50%, which reduces the SM capacitor voltage ripple by the same ratio. When the output voltage is higher than 0.5 p.u., the upper and lower arms are traditionally operational as a standard MMC.

In [71], a front-end MMC with FB-SMs is adopted as a grid-side rectifier not only to control the grid current to be sinusoidal and in phase with the grid voltage, but also to generate a constant dc current at the output. The regulated dc current is used to supply another MMC, connected in cascaded in a back-to-back configuration, to drive a three-phase machine, as shown in Fig. 3.11. The configuration is suitable for regenerative applications of the drive system, such as railway traction drives, since the power flow can be bidirectional. When a current source replaces the voltage source in a standard MMC topology, the equivalent dc-link voltage across MMC phase-legs is proportional to the operating speed of a machine running at a constant torque; that is, the ratio V_{dc}/ω is constant. When the motor runs at high speeds with light loading condition, the output voltage required at the motor terminals is high while the power is relatively low. To ensure power balance, the dc-link voltage cannot be too high, where the motor-side MMC must be able to generate high ac output voltage from low dc-link voltage. Thus, FB-SMs are adopted at the motor-side MMC. At standstill or ultra-low speeds, the ratio V_{dc}/ω cannot be maintained constant, where the dc-link voltage is required to be boosted to meet the motor constant-torque requirement. Therefore, the authors in [72] suggested employing HF injection methods to compensate the effect of the ripple power associated with the boosted dc-link voltage, to maintain the SM capacitor voltage ripple constant.

To reduce the component count employed by the back-to-back FB-MMC configuration, the grid-side MMC was modified into a hybrid version, employing FB-SMs only in the upper arms, while the lower arms are comprised of HB-SMs. Also, the motor-side FB-MMC was replaced by an HB-MMC [73].

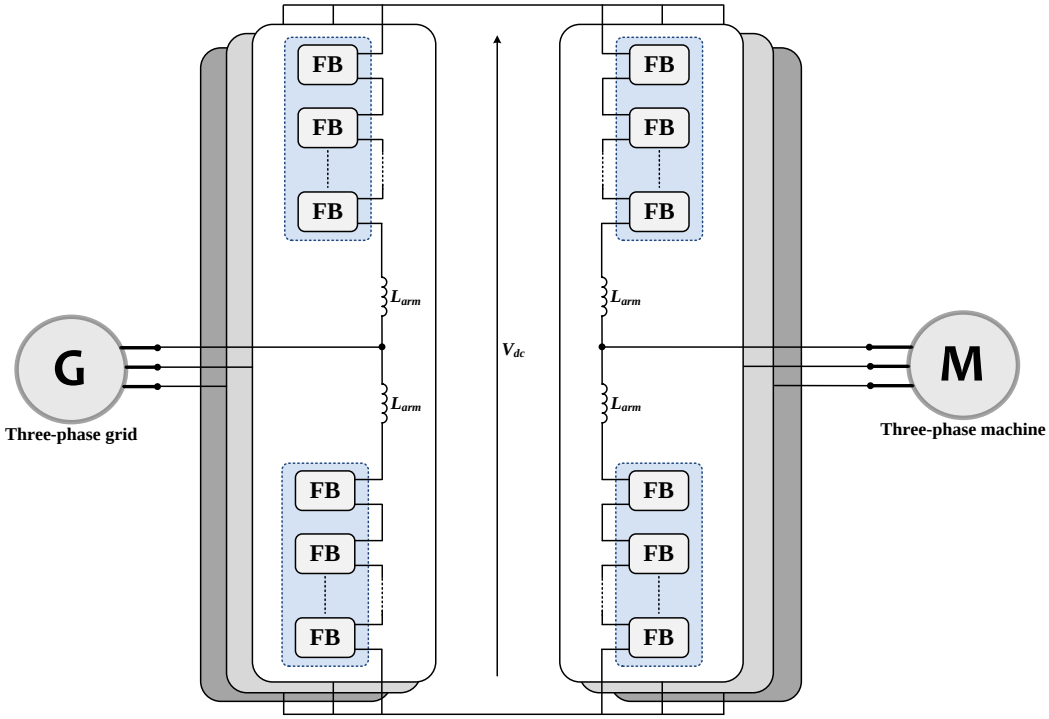

Fig. 3.11 Back-to-back MMC configuration using FB-SMs.

3.3.2 Quasi two-level Operation Mode

Quasi two-level (Q2L) operation mode was first proposed in [74] for NPC multilevel inverters, to facilitate the capacitor voltage control. In [75], the concept has been applied to MMC-based dc-dc converters for HVDC applications, achieving a significant reduction in SM capacitance. Recently, the Q2L operating mode has been combined with triangle-carrier-based PWM technique in order to emulate the PWM VSI operation using the MMC topology [76]–[80]. In this operation mode, the MMC generates PWM voltages with a controllable dv/dt by briefly employing the SM capacitors to synthesis intermediate voltage steps between the two dominant voltage levels of the ac output voltage. Thus, the SM capacitors are switched on/off in a delayed manner relative to each other, such that the rising and falling rates of the generated voltage are realized through a staircase waveform as shown by the idealized sketch in Fig. 3.12. The time spent at each intermediate voltage level is denoted as the dwell time, T_d, which is selected small enough (few microseconds) to reduce the energy storage requirement per SM capacitance for a given voltage-ripple.

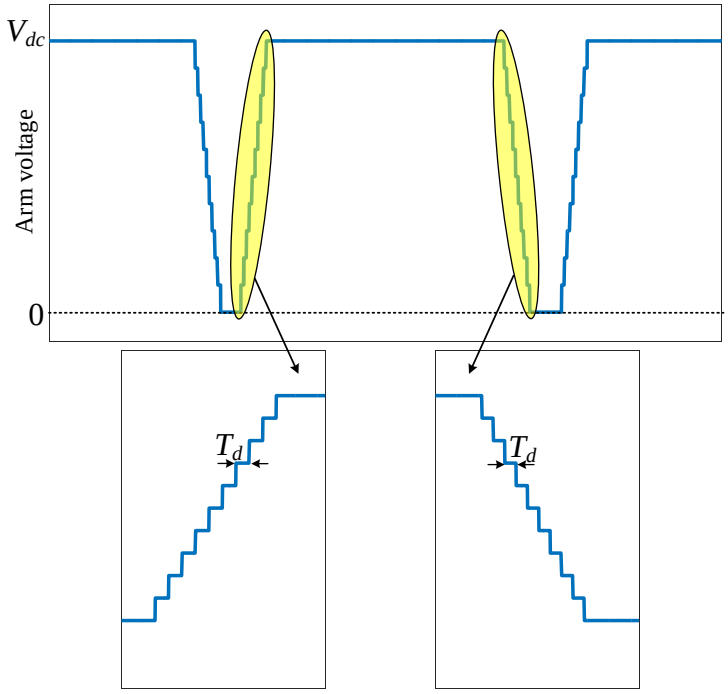

Fig. 3.12 Q2L approximation for two PWM switching cycles.

The Q2L-PWM operation mode needs to control both the upper and lower arms to conduct the load current in a complementary manner. At steady state, when the load current flows through either arm, all SMs of that arm are bypassed and those of the opposite one are attached to the dc link. Except for the brief switching times, high voltage and large current do not appear simultaneously in both arms. That is why there is no long-time charge or discharge for SM capacitors, which limits capacitor voltage fluctuation to short current transition times during commutation between two arms. Also, the inrush current due to the imbalance between the dc-link voltage and the sum of voltages across the SM capacitors will be considerably limited, resulting in a diminutive arm inductance which can be realized through parasitic inductance of connection paths. MMC operation under Q2L-PWM mode is further elaborated with the idealized waveforms shown in Fig. 3.13.

Although the Q2L PWM-based MMC efficiently operates at low frequencies with diminished SM capacitance, the multilevel property is lost. Thus, standard multilevel harmonic characteristics are sacrificed, compared to the traditional operation mode, causing current distortion at both the dc and ac sides. That is why a filtering capacitor must be installed at the dc side, while additional LC filter may

be installed at the ac output stage if machine inductance is not sufficient for current filtering at low operating speeds. Similar to a traditional two-level VSI, the Q2L-PWM mode implies both the upper and lower MMC arms carry the full load current, in a complementary manner. This doubles the current stress of the switching devices, compared to a normal multilevel operating mode. Also, a high CM voltage is unavoidable across the machine terminals, however with reduced dv/dt, since the sum of the three Q2L-PWM output voltages is significantly high.

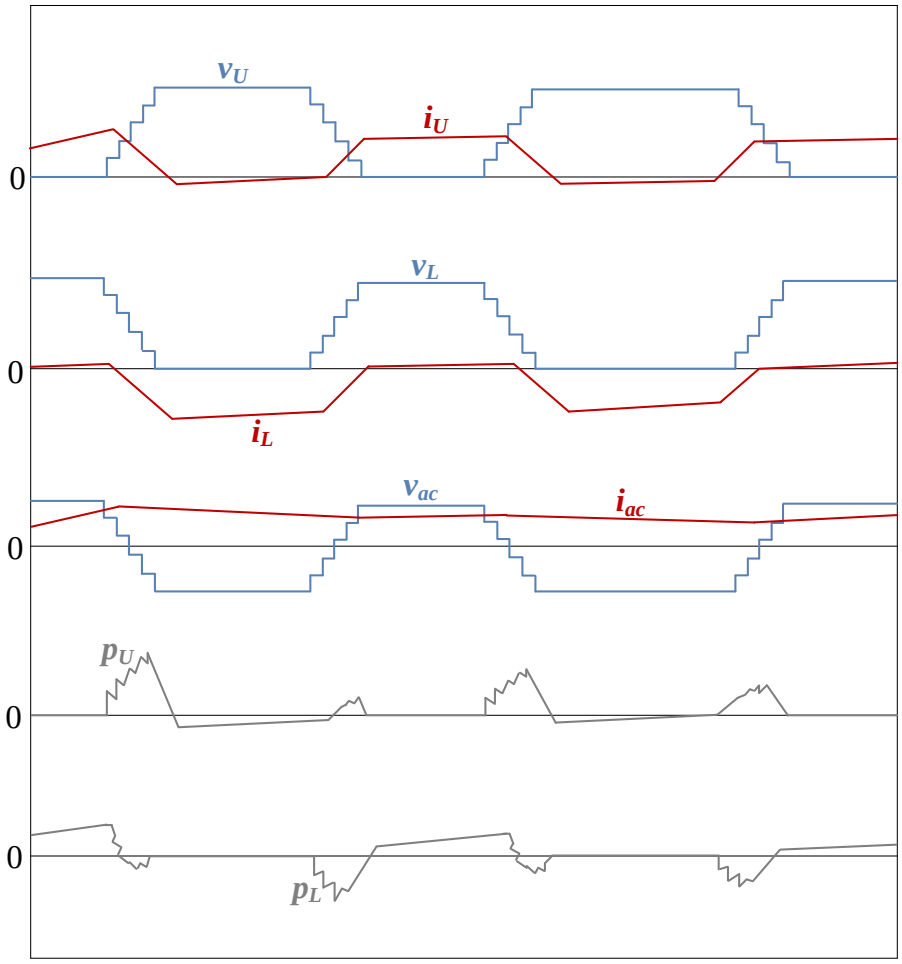

Fig. 3.13 Idealized waveforms of Q2L-PWM MMC operation mode for two PWM switching cycles.

3.4 Summary

In this chapter, the main approaches to suppress MMC fundamental ripple-power, for variable-speed drive applications, have been reviewed. A brief assessment is presented in Table 3.1, listing the main advantages and disadvantages of the different approaches, their ability to provide constant-torque operation over the full speed range, and whether they incur additional CM voltage and hardware.

The HF injection method is the mainstream solution to extend the MMC operation to low frequencies. Despite being a software-based solution, additional hardware has been combined with the HF injection approach for CM voltage reduction. Yet, both the software-based and promoted hardware-based HF injection methods increase the arm current magnitude, thus increase the power loss, compared to a standard MMC with traditional modulation. Although the research focus is directed to optimizing the injected signals waveform and altering the implementation method, there is remaining concerns to be overcame pertinent to tracking the HF circulating current at the limited switching frequency and providing a near-zero-frequency and standstill operation at the full-load torque. Other introduced methods achieve satisfactorily performance when operating at reduced frequencies, but with unavoidable trade-offs. Common to all reviewed approaches, no detailed verification has been provided for machine drives with scores of megawatts at the higher limit of the MV range. This raises concerns about the extendibility of these approaches for high-power drive systems, where increasing the dc-link voltage and load current decidedly alters the performance.

Table 3.1: Assessment of MMC approaches for low-frequency operation

	Constant-torque full speed range	**Additional CM voltage**	**Additional Hardware**	**Key advantages**	**Key disadvantages**
Sinusoidal HF injection	✗	✓	✗	Easy to track sinusoidal injected current	High current stress High CM voltage
Improved injection methods with reduced current stress	✗	✓	✗	Reduced current stress	High CM voltage Hard to track square wave injected current
Improved injection methods for full speed range	✓	✓	✗	Constant voltage-ripple within entire speed range	Hard to optimize SM capacitor nominal voltage
Improved injection methods with reduced CM voltage	✗	✗	✓	Reduced CM voltage	Massive hardware for only reduced CM voltage
Improved injection methods with FB-SMs	✗	✓	✓	dc fault ride-through capability	Doubled number of switching devices, compared to HB-SMs
Reduced dc voltage	✗	✗	✓	Easy implementation	Array of series switches [67] Phase-shifting transformer [69]
Back-to-back current-source MMC configuration	✓	✗	✓	Suitable for regenerative applications	Extra cost and complicated control strategy
Q2L-PWM operation mode	✓	✓	✗	Diminished SM capacitance	Multilevel property lost

Chapter 4

New MMC Topologies for Variable-Speed Drives

This chapter presents a family of new MMC configurations applying a ripple power decoupling approach between SMs, for capacitor voltage ripple compensation. The power decoupling approach employs energy balancers at the SM level, enabling the MMC arm ripple power be transferred from one SM to another for energy equalization. This results in a significant reduction in SM capacitor voltage ripple, offering reliable MMC configurations able to efficiently drive variable-speed machines over a wide range of operating frequencies at rated torque condition.

4.1 MMC Ripple Power Analysis

This section illustrates the problem to be solved by presenting the analysis of MMC arm power and SM capacitor voltage-ripple in order to characterize their different frequency components. The analysis is conducted for a general phase-leg *j* of the MMC system.

4.1.1 Arm Ripple Power

Referring to Fig. 2.1, the instantaneous MMC arm power is given as the product of the arm voltage and the corresponding arm current:

$$\begin{cases} p_{Uj} = v_{Uj}\, i_{Uj} \\ p_{Lj} = v_{Lj}\, i_{Lj} \end{cases} \tag{4.1}$$

Recalling (2.1)–(2.6) and substituting (4.1) yields:

$$p_{Uj} = \frac{V_{dc}\, I_o}{4}\left[\cos\left(\omega t + \theta_j - \varphi\right) - \frac{M^2}{2}cos(\varphi)\, cos\left(\omega t + \theta_j\right) - \frac{M}{2}cos\left[2\left(\omega t + \theta_j\right) - \varphi\right]\right] \tag{4.2a}$$

$$p_{Lj} = \frac{V_{dc}\, I_o}{4}\left[-\cos\left(\omega t + \theta_j - \varphi\right) + \frac{M^2}{2}cos(\varphi)\, cos\left(\omega t + \theta_j\right) - \frac{M}{2}cos\left[2\left(\omega t + \theta_j\right) - \varphi\right]\right] \tag{4.2b}$$

By rearranging the terms of (4.2), the instantaneous power in the upper and lower arms can be categorized into a CM component, p_{cm}, which is in phase in both arms, and a differential-mode (DM) component, p_{dm}, appearing anti-phase in the upper and lower arms, as:

$$\begin{cases} p_{Uj} = p_{cm} + p_{dm} \\ p_{Lj} = p_{cm} - p_{dm} \end{cases} \tag{4.3}$$

where

$$p_{cm} = -\frac{V_{dc}\, I_o M}{8}\, cos\left[2\left(\omega t + \theta_j\right) - \varphi\right] \tag{4.4a}$$

$$p_{dm} = \frac{V_{dc}\, I_o}{8}\sqrt{4 + \cos^2(\varphi)(M^4 - 4M^2)}\, cos\left(\omega t + \theta_j - \gamma\right) \tag{4.4b}$$

$$\gamma = \varphi + \tan^{-1}\frac{M^2 \tan\varphi \cos^2\varphi}{2 - M^2\cos^2\varphi} \tag{4.5}$$

The CM component alternates at twice the line frequency, and is a direct consequence of the active power at the dc-side being constant, whereas the phase-power at the ac-side pulsates at twice the line frequency. The DM component alternates with the fundamental line-frequency, and represents the power circulated back and forth internally between the upper and lower arms of the same leg. The CM and DM power components are graphically demonstrated in Fig. 4.1 along with the total arm power, where the DM power is the dominant component.

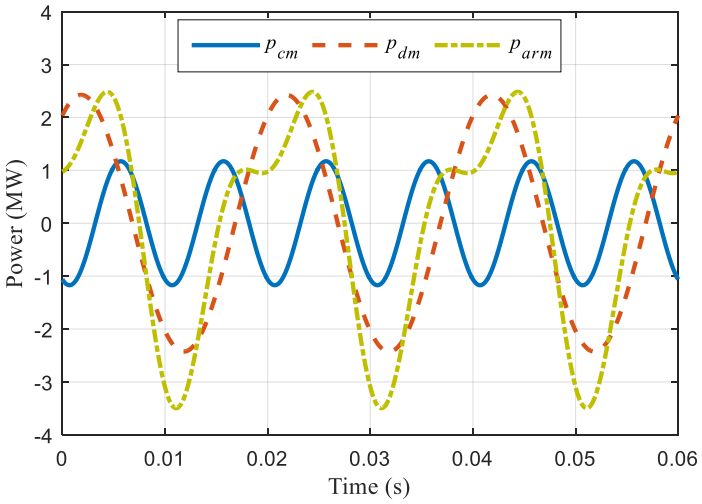

Fig. 4.1 MMC arm power components. (V_{dc} = 25 kV, I_o = 500 A, M = 0.75, and φ = 25°).

Similar to arm power analysis, the energy variation of MMC arms can be classified into a CM component, w_{cm}, and a DM component, w_{dm}, as:

$$w_{Uj} = w_{cm} + w_{dm} \tag{4.6a}$$

$$w_{Lj} = w_{cm} - w_{dm} \tag{4.6b}$$

where w_{Uj} and w_{Lj} are the alternating components of stored energy in the upper and lower arms, respectively. Integrating (4.4) yields the CM and DM components of energy variation as:

$$w_{cm} = -\frac{V_{dc}\, I_o M}{16\omega}\, sin\big[2\big(\omega t + \theta_j\big) - \varphi\big] \tag{4.7a}$$

$$w_{dm} = \frac{V_{dc}\, I_o}{8\omega}\sqrt{4 + \cos^2(\varphi)(M^4 - 4M^2)}\, sin\big(\omega t + \theta_j - \gamma\big) \tag{4.7b}$$

4.1.2 SM Capacitor Voltage Ripple

Due to the dual frequency alternation of capacitive energy stored in MMC arms, capacitor voltage fluctuations have CM and DM voltage-ripple components alternating at twice the fundamental frequency and at the fundamental frequency, respectively, as shown by (4.8).

$$\Delta v_{c_{Uj}} = -\frac{\Delta V_{c\,cm}}{2} sin\left[2\left(\omega t + \theta_j\right) - \varphi\right] + \frac{\Delta V_{c\,dm}}{2} sin\left(\omega t + \theta_j - \gamma\right) \quad (4.8a)$$

$$\Delta v_{c_{Lj}} = -\frac{\Delta V_{c\,cm}}{2} sin\left[2\left(\omega t + \theta_j\right) - \varphi\right] - \frac{\Delta V_{c\,dm}}{2} sin\left(\omega t + \theta_j - \gamma\right) \quad (4.8b)$$

where $\Delta v_{c_{Uj}}$ and $\Delta v_{c_{Lj}}$ are the capacitor voltage-variation of SMs in the upper and lower arms, respectively, while $\Delta V_{c\,cm}$ and $\Delta V_{c\,dm}$ are the absolute values of the peak-to-peak variation of the CM and DM components of SM capacitor voltage-ripple.

The variation of arm stored-energy is handled by the capacitors of the series-connected SMs in each arm, as demonstrated by (4.9).

$$\Delta W = \frac{NC}{2}\left(V^2{}_{c\,max} - V^2{}_{c\,min}\right) = NCV_c\,\Delta V_c \quad (4.9)$$

where ΔW and ΔV_c are the peak-to-peak variation of arm stored-energy and capacitor voltage-ripple of each SM, respectively. Since the nominal SM capacitor voltage is $V_c = V_{dc}/N$, the magnitude of the peak-to-peak capacitor voltage-ripple due to the CM and DM components, from (4.7) and (4.9) are:

$$\Delta V_{c\,cm} = \frac{I_o M}{8\omega C} \quad (4.10a)$$

$$\Delta V_{c\,dm} = \frac{I_o}{4\omega C}\sqrt{4 + \cos^2(\varphi)(M^4 - 4M^2)} \quad (4.10b)$$

The CM component of capacitor voltage-ripple is a direct result of the CM power given by (4.4a), which is inherited in the MMC due to the different frequency of the input and output power. Although the CM component is inevitable, it has a slight influence on capacitor voltage-ripple as depicted in (4.10a), where in variable-speed drives with Volt/Hertz control, the ratio M/ω is near constant, while the load current I_o is invariant. On the other side, when the operating frequency ω is reduced in (4.10b), while the ratio M/ω is constant for constant motor torque requirements, the DM component of capacitor voltage-ripple increases. Further, the direct proportionality of capacitor voltage-ripple to output current variation, at a constant operating frequency, is much higher in the DM component compared to the CM component. The significant influence of DM component on capacitor voltage-ripple is emphasized as shown in

Fig. 4.2, where the normalized peak-to-peak capacitor voltage-variation, for the CM and DM components, is illustrated with operating frequency variation in Fig. 4.2a, and with output current variation in Fig. 4.2b.

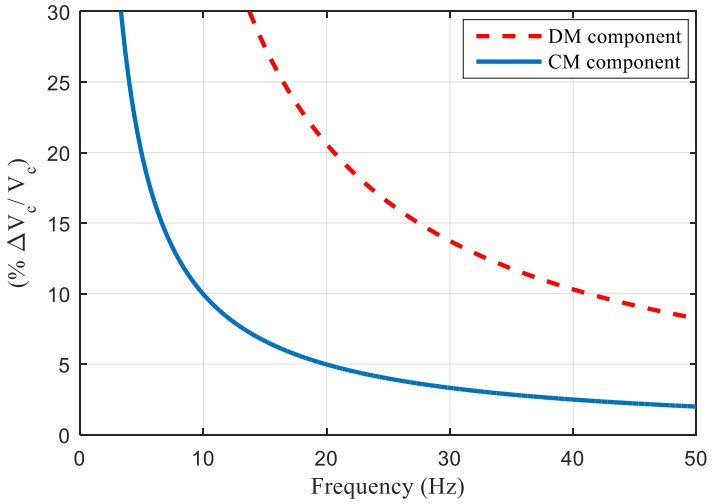

(a)

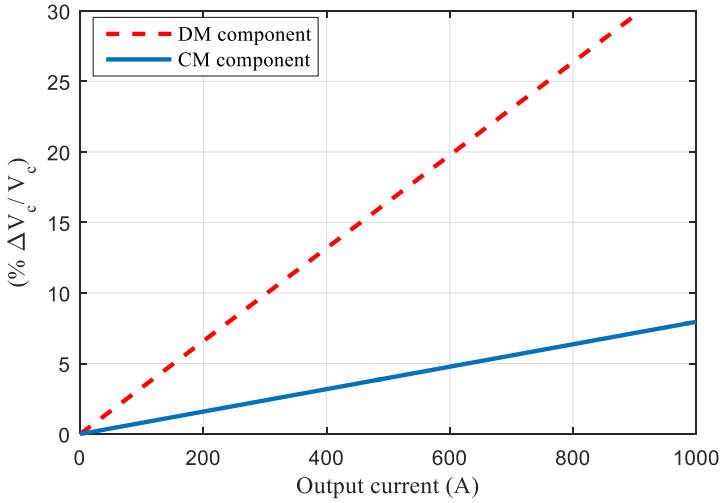

(b)

Fig. 4.2 Normalized components of capacitor voltage-ripple, with V_c = 2.5 kV, C = 3 mF, M = 0.75, and φ = 25º, at: (a) variable frequency and constant output current (I_o = 500 A) and (b) variable output current and constant frequency (f = 25 Hz).

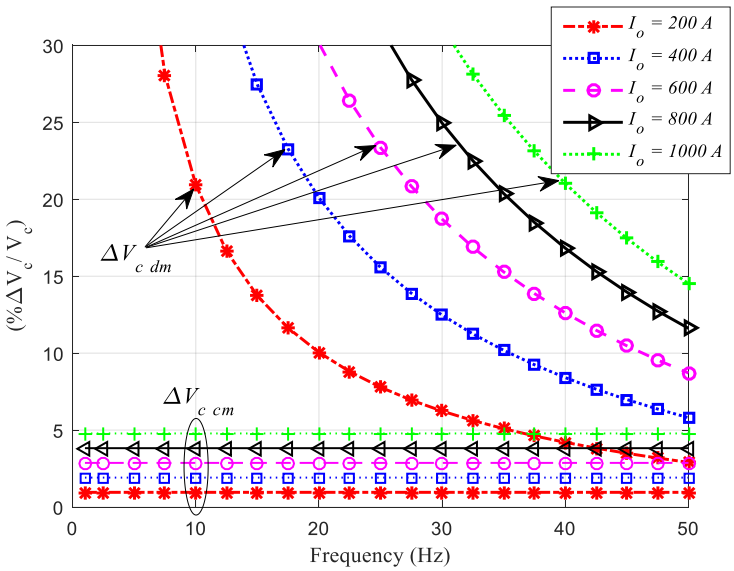

Fig. 4.3 Normalized components of capacitor voltage-ripple at constant M/ω. (C = 3 mF, V_c = 2.5 kV, and $\varphi = 25^0$).

Further assessment of capacitor voltage-ripple components is elucidated in Fig. 4.3, where the variation of normalized capacitor voltage-ripple for the CM and DM components is shown with operating frequency variation at different output currents, while the ratio M/ω is constant. The CM component of capacitor voltage-ripple exhibits a horizontal-line ripple profile with low magnitude, independent of operating frequency variation. Also, the ripple profile of the CM component is slightly affected by a corresponding increase in the output current from 200 A to 1000 A. In contrast, the capacitor voltage-ripple profile due to the DM component significantly increases at low operating frequencies, approaching infinity at near zero frequency. Also, the DM voltage-ripple significantly increases as the output current increases. This concludes the dominant component of capacitor voltage-ripple is the DM component, which should be controlled so that the capacitor voltage-ripple does not exceed prescribed values.

4.2 Ripple Power Decoupling

As established in the previous section, the amount of DM ripple power released by an MMC arm is equal to that absorbed by the complementary arm in the same MMC leg. Thus, to eliminate arm power fluctuation, the excess of energy stored in one arm can be transferred to the other arm of the leg, to source the lack of energy. This can be

realized by designing suitable power decoupling channels capable of controlling both the amount and direction of active power transfer between each upper and lower arm pair in the same MMC leg.

The basic idea of active power decoupling is to divert the pulsating power from one specific energy storage component to another, through an active circuit. A potential way to decouple MMC arm ripple power is to exchange it through the SMs dc capacitors. In order to avoid interfering with the capacitor function or interrupting the current path, the required power exchange must be transmitted through a parallel shunting path. That is, each pair of opposite SM capacitors of an upper and lower arm at the same MMC leg can be paralleled together through an intermediate dc-dc converter. The dc-dc converter acts as an energy balancer to redistribute the stored capacitive energy among each two opposite-arm SMs by allowing their ripple power to be transferred from one SM with an excess of capacitive stored energy to the other, in a closed loop, to recover the energy lack.

4.2.1 Power Decoupling Channels

A modular implementation of energy exchange between SMs can be achieved by employing HF transformer-based dc-dc converter modules as magnetic links between opposite-arm SM capacitors of the same MMC leg. Dc-dc conversion via an HF transformer achieves high power-density conversion with bidirectional power flow, galvanic isolation, high efficiency, low weight and size, and soft semiconductor switching [81]. The phase-shift dual active-bridge (DAB) converter is a common HF transformer-based dc-dc converter, in which two active bridges are interfaced through an HF transformer. The bridges are phase shifted relative to each other to control the power transferred from one dc voltage bus to the other. Two configurations among the phase-shift DAB dc-dc converters are the dual full-bridge (DFB) and dual half-bridge (DHB) converters [81]–[84], as shown in Fig. 4.4a and 4.4b, respectively.

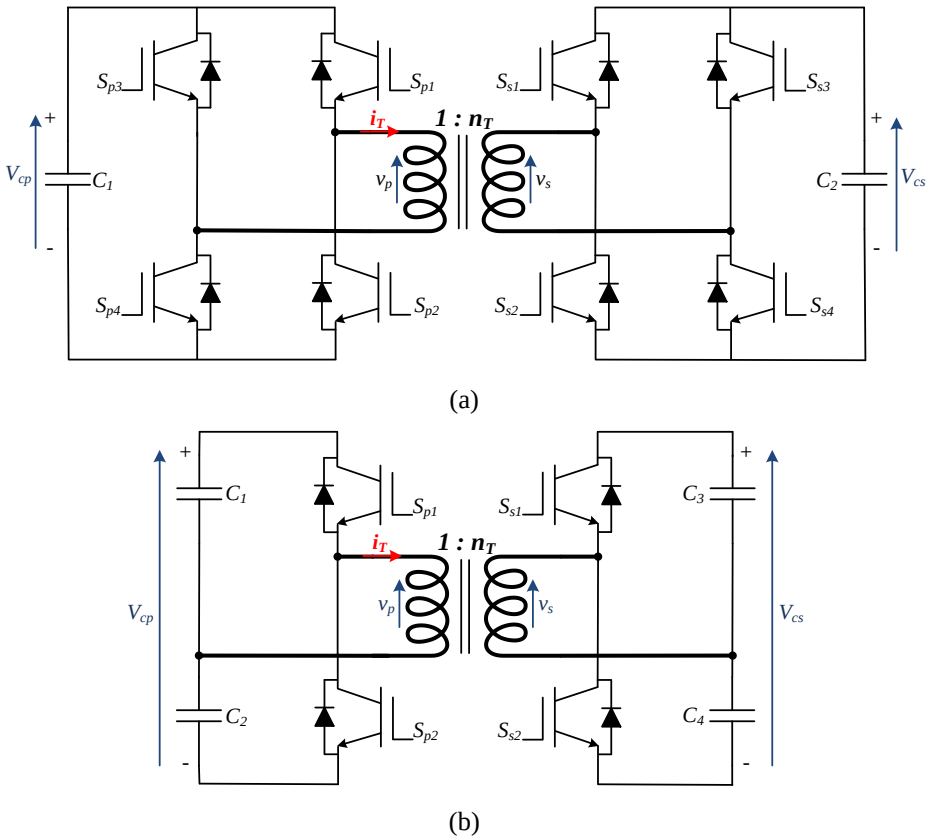

Fig. 4.4 Phase-shift dual-bridge dc-dc converter configuration using: (a) DFB and (b) DHB.

In comparison, the DHB topology has half the switching devices and corresponding drivers for the same power rating, resulting in an efficient power transfer. In addition, the transformer flux-swing of the DHB is only half of the DFB's when the same switching frequency and effective cross-sectional area of transformer core are employed. Therefore, the phase-shift DHB is employed as a dc-dc energy-exchange module to realize MMC ripple power decoupling.

4.2.2 DHB Principle of Operation

The DHB converter is composed of a pair of voltage-fed HB dc-ac inverters interfaced via an HF transformer with a turns ratio n_T. DHB configuration necessitates the capacitor bank at each bridge side be equally split with access to the centre-tap point, as shown in Fig. 4.4b. DHB parasitic components are exploited to achieve some operational characteristics. The leakage inductance of the HF transformer is utilized as an interface and energy transfer element between both voltage-source HB inverters, while the output capacitance of the switching devices is used to realize soft-switching

operation [85]. Both HB inverters generate fixed-frequency square-wave voltages with a constant duty ratio of 50%, applied to both transformer sides. The power flow between both bridge sides is controlled via the phase-angle difference, δ, between the primary and secondary voltage vectors. The most common approach for square wave generation at both converter sides is the phase-shift PWM in which each converter side is modulated with a triangular carrier signal of a frequency ω_h and a constant duty ratio, D, of 50% ($D = 0.5$). Depending on the phase-angle difference between the primary and secondary voltages, the amount of power transfer is [85]:

$$P = \frac{V_{cp}\, V_{cs}\, \delta(\pi - |\delta|)}{8\pi^2 f_h L_T} \tag{4.11}$$

where L_T is the transformer leakage inductance and f_h is the DHB switching frequency. To generate a phase difference δ between both DHB converter sides, two modulation signals are defined as [86]:

$$m_1 = D - \frac{\delta}{\pi} \tag{4.12a}$$

$$m_2 = |1 - m_1| \tag{4.12b}$$

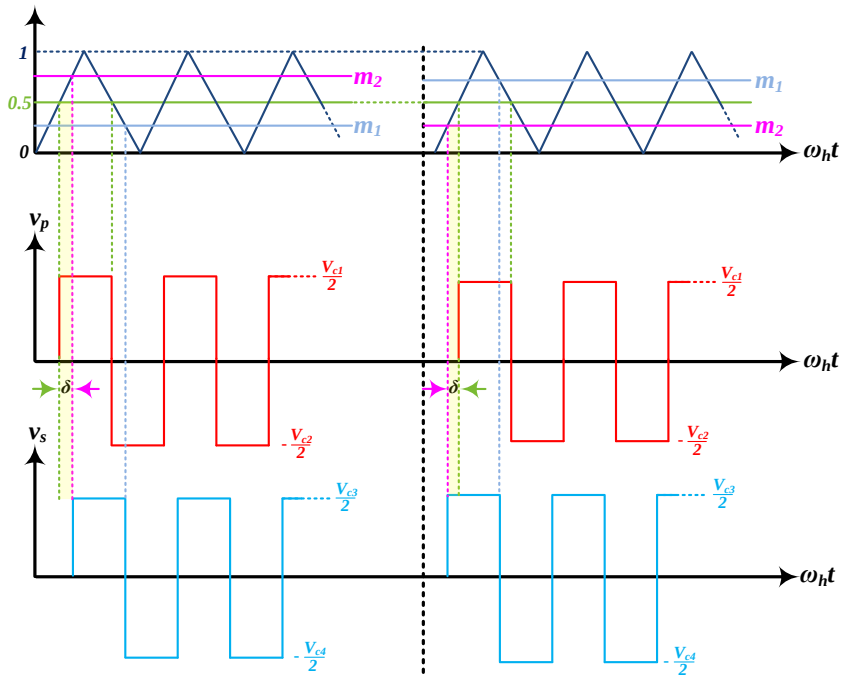

(a) (b)

Fig. 4.5 Sketch of the phase-shift PWM of a DHB converter for bidirectional power transfer during: (a) positive phase-shift angle and (b) negative phase-shift angle.

According to the sign of δ, bidirectional power can be transferred between the DHB converter sides as illustrated in Fig. 4.2, where v_p and v_s are the voltages applied on the primary and secondary transformer sides, respectively.

4.3 A Generalized DHB-Assisted MMC Drive System

In this section, the DHB-based power decoupling approach is realized for an MMC drive system with any number of machine phases and machine winding connection. In the generalized DHB-assisted MMC configuration, SM ripple power is decoupled and bi-directionally exchanged with the opposite-arm SM in a vertical basis within the same phase-leg. That is, each pair of upper- and lower-arm SMs are magnetically coupled through a DHB converter interfacing their capacitors. This is schematically illustrated in Fig. 4.6 for a three-phase MMC, where the configuration employs $3N$ DHB modules; that is, denoted as $3N$ DHB-assisted MMC. A further elaboration for one of the chain links of each pair of upper- and lower-arm SM is shown in Fig. 4.7.

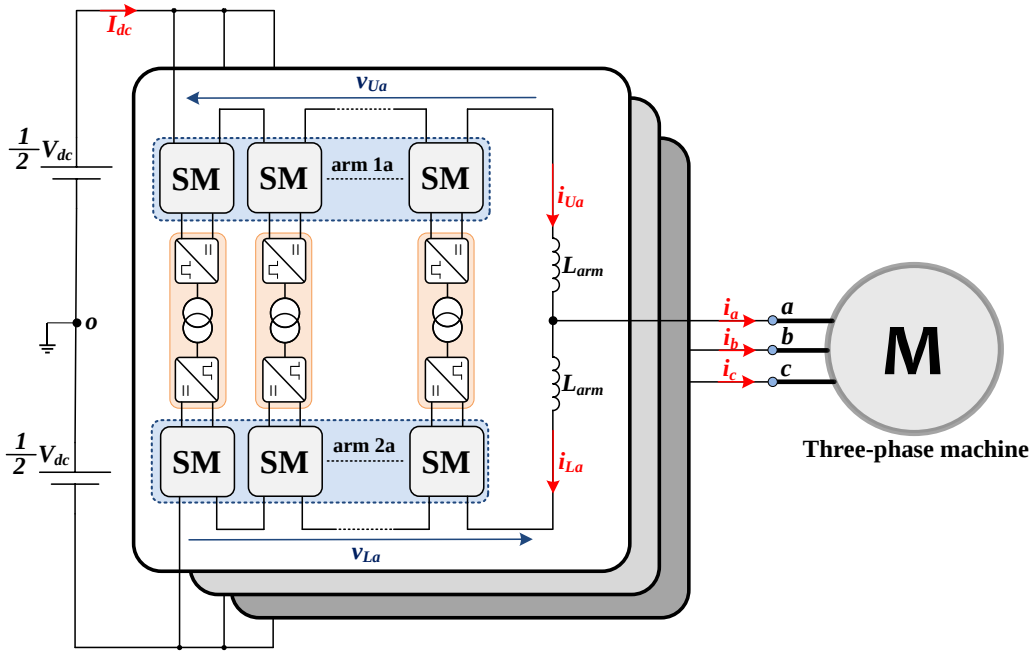

Fig. 4.6 Circuit diagram of a three-phase MMC assisted with DHB chains between pairs of opposite upper- and lower-arm SMs.

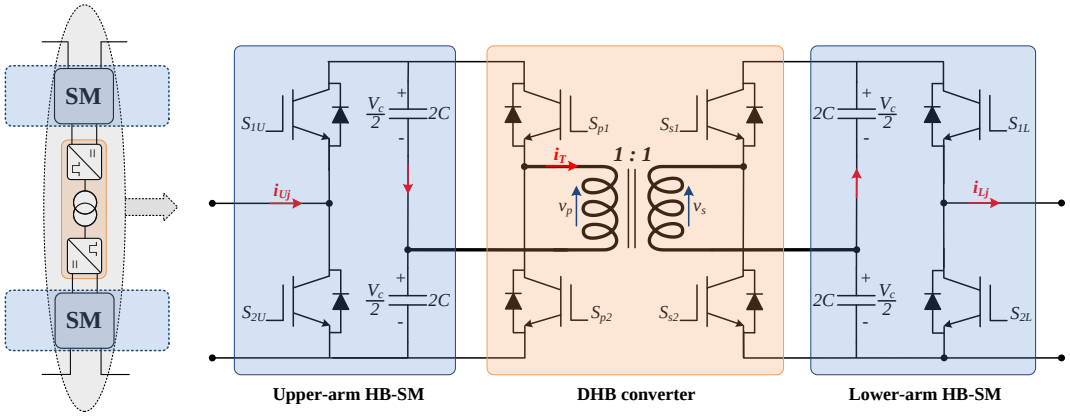

Fig. 4.7 DHB configuration linking two HB-SMs of opposite upper and lower MMC arms.

Referring to Fig. 4.7, the transformer turns ratio is 1:1 ($n_T = 1$), since the dc-dc conversion is only employed for energy exchange between bridge sides at the same voltage level, equal to the nominal MMC SM capacitor voltage. Also, the MMC HB-SM capacitor is equally split into two series connected capacitors each with a capacitance of $2C$ (each rated at half the SM voltage), to realize the same equivalent capacitance of a conventional MMC HB-SM.

4.3.1 Control of DHB as Energy Balancer

DHB control for ripple power decoupling is independent of the MMC main control loops. The DHB control considers the SM capacitor voltage as an input, where it is regulated to follow its nominal value. Thus, a control loop employing a PI controller is implemented for each DHB module. The PI controller sets the voltage difference of each DHB primary- and secondary-side capacitor pair (calculated as $V_{cp} - V_{cs}$) to zero, providing the necessary phase-angle difference, δ^*, which is utilized as an input to the DHB modulator. When V_{cp} is higher than V_{cs}, a positive phase-shift is obtained, yielding a forward power transfer, where the DHB primary-side voltage is leading the secondary-side one. The power transfer action is reversed when V_{cp} is lower than V_{cs}, where reverse power transfer with a negative phase-shift occurs associated with the reversal of both the leading and lagging bridge sides, compared to the forward power transfer case, as elucidated in Fig. 4.8.

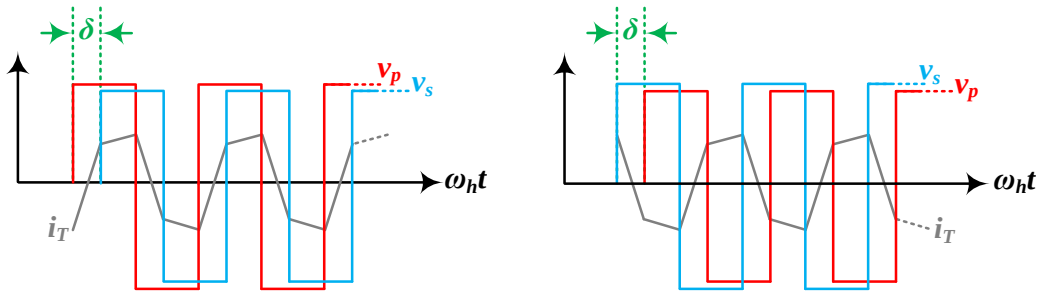

Fig. 4.8 Idealized waveforms of DHB converter for power transfer between a pair of opposite-arm MMC SMs during: (a) positive phase-shift angle and (b) negative phase-shift angle.

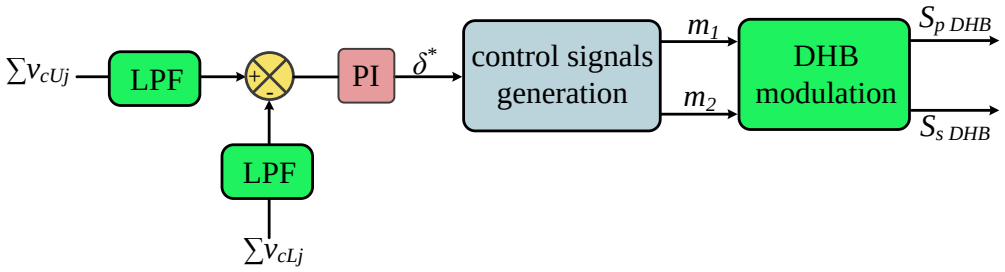

Fig. 4.9 Block diagram of DHB control as an energy balancer.

According to the reference phase-angle difference generated by the PI controller, the DHB modulator generates the control signals m_1 and m_2, as given by (4.12), that are compared with a triangular carrier signal to generate the DHB switching signals. This results in square wave voltages at both sides of the DHB converter, however shifted by the commanded angle. With fast modulation of MMC arms, the same phase-angle difference can be utilized for all of the N DHB modules located on the same MMC phase-leg. Thus, DHB control can be generalized for an MMC phase-leg j, as schematically represented in Fig. 4.9. The sum of SM capacitor voltages of the upper arm ($\sum v_{cUj}$) is subtracted from that of the lower arm ($\sum v_{cLj}$) to control the power flow through the DHB modules interconnecting the opposite SMs of phase j. A low-pass filter (LPF) is utilized to remove any harmonic wave distortion. The same control loop is adopted for each set of DHBs interfacing the opposite SMs of upper and lower arms, where for a three-phase MMC, three PI controllers are employed to control all the DHB modules.

4.3.2 Capacitor Voltage Variation

DHB control ensures the DM ripple power component of each pair of opposite-arm SMs is counterbalanced, eliminating the DM ripple component in the SM capacitor voltage. Thus, the voltage fluctuation across SM capacitors of the $3N$ DHB-assisted MMC is given by (4.13), with an absolute peak-to-peak value equal to the CM component, as shown in (4.14).

$$\Delta v_{c_{Uj\,DHB}} = \Delta v_{c_{Lj\,DHB}} = -\frac{I_o M}{16\omega C} sin\left[2\left(\omega t + \theta_j\right) - \varphi\right] \tag{4.13}$$

$$\Delta V_{c\,DHB} = \Delta V_{c\,cm} = \frac{I_o M}{8\omega C} \tag{4.14}$$

Based on (4.14), capacitor voltage-ripple of the $3N$ DHB-assisted MMC inherits the same behaviour as the CM voltage ripple component, shown in Figs. 4.2 and 4.3, which has the least influence on capacitor voltage variation.

The idealized waveforms of SM capacitor voltage variation for a conventional MMC and the $3N$ DHB-assisted MMC are shown in Fig. 4.10, with the same SM capacitance and nominal capacitor voltage of 2.5 kV. In Fig. 4.10a, the capacitor voltage variation of a conventional MMC alternates at the fundamental line-frequency, as a result of both the CM and DM components, in an anti-phase manner in both the upper and lower arms, while the peak-to-peak voltage ripple is 440 V ($\pm$8.8%). On the other hand, the proposed DHB-assisted MMC features a second-order sinusoidal voltage variation across the SM capacitors as shown in Fig. 4.10b, which appears with the same phase in both the upper and lower arms, with a peak-to-peak voltage ripple of 100 V ($\pm$2%).

Further assessment of decreased capacitor voltage-ripple is presented in Fig. 4.11, where the percentage reduction in capacitor voltage-ripple achieved by the proposed DHB-assisted MMC is depicted with respect to the capacitor voltage-ripple of a conventional MMC, as the modulation index varies. The sizing requirement of SM capacitance for both topologies is also compared in Fig. 4.11. The percentage capacitor voltage-ripple reduction is 60% at unity modulation index, with further improvement as the modulation index decreases. The ratio between SM capacitances, that result in the same capacitor voltage-ripple, for a conventional MMC with respect to the DHB-assisted MMC varies between 2 at unity modulation index, up to 50 times at low

modulation indices. For simplicity, the reduction in capacitor voltage-ripple shown in Fig. 4.11 is assessed while considering only the DM component as the dominant voltage-ripple component of the conventional MMC.

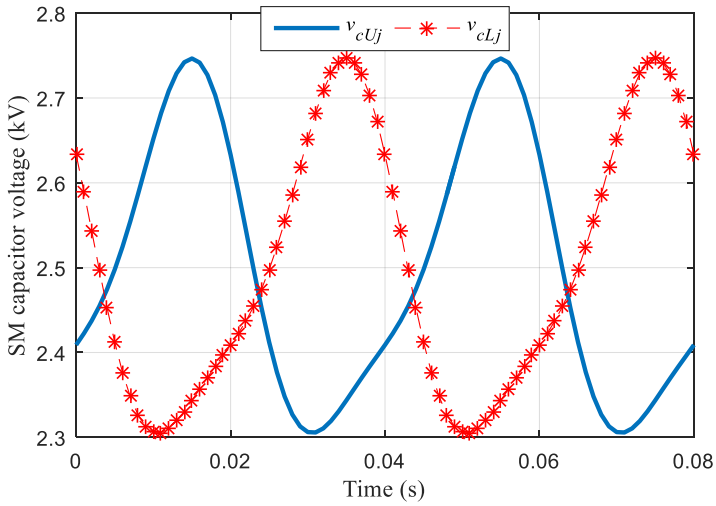

(a)

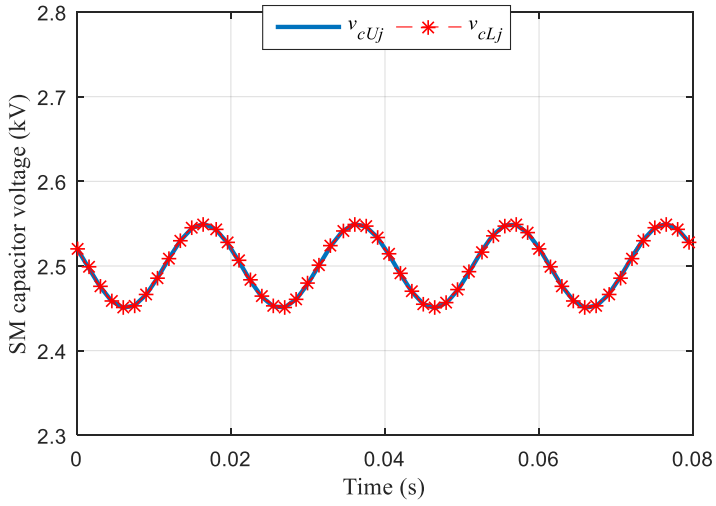

(b)

Fig. 4.10 Idealized waveforms of capacitor voltage variation for SMs in upper and lower arms for: (a) conventional MMC and (b) 3N DHB-assisted MMC. (C = 3 mF, f = 25 Hz, V_c = 2.5 kV, I_o = 500 A, M = 0.75, and φ = 25º)

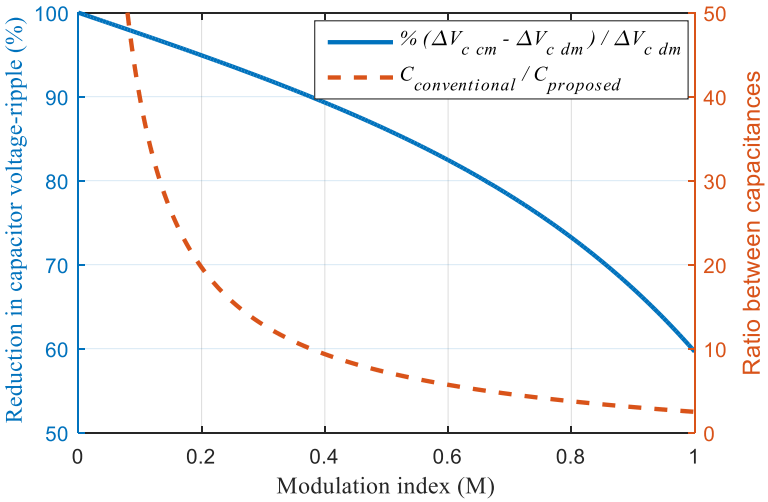

Fig. 4.11 Assessment of voltage ripple reduction and SM capacitance size for conventional MMC and the 3*N* DHB-assisted MMC (φ =25º).

4.3.3 Operation at Zero Motor-Speed/Frequency

In a conventional MMC, the unidirectional current passing through MMC arms during near zero-frequency power conversion results in a unidirectional change in SM capacitor voltage, where the peak voltage variation exceeds the rated voltage of both SM capacitors and IGBTs. In contrast, one of the salient advantages of the proposed DHB-assisted MMC is its ability to start a machine at full-load torque from a standstill condition with a ripple-free SM capacitor voltage profile. At near zero frequency, the provided output power is near dc, where the variation of the CM power in MMC arms will be almost zero. Also, with unidirectional transfer of dc DM power component between SMs of opposite-arm pairs, the resultant pulsating power in different arms will be almost zero. Thus, the capacitive energy stored in MMC arms is evenly redistributed at a constant level among all SMs, resulting in a constant voltage across the SM capacitors.

4.3.4 DHB Design Guidelines

A. Transformer leakage inductance

Referring to Fig. 4.7, the HF transformer can be represented by a T-type equivalent circuit as shown in Fig. 4.12, where L_p and L_s are the leakage inductance of the

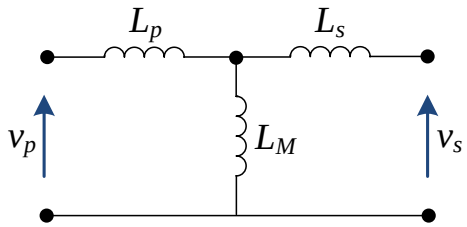

Fig. 4.12 T-type equivalent circuit of DHB transformer.

primary and secondary sides, respectively, while L_m is the magnetizing inductance. It should be noted that $L_p = L_s$, since the transformer has a unity turns ratio. Neglecting the magnetizing inductance, the transformer leakage inductance is given as:

$$L_T = L_p + L_s \tag{4.15}$$

Referring to (4.10), the power transmitted through the transformer is governed by the phase-shift angle and transformer leakage inductance when the DHB's switching frequency is constant. The maximum power transfer occurs when the phase-shift angle $\delta = ½\,\pi$. Therefore, the maximum power transfer is:

$$P_{T_{max}} = \frac{{V_c}^2}{32 f_h L_T} \tag{4.16}$$

where V_{cp} and V_{cs} in (4.10) are set to V_c. Since the DM component of arm power alternates as shown in (4.4b), the peak decoupled DM power component for each pair of opposite-arm SMs is:

$$P_{dm_{SM}} = \frac{V_{dc}\, I_o}{4N} \tag{4.17}$$

where $P_{dm_{SM}}$ must be less than the maximum power-transfer ability of the transformer. Substituting $P_{dm_{SM}} \leq P_{T_{max}}$ gives a boundary condition for the transformer leakage inductance:

$$L_T \leq \frac{V_{dc}}{8 N I_o f_h} \tag{4.18}$$

B. Ratings of transformer

The voltage applied on both transformer windings is $½V_c$, while the maximum transformer current is related to the peak decoupled DM power, where it is limited to half the output current amplitude, and is given by:

$$I_{T_{max}} = \frac{2P_{dm_{SM}}}{V_c} = ½I_o \tag{4.19}$$

C. Ratings of switching devices

The voltage rating of the DHB switching devices is V_c, while the current rating is $½I_o$.

4.3.5 DHB Soft Switching

Generally, DAB converters offer natural zero-voltage switching (ZVS) transitions for the turn-on of all devices (due to the leakage inductance). A snubber capacitor across each switching device extends the ZVS action to the turn-off instants. For both switching devices of each HB inverter, the ZVS condition is that the net current leaving the leg pole (middle access-point of the leg) lags the voltage of the pole. With the necessity of inserting a dead time between switching devices in the same bridge leg, the net leg output current should not change direction during the dead time until the opposite switching device is turned on. During the dead time, the leg current charges one snubber capacitor and discharges the other in the same leg, resulting in a soft dv/dt. For turn-on ZVS, each switching device at each bridge side should have a negative current just before turning on, such that the anti-parallel diode is conducting, while the voltage across the switching device is almost zero. On the other side, when the switching device is turned off, the voltage across the snubber capacitor is almost zero and the switching device current will divert to the snubber capacitor, which slightly increases the snubber capacitor voltage at the turn-off instant. Since the proposed MMC configuration employs DHB modules with a unity voltage conversion ratio, ZVS operation is ensured for any loading condition [83].

4.4 DHB-Assisted Dual MMC for Open-End Stator Winding Machines

In this section, the DHB-based power decoupling approach is applied to a dual MMC topology, and is applicable to open-end stator winding machines, however with different placement of the DHB modules relevant to the MMC SMs.

4.4.1 Traditional Dual Multilevel Converter

Machines with open-end stator windings are a possible alternative to conventional star- and delta-connected stators, that not only suppress the switching CM voltages but also improve the output voltage quality [87]–[91]. The concept of employing a dual-inverter topology feeding an open-end stator winding induction motor was first introduced in [92] for MV high-power machine drive applications. The topology has been implemented using two two-level inverters, where it is capable of generating three-level output voltage with half the dc-link voltage, compared to a single-sided three-level inverter topology. Similarly, a dual three-level inverter topology with a single dc-link voltage was proposed for five-level operation [93]. Thereafter, several multilevel topologies have been considered for open-end stator winding machines with various topologies [94]–[96]. Recently, a dual inverter topology based on the MMC has been proposed with many advantages, where it offers single dc-source operation regardless of the number of output voltage levels, which eliminates bulky and expensive multi-winding isolation transformers to provide isolated dc sources [97]. Also, the dual MMC topology achieves the same maximum output voltage-magnitude as the conventional single-sided MMC with half the dc-link voltage, which reduces the insulation requirement. If one converter fails, the other converter can continue operation with a reduced output power while reconfiguring the machine end-terminals at the faulty converter side to be connected in either star or delta, which gives the dual inverter topology intrinsic fault-tolerant capability. Further, the dual MMC topology offers more redundant switching state combinations, compared to a single-sided MMC with the same number of output voltage levels, that can be exploited in voltage balancing of the SM capacitors.

4.4.2 Dual MMC Topology

The circuit diagram of a three-phase dual MMC topology is shown in Fig. 4.13, comprising two three-phase MMCs each feeding three end-terminals of open-end stator winding machine, while both MMCs are modulated out-of-phase. Although the number of arm inductors is doubled compared to a conventional single-sided MMC topology, the equivalent arm inductance of the dual MMC topology remains the same. The dual MMC structure can be considered as a direct consequence of splitting each phase-leg of a conventional single-sided MMC into dual complemented legs with half the number of SMs, compared to the single-sided phase leg. Thus, for the same power level, the total number of SMs employed in a dual MMC topology is same as the number of SMs in a conventional single-sided topology. Also, the voltage and current stress on the SM capacitors and switching devices is identical in both MMC topologies.

Circuit analysis of the dual MMC topology is slightly different than that of the single-sided MMC. Thus, compared to the single-sided MMC, any different voltage and current relationships for the dual MMC topology will be distinguished by the subscript '*D*'.

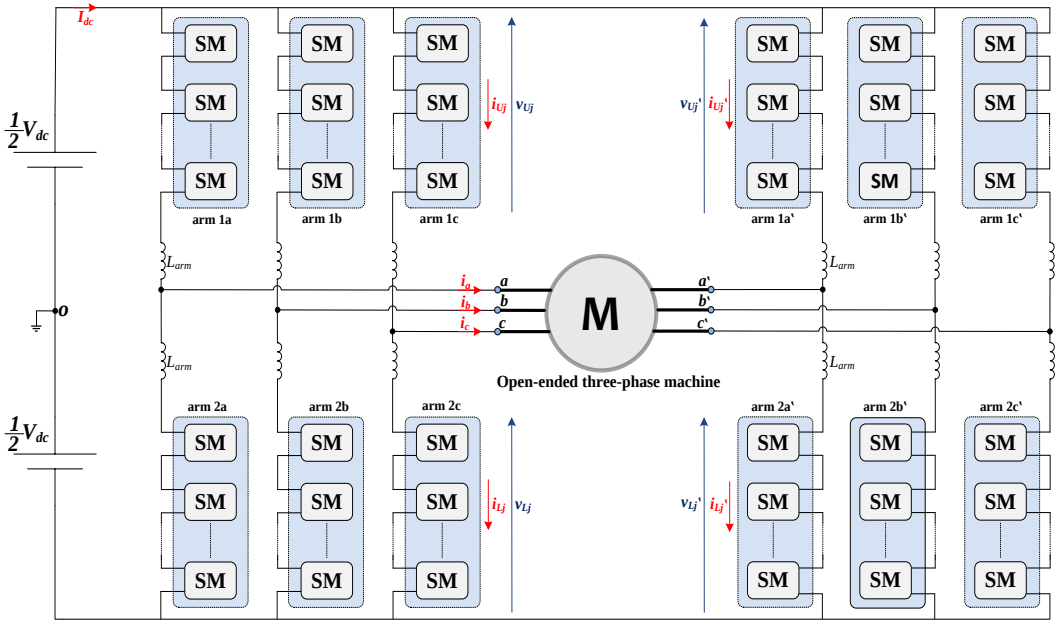

Fig. 4.13 Circuit configuration of a three-phase dual-MMC-fed open-end stator winding machine.

Referring to Fig. 4.13, the open-end machine terminal windings connected to the left-side MMC are denoted by a, b, c, while a', b', c' represent the terminal-ends connected to the right-side MMC. With $j \in \{a, b, c\}$, the voltage across each machine phase-winding is the differential voltage between both machine winding terminals, and is denoted by $v_{jj'}$ as shown in (4.20).

$$v_{jj'} = V_{o_D} \cos(\omega t + \theta_j) \tag{4.20}$$

where V_{o_D} is the magnitude of the ac voltage generated by the dual MMC. Compared to a conventional single-sided MMC, dual MMC topology doubles the maximum attainable ac voltage magnitude, for the same dc-link voltage. That is, the ac output voltage magnitude is defined as:

$$V_{o_D} = MV_{dc} \tag{4.21}$$

Since the MMC legs with a common machine winding (complementary legs) have out-of-phase modulation, the dual MMC arm voltages are:

$$\begin{cases} v_{Uj_D} = v_{Lj'_D} = \frac{1}{2}V_{dc} - \frac{1}{2}v_{jj'} \\ v_{Lj_D} = v_{Uj'_D} = \frac{1}{2}V_{dc} + \frac{1}{2}v_{jj'} \end{cases} \tag{4.22}$$

Similarly, the arm currents are defined as:

$$\begin{cases} i_{Uj_D} = i_{circ\,j_D} + \frac{1}{2}i_j \\ i_{Lj_D} = i_{circ\,j_D} - \frac{1}{2}i_j \\ i_{Uj'_D} = i_{circ\,j'_D} - \frac{1}{2}i_j \\ i_{Lj'_D} = i_{circ\,j'_D} + \frac{1}{2}i_j \end{cases} \tag{4.23}$$

where $i_{circ\,j_D}$ and $i_{circ\,j'_D}$ are the circulating currents of the complemented legs, where they have out-of-phase even-harmonics profile due to the opposite modulation of the left- and right-side MMC. With even-harmonics suppression, both currents are dc components equal to the circulating current of conventional single-sided MMC, as shown by (4.24).

$$i_{circ\,j_D} = i_{cm\,j'_D} = \frac{I_{dc}}{6} = \frac{MI_o \cos\varphi}{4} \tag{4.24}$$

4.4.3 DHB-Assisted Dual MMC Topology

The dual MMC topology implies each machine phase-winding be connected differentially between two MMC legs modulated out-of-phase. The out-of-phase modulation associated with a given machine winding results in the DM component of the energy stored in one MMC arm alternating antiphase to the energy component stored in the adjacent arm of the complemented leg. Thus, an alternative placement of DHB balancers is possible by exchanging the ripple power between adjacent (horizontal) MMC arms of a common machine winding. That is, each pair of front-to-front SM is interfaced through a DHB converter, as shown in Fig. 4.14. Similar to the generalized DHB-MMC configuration, the DHB-assisted dual MMC topology employs $3N$ DHB modules. A DHB chain link between each front-to-front SMs will be similar to that shown in Fig. 4.7, but interfacing a pair of adjacent left- and right-arm HB-SMs. The control of the DHB balancers adopted in the dual MMC topology uses the same control algorithm as the generalized DHB-MMC configuration, where the sum of SM capacitor voltages of the upper arm of phase j ($\sum v_{cUj}$), are subtracted from that of the upper arm of phase j' ($\sum v_{cUj'}$) to control the power flow through the DHB modules interconnecting the front-to-front SMs of both phase j and j'.

The incorporation of DHB balancers between each pair of front-to-front SMs of the dual MMC topology decouples the DM component in MMC arm power, with the CM component unchanged, but evenly distributed among the arms. This results in SM capacitor voltage ripple pulsating due to the CM voltage ripple component at twice the fundamental frequency, inheriting the performance of the generalized DHB-assisted MMC.

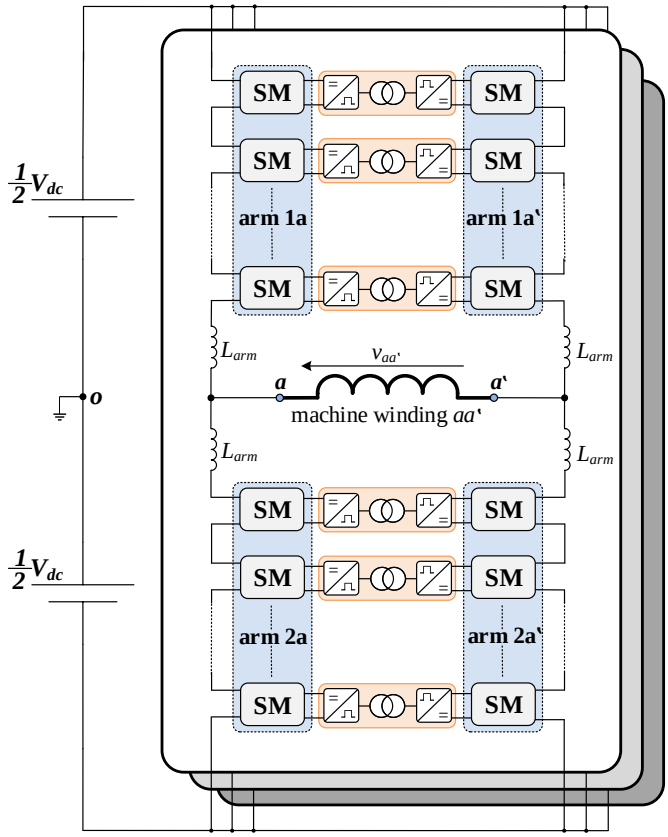

Fig. 4.14 A Circuit diagram for DHB-assisted dual MMC topology for open-end stator winding machines.

4.5 Verification of 3*N* DHB-Assisted MMC Configurations

In this section, the effectiveness of the MMC topology with the 3N DHB-based power decoupling is investigated using both simulation and experimentation. The first part of the simulation study highlights the main characteristics of the 3N DHB-based power decoupling approach when applied to a single-sided MMC in comparison to a dual MMC topology. The second part of the simulation study as well as the experimental study focus on the 3N DHB-based dual MMC topology, being advantageous in delivering the same power as a single-sided topology with the same number of SMs, however with half the dc-link voltage.

4.5.1 Simulation Verification

A. Simulation using RL load

A 10 MW MATLAB/SIMULINK model is used, where the MMC feeds a three-phase *RL* load while providing a phase voltage of 8 kV ac across the load terminals. The simulation parameters are listed in Table 4.1 for both the single-sided and dual-sided MMC topologies. Figs. 4.15 and 4.16 show the fundamental waveforms of steady-state operation of the $3N$ DHB-based power decoupling when applied to a single-sided and a dual-sided MMC topology, respectively, at both the rated output current and frequency in Table 4.1. The single-sided MMC feeds a three-phase star-connected *RL* load with a neutral point n, via three standard MMC phase-legs each of 10 SMs per arm (total number of SMs is 60), and is supplied from a 25 kV dc-link voltage. The dual MMC feeds a three-phase *RL* load connected in an open-end configuration via three-paralleled dual-legs each with 5 SMs per arm (total number of SMs is 60), and is supplied from a 12.5 kV dc input voltage. For both configurations, the modulation index is set to 0.904 to generate 8 kV output phase-voltage (13.8 kV line-to-line voltage for the single-sided configuration). Comparing the results in Figs. 4.15 and 4.16, the differential output voltage across the terminals of the open-end load in the dual-sided MMC, $v_{jj'}$, has half the number of voltage levels compared to the phase voltage, v_{jn}, of the single-sided MMC. Nonetheless, the quality of the output currents for both configurations is the same, with a current peak equal to the rated value of 655 A. In both configurations, the currents in the upper and lower arms are controlled to suppress the second- and fourth-order harmonic components to maintain a near constant circulating current, as assumed in the mathematical analysis of Chapter 2. Common to both MMC configurations, the peak arm current is 510 A while the average circulating current is 135 A. Also, the SM capacitor voltage-ripple alternates at twice the line frequency, due to the CM component, with $\pm$6% voltage-ripple for an equivalent SM capacitance of 1 mF. The current drawn from the input supply, I_{dc}, is doubled in the dual-sided topology compared to the single-sided topology since the former operates at halved dc-link voltage. The CM voltage of the dual-sided topology is shown to be lower than that of the single-sided topology due to exploitation of the available redundant states offered by dual-sided configurations. Generally, the CM voltage, v_{cm}, of a single-sided inverter is the average of the three-phase voltages

measured to the ground point, as shown by (4.25). For a dual-sided inverter, two CM voltages are calculated for each individual inverter, where the resultant CM voltage is the difference between them.

$$v_{cm} = \frac{1}{3}(v_{ao} + v_{bo} + v_{co}) \tag{4.25}$$

Table 4.1: Simulation parameters of *3N* DHB-assisted MMC configurations feeding *RL* load

	Single-sided MMC	**Dual MMC**
Rated active power	10 MW	
Input dc voltage (V_{dc})	25 kV	12.5 kV
Number of SMs per arm (N)	10	5
Nominal SM capacitor voltage (V_c)	2.5 kV	
Rated phase voltage	8 kV	
Rated current magnitude (I_o)	655 A	
Fundamental output frequency (f_o)	50 Hz	
Carrier frequency (f_c)	2 kHz	
DHB switching frequency (f_h)	10 kHz	
Arm inductance (L_{arm})	2 mH	1 mH
SM capacitance (C)	1 mF	
Load resistance	$15.5\times\frac{f_o}{50}\,\Omega$	
Load inductance	24 mH	

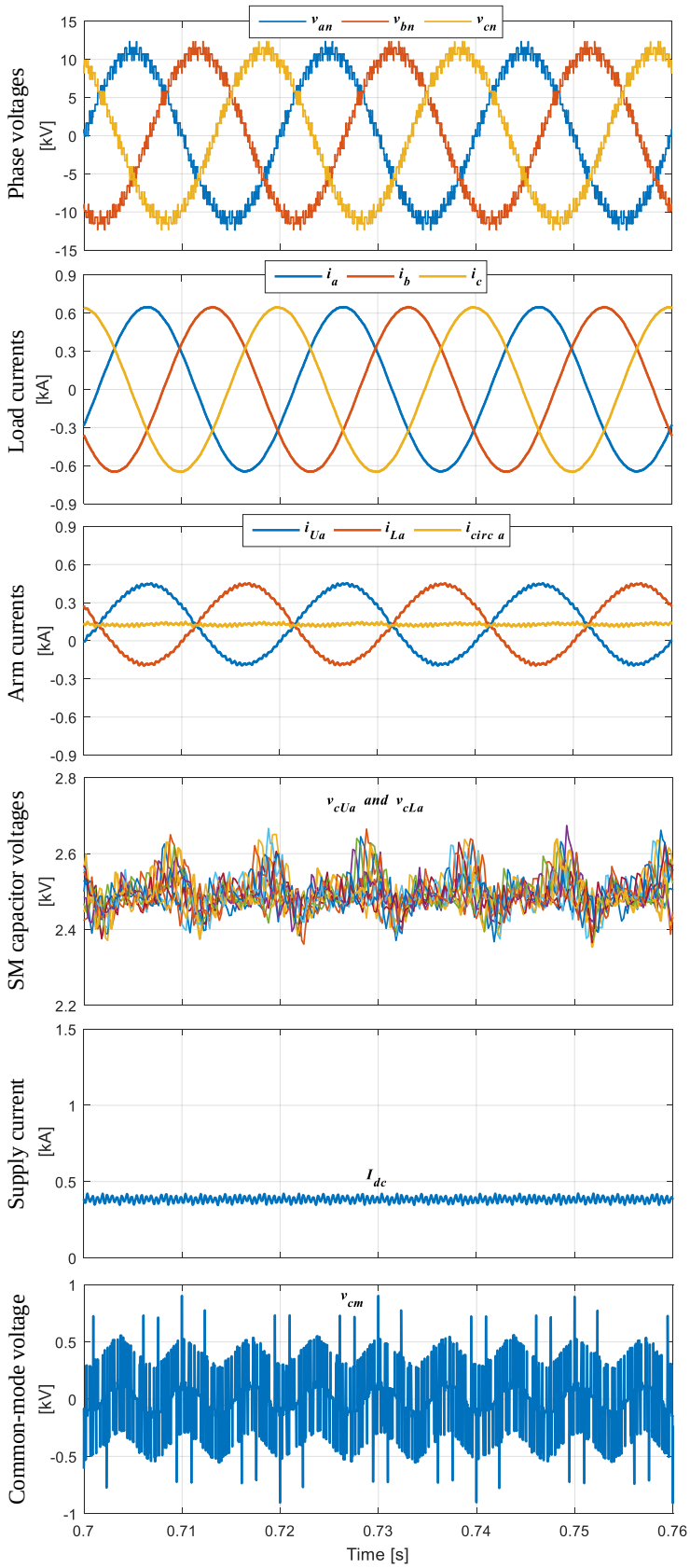

Fig. 4.15 Simulation waveforms for steady-state operation of 3N DHB-assisted single-sided MMC at 50 Hz.

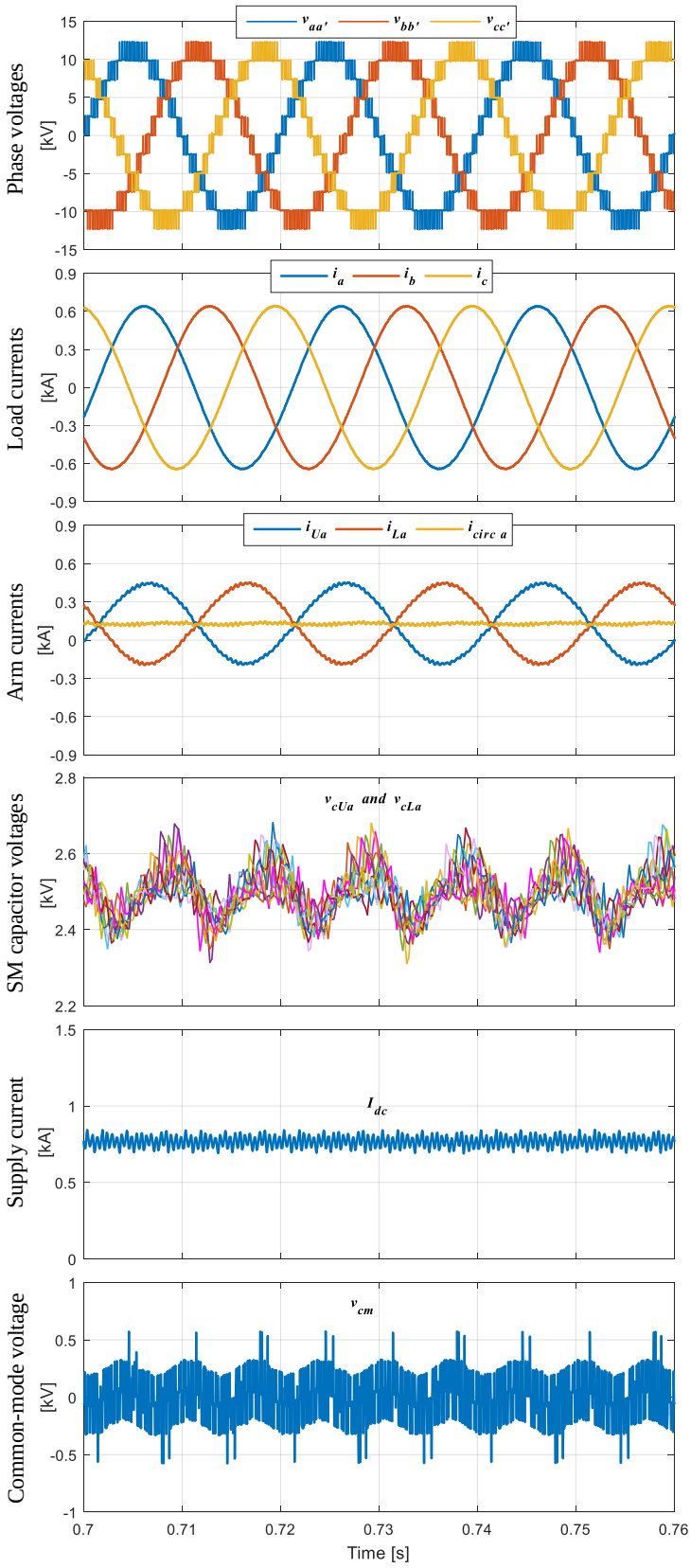

Fig. 4.16 Simulation waveforms for steady-state operation of 3*N* DHB-assisted dual MMC topology at 50 Hz.

Fig. 4.17 shows the voltage across each side of one of the employed HF transformers along with the transformer current, i_T, during positive and negative half cycles of the arm current of the DHB-assisted dual MMC. The voltage across both transformer sides is near 1.25 kV which is half the nominal SM capacitor voltage. In Fig. 4.17a, the waveforms are obtained when the arm current is charging the capacitors connected to the primary side, while discharging the capacitors connected to the secondary side. That is why the voltage at the primary side is higher than the voltage at the secondary side with a leading phase-shift, resulting in a forward power transfer from the primary to the secondary side. The opposite case is shown in Fig. 4.17b, where the primary voltage lags with a lower magnitude than the secondary voltage, producing reverse power transfer, from the secondary to the primary side.

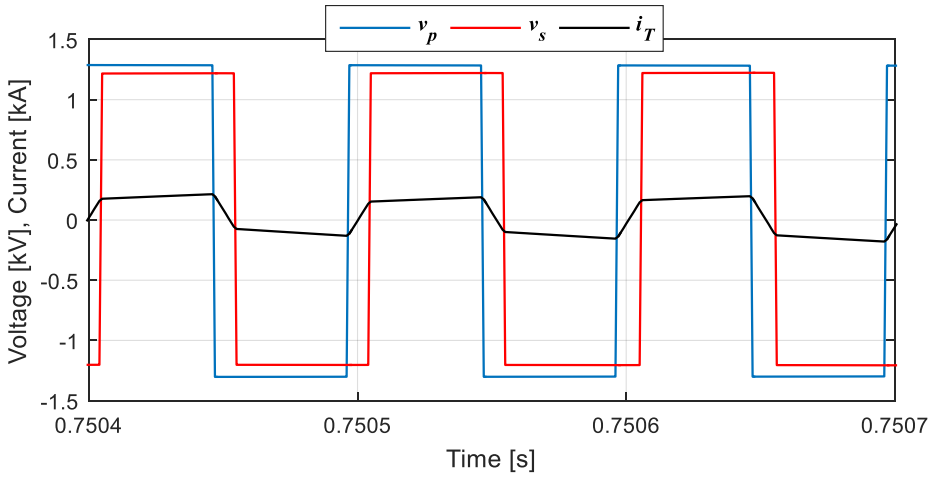

(a)

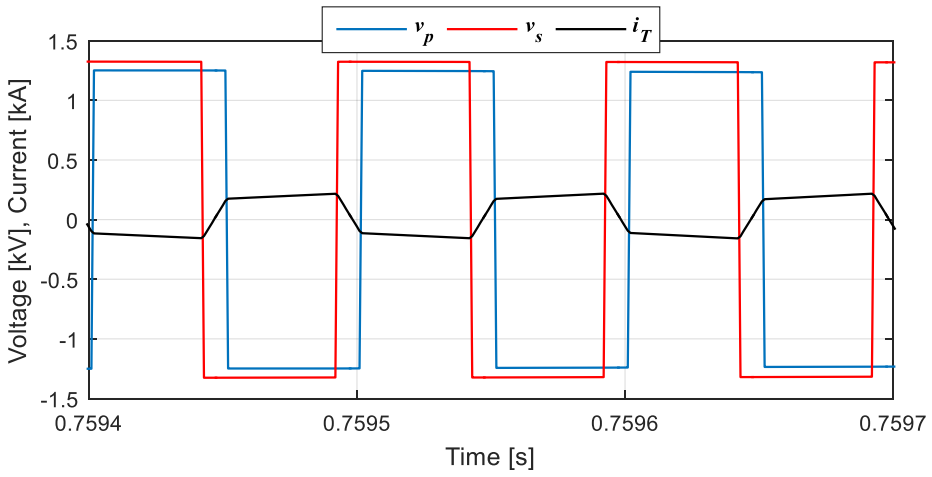

(b)

Fig. 4.17 Simulation waveforms of the phase-shift DHB converter when: (a) primary voltage is leading and (b) primary voltage is lagging.

Figs. 4.18−4.20 show DHB-assisted dual MMC performance at low frequencies, according to a Volt/Hertz control scheme, where the results are obtained for continuous operation at 10, 5, and 1 Hz, respectively. In this case study, the output voltage is reduced in accordance to the operating frequency reduction, while the load resistance is varied linearly with the operating frequency to maintain the output current constant at the rated value, at all frequencies, to emulate the constant torque characteristic of variable-speed machines. The output currents are high-quality sinusoidal waveforms with a peak of 655A, while the arm currents are maintained free of dominant even-harmonic components. Importantly, the SM capacitor voltages are balanced and not affected by the reduction in both the modulation index and operating frequency. The SM capacitor voltage-ripple is ±5%, for 1 mF equivalent SM capacitance.

To assess the reduction in capacitor voltage-ripple achieved by the 3N DHB-assisted dual MMC configuration, Fig. 4.21 shows capacitor voltage variation with DHB switching signal deactivation at the mid-time of simulation, at low operating frequencies. When the DHB PWM signals are inhibited, the configuration is reduced to a conventional dual-sided MMC which inherits the same capacitor voltage ripple profile as the standard single-sided MMC. At the time of the energy balancing deactivation, the capacitor voltage-ripple significantly increases especially as the operating frequency is reduced. While the voltage ripple of SM capacitors is near constant at ±5% at the three different frequencies when the DHB modules are in operation, the voltage ripple after DHB deactivation is ±33%, ±50%, and ±66% at 10, 5, and 1 Hz, respectively. Although the latter voltage ripple percentages are impractically high, they highlight the significant reduction in the SM capacitance sizing requirement, due to counter-balancing the DM ripple power between adjacent-arm SMs of the dual MMC legs through DHB incorporation.

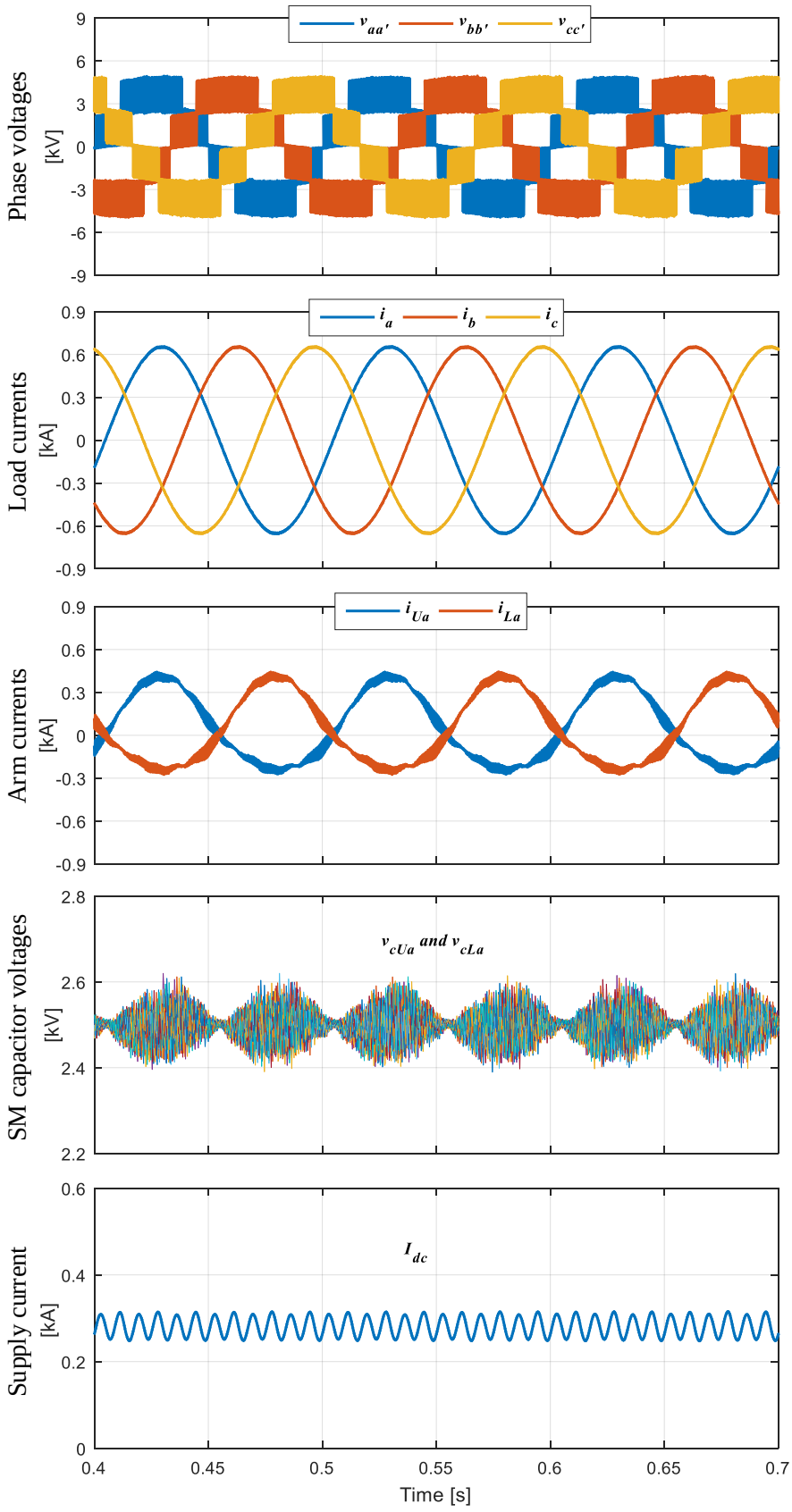

Fig. 4.18 Simulation results for a continuous operation of $3N$ DHB-assisted dual MMC at 10 Hz.

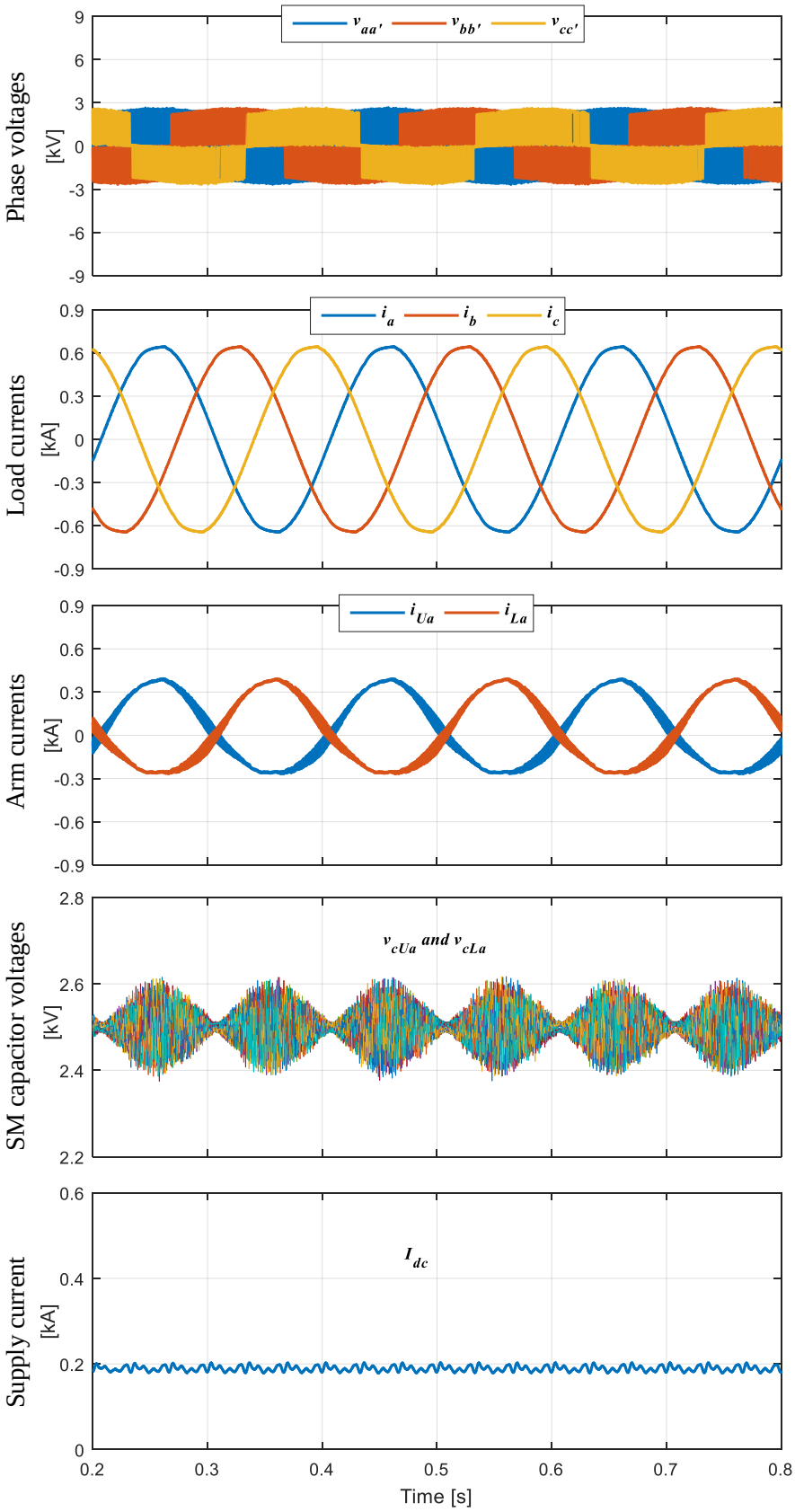

Fig. 4.19 Simulation results for a continuous operation of 3N DHB-assisted dual MMC at 5 Hz.

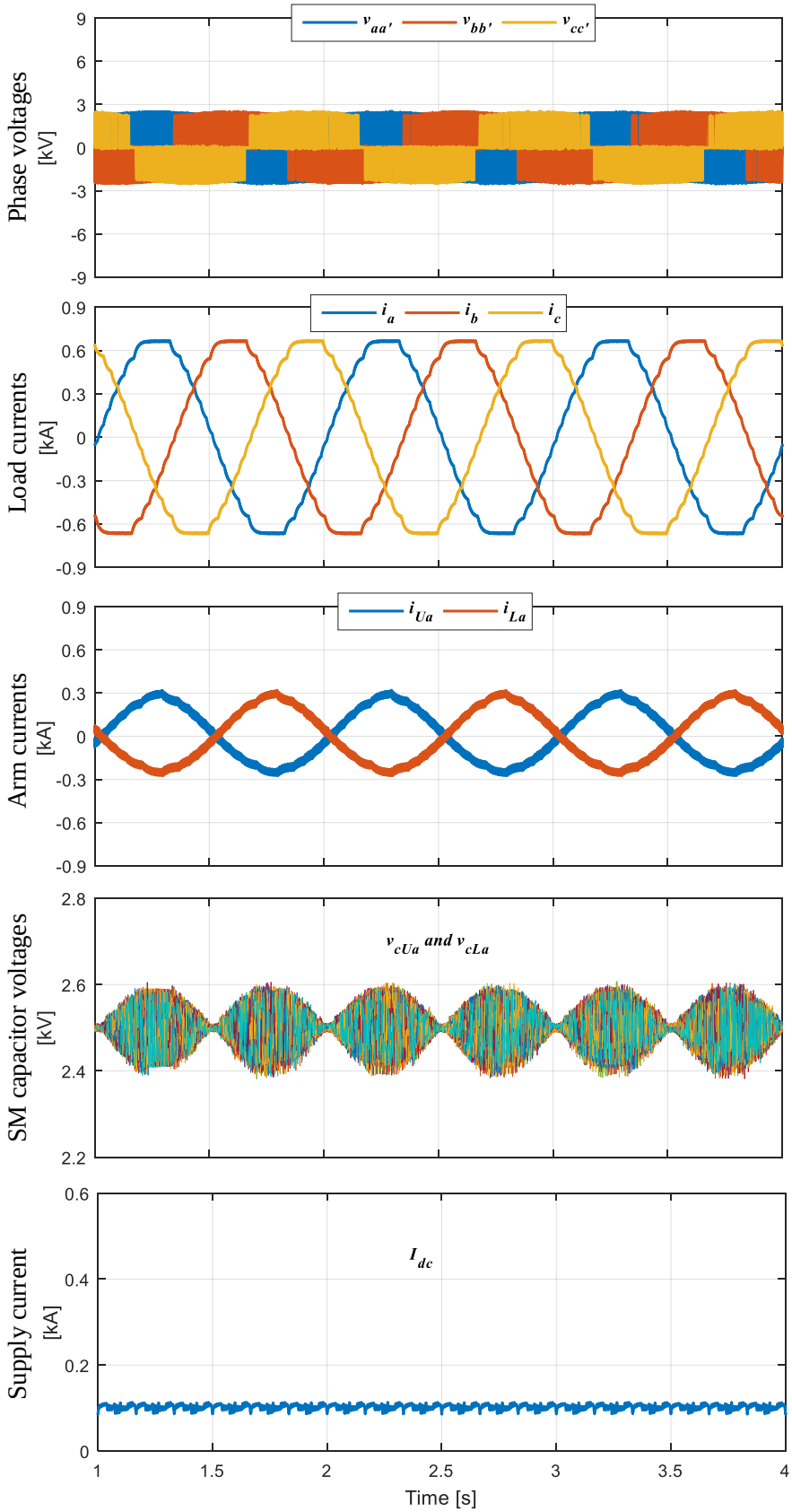

Fig. 4.20 Simulation results for a continuous operation of 3*N* DHB-assisted dual MMC at 1 Hz.

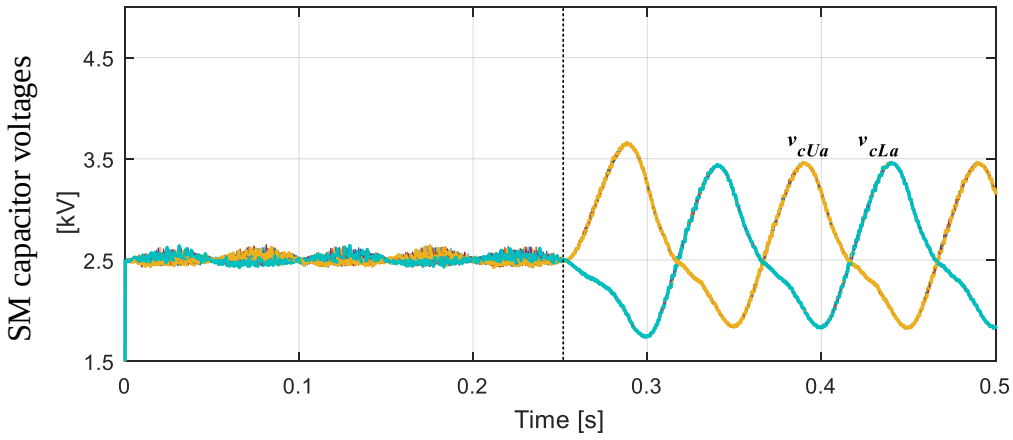

(a)

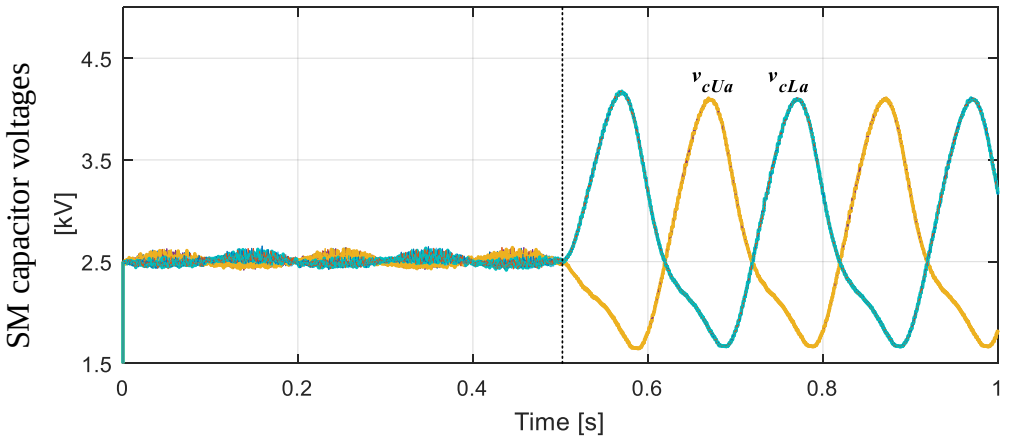

(b)

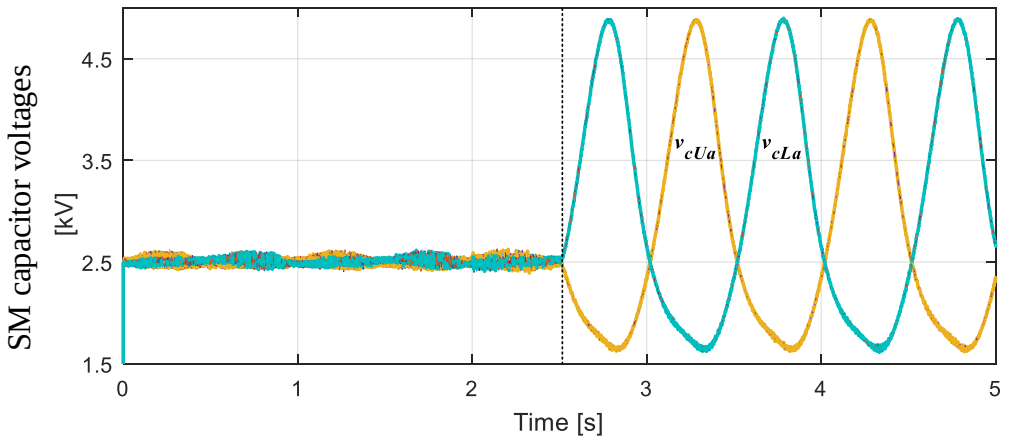

(c)

Fig. 4.21 Simulation results for capacitor voltage-fluctuation of 3N DHB-assisted dual MMC with deactivation of DHB modules at simulation mid-time, at: (a) 10 Hz, (b) 5 Hz, and (c) 1 Hz.

B. Simulation using an open-end winding machine

To investigate the dynamic performance of the DHB-assisted dual MMC and to establish its ability to extend the output power to scores of megawatts, Fig. 4.22 presents the simulation results of a 100 MW 8 kV open-end winding machine, driven from stand-still to the rated speed at full-load torque. The simulation parameters are listed in Table 4.2. The results in Fig. 4.22 show that the output currents are of high quality over the entire speed range, while the SM capacitor voltages are balanced with limited voltage-ripple regardless of the operating frequency and modulation depth. Also, the DHB-assisted dual MMC is able to operate at near zero frequency, with constant SM capacitor voltage ripple. It is worth noting that the capacitor voltage-ripple is slightly increasing at frequencies near the rated frequency compared to the voltage ripple at low frequencies, where the voltage-ripple varies between $\pm 1\%$ at near 0 Hz and $\pm 10\%$ at 50 Hz. The increase in capacitor voltage-ripple at higher motor speeds is due to the growth of the CM current which in turn increases the CM voltage-ripple component.

Table 4.2: Simulation parameters of *3N* DHB-assisted dual MMC feeding an open-end winding machine

Rated active power	100 MW
Input dc voltage (V_{dc})	12.5 kV
Number of SMs per arm (N)	5
Nominal SM capacitor voltage (V_c)	2.5 kV
Rated phase voltage	8 kV
Fundamental output frequency (f_o)	50 Hz
Carrier frequency (f_c)	2 kHz
DHB switching frequency (f_h)	10 kHz
Arm inductance (L_{arm})	2.4 mH
SM capacitance (C)	2 mF
Rated motor speed	600 rpm
Number of poles	10

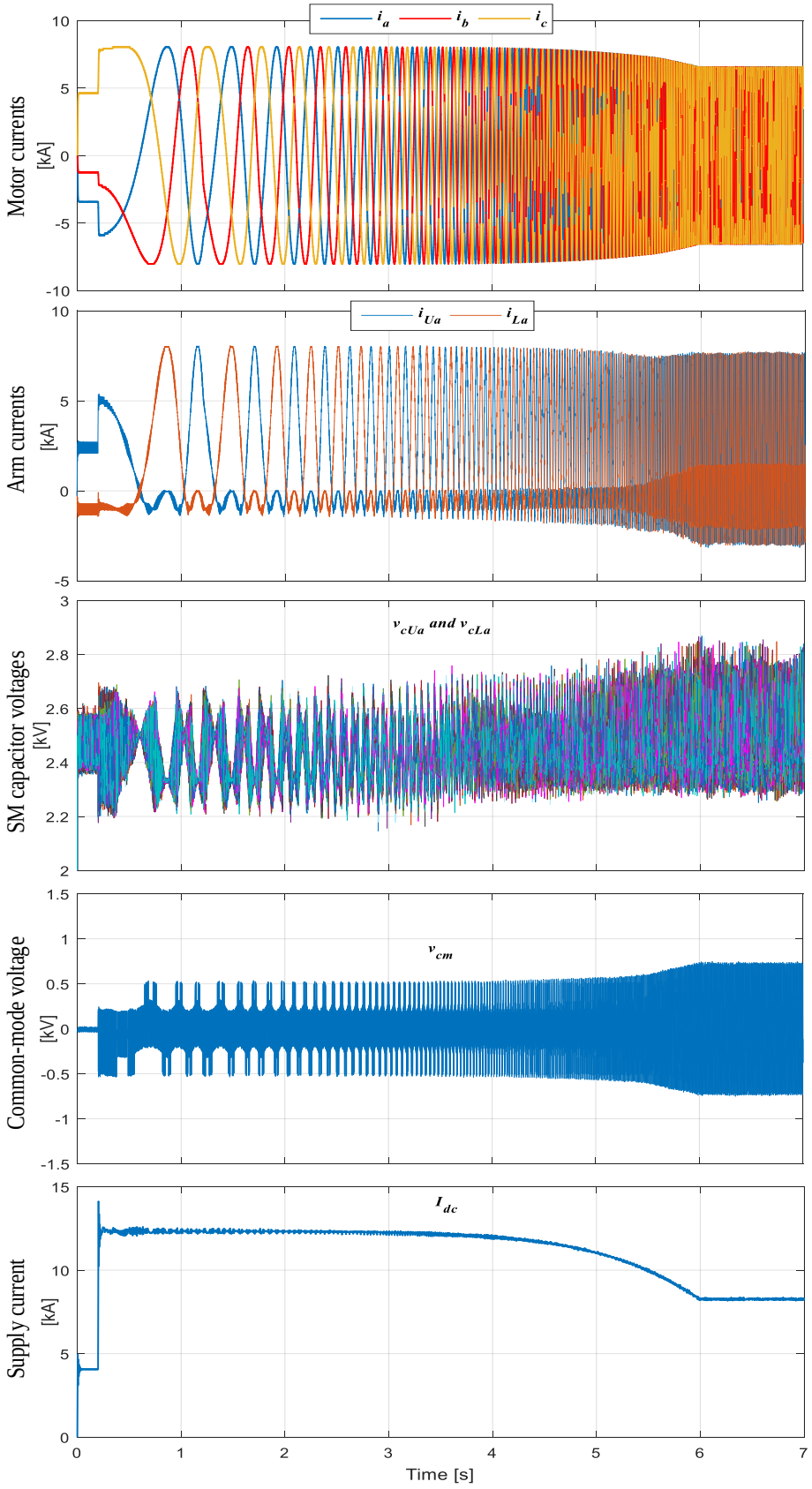

Fig. 4.22 Simulation of transient operation of 3*N* DHB-assisted dual MMC driving an open-end stator winding motor from stand-still to the rated speed at constant full-load torque.

4.5.2 Experimental Verification

A scaled-down prototype of the 3*N* DHB-assisted dual MMC is used to practically verify the effectiveness of the power decoupling concept. The experimental prototype has 3 SMs per arm (12 SMs for each dual leg), and is rated at 4 kW and 210 V. The dc-link voltage is 300 V, thus the nominal SM capacitor voltage is 100 V. Front-to-front SMs are interfaced through DHB converters employing a nano-crystalline core-based HF transformer with a saturation flux density of 1.2 T and a unity turns ratio. The control system is implemented using TMS320F28335 DSPs, and experimentation parameters are listed in Table 4.3. Three-phase *RL* load, configured in an open end connection, is connected to the dual MMC topology to assess its steady-state performance at different operating frequencies, starting from the rated frequency down to 1 Hz, while the load resistance is varied linearly with the output frequency to emulate the constant torque condition of an induction motor. Results are obtained during both the activation and deactivation of DHB balancers to confirm their influence. The experimental results are presented in Figs. 4.23–4.29.

Table 4.3: Parameters for experimentation of *3N* DHB-assisted dual MMC

Rated active power	4 kW
Input dc voltage (V_{dc})	300 V
Number of SMs per arm (*N*)	3
Nominal SM capacitor voltage (V_c)	100 V
Rated phase voltage	210 V
Rated current magnitude (I_o)	9.5 A
Fundamental output frequency (f_o)	50 Hz
Carrier frequency (f_c)	2 kHz
DHB switching frequency (f_h)	10 kHz
Arm inductance (L_{arm})	2.8 mH
SM capacitance (*C*)	1.1 mF
Load resistance	$30\times\frac{f_o}{50}\ \Omega$
Load inductance	20 mH
Transformer turns ratio (n_T)	1
Transformer auxiliary leakage inductance	100 µH

Fig. 4.23 shows the differential voltages across two phases of the open-end load terminals ($v_{aa'}$ and $v_{bb'}$) and their currents (i_a and i_b) when the dual MMC is operated at 50 Hz and 0.9 modulation index. The output voltages have three voltage levels with peak voltage equals the dc-link voltage, while the output currents are high quality with a magnitude of 9.5 A. Since the three-phase configuration is balanced, the differential voltage $v_{cc'}$ and the load current i_c will have $^2/_3\pi$ phase displacement. Fig. 4.24 shows samples of SM capacitor voltages in the four arms of the dual phase-leg aa', where they are balanced around 100 V and alternating at 100 Hz due to the CM ripple component. The switching waveforms of the phase-shift DHB converter in Fig. 4.25, show the voltages across both transformer sides in addition to the transformer current during forward and reverse power flow. The DHB converter operates at 10 kHz, while an auxiliary inductance of 100 µH is connected in series with the transformer primary side. Both primary- and secondary-side voltages are square waveforms with a constant duty cycle of 50% and near 50 V peak, which is half the nominal voltage across each SM capacitor. Also, the peak transformer current is near 6 A.

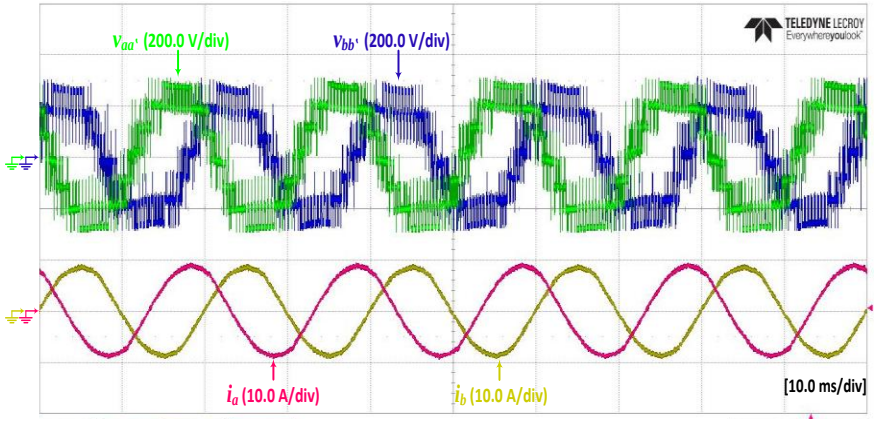

Fig. 4.23 Voltage and current waveforms for steady-state operation of 3N DHB-assisted dual MMC at 50 Hz.

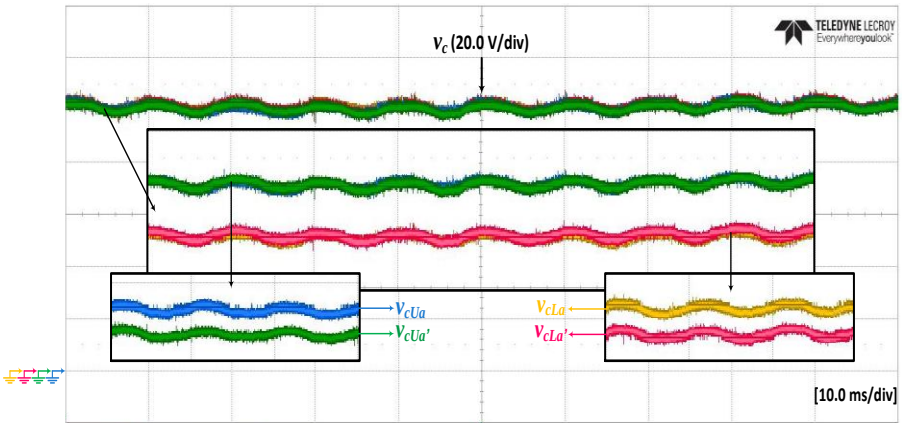

Fig. 4.24 SM capacitor voltages of $3N$ DHB-assisted dual MMC at 50 Hz.

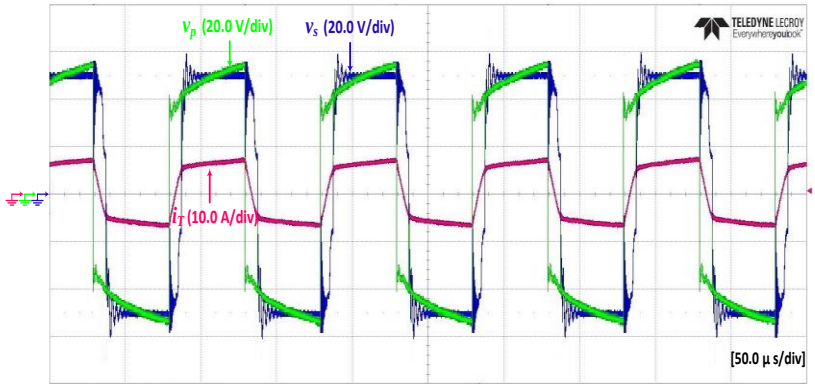

(a)

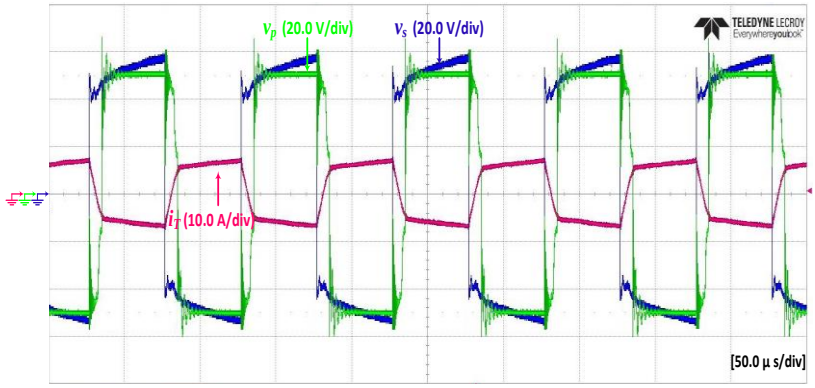

(b)

Fig. 4.25 Switching waveforms of the phase-shift DHB converter interfacing front-to-front SMs of the dual MMC, during: (a) forward power flow and (b) reverse power flow.

Further experimental results of the $3N$ DHB-assisted dual MMC configuration that assess the SM capacitor voltage-ripple at different operating frequencies are presented in Figs. 4.26–4.29 with suffix "*a*" when the DHB modules are deactivated, while suffix "*b*" means the DHB modules are operational. Only the voltage of one SM from each arm is shown, since the other waveforms are virtually identical, in addition to the output current, arm currents, and the circulating current. The output voltage is reduced in-line with operating frequency reduction, while the load resistance is varied linearly with the operating frequency to maintain constant rated output current. When the DHB modules are deactivated in the dual MMC configuration, it exhibits the performance of a conventional MMC. At 50 Hz, Fig. 4.26 shows that the capacitor voltage-ripple of a conventional MMC is 14 V (±7%), while it is reduced to 7 V (±3.5%) when the DHB modules are activated. In both cases, the output current is regulated at the rated value, while the circulating current includes second-order harmonics, since it has not been controlled to experimentally suppress even-order harmonics, so clearly affects both arm current waveforms. In Fig. 4.27, the operating frequency is reduced to 10 Hz, where the capacitor voltage-ripple is 23 V (±11.5%) for the conventional MMC, and 11 V (±5.5%) with DHB activation. With further operating frequency reduction, to 5 Hz (Fig. 4.28) and 1 Hz (Fig. 4.29), the capacitor voltage-ripple significantly increases to 42 V (±21%) and 115 V (±57.5%), respectively, for a conventional MMC topology, while is reduced to 14 V (±7%) and 18 V (±9%), respectively, with DHB balancers operation. As the operating frequency is reduced, the output current of the conventional MMC can no longer be controlled at the rated value, since the increased capacitor voltage-ripple results in a loss of control. In contrast, the output current of the DHB-assisted MMC is always regulated at the rated value, regardless of the operating frequency. The quality of the load current waveforms is adversely affected with the operating frequency reduction since the number of voltage levels is reduced. The percentage reduction in the capacitor voltage-ripple, and hence the reduction in the required SM capacitance, achieved by DHB activation is 66% and 84% at 5 and 1 Hz, respectively, although the output currents are much lower than the rated value when the DHB modules are deactivated at these low operating frequencies.

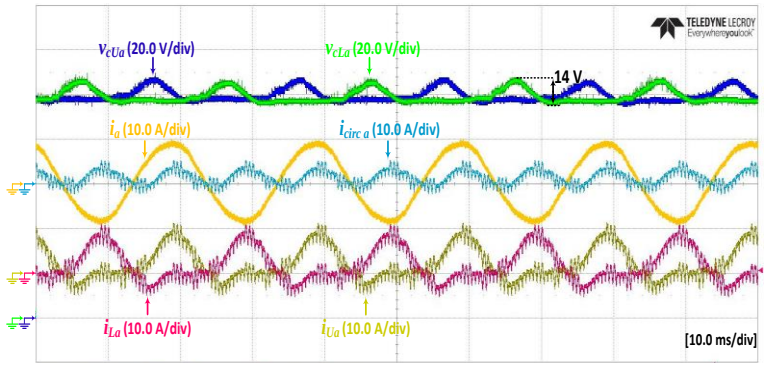

(a)

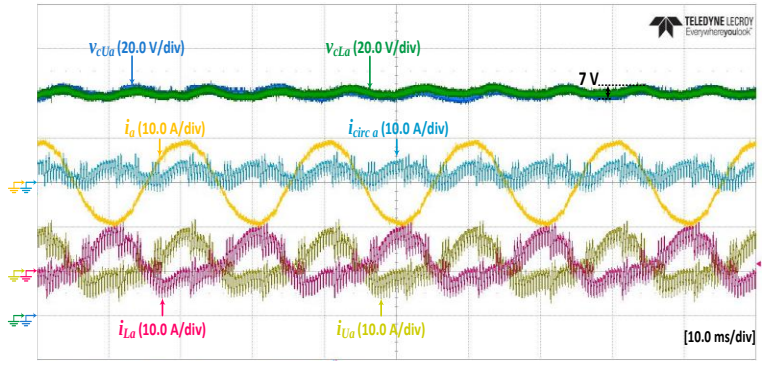

(b)

Fig. 4.26 Experimental results of DHB-assisted dual MMC topology at 50 Hz when DHB balancers are: (a) deactivated and (b) activated.

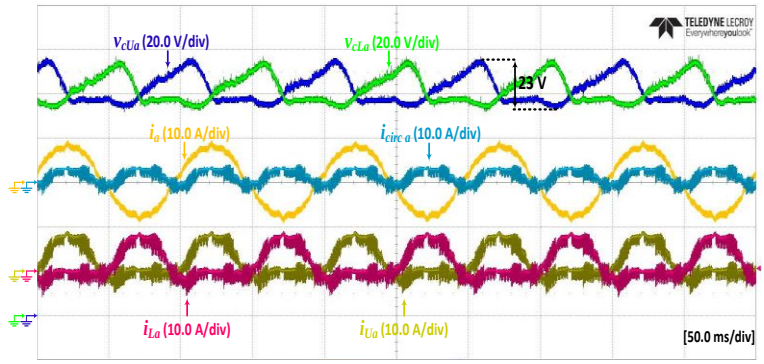

(a)

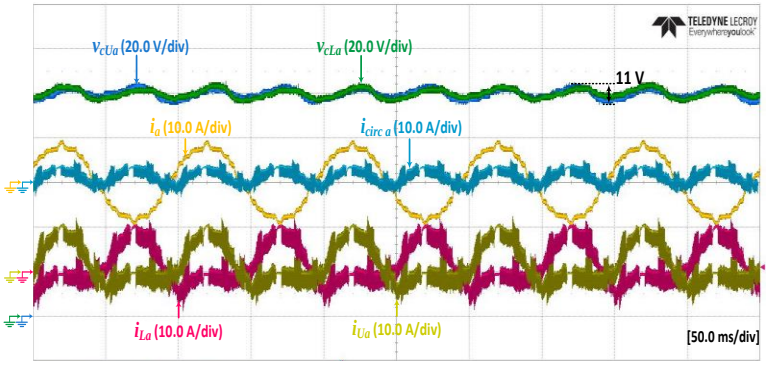

(b)

Fig. 4.27 Experimental results of DHB-assisted dual MMC topology at 10 Hz when DHB balancers are: (a) deactivated and (b) activated.

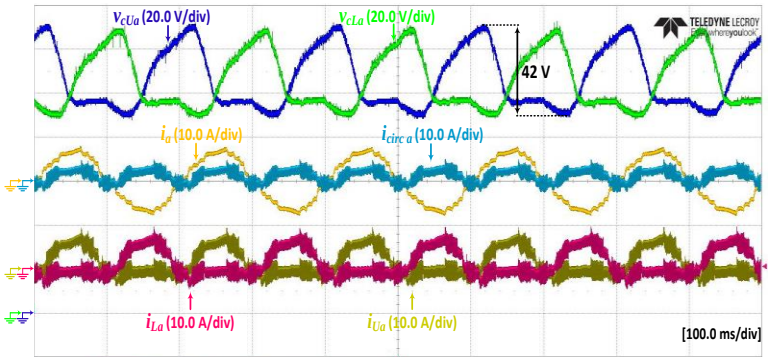

(a)

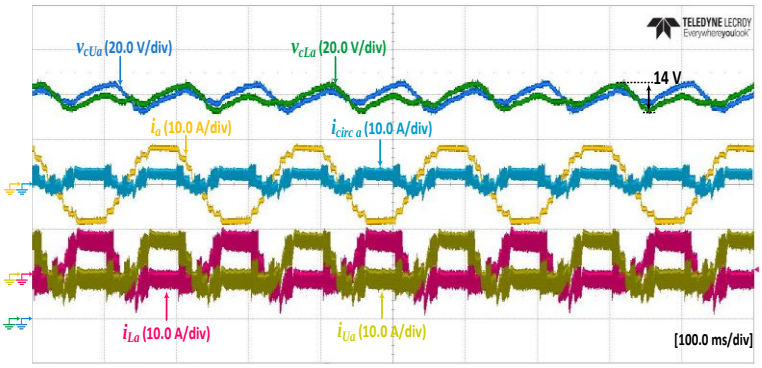

(b)

Fig. 4.28 Experimental results of the DHB-assisted dual MMC topology at 5 Hz when DHB balancers are: (a) deactivated and (b) activated.

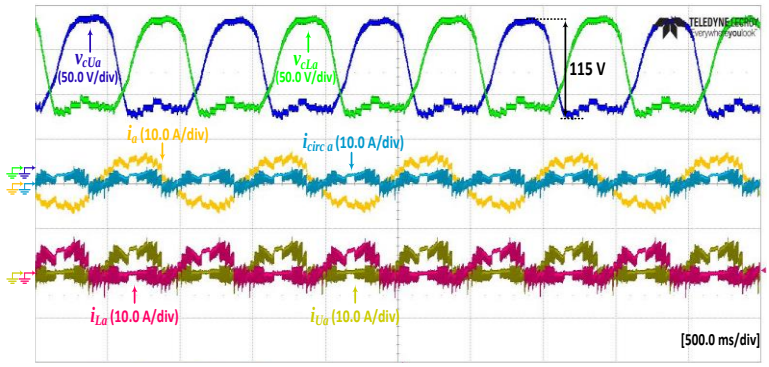

(a)

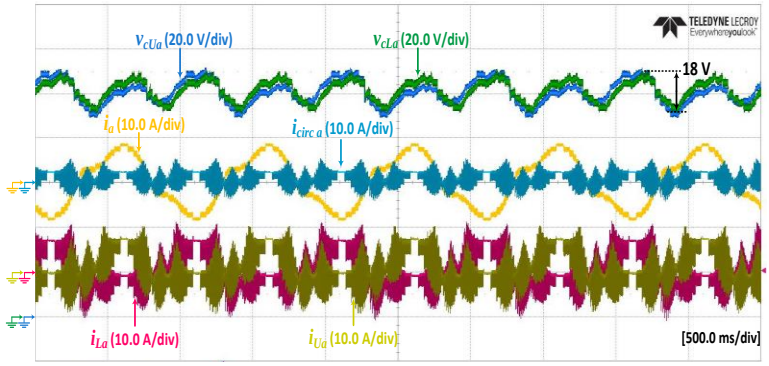

(b)

Fig. 4.29 Experimental results of DHB-assisted dual MMC topology at 1 Hz when DHB balancers are: (a) deactivated and (b) activated.

4.6 DHB-Assisted MMC for CM and DM Power Decoupling

In this section, the ripple power decoupling approach is extended to compensate for both the CM and DM power components in the MMC arms. Specifically, an MMC drive system configuration is proposed for variable-speed drives employing three-phase machines with star/delta connections, where modular DHB-based chain-links are adopted to interface each three adjacent-arm SMs at the same level. With symmetrical modulation of the three MMC phase-legs, the pulsating powers in each three adjacent-arm SMs can be eliminated, since their vectorial sum is zero. This occurs by transferring the ripple powers through three magnetically-interfaced SMs, between three phase-legs, with a capacitor voltage-ripple control scheme that ensures ripple free SM capacitor voltage. Ripple power decoupling of MMC arms results in a significant reduction in SM capacitance and MMC stored energy. Two configurations are proposed for CM and DM power decoupling, each with a different number of employed DHB balancers.

4.6.1 MMC Configuration with $6N$ DHB Balancers

A DHB-assisted MMC configuration for both CM and DM power decoupling is shown in Fig. 4.30, which employs magnetic chains with DHB power channels linking adjacent-arm SMs. A detailed circuit diagram for one of the magnetic chains linking adjacent-arm SMs is illustrated in Fig. 4.31, where three HB-SMs are interconnected through three DHB converters. Since the total number of employed DHB balancers is $6N$, the configuration is denoted as $6N$ DHB-assisted MMC.

Referring to (4.4), the CM and DM power components symmetrically pulsate in the MMC's three-phase arms, as represented in the frequency domain of Fig. 4.32. The symmetrical alternation of both power components results in a symmetrical fluctuation in the total arm power, as shown in Fig. 4.33a, which is reflected in the corresponding SM capacitor voltage variation, as presented in Fig. 4.33b. That is, the capacitor voltage-ripple of an upper-arm SM alternates with a $⅔\pi$ phase-shift to the capacitor voltage-ripple of adjacent SMs in other upper phase-arms, while it alternates anti-phase to the capacitor voltage-ripple of an SM in corresponding lower arm due to the predominance of the DM component. The proposed $6N$ DHB-assisted MMC

redistributes the stored capacitive-energy among each three adjacent-arm SMs by allowing their ripple power to be transferred from one SM with an excess of capacitive stored energy to the other SMs, in a closed magnetic loop, to source the lack of energy. With zero vector sum of symmetrical three-phase components, the CM and DM power components are decoupled in each chain link of adjacent-arm SMs. Ideally, this results in a ripple-free SM capacitor voltage profile, where the capacitors need only to withstand voltage ripple at the switching frequency.

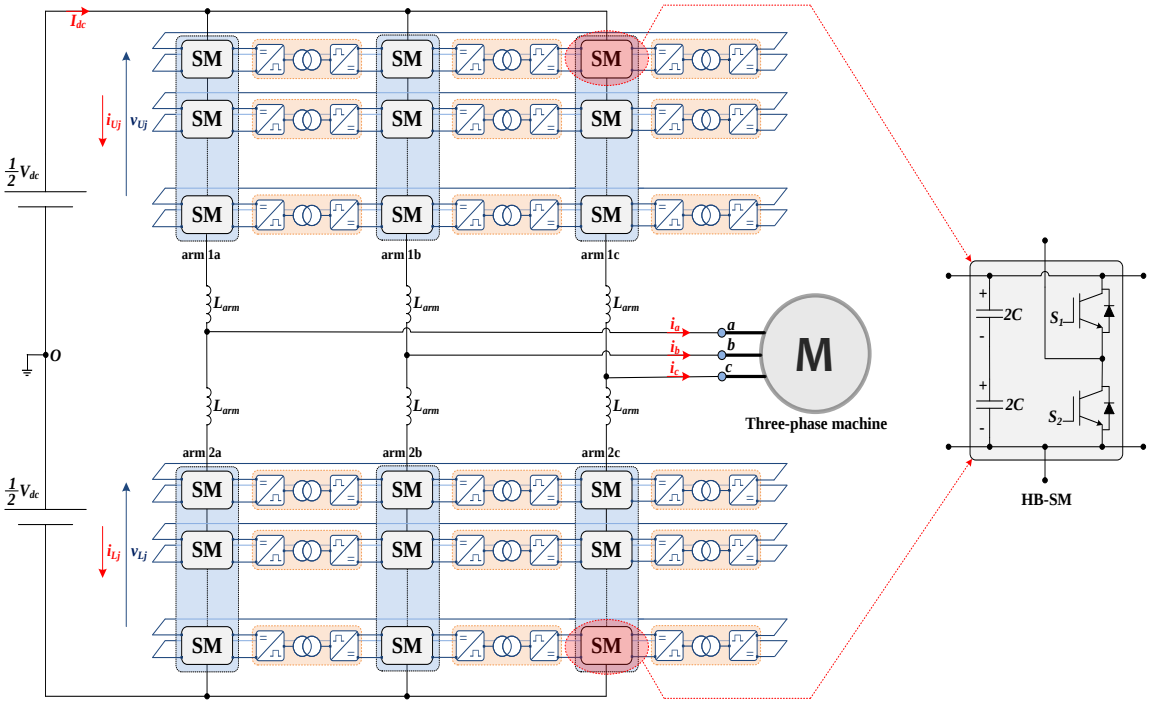

Fig. 4.30 Circuit diagram of 6*N* DHB-assisted MMC configuration for CM and DM power decoupling.

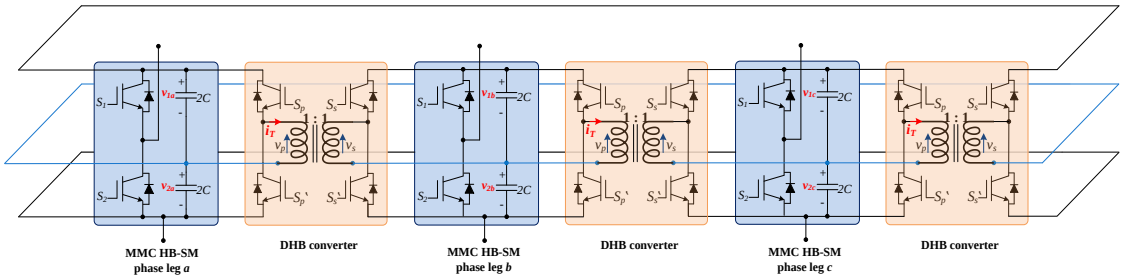

Fig. 4.31 A DHB-based power decoupling chain for three MMC adjacent-arm HB-SMs.

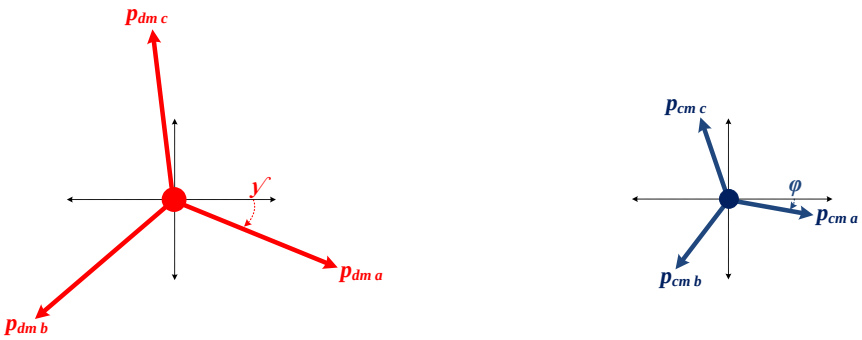

(a) (b)

Fig. 4.32 Phasor representation of MMC arm power components in: (a) fundamental-frequency domain and (b) second-order frequency domain.

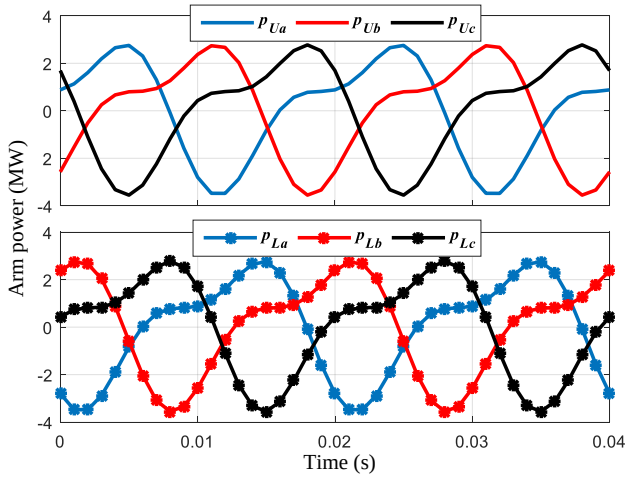

(a)

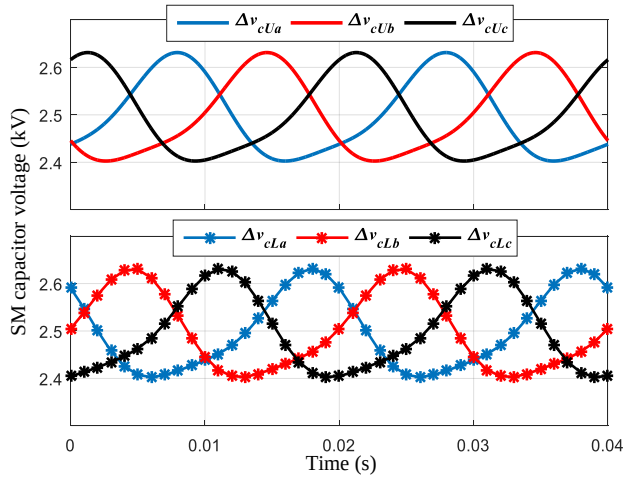

(b)

Fig. 4.33 Symmetrical alternation of: (a) three-phase arm powers and (b) three-phase SM capacitor voltages. (V_{dc} = 25 kV, V_c = 2.5 kV, C = 3 mF, I_o = 500 A, M = 0.75, and φ = 25°).

Although the $6N$ DHB-assisted MMC completely decouples SM ripple power (both CM and DM components), the decoupled power can be approximated as the DM power, being the major contributor in the arm ripple power. Thus, the maximum SM decoupled power can be calculated from (4.4b), as:

$$P_{SM_{max}} = \frac{P_{dm_{max}}}{N} = \frac{V_{dc}\, I_o}{4N} \tag{4.26}$$

where $P_{SM_{max}}$ and $P_{dm_{max}}$ are the peak decoupled SM power and DM arm power, respectively. Since each SM capacitor is shared between two DHB balancers, the SM ripple power can be transferred through two power paths. The DHB control algorithm limits the maximum power transferred through each DHB module to half the SM decoupled power. Thus, each DHB module is rated at half the SM power as given by (4.27), where $P_{DHB_{max}}$ is the peak power transferred through each DHB module.

$$P_{DHB_{max}} = \frac{P_{SM_{max}}}{2} = \frac{V_{dc}\, I_o}{8N} \tag{4.27}$$

Since the voltage applied on both transformer windings is $½V_c$, the maximum transformer current, $I_{T_{max}}$, is:

$$I_{T_{max}} = \frac{2P_{DHB_{max}}}{V_c} = \frac{I_o}{4} \tag{4.28}$$

Therefore, the voltage rating of the DHB switching devices is V_c, while the current rating is $¼I_o$.

4.6.2 MMC Configuration with $4N$ DHB Balancers

A variation of the $6N$ DHB-assisted MMC can be realized as shown in Fig. 4.34, where the number of employed DHB modules is reduced by 33%. In this alternative configuration, each three adjacent-arm SMs are linked through a magnetic chain of two DHB balancers. Thus, the total number of employed DHB balancers is $4N$, so the topology is denoted as $4N$ DHB-assisted MMC.

Referring to Fig. 4.34, each SM in the middle phase-leg is interfaced with the right and left phase-leg SMs of the same level through a separate DHB balancer. This keeps the SMs at the right and left phase-legs implicitly connected via the corresponding middle phase-leg's SMs. Thus, the number of employed DHB modules in this alternative configuration is reduced to $2/3$ the number of MMC SMs. However, each DHB module is rated at the full SM decoupled power, which doubles the current stress of the DHB switching devices, compared to the $6N$ DHB-assisted MMC.

It is worth mentioning that both the $6N$ and $4N$ DHB-assisted MMC topologies provide the same power decoupling performance which results in same SM capacitor voltage-ripple profile. However, the $6N$ DBH-assisted MMC is preferred for high power drives, since lower power is transmitted through the DHB balancers. The $4N$ DBH-assisted MMC may be applicable at lower power ratings, where the size of the drive system is prioritized.

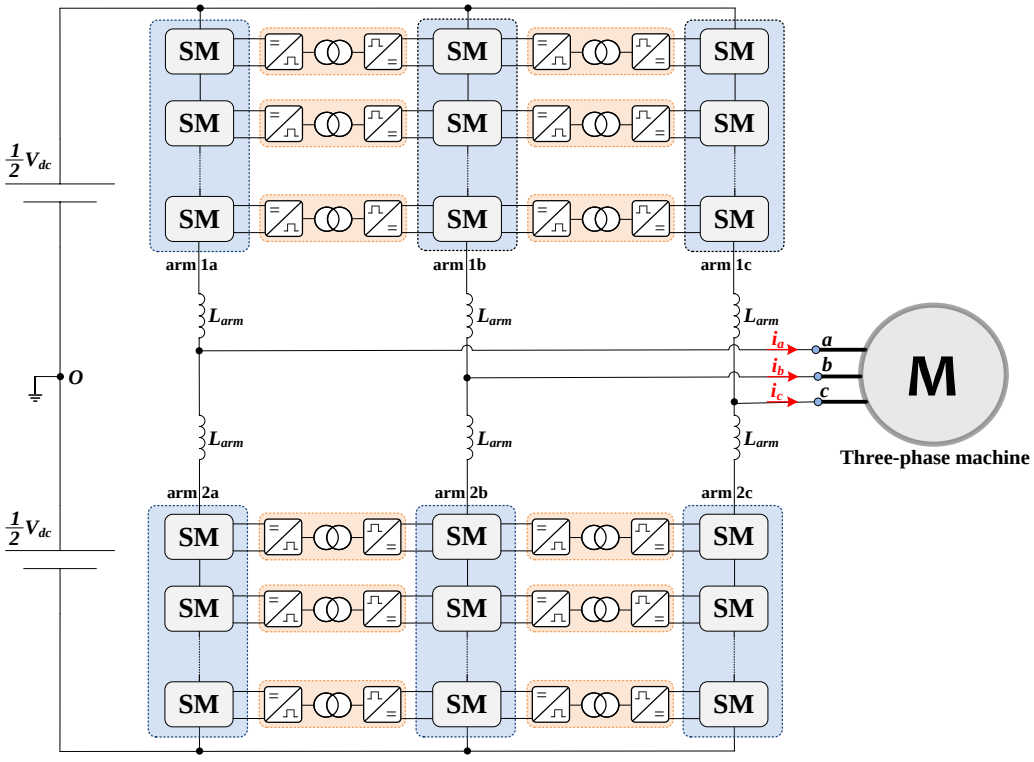

Fig. 4.34 $4N$ DHB-assisted MMC configuration for CM and DM power decoupling.

4.7 Verification of $6N$ and $4N$ DHB-Assisted MMC Configurations

The performance of the DHB-based power decoupling approach for both CM and DM components is investigated using MATLAB/SIMULINK simulation models, in addition to experimentation using a scaled-down laboratory prototype. In both verification methods, steady-state and dynamic performances are examined during different operating scenarios.

4.7.1 Simulation Verification

In the simulation study, the $6N$ DHB-assisted MMC configuration is implemented, where a chain link of three DHB balancers interfaces the adjacent-arm SMs at the same level. With 166 kW indicating the achieved maximum power rating of practically implemented HF transformers [98], the $6N$ DHB-assisted MMC simulation model is rated at 20 MW with 10 SMs per arm. The rest of simulation parameters is listed in Table 4.4.

A. Simulation using RL load

The steady-state fundamental waveforms of the $6N$ DHB-assisted MMC supplying a three-phase star-connected *RL* load at rated parameters are shown in Fig. 4.35, while Fig. 4.36 shows the waveforms of the DHB balancers. In Fig. 4.35, the three-phase line voltages and load currents are high-quality sinusoidal waveforms. The arm currents are controlled to eliminate the second- and fourth-order harmonics using the PR-based circulating current regulation method. That is, the PR controllers are tuned at 100 Hz and 200 Hz, respectively, resulting in a near dc circulating current. Different capacitor voltage samples for upper- and lower-arm SMs are shown balanced around 2.2 kV with $\pm 10\%$ voltage ripple. The supply current is near constant with only switching harmonics, due to the suppression of even harmonics in the arm currents.

Fig. 4.36 shows the switching waveforms of one DHB balancer interfacing a pair of upper-arm SMs located in phase a and b, within two switching cycles in different time spans. The voltages across the primary and secondary transformer winding are shown, along with the transformer current. The amount of power transfer is proportional to the magnitude of the phase-angle difference, where forward or reverse power transfer is designated depending on the polarity of δ.

Table 4.4: Simulation parameters for *6N* DHB-assisted MMC configuration

MMC parameters	
Rated active power	20 MW
Input dc voltage (V_{dc})	22 kV
Number of SMs per arm (N)	10
Nominal SM capacitor voltage (V_c)	2.2 kV
Rated line voltage	13.2 kV
Rated current magnitude (I_o)	1.3 kA
Fundamental output frequency (f_o)	50 Hz
PWM Carrier frequency (f_c)	2 kHz
Arm inductance (L_{arm})	2 mH
Equivalent SM capacitance (C)	1 mF
DHB parameters	
Transformer turns ratio	1
Auxiliary leakage inductance (L)	100 µH
DHB switching frequency (f_h)	10 kHz
***RL* load parameters**	
Load resistance	$7.88\times\frac{f_o}{50}$ Ω
Load inductance	8.25 mH
Motor parameters	
Rated output power	20 MW
Rated line voltage	13.2 kV
Fundamental frequency	50 Hz
Rated speed	600 rpm
Number of poles	10

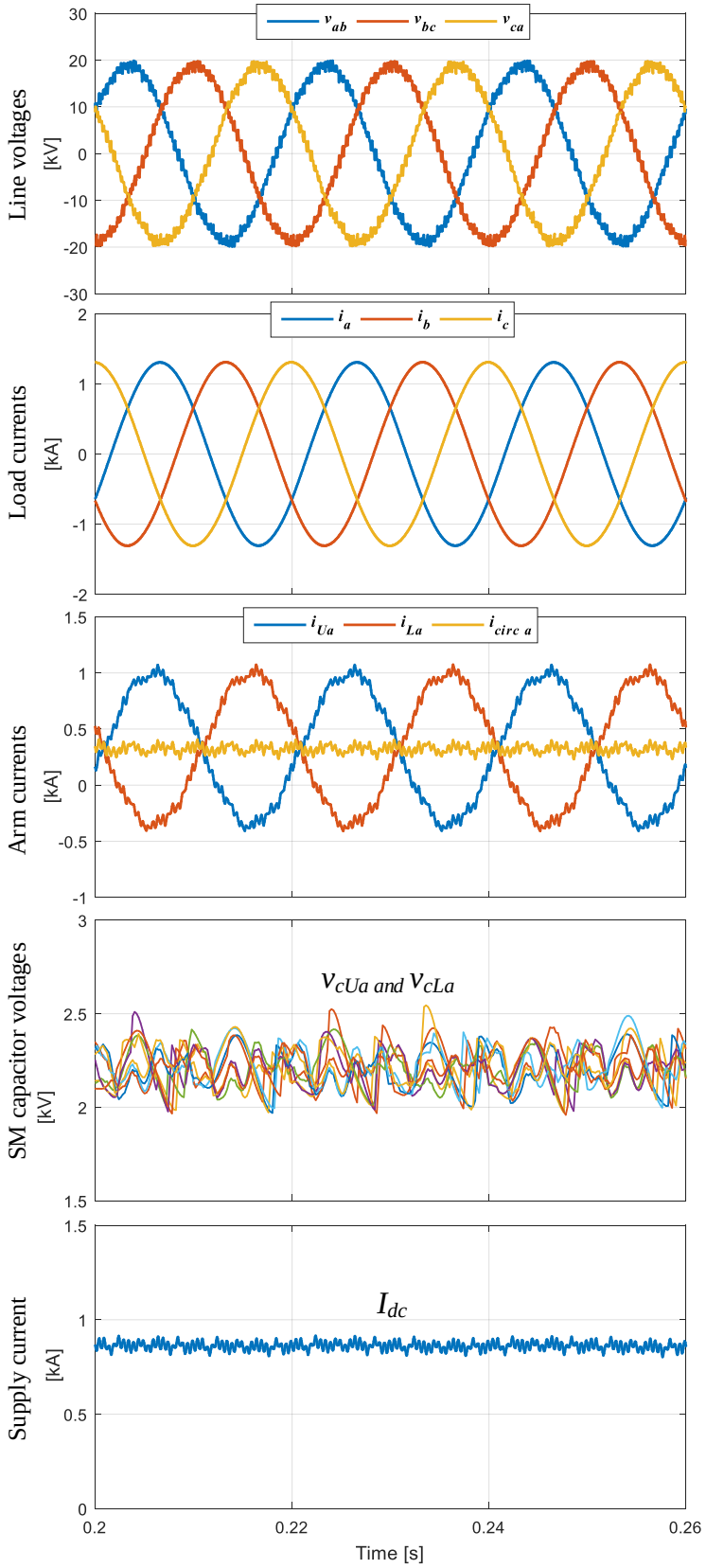

Fig. 4.35 Simulation results of 6*N* DHB-assisted MMC at rated parameters.

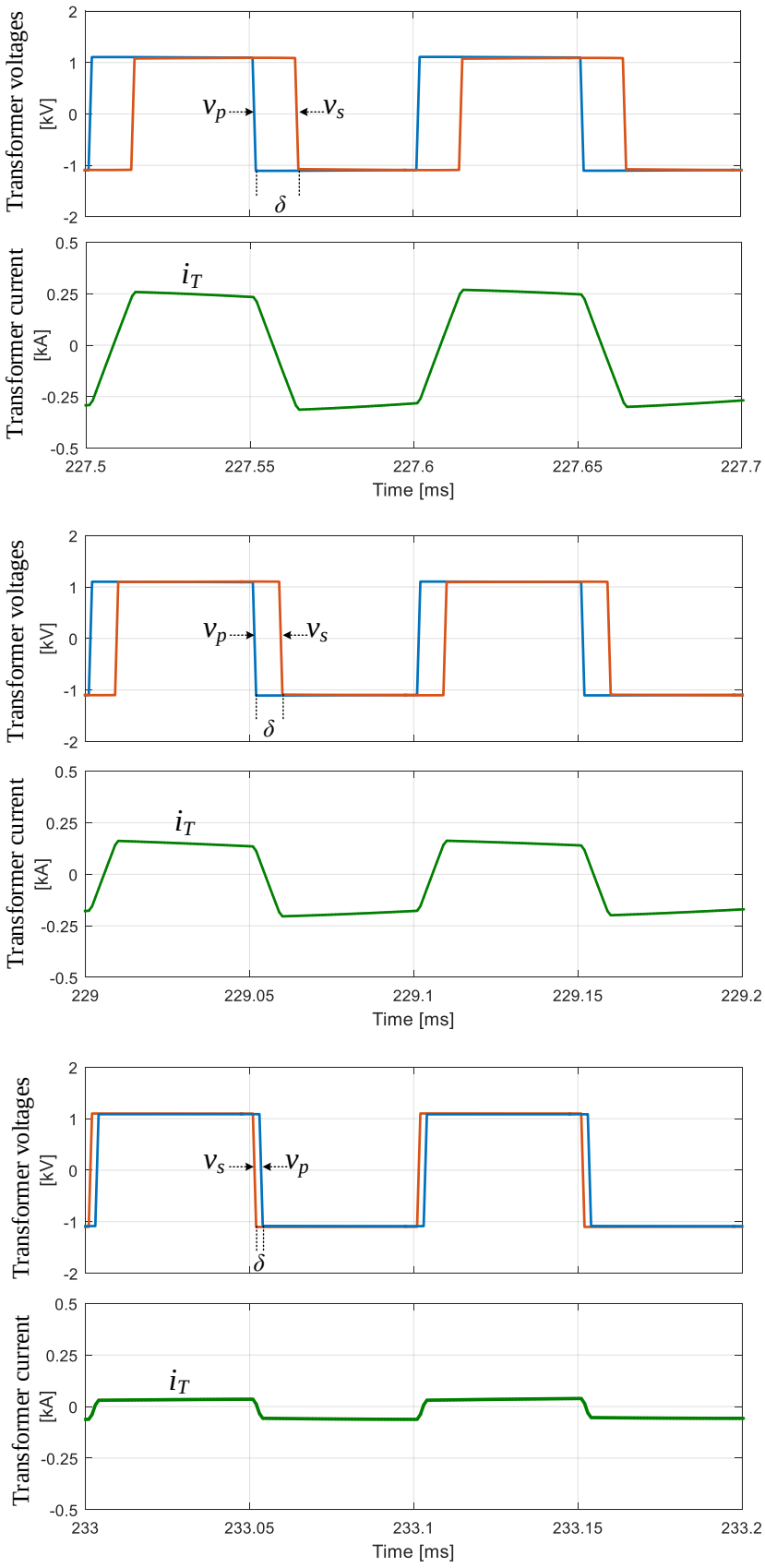

Fig. 4.36 Simulated switching waveforms of the phase-shift DHB converter at rated parameters.

To highlight the effectiveness of the $6N$ DHB-based power decoupling scheme, the simulation is performed at low operating frequencies, while the load resistance is varied linearly with the frequency reduction to maintain the load current constant at the rated value. The DHB balancing scheme is initially deactivated, and the MMC system behaves as a conventional MMC, (the results are obtained for one operating cycle). Then, the DHB balancing scheme is activated, and the system performance is monitored for two cycles, as shown in Figs. 4.37 and 4.38 for operation at 10 and 5 Hz, respectively. Common to both cases is the quality of both line voltages and load currents is enhanced with the activation of power decoupling scheme. Also, with the fundamental and second-order arm powers decoupled in the three-phase MMC legs, the arm currents are near even harmonics free without applying any harmonic suppression control. SM capacitor voltages exhibit significant ripple reduction with the DHB energy balancing scheme, where at 10 Hz, the voltage ripple is reduced from $\pm 52\%$ to $\pm 5\%$, and from $\pm 90\%$ to $\pm 5\%$ at 5 Hz. Although operation with such extreme voltage ripple percentages without DHB scheme incorporation is impractical, it concludes the significant reduction possibly achieved in SM capacitance when the power decoupling scheme is employed.

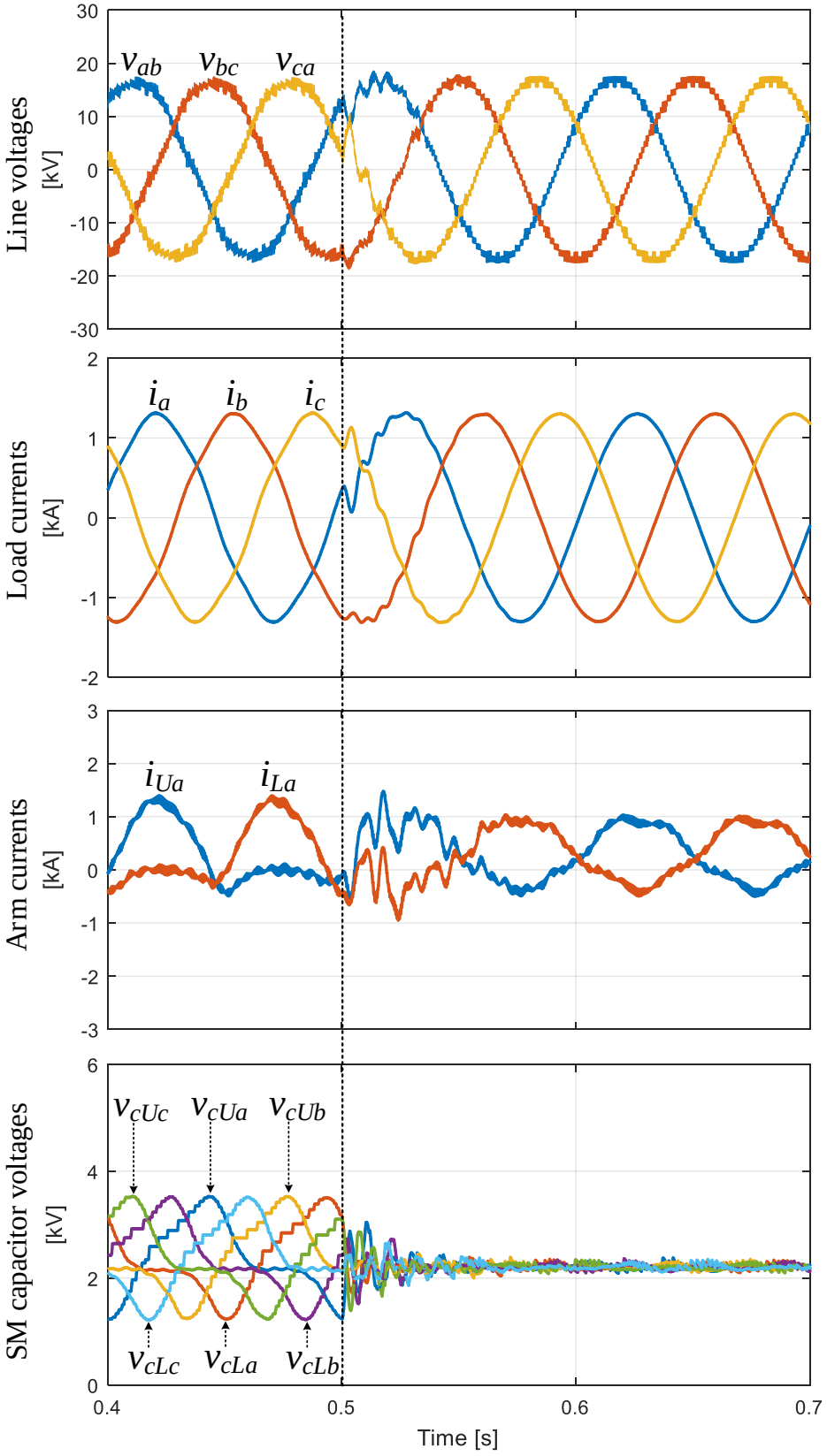

Fig. 4.37 Performance of 6*N* DHB-assisted MMC at 10 Hz before and after DHB power decoupling scheme activation.

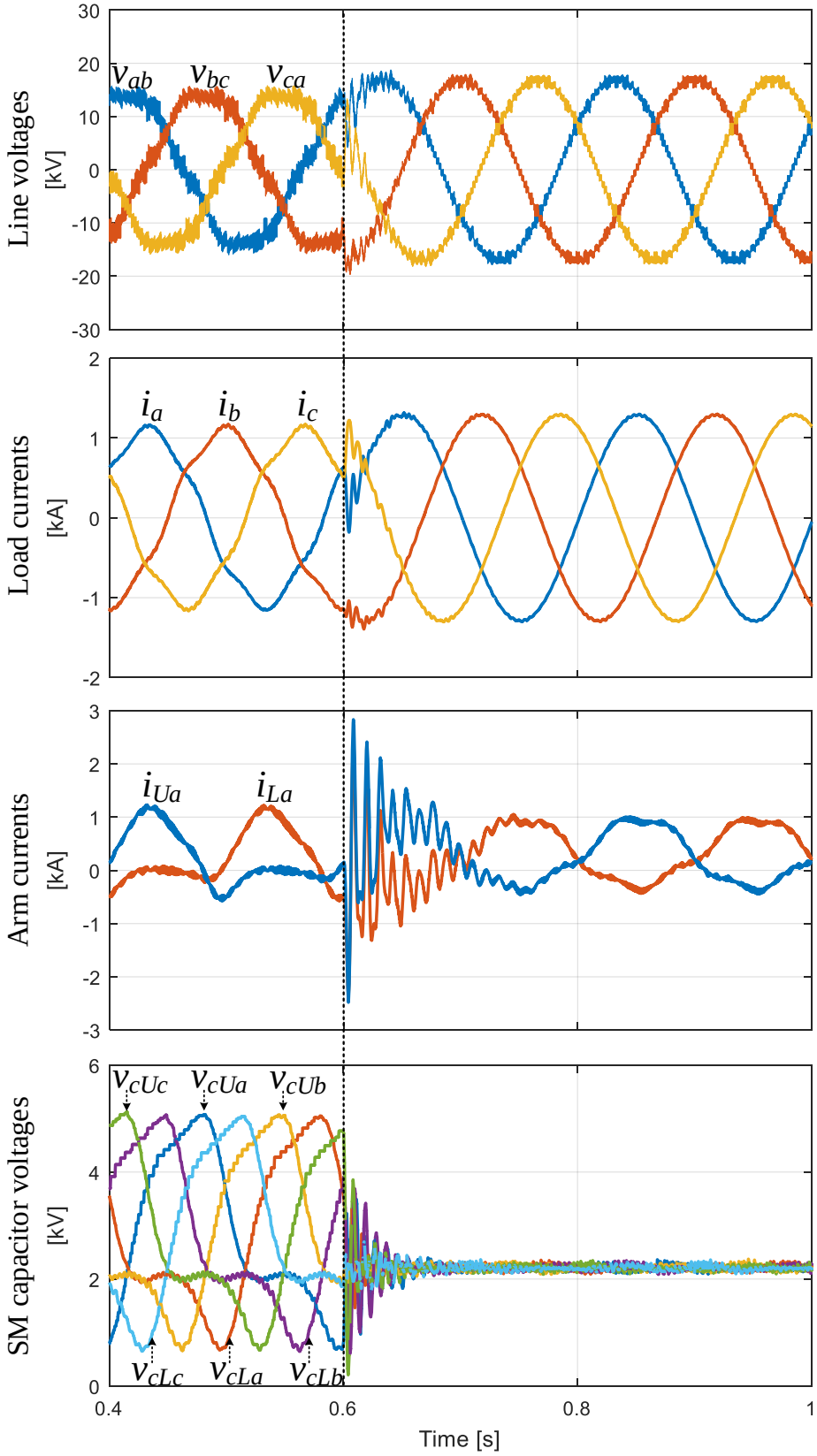

Fig. 4.38 Performance of 6*N* DHB-assisted MMC at 5 Hz before and after DHB power decoupling scheme activation.

B. Simulation using an induction machine

Figs. 4.39 and 4.40 show the dynamic performance of the $6N$ DHB-assisted system when driving a 20 MW 13.2 kV three-phase induction machine. In Fig. 4.39, the MMC system drives the motor from standstill to the rated speed, at the rated torque. The motor currents maintain a high-quality sinusoidal profile over the entire speed range, where initial conditions are set in the simulation model to avoid high starting motor currents. The SM capacitor voltage ripple is limited within a narrow ripple band, even at near zero frequency. The CM voltage at the machine terminals swings with a 1.5 kV amplitude. The supply current is continuous with only switching harmonics, while slightly reduced when the motor reaches steady-state at rated speed.

Fig. 4.40 shows the performance of the MMC-DHB system with a step change in the motor speed, where the operating frequency is changed from 50 Hz to 25 Hz after 0.04 seconds of simulation time, while is changed down to 5 Hz at 0.12 seconds. The results show that the MMC-DHB system has fast dynamic response due to the change in the operating frequency, where the waveforms promptly stabilize at the new operating condition.

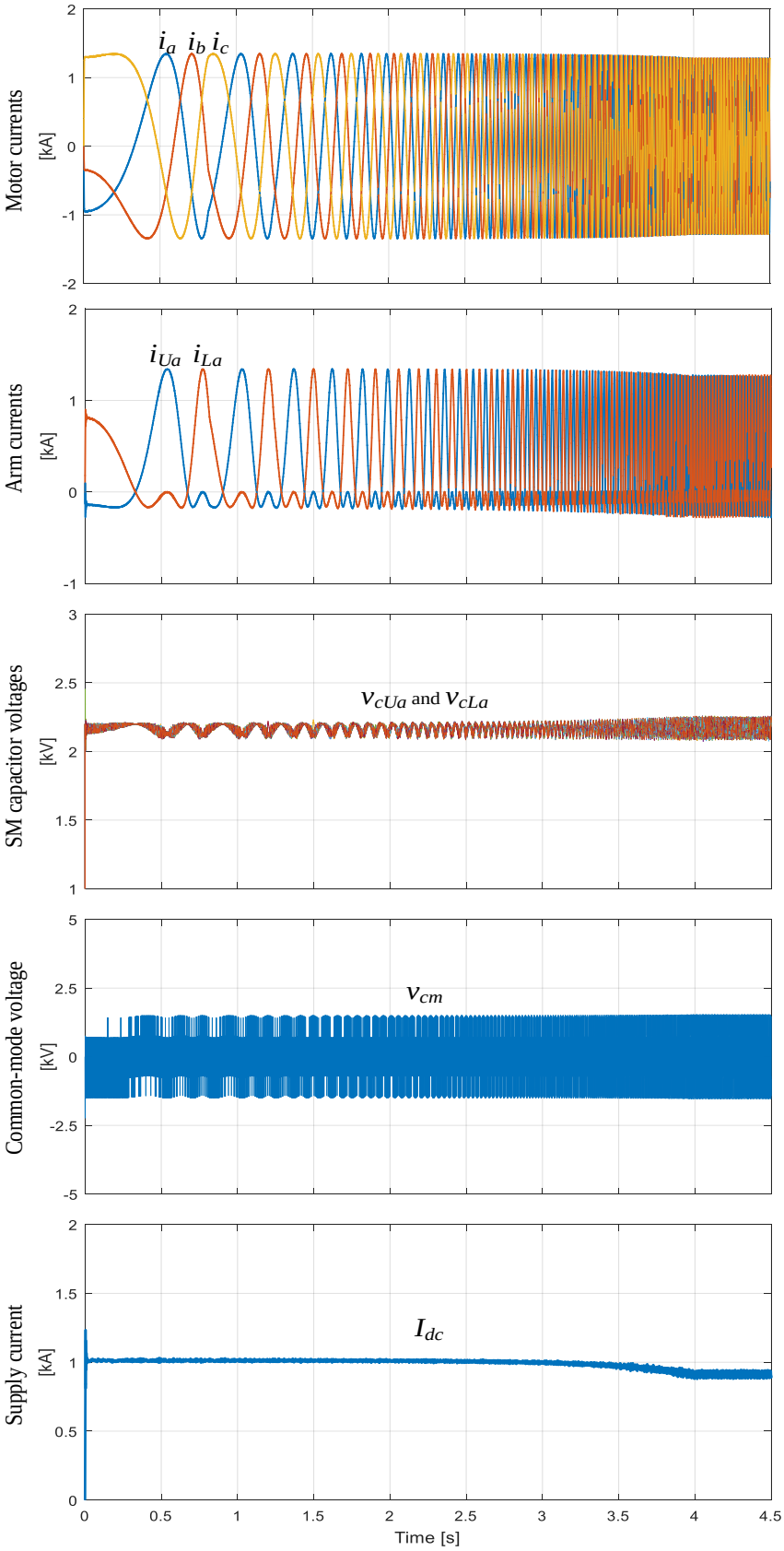

Fig. 4.39 Dynamic performance of 6*N* DHB-assisted MMC system when driving a 20 MW induction machine from standstill to rated speed.

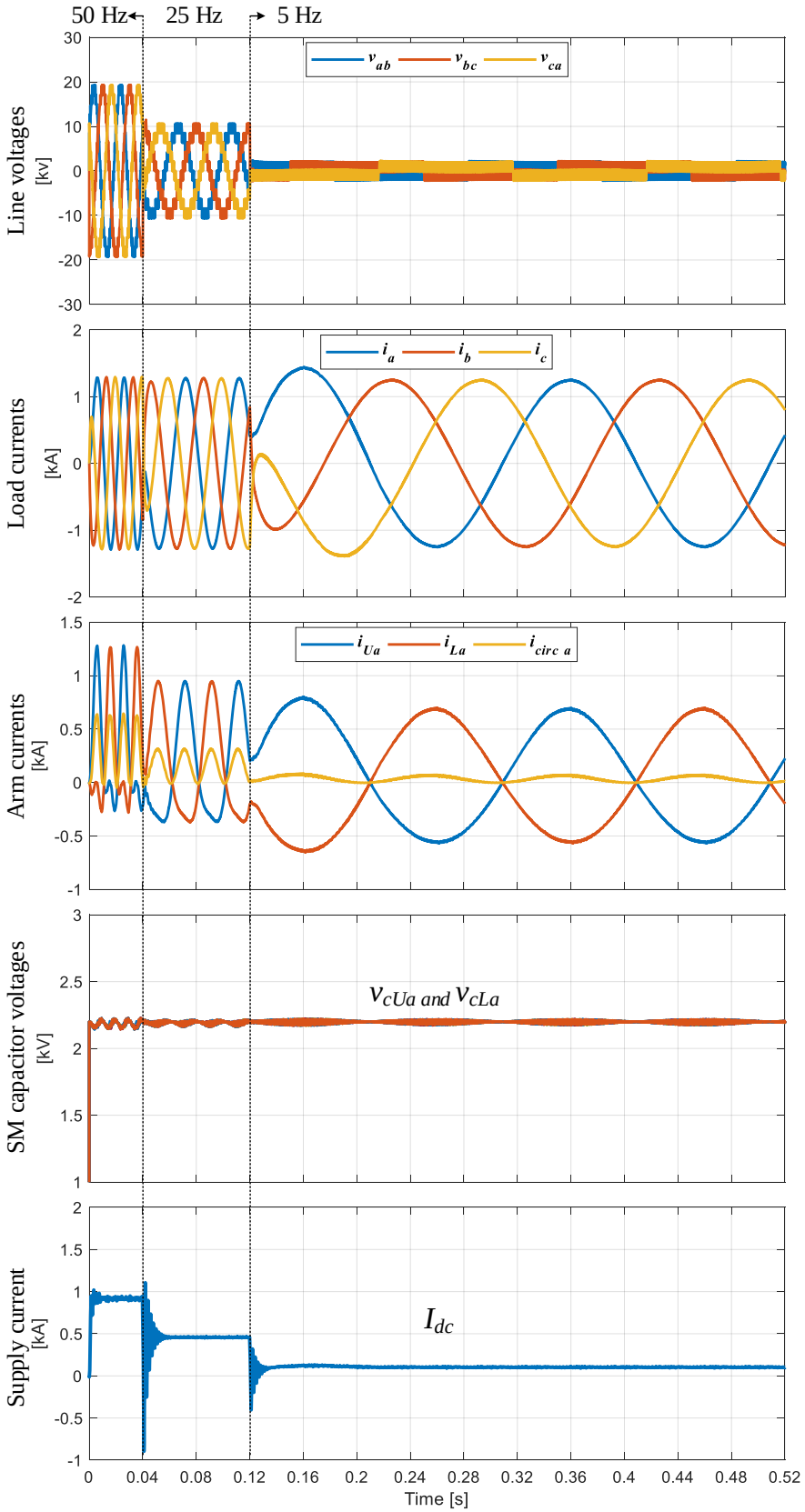

Fig. 4.40 Dynamic performance of 6*N* DHB-assisted MMC system when driving a 20 MW induction machine from standstill to rated speed.

4.7.2 Experimental Verification

Practical validation uses a scaled down laboratory prototype comprising a three-phase MMC rated at 6 kW and 360 V, with 3 SMs per arm, supplied from 600 V dc. To reduce the number of employed SM balancers, the $4N$ DHB-based power decoupling approach is adopted, where central arm SMs are interfaced through two DHB balancers. Parameters for experimentation are listed in Table 4.5. The control system is implemented in TMS320F28335 DSPs. Both steady-state and dynamic performance of the $4N$ DHB-assisted MMC system are examined under different operating scenarios. Steady-state results at different operating frequencies are obtained while the MMC is supplying a three-phase *RL* load, where the resistance is varied linearly with frequency variation to emulate constant Volt/Hertz operation. Dynamic results are obtained during starting of a three-phase induction machine from standstill to the rated speed. Experimental waveforms are presented in Figs. 4.41–4.46.

A. Steady-state performance

Fig. 4.41 shows the MMC fundamental waveforms at the rated parameters in Table 4.5, where the MMC is supplying a three-phase *RL* load at 50 Hz. The phase voltage waveforms are shown with respect to the virtual ground of the dc-link midpoint, so have seven voltage-levels between ±300 V. The CM voltage is shown as the average of the measured phase voltages with 70 V amplitude. The three-phase line voltages and corresponding load currents are balanced. Arm currents of phase a and its circulating current are shown, where the arm currents are free of dominant even-harmonics due to circulating current control, resulting in a near dc circulating current.

Figs. 4.42–4.45 practically assess the influence of DHB power decoupling by presenting SM capacitor voltage fluctuation at different operating frequencies, before and after the DHB balancers' operation. Three samples of upper-arm SM capacitor voltages are shown for the three phase-legs. At 50 Hz, Fig. 4.42 shows that capacitor voltage ripple is reduced from $\pm 5.6\%$ to $\pm 2.5\%$ with DHB balancing scheme incorporation. A more significant reduction in capacitor voltage ripple, with the activation of the energy balancing scheme, occurs at reduced operating frequencies, where at 10 Hz (see Fig. 4.43) the capacitor voltage ripple decreases from $\pm 11.25\%$ to $\pm 4.25\%$, while at 5 Hz (see Fig. 4.44) the voltage ripple decreases from $\pm 21\%$ to

$\pm 5.25\%$. At 1 Hz, Fig. 4.45a shows that the capacitor voltage ripple using a conventional MMC is extreme; $\pm 67\%$, possibly threatening the safe operation of MMC components and results in a loss of system controllability. The DHB scheme efficiently restores the MMC balance as shown in Fig. 4.45b, where the capacitor voltage ripple is $\pm 6\%$. Although the capacitor voltage ripple, with the DHB scheme is in operation, slightly increases with frequency reduction, the ripple is maintained within tolerated limits at all operating frequencies.

Table 4.5: Experimentation parameters for *4N* DHB-assisted MMC

MMC parameters	
Rated active power	6 kW
Input dc voltage (V_{dc})	600 V
Number of SMs per arm (N)	3
Nominal SM capacitor voltage (V_c)	200 V
Rated line voltage	360 V
Rated current magnitude (I_o)	16.5 A
Fundamental output frequency (f_o)	50 Hz
PWM Carrier frequency (f_c)	2 kHz
Arm inductance (L_{arm})	2.4 mH
SM capacitance (C)	1.1 mF
DHB parameters	
Transformer turns ratio	1
Auxiliary leakage inductance (L)	70 µH
DHB Switching frequency (f_h)	10 kHz
***RL* load parameters**	
Load resistance	$16\times\frac{f_o}{50}\ \Omega$
Load inductance	26 mH
Motor parameters	
Rated output power	4 kW
Rated line voltage	380 V
Fundamental frequency	50 Hz
Rated speed	1440 rpm
Number of poles	4

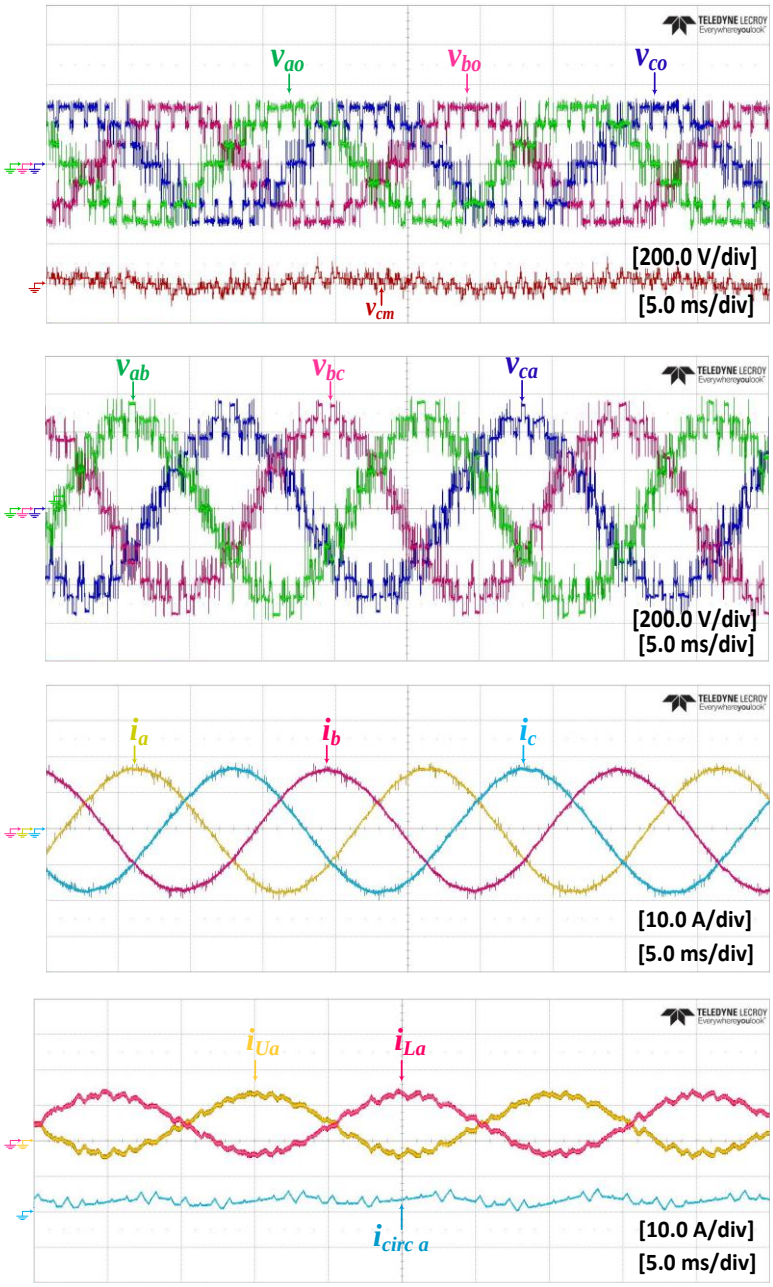

Fig. 4.41 Experimental waveforms of 4*N* DHB-assisted MMC at rated parameters.

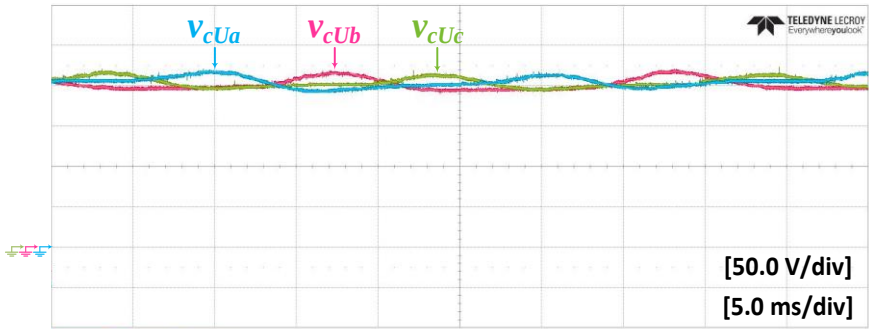

(a)

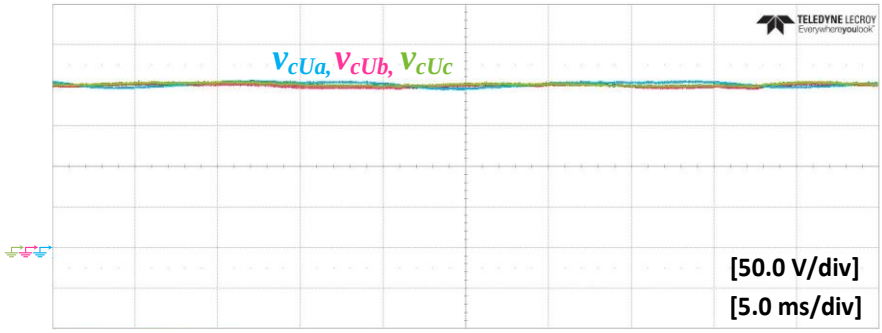

(b)

Fig. 4.42 SM capacitor voltage fluctation of 4N DHB-assisted MMC at 50 Hz when the DHB scheme is: (a) deactivated and (b) activated.

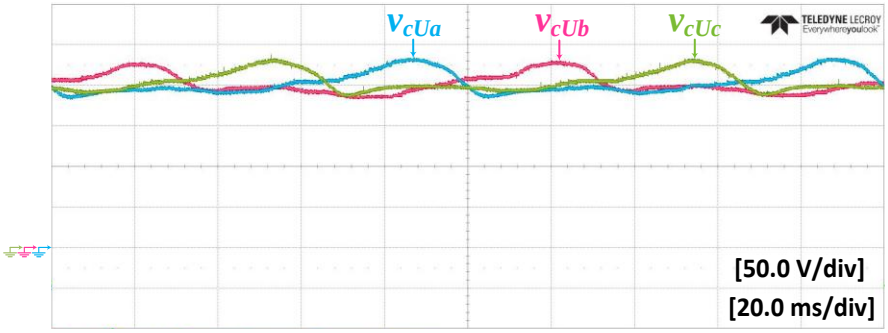

(a)

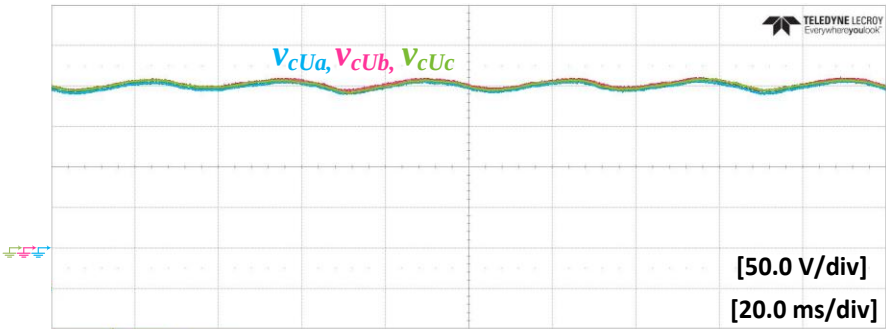

(b)

Fig. 4.43 SM capacitor voltage fluctation of 4N DHB-assisted MMC at 10 Hz when the DHB scheme is: (a) deactivated and (b) activated.

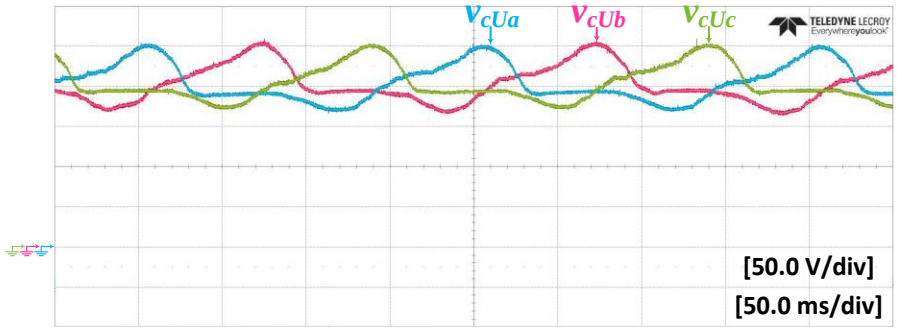

(a)

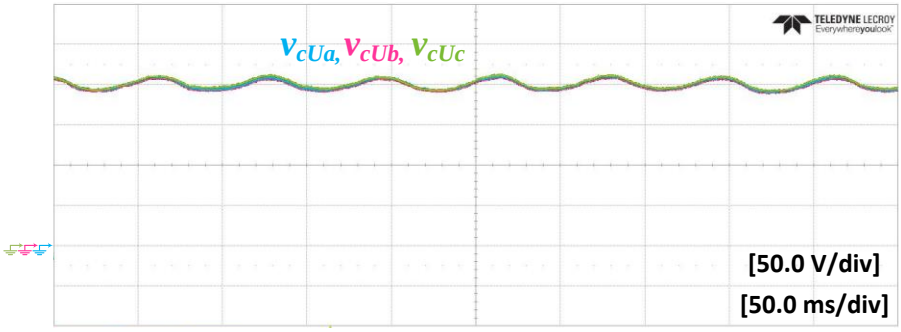

(b)

Fig. 4.44 SM capacitor voltage fluctation of 4*N* DHB-assisted MMC at 5 Hz when the DHB scheme is: (a) deactivated and (b) activated.

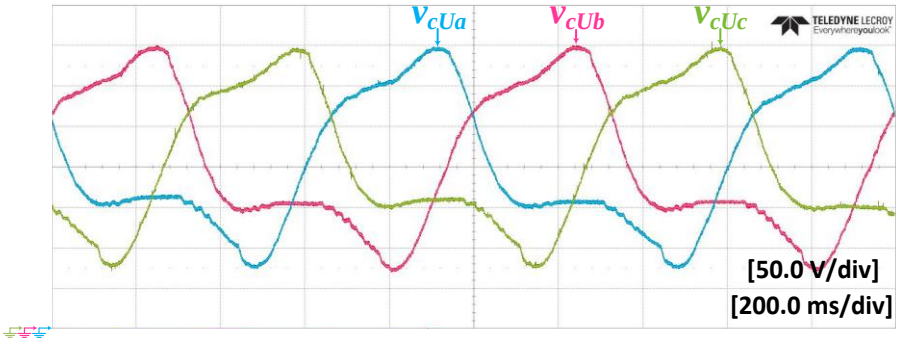

(a)

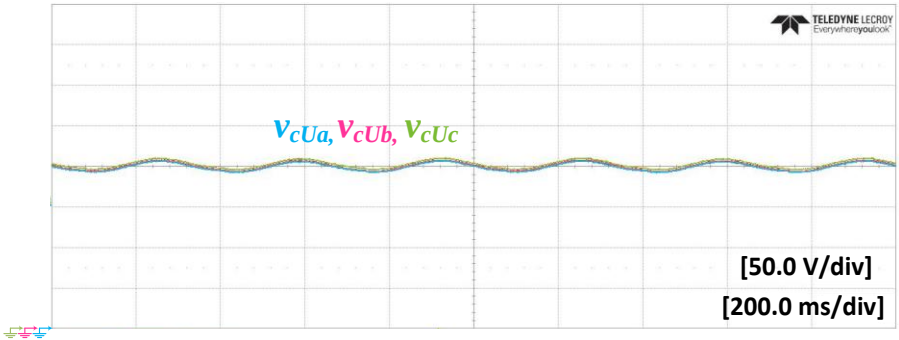

(b)

Fig. 4.45 SM capacitor voltage fluctation of 4*N* DHB-assisted MMC at 1 Hz when the DHB scheme is: (a) deactivated and (b) activated.

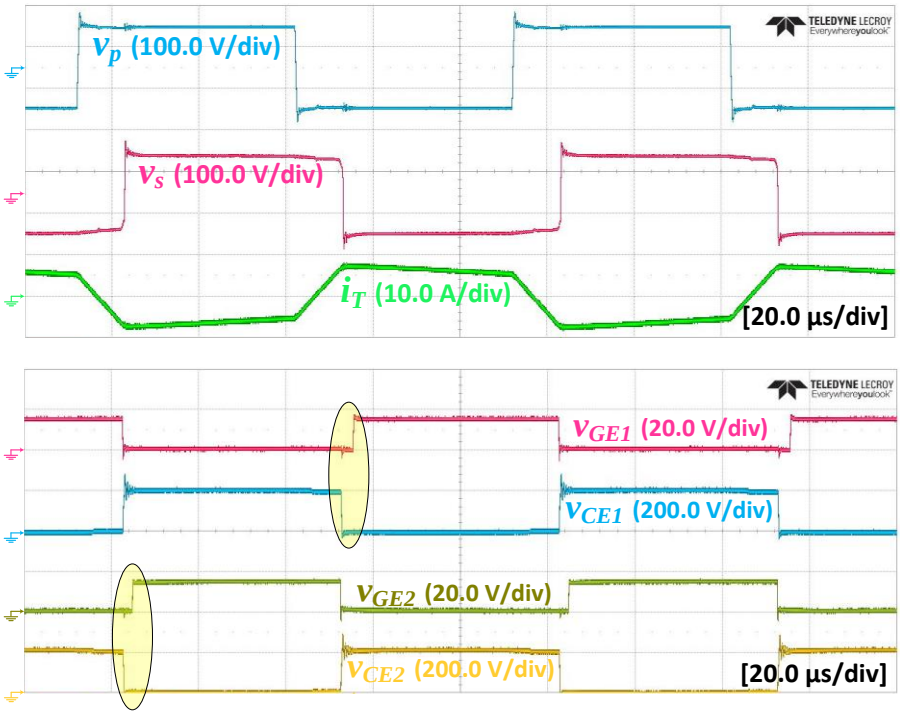

Fig. 4.46 Experimental switching waveforms of the DHB balancer at rated parameters.

Fig. 4.46 shows one DHB balancer waveforms at rated parameters. The square wave voltages across the primary and secondary sides of the HF transformer are shown along with the transformer current at a time instant when the primary-side HB is leading the secondary-side HB. The switching waveforms across the IGBTs are shown to illustrate the ZVS. Both the gate-to-emitter (v_{GE}) and collector-to-emitter (v_{CE}) voltages are shown at the DHB converter primary side.

B. Dynamic performance

The dynamic performance of the $4N$ DHB-assisted MMC is experimentally examined as a motor acceleration process from standstill to the rated speed, at the full load torque throughout, as shown in Fig. 4.47. The phase voltage and motor current are recorded for phase a, where the MMC system, with the aid of the DHB power decoupling scheme, is able to generate a near dc voltage as briefly as required by the motor at zero speed with an acceptable SM capacitor voltage ripple profile. Sample upper and lower SM capacitor voltages are shown to have a near constant ripple profile within the entire speed range, limited to within $\pm 5\%$.

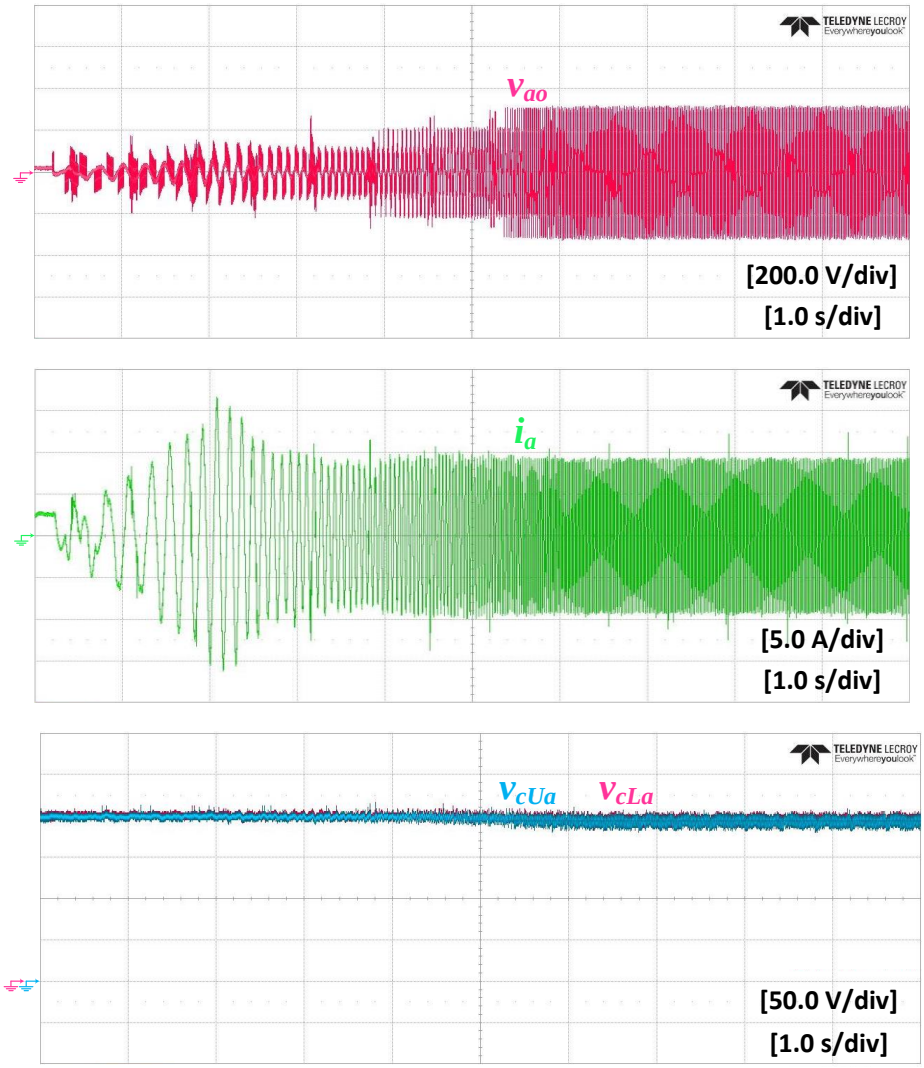

Fig. 4.47 Dynamic performance of 4*N* DHB-assisted MMC drive system when starting an induction motor from standstill to rated speed, at rated torque.

4.8 Discussion and Assessment

Compared with currently accepted MMC configurations and control approaches for extending MMC operation to low frequencies, the proposed power decoupling approach is characterized as an innovative solution able to drive MV multi-megawatt machines at full-load torque, in a scheme independent of the operating frequency, even at zero speed/frequency. Unlike the mainstream HF injection methods, the power decoupling approach does not increase MMC arm current magnitude nor does it introduce additional CM voltage at the machine terminals.

Ripple power decoupling is realized by incorporating DHB balancers between SMs, forming auxiliary branches for the MMC topology to maintain SM capacitor voltage balance over whole frequency range. Thus, the DHB-assisted MMC configuration has a power branch and an auxiliary balance branch, with the former to perform the necessary power conversion, while the latter decouples the ripple power components for energy equalization. It is worth to mention that the DHB-assisted MMC retains the modularity feature since the auxiliary balance branches have a modular scheme. Importantly, there is no interaction between the control of the DHB balancing scheme and the basic MMC control loops.

The decoupling of either the fundamental or both the fundamental and second-order ripple power components inherent in MMC arms, through the DHB modules, results in a significant reduction in the SM capacitance. This reduction is achieved at the expense of added hardware to the basic MMC structure, where the DHB balancers append additional size to the MMC system, countering the capacitor size reduction. Since the HF transformer is an energy transfer element, the DHB-assisted MMC reduces the overall stored energy in the motor drive system.

4.8.1 General Assessment

The power decoupling approach has been realized in four different MMC configurations, employing $3N$, $4N$, and $6N$ DHBs. The $3N$ DHB-assisted MMC is implemented in a generalized configuration adaptable with any machine winding layout and any phase number, in addition to a dual configuration for open-end winding machines. Common to both configurations, the DM ripple power component is entirely decoupled, yielding the SM capacitor voltage ripple pulsate at twice the fundamental frequency due to the remaining CM component. The $4N$ and $6N$ DHB-assisted MMCs are only suitable for multiple three-phase winding machines, where they decouple both CM and DM ripple power components based on symmetrical pulsation of three-phase components, resulting in a near ripple-free SM capacitor voltage.

The insulation voltages of the HF transformers adopted by each individual configuration are not identical, where DHB balancers closer to the MMC ac poles are subjected to higher transformer inter-winding insulation stresses than those close to

Table 4.6: Comparison between different DHB-assisted MMC configurations

	3*N* DHB-MMC		**4*N* DHB-MMC**	**6*N* DHB-MMC**
	Generalized configuration	Dual-sided configuration		
Number of DHB balancers	*3N*		*4N*	*6N*
DHB rated power	P_{SM}		P_{SM}	$½P_{SM}$
Number of extra switching devices	*12N*		*16N*	*24N*
Semiconductors rated voltage	$½V_c$		$½V_c$	$½V_c$
Semiconductors rated current	$½I_o$		$½I_o$	$¼I_o$
Decoupled ripple component	DM		CM and DM	CM and DM
Suitable machine winding layout	Any winding	Open-end winding	Multiple three-phase winding	Multiple three-phase winding
DC-link voltage	V_{dc}	$½V_{dc}$	V_{dc}	V_{dc}
HF transformer maximum insulation voltage	V_{dc}	$½V_{dc}$	V_{dc}	V_{dc}

the dc poles. Nonetheless, to avoid different insulation voltages and to retain modularity and inter-changeability, the transformer windings of all DHB balancers are designed to withstand the maximum insulation level equal to the dc-link voltage. Since the DHB-based power decoupling is proposed for MMC MV applications, transformer winding insulation is not practically hard to be maintained at such voltage levels.

Table 4.6 summarizes the main differences between the four DHB-assisted MMC configurations. The 3*N* DHB-assisted dual MMC is superior to its counterparts, being able to provide the same voltage magnitude, at half the dc-link voltage. Thus the insulation voltage of HF transformers adopted by the dual configuration is 50% lower than that of single-sided-based MMC configurations.

4.8.2 DHB Switching Frequency

Since the semiconductors at both DHB sides are required to block voltages in the kV range, IGBTs are a very attractive choice for practical implementation. The IGBT switching frequency limit is determined by the maximum allowable junction operating temperature. Since the DHB module operates with zero turn-on losses (at any loading condition, since the transformer turns ratio is unity), both the on-state and turn-off losses, in conjunction with the cooling assembly, will specify the maximum switching

frequency. To achieve a faster dynamic response in addition to a reduced size/weight of both the SM capacitance and HF transformer, the DHB switching frequency should be selected in the medium-frequency range. IGBT operation at medium frequency range results in high switching losses, unless the IGBT current is conveniently shaped during its conduction phase in order to achieve zero-current switching (ZCS). Thus, DHB switching frequency is selected as a trade-off between drive system size and efficiency.

Several schemes have been proposed in the literature to realize ZCS for DAB converters to reduce switching losses, as reviewed in [99]. Based on these schemes, the medium-frequency-based DAB converters could operate at 20 kHz with a 166 kW rated power using IGBTs, achieving 99.4% efficiency at a power density of 44 kW/dm^3, with experimental verification and switching loss assessment as described in [98] and [100]–[102].

In this thesis, 10 kHz is selected as the DHB switching frequency to reduce reactive components size, however, at the expense of the efficiency. Nonetheless, the DHB-assisted MMC efficiency is still comparable to that of a conventional MMC system with the mainstream HF injection methods, as will be highlighted later on, especially at low operating frequencies, where HF injection methods almost double the MMC arm currents, which accordingly increases the power losses.

4.8.3 Size Assessment

A comparison of the DHB-assisted MMC configuration with conventional MMC topology in terms of component size is presented for a 10 MW system case study. The generalized $3N$ DHB-assisted MMC is considered in the comparison, since it can be utilized with any machine winding layout and phase number. Since SM numebr is the same, and identical, in both conventional and DHB-assisted MMCs, the comparison is conducted for only one SM.

A. Switching devices

For the power branch, the 5SNA1200G450350 IGBT (4.5 kV 1200 A) is chosen [103], while the balancing branch can utilize 5SNA0650J450300 IGBTs (4.5 kV 650 A) [104]; both from ABB. The volume of the power-branch and balancing-branch IGBTs

is 1.28 L and 0.87 L respectively. For the conventional MMC topology, two power-branch IGBTs are required, while the 3*N* DHB-assisted MMC requires two balancing-branch IGBTs in addition to the conventional two power-branch IGBTs. As a result, the volume of the switching devices per SM is increased by 68%.

B. SM capacitors

From the simulation results in Figs. 4.18–4.20, each SM in the 3*N* DHB-assisted MMC employs two 2 mF, 1.4 kV capacitors. This capacitance enables the DHB-MMC configuration to operate the 10 MW system continuously at any operating frequency, even at near zero frequency, with a ±5% capacitor voltage-ripple. To achieve the same voltage-ripple suppression effect, according to the simulation results in Fig. 4.21 at 1 Hz, the capacitance of the conventional MMC topology should be 13 times the equivalent SM capacitance of the DHB-assisted MMC configuration. Therefore, the conventional MMC topology requires one capacitor with 13 mF and 2.8 kV, while being unable to drive such 10 MW system at near zero frequency. The capacitive energy stored in each SM in the conventional MMC topology is 51 kJ, while only 4 kJ for the DHB-assisted MMC configuration. Accordingly, the percentage reduction in the capacitive stored-energy achieved by the DHB-MMC configuration is 92%. To assess the reduction in the capacitors size, according to EPOCS oil-impregnated power capacitors [105], the volume of capacitors combination required to match the parameters of the SM capacitor of a conventional MMC is 440 L, while the volume of the SM split-capacitor for the DHB-assisted MMC configuration is only 38 L, with a 91% volume reduction.

C. HF transformer

For full decoupling of the fundamental ripple-power component, each two opposite-arm SMs require an HF transformer with 1:1 turns ratio, 1.25 kV and 330 A. An estimation for the transformer size can be obtained based on practical assemblies for HF transformers designed for high-power applications in previous studies [98], [101], [106], where the HF transformer volume for the mentioned ratings can be 17 L.

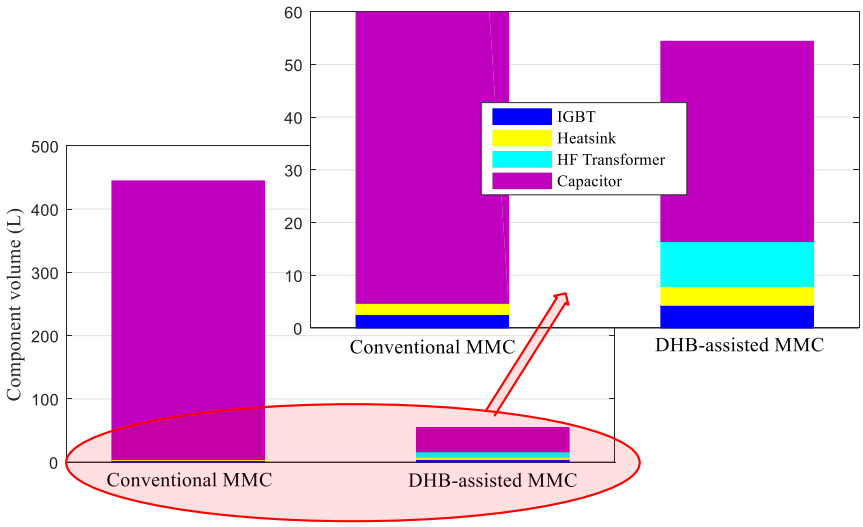

Fig. 4.48 Component volume comparison per SM for conventional and DHB-assisted MMCs.

Fig. 4.48 compares the volume of the main components of each SM for both MMC approaches. By using the DHB-assisted MMC configuration, the component volume can be reduced from 445 L to 55 L, resulting in an 87% reduction in the overall SM volume. It should be noted that this is only a comparison for the volume of the main SM components (capacitor, HF transformer, IGBT, and heatsink), rather than a comparison of the volume of real SM enclosures (in which there are more components). Nevertheless, a significant decrease in the main component volume enables a more compact and lighter layout design of an SM enclosure.

4.8.4 Efficiency Assessment

Considering DHB-assisted MMC efficiency, the four DHB switching devices in addition to the HF transformer inevitably increase power loss and reduce overall system efficiency, compared to a conventional MMC topology. However, since conventional MMC topologies cannot drive multi-megawatt machines at very low speeds, power loss analysis is investigated to compare the efficiency of the DHB-assisted MMC with the efficiency of MMC topologies that adopt HF circulating current injection. The 10 MW simulation case study of the generalized $3N$ DHB-assisted MMC is considered for power loss calculation. The method in [107] is used to calculate IGBT conduction and switching losses with the parameters given in its datasheet. A MATLAB/SIMULINK model for an MMC system with HF injection is used for efficiency comparison, operating with the same parameters as the DHB-

assisted MMC. The injected HF voltage is a square waveform, while the injected HF circulating current is a third-harmonic injected sinusoidal waveform. A power loss comparison cannot be held at extreme low frequencies (for example 1 Hz), as the HF injection-based MMC experiences large voltage fluctuation across the SM capacitors. Thus, 25 Hz is selected as a medium-range frequency for power loss comparison. Arm current magnitudes of the HF injection-based MMC are almost doubled (900 A), compared to that of the DHB-assisted MMC (475 A). Accordingly, the $3N$ DHB-assisted MMC efficiency is 96 %, while the HF injection-based MMC efficiency is 96.2%. Although this numerical efficiency assessment is case specific, a conclusion can be drawn that the DHB-assisted MMC efficiency is close to that of the main stream HF injection-based MMC, where the extra conduction and switching losses in the DHB balancers are roughly equivalent to the power losses associated with doubling the arm current magnitude when the HF injection scheme is adopted with a standard MMC.

4.8.5 Shortcomings

Compared to a standard MMC, the $3N$ DHB-assisted MMC has doubled number of IGBTs ($12N$ IGBTs for power branches and $12N$ IGBTs for balance branches). Nonetheless, the total power rating of the IGBTs employed by the $3N$ DHB-assisted MMC is about the same as that of a standard MMC with HF circulating current injection. That is, the current stress on the extra IGBTs in the balance branches is roughly the same as the increased arm current stress in the power branch IGBTs, when HF signals are injected in the circulating current. Thus, there is no significant disparity in the cost of the switching devices of the $3N$ DHB-assisted MMC and the HF injection-based MMC. But the HF transformer in the DHB-assisted MMC incurs extra cost for the drive system.

The reliability of the DHB-assisted MMC configurations is negatively influenced, compared to a conventional MMC system, since each two/three SMs are coupled together through a magnetic chain of two/three DHB balancers. Thus, the failure of any MMC SM implies deactivating the other SMs and DHB balancers within the associated chain link. Similar to a conventional MMC system, there are two methods that can be applied to enhance the reliability of the DHB-assisted MMC system:

A. The redundant SM configuration

This method implies the MMC has redundant chains of DHB-based interconnected SMs, where the simplest mode of operation when an SM fails is to bypass it along with the other associated SMs at that level, while inhibiting the DHB balancers in the involved chain. Assuming the number of required voltage levels at the output is $N + 1$, the minimal number of SMs per arm that must be functioning is N. For redundancy purposes, there are N_R additional SMs involved in each arm of the MMC, where the faulty SM will be bypassed (along with its associated chain incorporating the SMs and DHB balancers), while the MMC operation is uninterrupted. The number of redundant SMs is carefully selected as a trade-off between reliability and construction cost, as would be the case in HVDC applications of the MMC.

B. Periodic preventive maintenance

This method is a maintenance program that replaces the faulty SMs before their number becomes large enough to result in a whole converter shutdown, with unscheduled repair afterwards.

4.9 Summary

In this chapter, a decoupling approach for MMC ripple power has been presented to control the SM capacitor voltage ripple, where the advantages and shortcomings of this approach are summarized in Table 4.7 in comparison with other approaches in the literature. The power decoupling approach diverts excess SM capacitor stored energy to another with an energy lack, providing energy equalization among all SMs. This is achieved by interfacing SM capacitors through magnetic chain links equipped with DHB converters acting as energy balancers. With a bidirectional transfer scheme, the ripple power is counterbalanced between the magnetically coupled MMC SMs, resulting in a significant reduction in SM capacitor voltage ripple and SM capacitance. The power decoupling approach has been applied to the MMC system in different implementations comprising a different number of employed DHB energy balancers. The different configurations were verified through simulation and experimentation, while they have been compared with conventional MMC solutions for capacitor voltage-ripple reduction.

Table 4.7: Assessment of MMC ripple power decoupling approach compared to other introduced approaches

	Constant-torque full speed range	**Additional CM voltage**	**Additional Hardware**	**Key advantages**	**Key disadvantages**
Ripple power decoupling	✓	×	✓	Limited SM capacitor voltage ripple independent of the operating frequency and loading condition	Slightly lower reliability Cost of employed HF transformers
Sinusoidal HF injection	×	✓	×	Easy to track sinusoidal injected current	High current stress High CM voltage
Improved injection methods with reduced current stress	×	✓	×	Reduced current stress	High CM voltage Hard to track square wave injected current
Improved injection methods for full speed range	✓	✓	×	Constant voltage-ripple within entire speed range	Hard to optimize SM capacitor nominal voltage
Improved injection methods with reduced CM voltage	×	×	✓	Reduced CM voltage	Massive hardware for only reduced CM voltage
Improved injection methods with FB-SMs	×	✓	✓	dc fault ride-through capability	Doubled number of switching devices, compared to HB-SMs
Reduced dc voltage	×	×	✓	Easy implementation	Array of series switches [67] Phase-shifting transformer [69]
Back-to-back current-source MMC configuration	✓	×	✓	Suitable for regenerative applications	Extra cost and complicated control strategy
Q2L-PWM operation mode	✓	✓	×	Diminished SM capacitance	Multilevel property lost

Chapter 5

New MMC Topologies for Six-Phase Machine Drives

This chapter addresses MMC application to multiphase machines by presenting a class of topologically-reduced MMC structures for six-phase machine drives. The presented topologies are studied for constant-speed drives; however, they are adaptable with any approach that enhances traditional three-phase MMC performance at low frequency.

5.1 Multiphase Machines

Over time, three-phase machines have been adopted as a standard choice for motor drives realization. Nonetheless, in the last few decades, multiphase machines (i.e. more than three phases) have re-emerged as a potential alternative for various industrial applications. The main driving force is the specific applications, predominantly related to the green agenda, such as electric and hybrid electric vehicles, locomotive traction, ship propulsion, more-electric aircraft, remote offshore wind farms for electric energy generation, and general high-power industrial applications. An additional motivation is offered by advancements in power electronics, which facilitate synthesizing any number of phase voltages using power electronic converters [108].

Multiphase machines offer numerous potential advantages over their three-phase counterparts. The most important ones are: 1) the multiphase system power can be split over more than three phases, thus reducing the power rating requirements of the semiconductor devices of the drive system, 2) only two degrees of freedom (i.e., two independently controllable currents) are required for independent flux and torque control of a multiphase machine, regardless of the number of phases, 3) enhanced fault tolerance capability, where the loss of one phase still leaves possibility for the other remaining phases to continue operation with asymmetrical winding structure

and unbalanced excitation, producing part of the full-load torque, and 4) higher torque density with reduced torque pulsations. Consequently, multiphase drives are progressively breaking technical barriers, finding a place in applications where reliability and fault tolerance are a prime concern [109]–[111]. For instance, large multiphase machines for ship propulsion have already been industrially prototyped, and are currently undergoing commercial evaluation [112].

5.1.1 Six-Phase Machines

Theoretically, a multiphase stator winding can be designed with any phase order. Nonetheless, the corresponding multiphase converter complexity stands out as a serious technical limitation restricting the phase order selection within certain practical and compromised options. Thus, most research has focused on addressing the five- and six-phase examples [113]–[115]. Although the number of machine phases can be either a prime or a composite number, the latter allows for different stator winding arrangements and enables the use of multiple winding sets. That is, multiphase machines with multiple of three-phase winding sets are the most attractive selections in many industrial sectors since well-established three-phase technology and, therefore, the readily off-the-shelf three-phase converters can be employed [116]–[118].

Among the multiple three-phase winding alternatives, six-phase machines (also known as dual three-phase machines) have garnered a specific attraction. In addition to their ready adaptation with standard three-phase converter topologies, dual three-phase machines can be readily realized through rewinding existing three-phase stators [119]. This permits varying the relative space-orientation of the two three-phase sets. Most popular space angles are 30° and 60°, yielding a six-phase machine with asymmetrical and symmetrical winding layouts, respectively, as shown in Fig. 5.1. The asymmetrical type has better fundamental flux content over the symmetrical type, with the former eliminating air-gap harmonics of order $6n \pm 1$ ($n = 1, 3, 5, ...$). Accordingly, all the rotor copper losses produced by these harmonics as well as all the torque harmonics of the $6n$ order are eliminated [120]. Nonetheless, the asymmetrical type has slightly lower fault-tolerance capability than the symmetrical

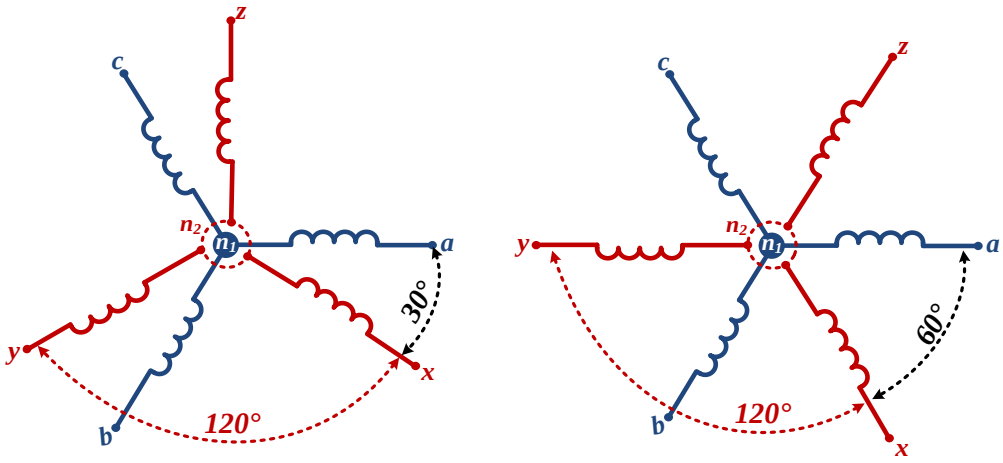

Fig. 5.1 Dual three-phase machine winding layout with isolated neutral points using: (a) asymmetrical and (b) symmetrical arrangements.

winding layout [121]. Through an enriched body of literature, six-phase machines have been studied with different aspects pertinent to their modelling, new winding layouts, control, and applications [122]–[127].

5.1.2 Six-Phase Machine Drives

Since multiphase supplies are not readily available, they have to be created from the available three-phase grid. Generally, a simple solution is to design a three-phase to *n*-phase transformer, such as three-phase to five-phase [128], six-phase [129], and seven-phase [130] transformers. Nevertheless, the usefulness of such transformers is limited, and they are only a viable solution for laboratory testing of multiphase machines under sinusoidal supply conditions. In real-world applications, any multiphase machine operating under adjustable-speed conditions necessitates a multiphase power electronic converter which can be easily configured from the hardware point of view. It is only necessary to make the number of inverter legs equal to the number of phases in case of a dc-ac inverter, or to increase the number of switching devices in accordance with the output phase number in the case of an ac-ac matrix converter.

Considering a six-phase machine, the dual three-phase inverter is the off-the-shelf drive topology, comprising two three-phase inverters independently controlled to generate two sets of three-phase voltages with the appropriate phase displacement

angle. The dual three-phase inverter can be realized through any of the state-of-the-art three-phase dc-ac converter configurations. However, the multilevel converter topologies are preferred to supply multiphase machines, being able to extend their output power. Dual three-phase machine drives are not commonly reported in the literature, either the design or operating principle, since they inherit the same performance characteristics as their three-phase ancestors. Nonetheless, the increased number of converter legs along with the associated components has triggered interest in developing new six-phase drive configurations with reduced structures, to alleviate the cost, size, and complexity.

5.1.3 Control of Six-Phase Machine Drives

Multiphase machines control methods are in principle the same as for three-phase machines. For dual three-phase machines, a special concern is directed to the control of unbalanced current sharing between the two three-phase winding sets, due to small asymmetries that cannot be eliminated [131]. The current control is fundamentally introduced to eliminate the stator dynamics, where it forms an inner loop of the overall control system, receiving reference currents from the outer loops that control both the flux and speed. Among the various types of current control, synchronous frame control is widely used, where the motor currents are measured and transformed to a synchronous reference frame to be compared with the reference values of the flux-producing and torque-producing stator current components. The synchronous reference frame is aligned with the flux using the FOC strategy, as explained in Chapter 2. Since the steady-state currents are dc components, the use of PI controllers result in zero steady-state error. Thus, the control method discussed in Chapter 2 for three-phase machines can be readily extended to six-phase machines, but without compensating for the inherent asymmetries of the dual three-phase machine.

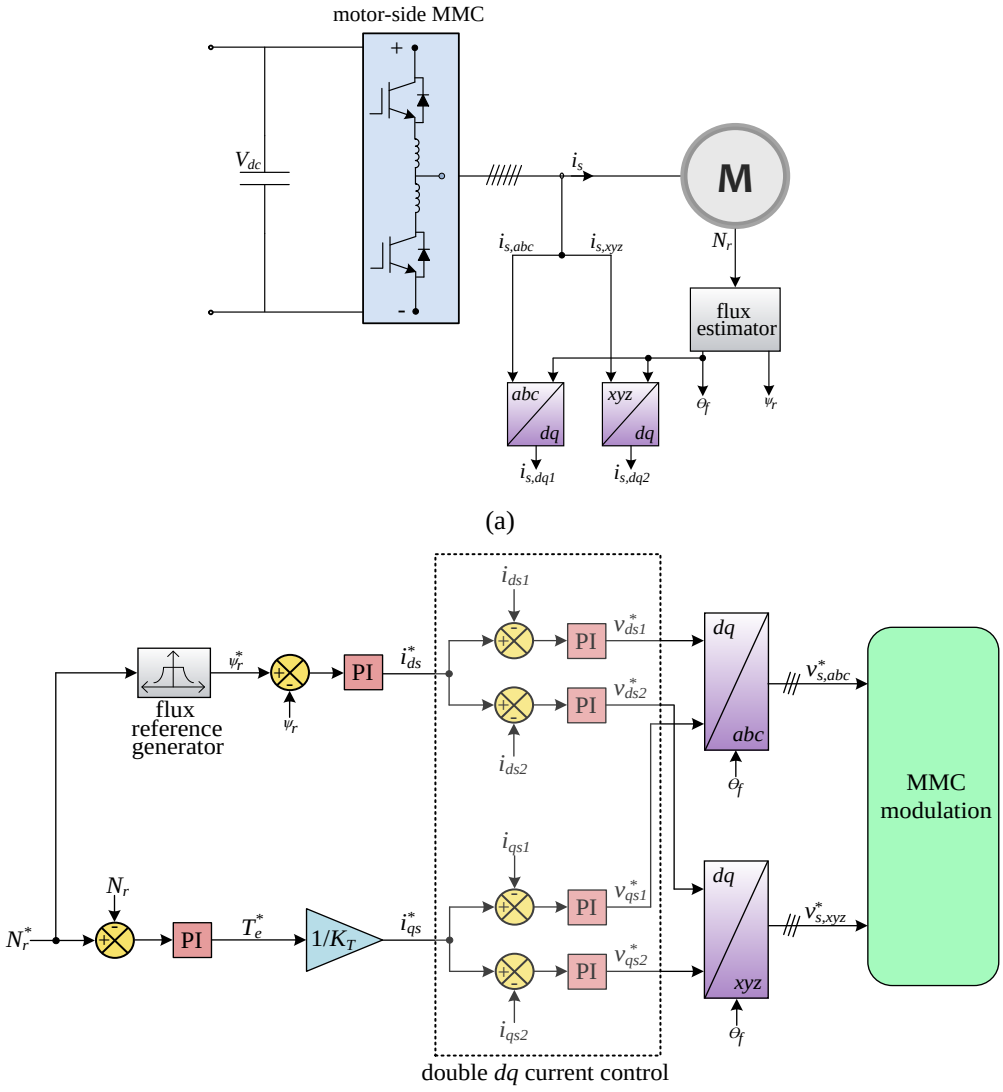

Fig. 5.2 Dual three-phase motor-side MMC control: (a) circuit diagram and (b) IFOC block diagram.

Due to stator windings asymmetries, the two sets of three-phase stator currents have different amplitudes depending on operational conditions. A possible solution is to use current control in phase coordinates, however six current controllers are required [131]. Also, the steady-state currents are ac components, where simple PI controllers cannot achieve zero steady-state error and will require special feedforward compensation techniques [132]. Alternatively, double synchronous frame current control can be used, as elaborated in Fig. 5.2 [133]. This current control scheme adopts four PI current controllers instead of six, and is capable of compensating the drive asymmetries since the currents of the two stator winding sets

are independently controlled. Referring to Fig. 5.2, the two sets of the synchronous reference frame current components, (i_{ds1}, i_{qs1}) and (i_{ds2}, i_{qs2}), are obtained and compared with i^*_{ds} and i^*_{qs}, respectively. The outputs of the current controllers are the reference components of two voltage vectors that are transformed back to the rotating reference frame and applied to the PWM modulator of the dual three-phase converter. In this way, the two sets of three-phase stator currents are independently controlled and kept balanced for all possible operational conditions.

5.2 Dual Three-Phase MMC

The traditional approach to drive a six-phase machine using the MMC topology is to employ a dual three-phase MMC to generate two sets of three-phase voltages electrically shifted by 30° or 60° for either asymmetrical- [134] or symmetrical-winding machines [135], respectively. A circuit diagram for dual three-phase MMC is shown in Fig. 5.3, where it incorporates six phase-legs while each leg inherits the same structure as a standard MMC phase leg. That is, each leg is formed by two arms connected in series through arm inductors, and each arm is formed by N series connected HB-SMs. Since the dual three-phase MMC employs twelve arms, it is denoted hereafter as the twelve-arm MMC (12A-MMC).

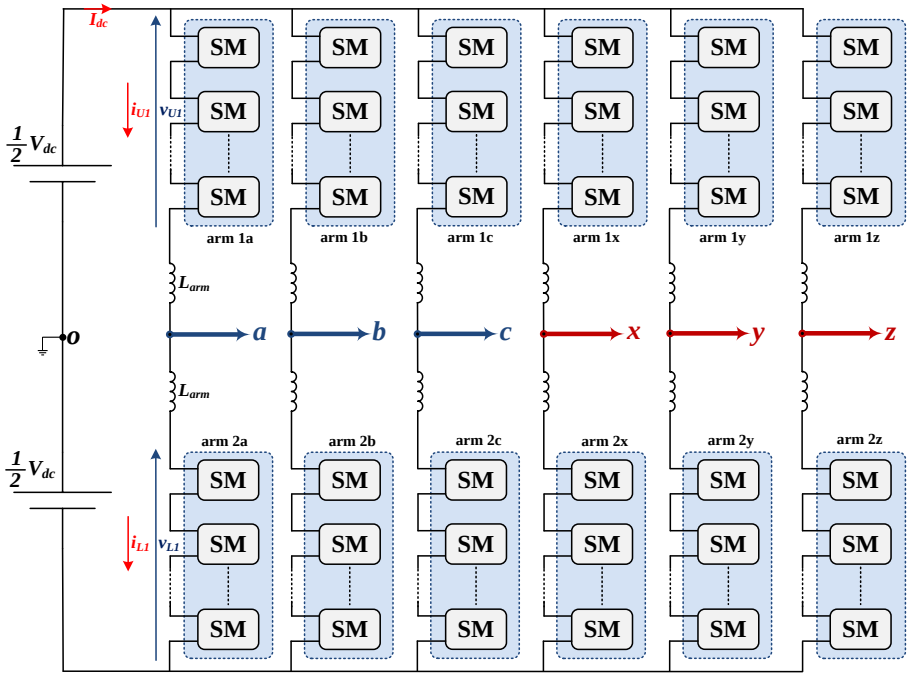

Fig. 5.3 Circuit diagram of the 12A-MMC for six-phase machine drives.

Referring to Fig. 5.1, a general form for the two three-phase voltage sets required to drive a six-phase machine is:

$$\begin{cases} v_{jn_1} = V_o \cos\left(\omega t - \frac{2\pi}{3}k\right), k = 0,1,2 \; for \; j = a,b,c \\ v_{jn_2} = V_o \cos\left(\omega t - \frac{2\pi}{3}k + \sigma\right), k = 0,1,2 \; for \; j = x,y,z \end{cases} \quad (5.1)$$

where n_1 and n_2 are the isolated neutral points of the abc and xyz three-phase winding sets, respectively, while σ is the phase angle between the two three-phase voltage sets. The output voltage magnitude V_o is defined in a similar way to a standard three-phase MMC, as given in (2.2). The six-phase currents passing through the machine windings can be generally described as:

$$\begin{cases} i_j = I_o \cos\left(\omega t - \frac{2\pi}{3}k - \varphi\right), k = 0,1,2 \; for \; j = a,b,c \\ i_j = I_o \cos\left(\omega t - \frac{2\pi}{3}k + \sigma - \varphi\right), k = 0,1,2 \; for \; j = x,y,z \end{cases} \quad (5.2)$$

where I_o is the magnitude of the machine current and φ is the machine power-factor angle.

Being the MMC-based off-the-shelf topology for six-phase machine drives, the 12A-MMC will be utilized as a reference to assess the reduced MMC structures that will be presented in the next sections. Thus, it is necessary to characterize the 12A-MMC's performance and quantitatively assess its employed components.

5.2.1 Simulation

To investigate 12A-MMC performance, a 3.2 MW MATLAB/SIMULINK simulation model is used where the 12A-MMC is feeding a six-phase *RL* load with asymmetrical modulation (σ = 30°). The simulation parameters are listed in Table 5.1, while the simulation results are shown in Fig. 5.4. The six-phase line voltages and load currents are high quality sinusoidal waveforms with 30° phase shift between the abc and xyz three-phase sets. Both the upper- and lower-arm voltages step from 0 to 10 kV through 11 voltage levels. Using a parallel-resonant filter, the second-order harmonic is eliminated in the circulating current, that is, both the upper- and lower-arm currents show an out-of-phase sinusoidal profile, where the circulating

current is a dc component. Similar to a traditional three-phase MMC, the SM capacitor voltage alternates due to both the first- and second-frequency components, with ±5% voltage ripple using 3 mF SM capacitance.

Table 5.1: Parameters for 12A-MMC simulation

Number of SMs per arm (N)	10
Rated active power	3.2 MW
Input dc voltage (V_{dc})	10 kV
Nominal SM capacitor voltage (V_c)	1 kV
Rated line voltage	6 kV
Rated current magnitude (I_o)	250 A
Fundamental output frequency (f_o)	50 Hz
Carrier frequency (f_c)	2 kHz
Arm inductance (L_{arm})	5 mH
SM capacitance (C)	3 mF
Load resistance	15 Ω
Load inductance	30 mH

5.2.2 Quantitative Assessment

Multiphase converter complexity is one of the concerns that restrict the wide spread utilization of multiphase machines. For instance, six-phase machines necessitate a doubled component-count implemented in a dual three-phase converter, as compared to the three-phase version. Since multilevel converters are much preferred to drive multiphase machines, the number of components employed by a multiphase multilevel converter will be significantly high, resulting in increased drive system size, cost, and complexity.

A quantitative assessment for the 12A-MMC is listed in Table 5.2, including both component count and rating. Assuming the number of SMs per arm is 10, as set in the simulation case study, the 12A-MMC employs 240 units of both the IGBT modules and gate-drive circuits, in addition to 120 SM capacitors. Such a doubling of converter main components can be seen as an obstacle to commercialize dual three-phase MMCs for six-phase MV machine drives.

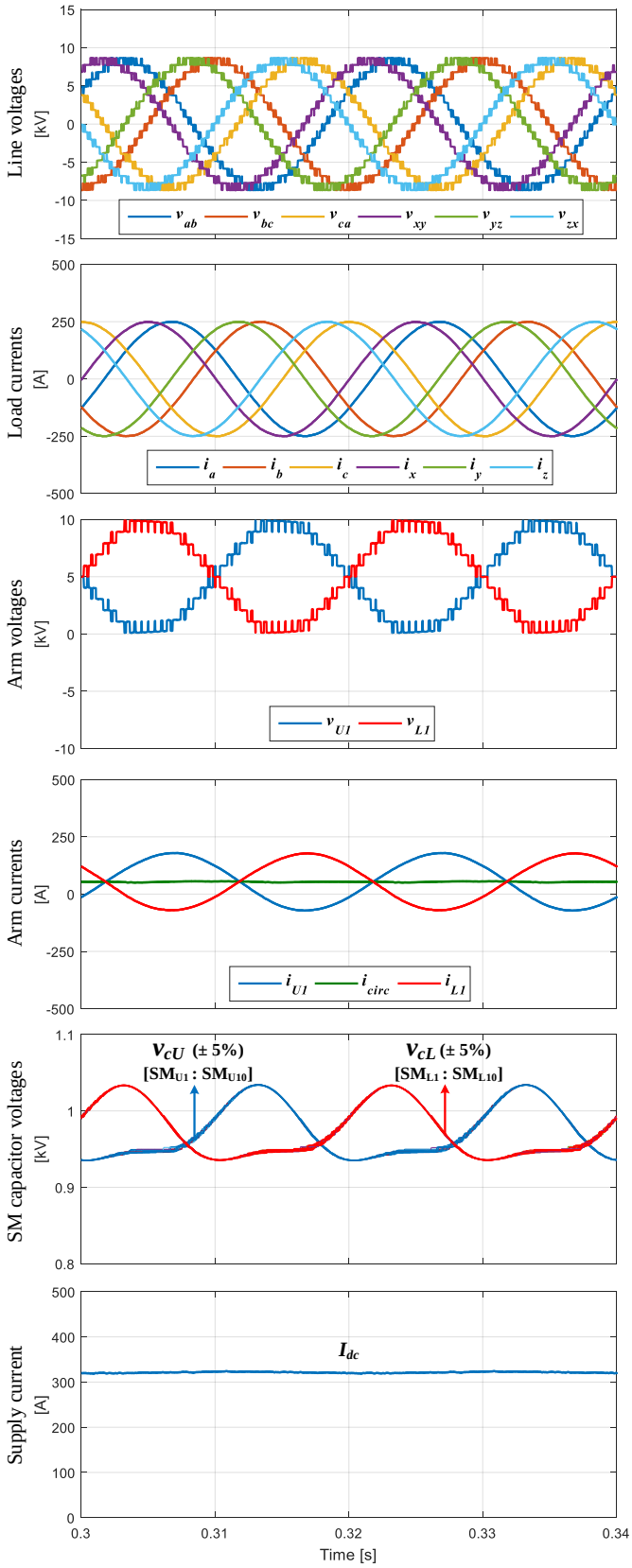

Fig. 5.4 Simulation results of the 12A-MMC supplying six-phase *RL* load with asymmetrical modulation.

Table 5.2: Component count and rating of the 12A-MMC

DC link voltage	V_{dc}
Maximum AC voltage	½ V_{dc}
Number of SMs	12N HB-SMs
Number of IGBTs	24N
Number of arm inductors	12
Number of SM capacitors	12N
IGBT rated voltage	V_{dc}/N
IGBT rated current	$⅙I_{dc} + ½I_o$
Combined power rating	$12V_{dc}I_o + 4V_{dc}I_{dc}$
SM capacitance	C
Total capacitive stored energy	$12N$ [½ C $(V_{dc}/N)^2$]
Arm Inductance	L
Total reactive elements	$12NC + 12L$

Reducing the number of both passive and active components adopted by the power electronic converter is one of the developmental trends pursued by researchers to alleviate the overall converter cost and size. Several examples for reduced component-count topologies have been extensively reported in the literature with many diversified philosophies of component-count savings [136]–[144]. The passive components in the context of the MMC are mainly the SM capacitors, where the main interest is to minimize the capacitance or to reduce the number of capacitors and their accompanied voltage transducers, where the capacitors are bulky, costly, and increase system stored energy. On the other hand, reducing the number of MMC active switching devices and their accompanied driver circuitry is also of an interest, where a reduced switch-count MMC will result in reduced cooling requirements, PWM signals, and physical layout. Thus, the next sections address three reduced MMC structures for six-phase machine drive applications, where their performance and pros and cons are assessed.

5.3 Eight-Arm MMC

The eight-arm MMC (8A-MMC) is a reduced MMC structure for six-phase machine drive applications, achieving a 33% reduction in the number of employed arms compared to a traditional 12A-MMC. Topologically, the 8A-MMC inherits the same structure as the 12A-MMC, but omits two entire phase-legs. The two omitted legs are compensated based on utilization of the mid-point of a dc-link split capacitor bank, as shown in Fig. 5.5, where the 8A-MMC is feeding a six-phase machine with isolated neutral points. The concept of compensating a converter phase-leg with a split-capacitor bank was first adopted in two-level three-phase VSIs for low-voltage machine drives yielding a four-switch three-phase inverter [136], [137]. Thereafter, the concept was generalized for a back-to-back four-leg (eight-switch) three-phase ac-ac converter [138], [139]. Further, a six-phase VSI with five phase-legs (ten-switch) is reported in [140] for six-phase machine drives. Recently, the phase-leg reduction concept has been inspirationally applied to the three-phase MMC, yielding a two-leg three-phase MMC with four employed arms, to reconfigure the traditional six-arm MMC in case of one-leg failure [145]. That is, the presented 8A-MMC topology is the dual three-phase version of the four-arm MMC.

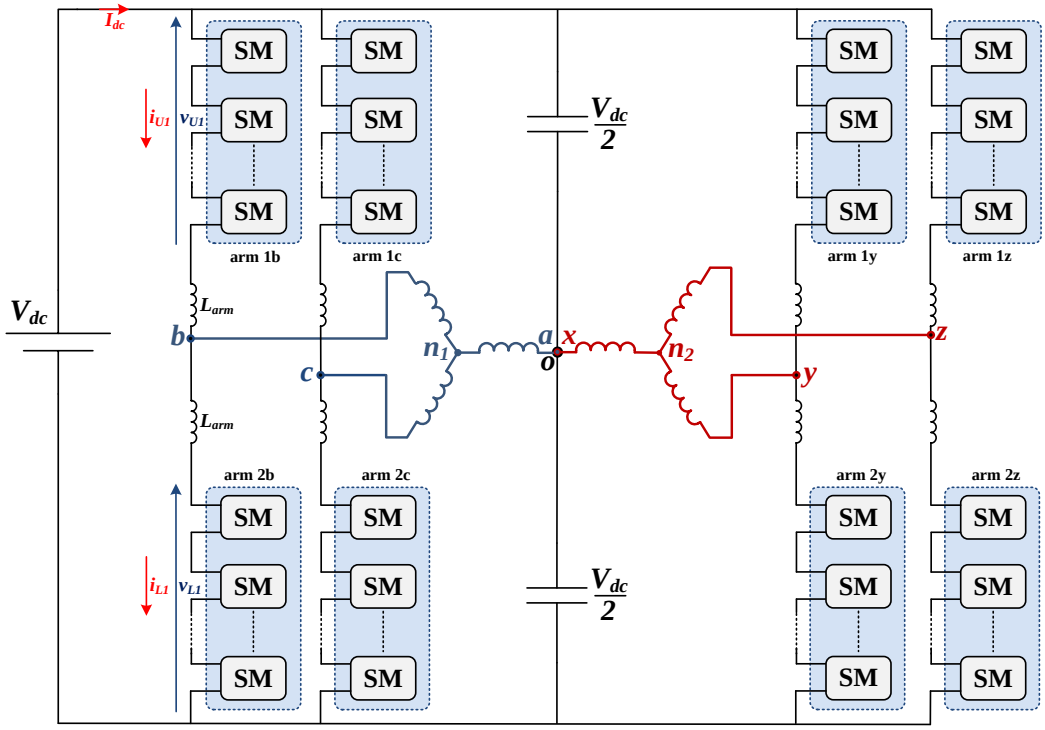

Fig. 5.5 Circuit diagram of the 8A-MMC feeding a six-phase machine with isolated neutral points.

In the past efforts of developing reduced component-count topologies [136]–[144], a summarizing observation noted is that performance trade-offs are always unavoidable if fewer components are adopted for realization. Common trade-offs are limited voltage amplitude and phase shift and usually higher stresses experienced by the remaining components. In this context, limitations are imposed on the utilization of the dc-link voltage supplying the 8A-MMC. Referring to Fig. 5.5, the machine winding terminals a and x are connected to the dc-link capacitor mid-point o, while the other four terminals are connected to the four involved MMC phase-legs. The voltage established between any of the four MMC phase-legs and the dc-link mid-point o equals the line voltage. Thus, the 8A-MMC implies the ac component of the arm voltage equal to the line voltage. Referring to (5.1), the line voltages v_{ab} and v_{xy} are defined as:

$$v_{ab} = \sqrt{3}V_o \cos\left(\omega t - \frac{\pi}{6}\right) \tag{5.3a}$$

$$v_{xy} = \sqrt{3}V_o \cos\left(\omega t - \frac{\pi}{6} + \sigma\right) \tag{5.3b}$$

Therefore, the arm voltages of leg-1 of the 8A-MMC, supplying terminal b of the six-phase machine windings, are described as:

$$v_{U1} = \frac{1}{2}V_{dc} + v_{ab} \tag{5.4a}$$

$$v_{L1} = \frac{1}{2}V_{dc} - v_{ab} \tag{5.4b}$$

Since the maximum MMC arm voltage cannot exceed V_{dc}, the maximum 8A-MMC line voltage magnitude is $½V_{dc}$. Therefore, the maximum attainable phase-voltage is defined in relation to both the modulation index (ranges from 0 to 1) and the dc-link voltage as:

$$V_o = \frac{1}{2\sqrt{3}} MV_{dc} \tag{5.5}$$

From (5.5), the 8A-MMC experiences a 42% reduction in dc-link voltage utilization, compared to the 12A-MMC. Thus, to achieve the same level of power delivery as the 12A-MMC, the dc-link voltage of the 8A-MMC should be $\sqrt{3}V_{dc}$, which increases

the nominal voltage across both the IGBTs and SM capacitors by 73%, compared to traditional MMC nominal cell voltage.

It is worth mentioning that the dc-link split capacitor of the 8A-MMC topology experiences voltage fluctuation due to the circulation of both machine currents i_a and i_x, where the split capacitor peak current is $1.93I_o$ and $1.73I_o$ for asymmetrical and symmetrical six-phase machines, respectively. This necessitates increasing the dc-link capacitance to avoid threating the safe operation of the IGBTs and SM capacitors. Nonetheless, for a symmetrical six-phase machine, the voltage ripple across the dc-link capacitor can be avoided if two machine windings with spatial phase opposition are connected to the dc-link capacitor mid-point (for example, a and y), where the net current passing through the dc-link capacitor is ideally zero.

The control of the 8A-MMC is similar to traditional MMC control, however the ac component of the reference arm voltages is calculated in terms of the desired line voltage.

5.3.1 Simulation

Similar to the 12A-MMC simulation case study, 8A-MMC performance is investigated using a 3.2 MW MATLAB/SIMULINK model, where the 8A-MMC feeds a six-phase *RL* load with asymmetrical modulation (σ = 30°). The dc-link voltage is 17.5 kV (73% higher than the 12A-MMC dc-link voltage), while other operating conditions are maintained similar to the 12A-MMC, as listed in Table 5.3. The simulation results are shown in Fig. 5.6. The line voltages of the 8A-MMC traverse with 11 voltage levels (19 voltage levels for the 12A-MMC), since the line voltages are directly maintained from the arm voltages. Nonetheless, the six-phase load currents show a good sinusoidal profile. Similar to the 12A-MMC, both the upper- and lower-arm voltages alternate out-of-phase in 11 voltage levels, however from 0 to 17.5 kV. Both the upper- and lower-arm currents are sinusoidal without even-order harmonics, while the circulating current is almost dc lower than the 12A-MMC's circulating current due to the increase in the dc-link voltage. The SM capacitor voltages pulsate similar to the traditional 12A-MMC with ±5.3% voltage ripple, however using 1.5 mF SM capacitance. The average supply current is 180 A, which is 73% lower than the 12A-MMC's supply current.

Table 5.3: Parameters for 8A-MMC simulation

Number of SMs per arm (N)	10
Rated active power	3.2 MW
Input dc voltage (V_{dc})	17.5 kV
Nominal SM capacitor voltage (V_c)	1.75 kV
Rated line voltage	6 kV
Rated current magnitude (I_o)	250 A
Fundamental output frequency (f_o)	50 Hz
Carrier frequency (f_c)	2 kHz
Arm inductance (L_{arm})	8.5 mH
SM capacitance (C)	1.5 mF
Load resistance	15 Ω
Load inductance	30 mH

5.3.2 Quantitative Assessment

Table 5.4 shows the number of components employed by the 8A-MMC, in addition to IGBTs rating and passive elements reactance. Compared to the 12A-MMC, the 8A-MMC achieves 33% reduction in the number of employed IGBTs, SM capacitors, and arm inductors. This reduction comes at the expense of a 42% reduction in the dc-link voltage utilization, compared to the 12A-MMC. This requires increasing the dc-link voltage by 73% to maintain the same power delivery, reducing the dc supply current by the same ratio. That is, the nominal voltage of the IGBTs and SM capacitors is increased by 73%, compared to the 12A-MMC, while the reduced dc supply current is distributed among 4 legs, compared to 6 legs in the 12A-MMC. Accordingly, the combined power rating of the 8A-MMC is 11.5% higher than that of the 12A-MMC.

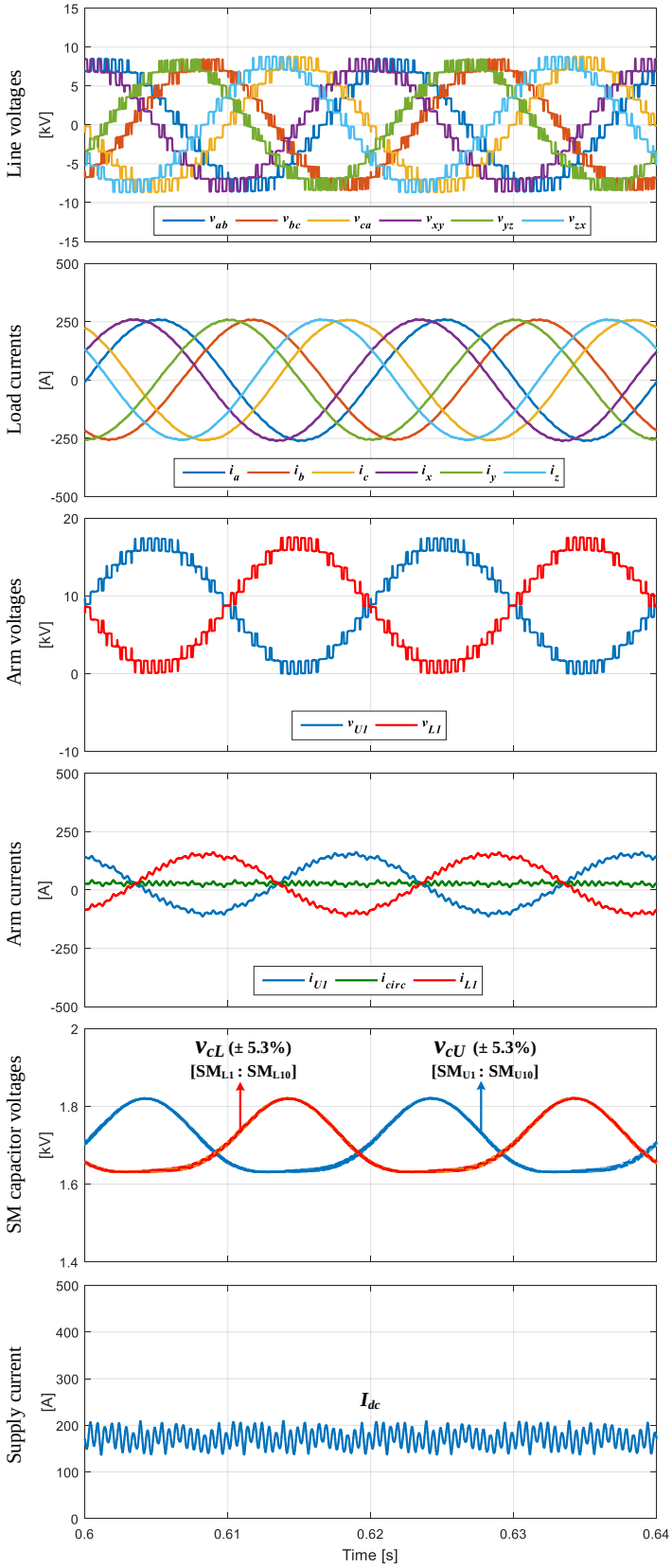

Fig. 5.6 Simulation results of the 8A-MMC supplying six-phase *RL* load with asymmetrical modulation.

To achieve the same SM capacitor voltage ripple profile, the SM capacitance of the 8A-MMC is reduced by 50%, compared to the 12A-MMC. The reduced SM capacitance ensures the converter energy storage constant (defined as the ratio between the overall stored energy and the converter rated power) is identical for both the 8A-MMC and the 12A-MMC [35].

According to [32], the 73% increase in the 8A-MMC dc-link voltage implies the arm inductance be increased by the same ratio, compared to the 12A-MMC, to ensure the same circulating current peak at the same power level.

Table 5.4: Component count and rating of the 8A-MMC, compared to the 12A-MMC

	12A-MMC	**8A-MMC**
DC link voltage	V_{dc}	$\sqrt{3}V_{dc}$
Maximum AC voltage	½ V_{dc}	½ V_{dc}
Number of SMs	12N HB-SMs	8N HB-SMs
Number of IGBTs	24N	16N
Number of arm inductors	12	8
Number of SM capacitors	12N	8N
IGBT rated voltage	V_{dc}/N	$\sqrt{3}V_{dc}/N$
IGBT rated current	$⅙I_{dc} + ½I_o$	$\frac{1}{4\sqrt{3}}I_{dc} + ½I_o$
Combined power rating	$12V_{dc}I_o + 4V_{dc}I_{dc}$	$8\sqrt{3}V_{dc}I_o + 4V_{dc}I_{dc}$
SM capacitance	C	$0.5C$
Total capacitive stored energy	$12N\ [½\ C\ (V_{dc}/N)^2]$	$12N\ [½\ C\ (V_{dc}/N)^2]$
Arm Inductance	L	$\sqrt{3}L$
Total reactive elements	$12NC + 12L$	$4NC + 8\sqrt{3}L$

5.4 Nine-Arm MMC

The nine-arm MMC (9A-MMC) is another reduced MMC structure for six-phase machine drive applications, which achieves a 25% reduction in the number of arms compared to the 12A-MMC [146]. As the name implies, the 9A-MMC consists of nine arms evenly assorted in three legs, each formed by upper, middle, and lower arms, where each arm employs N HB-SMs. The six-phase load terminals are realized

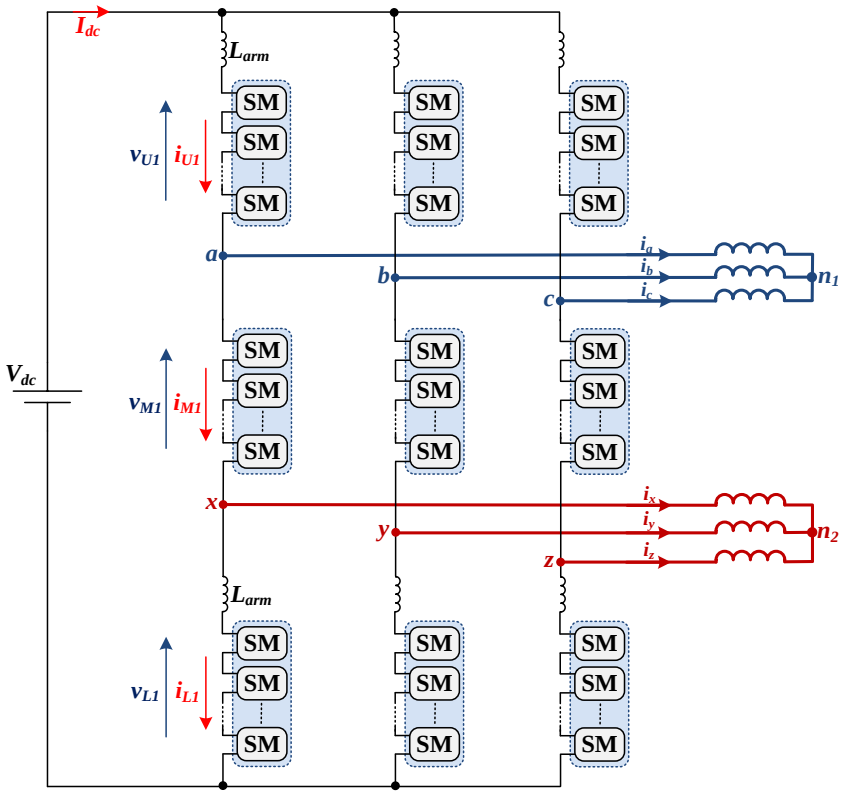

Fig. 5.7 9A-MMC with identical HB-SMs, feeding a six-phase machine with isolated neutral points.

through the intermediary nodes between each two series connected arms, as shown in Fig. 5.7. The 25% reduction in the number of arms, compared to the 12A-MMC, arises from the fact that the 9A-MMC is a direct consequence of integrating two three-phase MMCs, with dual function middle arms. The 9A-MMC is inspired by the nine-switch VSI which was first evolved to supply two independent three-phase machines [147], while recently it has been adopted as a six-phase machine drive [126].

5.4.1 9A-MMC Analysis

Since the 9A-MMC employs three arms per leg, the dc component in the upper-, middle-, and lower-arm voltage is $⅓V_{dc}$. With identical upper, middle, and lower arm HB-SMs, the voltage across the three arms pulsates from 0 to $⅔V_{dc}$, while the nominal SM capacitor voltage is $2V_{dc}/3N$. Therefore, at any instant, the total number of inserted SMs in each leg is $1.5N$. The 25% arm reduction achieved in the 9A-MMC topology imposes an operational limit in the dc-link voltage utilization due

to the dual functionality of the middle arms. That is, the utilization of the dc-link voltage is reduced by 33%, compared to the 12A-MMC, reducing the delivered output power. The attainable output voltage magnitude of the 9A-MMC is described as a function of both the modulation index (ranges from 0 to 1) and the input dc voltage V_{dc} as:

$$V_o = \frac{1}{3} M\, V_{dc} \tag{5.6}$$

To deliver the same power as a 12A-MMC, the dc-link voltage is increased by 50%, where at this voltage level, the SM capacitor nominal voltage is maintained as a 12A-MMC at $V_c = V_{dc}/N$.

A. Arm Voltages

Referring to Fig. 5.7, and considering the MMC phase-leg supplying the machine terminals a and x (denoted as leg-1), the voltages across the upper and lower arms are:

$$v_{U1} = \frac{1}{3} V_{dc}\,[1 - M\cos(\omega t)] \tag{5.7a}$$

$$v_{L1} = \frac{1}{3} V_{dc}\,[1 + M\cos(\omega t + \sigma)] \tag{5.7b}$$

To ensure zero voltage sum in the loops incorporating the MMC phase-legs and the dc-link, the middle-arm voltage is:

$$\begin{aligned} v_{M1} &= V_{dc} - v_{U1} - v_{L1} \\ &= \frac{V_{dc}}{3}[1 + M\cos(\omega t) - M\cos(\omega t + \sigma)] \end{aligned} \tag{5.8}$$

where the subscript *M* refers to the corresponding 'middle' arm. From (5.8), the middle-arm voltage magnitude depends on the phase angle between the two generated three-phase voltage sets, as graphically demonstrated in Fig. 5.8. When the phase angle is less than or equal to 60°, the middle-arm voltage is unipolar (ranging from 0 to $2M/3V_{dc}$ at $\sigma = 60°$), and can be realized using HB-SMs. However, when the phase angle is higher than 60°, the middle-arm voltage becomes bipolar, where FB-SMs are employed to generate the negative part of the arm voltage.

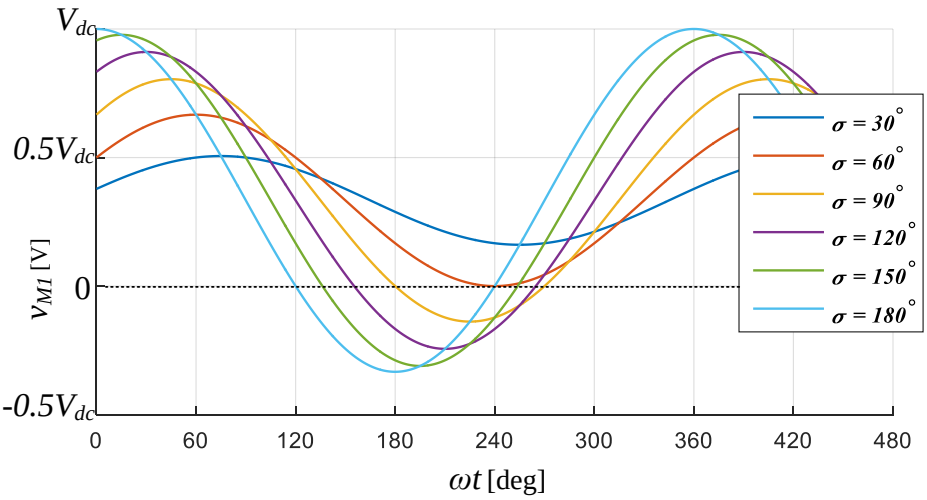

Fig. 5.8 Middle-arm voltage variation of the 9A-MMC, relative to the phase-shift angle, at $M = 1$.

Since the 9A-MMC is fundamentally introduced as a six-phase machine drive, the phase angle between the two output voltage sets will be either 30° or 60° for asymmetrical and symmetrical winding layout, respectively. Thus, the middle-arm voltage will be always unipolar, employing only HB-SMs.

B. Arm Currents

Due to the asymmetrical operational behaviour of the 9A-MMC, the arm currents have different alternation in the upper, middle, and lower arms. Referring to Fig. 5.7, applying KCL at the intermediary points of leg-1 yields:

$$i_{M1} = i_x + i_{L1} \tag{5.9a}$$

$$\begin{aligned} i_{U1} &= i_a + i_{M1} \\ &= i_a + i_x + i_{L1} \end{aligned} \tag{5.9b}$$

where the upper-arm current carries both machine currents i_a and i_x in addition to the lower-arm current, while the middle-arm current carries the machine current i_x along with the lower-arm current. Since the sum of machine currents i_a and i_x has a magnitude of $1.93I_o$ and $1.73I_o$ for asymmetrical and symmetrical machines, respectively, the upper-arm current is almost twice the middle-arm current, while the latter is twice the lower-arm current.

Due to different arm-current alternation, the SM capacitor voltage fluctuation differs in the upper, middle, and lower arms. The capacitor voltage ripple of upper-arm SMs is almost twice the voltage ripple of middle-arm SM capacitors, while the latter has double the voltage ripple of lower-arm SMs. To achieve the same voltage ripple, the SM capacitance of the middle arm is designed as twice the SM capacitance of the lower arm. Likewise, the SM capacitance of the upper arm is designed as twice the SM capacitance of the middle arm.

5.4.2 9A-MMC Control

A PD PWM-based modulator is utilized for each leg of the 9A-MMC to command a varying number of SMs to be inserted at each time instant in the different arms. This is schematically illustrated in Fig. 5.9 for one leg of the 9A-MMC. Both the upper- and lower-arm reference voltages, given by (5.7), are utilized as inputs to the modulator which accordingly determines the necessary number of SMs to be inserted in the upper and lower arms, as denoted by n_{U1} and n_{L1}, respectively. To ensure a zero voltage summation in the outer loop, the number of SMs to be inserted in the middle arm is calculated as $n_{M1} = 1.5N - n_{U1} - n_{L1}$. A capacitor voltage balancing algorithm is applied, as discussed in Chapter 2, to maintain all SM capacitors balanced around the nominal value.

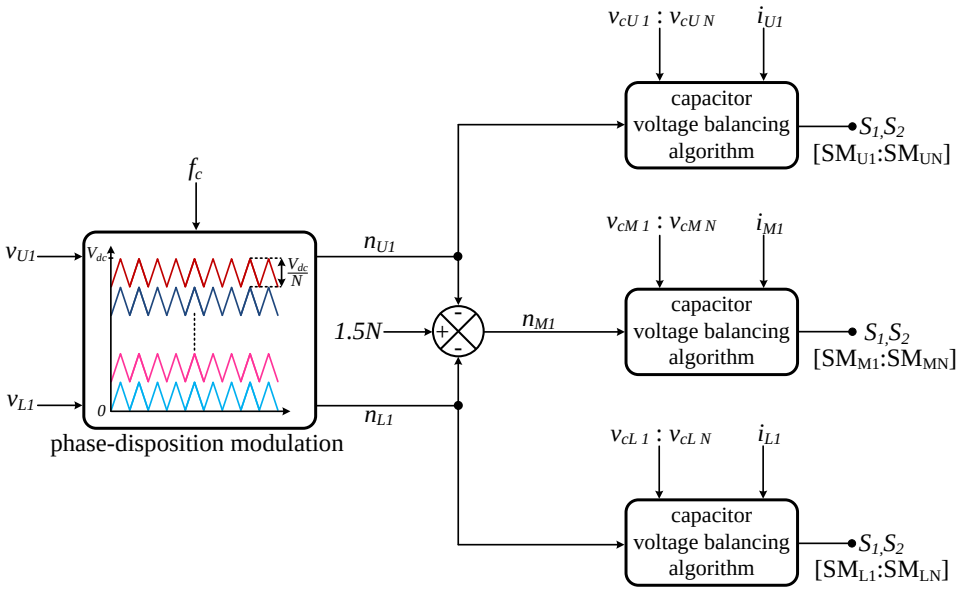

Fig. 5.9 A schematic diagram for the modulation and control of one leg of the 9A-MMC.

5.4.3 Simulation

The performance of the 9A-MMC with identical HB-SMs is investigated using a 3.2 MW simulation model. The 9A-MMC is generating asymmetrical six-phase voltages, while feeding a six-phase *RL* load. The dc-link voltage is 50% higher than that of a traditional 12A-MMC to maintain the same loading condition. Simulation parameters are listed in Table 5.5, while simulation results are depicted in Fig. 5.10. The six-phase line voltages and load currents are maintained similar to those of the 12A-MMC. Both the upper- and lower-arm voltages transit between 0 and 10 kV in 11 voltage steps, and have a 30° phase shift, while the middle-arm voltage steps between 2 and 8 kV. The arm currents are sinusoidal, however with different magnitudes, where $i_U > i_M > i_L$. The SM capacitance of the three arms is 12 mF, where the capacitor voltage variations are ±5%, ±3%, and ±2% for the upper-, middle, and lower-arm SMs, respectively. To maintain the same ±5% voltage ripple across all-arm SM capacitors, the SM capacitance can be reduced to 6 and 3 mF for the middle- and lower-arm SMs, respectively.

Table 5.5: Parameters for 9A-MMC simulation

Number of SMs per arm (N)	10
Rated active power	3.2 MW
Input dc voltage (V_{dc})	15 kV
Nominal SM capacitor voltage (V_c)	1 kV
Rated line voltage	6 kV
Rated current magnitude (I_o)	250 A
Fundamental output frequency (f_o)	50 Hz
Carrier frequency (f_c)	2 kHz
Arm inductance (L_{arm})	7.5 mH
SM capacitance (C)	12 mF
Load resistance	15 Ω
Load inductance	30 mH

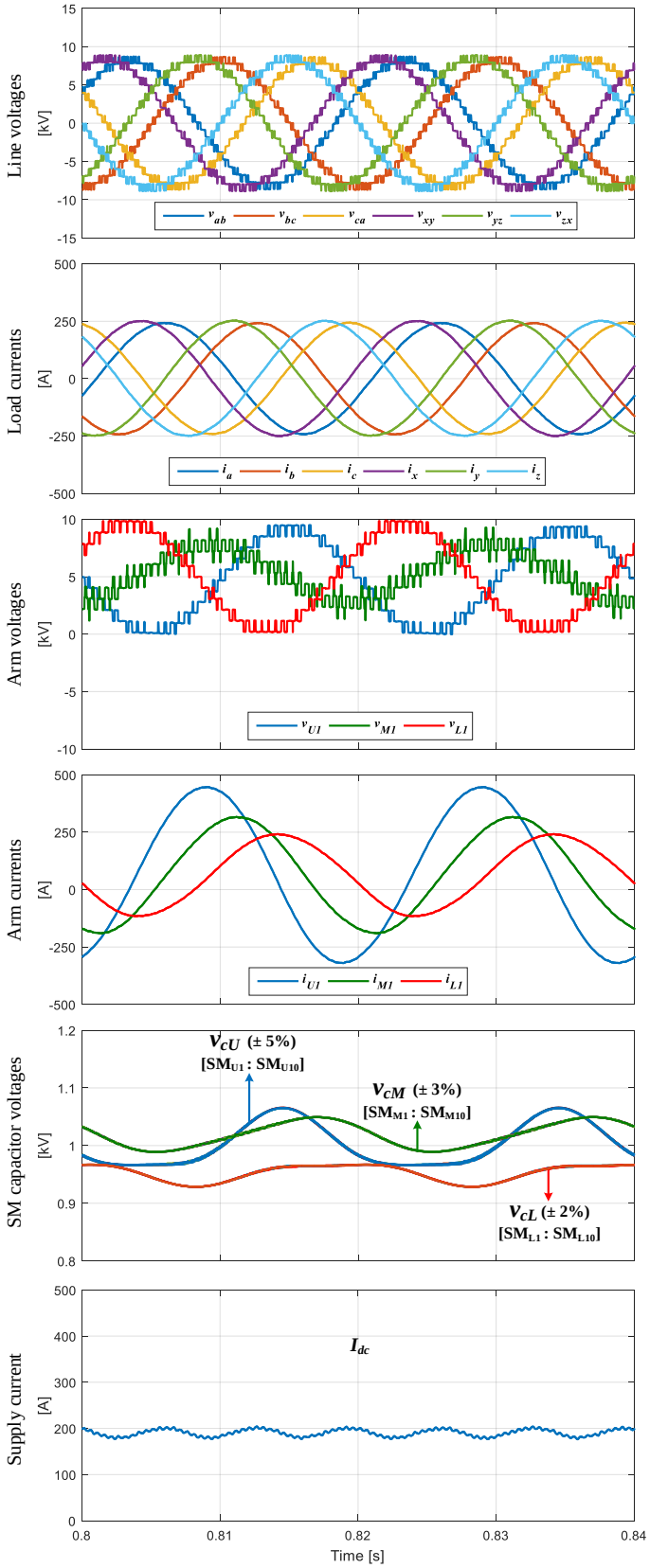

Fig. 5.10 Simulation results of the 9A-MMC supplying six-phase *RL* load with asymmetrical modulation.

5.4.4 Quantitative Assessment

Table 5.6 allows assessing the 9A-MMC component count and design, compared to the 12A-MMC. The 9A-MMC achieves 25% reduction in the number of employed components, compared to the 12A-MMC, at the expense of 33% reduction in the dc-link voltage utilization. To deliver the same output power as the 12A-MMC, the dc-link voltage of the 9A-MMC is increased by 50%. Nonetheless, the nominal voltage across the IGBTs and SM capacitors is the same as that of the 12A-MMC. The dc input current drawn by the 9A-MMC is 67% less than that of the 12A-MMC, and is distributed among 3 legs. Approximating the ac component amplitude of the arm current to $2I_o$, I_o, and $0.5I_o$ for the upper-, middle-, and lower-arm currents, respectively, the combined power rating of the 9A-MMC is $21V_{dc}I_o + 4V_{dc}I_{dc}$ (52.5% higher than the 12A-MMC). To achieve the same voltage ripple across all SM capacitors of the 9A-MMC, as compared to the 12A-MMC's voltage ripple, the SM capacitance is designed as $4C$, $2C$, and C for the upper-, middle-, and lower-arm SMs, respectively, where C is the SM capacitance of the 12A-MMC. Also, the arm

Table 5.6: Component count and rating of the 9A-MMC, compared to the 12A-MMC

	12A-MMC	**9A-MMC**
DC link voltage	V_{dc}	$1.5V_{dc}$
Maximum AC voltage	½ V_{dc}	½ V_{dc}
Number of SMs	12N HB-SMs	9N HB-SMs
Number of IGBTs	24N	18N
Number of arm inductors	12	6
Number of SM capacitors	12N	9N
IGBT rated voltage	V_{dc}/N	V_{dc}/N
IGBT rated current	$\frac{1}{6}I_{dc} + \frac{1}{2}I_o$	$\frac{2}{9}I_{dc} + 2I_o$ for upper-arm IGBTs, $\frac{2}{9}I_{dc} + I_o$ for middle-arm IGBTs, and $\frac{2}{9}I_{dc} + 0.5I_o$ for lower-arm IGBTs
Combined power rating	$12V_{dc}I_o + 4V_{dc}I_{dc}$	$21V_{dc}I_o + 4V_{dc}I_{dc}$
SM capacitance	C	$4C$ for upper-arm SMs, $2C$ for middle-arm SMs, and C for lower-arm SMs
Total capacitive stored energy	$12N$ [½ C $(V_{dc}/N)^2$]	$21N$ [½ C $(V_{dc}/N)^2$]
Arm Inductance	L	$1.5L$
Total reactive elements	$12NC + 12L$	$21NC + 9L$

inductance of the 9A-MMC is increased by 50%, compared to the 12A-MMC, due to the 50% increase in the dc-link voltage for the same power delivery.

5.5 Hybrid Nine-Arm MMC

To promote the dc-link voltage utilization of the 9A-MMC, with further reduction in topology components, this thesis proposes a hybrid 9A-MMC (H9A-MMC) which inherits the same structure of the standard 9A-MMC, however, incorporates mixed SM cells. The H9A-MMC is shown in Fig. 5.11, feeding a six-phase machine with isolated neutral points. Both the upper and lower arms are formed by N series connected HB-SMs, while the middle arm is composed of K series connected FB-SMs. The value of K is determined as a portion of N, depending on the phase shift between the two sets of three-phase output voltages. By employing the FB-SM's negative-voltage state, the middle-arm voltage is bidirectional with zero average voltage. This allows both the upper- and lower-arm voltages to extend their dc component to $½V_{dc}$, which enhances the dc-link voltage utilization without any compromise, compared to the 9A-MMC.

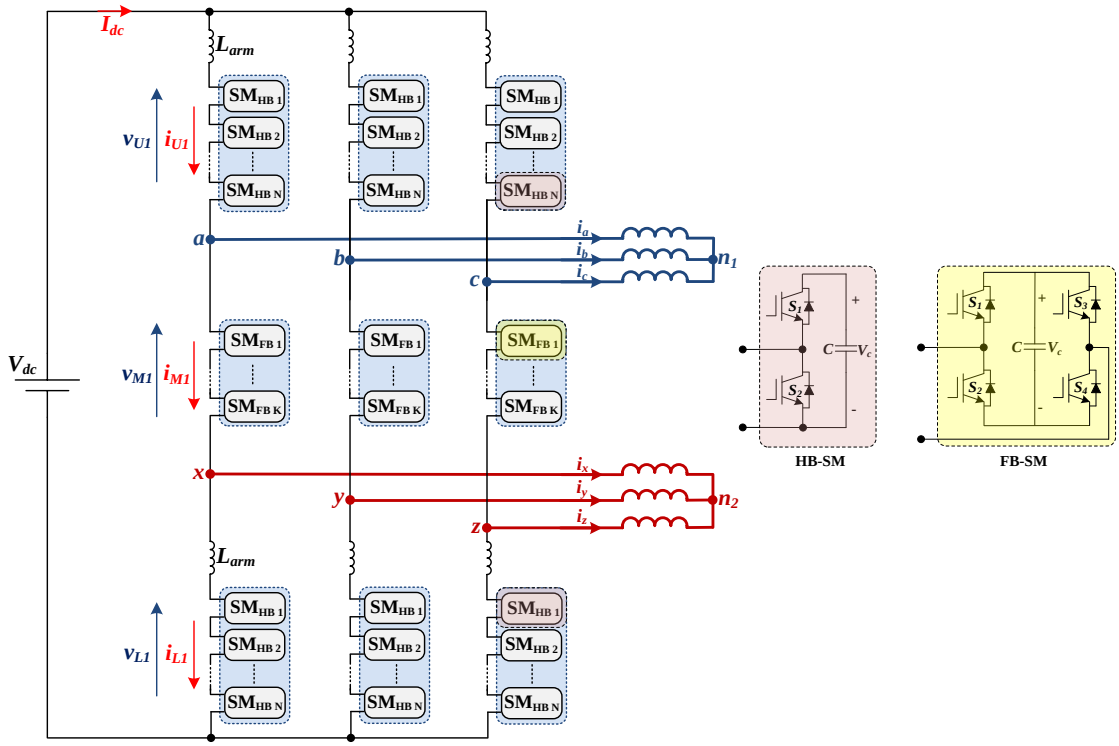

Fig. 5.11 Hybrid 9A-MMC feeding a six-phase machine with isolated neutral points.

5.5.1 H9A-MMC Analysis

A. Arm voltages

The dc-link voltage utilization of the H9A-MMC is defined similar to a standard MMC as given by (2.2). Both the upper and lower arms are controlled to generate a unidirectional voltage ranging from 0 to MV_{dc}. Considering leg-1 of the H9A-MMC, which provides the machine phase-terminals a and x, the voltage across the upper and lower arms is:

$$v_{U1} = \frac{1}{2}V_{dc}\,[1 - M\,\cos(\omega t)] \tag{5.10a}$$

$$v_{L1} = \frac{1}{2}V_{dc}\,[1 + M\,\cos(\omega t + \sigma)] \tag{5.10b}$$

The voltage balance between the dc-link voltage and the H9A-MMC legs implies the middle-arm voltage be bidirectional, as follows.

$$\begin{aligned} v_{M1} &= V_{dc} - v_{U1} - v_{L1} \\ &= \frac{1}{2}MV_{dc}\sqrt{2(1-\cos\sigma)}\,\cos(\omega t + \alpha) \end{aligned} \tag{5.11}$$

$$\alpha = \tan^{-1}\frac{\sin\sigma}{\cos\sigma - 1} \tag{5.12}$$

As exposed by (5.11), the magnitude of the middle-arm voltage depends on the phase angle σ, which is graphically demonstrated in Fig. 5.12 for different values of σ, at unity modulation index. Unlike both the upper- and lower-arm voltages, the middle-arm voltage is comprised only of an ac component with a magnitude that is directly proportional to the angle σ, with a maximum swing of $\pm V_{dc}$. The bidirectional middle-arm voltage can only be realized by incorporating FB-SMs in the middle arm, where the number of employed FB-SMs is determined according to the angle σ. The magnitude of the middle-arm voltage is $0.258V_{dc}$ for asymmetrical machines and $0.5V_{dc}$ for symmetrical machines. Thus, the number of FB-SMs in the middle arm is designed as 30% and 50% the number of employed HB-SMs in either the upper or lower arms for asymmetrical and symmetrical machines, respectively.

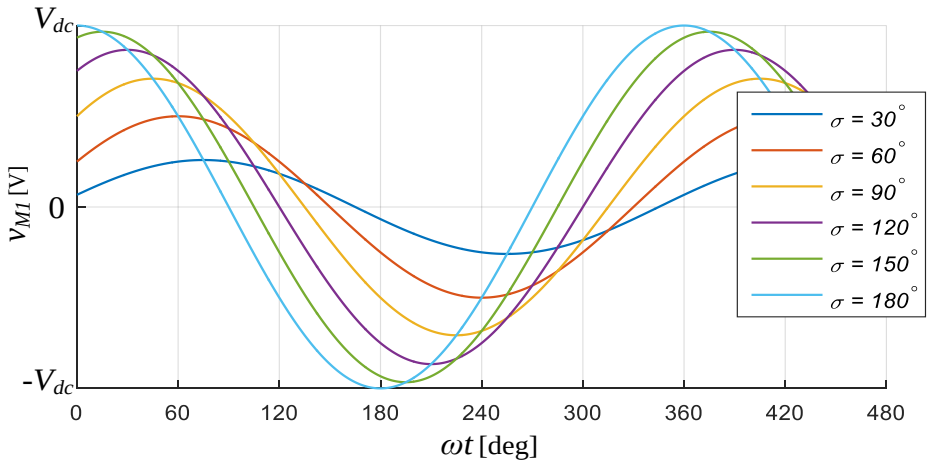

Fig. 5.12 Middle-arm voltage variation of H9A-MMC, relative to the phase-shift angle, at M = 1.

B. Arm currents

The arm currents of leg-1 are defined in relation to the corresponding machine currents i_a and i_x as:

$$i_{U1} = i_{circ} + i_a \tag{5.13a}$$

$$i_{M1} = i_{circ} \tag{5.13b}$$

$$i_{L1} = i_{circ} - i_x \tag{5.13c}$$

where i_{circ} is the circulating current through the dc loops comprising the dc side and each converter leg. Unlike a standard MMC, the circulating current of the H9A-MMC experiences both even and odd harmonics, while their magnitudes depend on the modulation phase angle between the upper and lower arms. Among these low-order harmonics, the second-order harmonic has the largest magnitude, and then the third-order harmonic with a lower magnitude. Due to its dominant effect, the second-order harmonic is suppressed through several approaches as discussed in Chapter 2, while the effect of the remaining third-order harmonic on the circulating current can be neglected without affecting the forthcoming analysis. Accordingly, the circulating current is assumed to be only the dc component, and is defined as one third the dc input current I_{dc}, as:

$$i_{circ} = \frac{I_{dc}}{3} = \frac{M I_o \cos\varphi}{2} \tag{5.14}$$

C. SM capacitor voltage ripple

Due to the asymmetric operational behavior of the H9A-MMC, the capacitive energy stored in the middle arm will have different alternation than that of both the upper and lower arms, which is eventually manifested in the corresponding SM capacitor voltage with different ripple profiles. With the modulation of (5.10) and (5.11), the capacitor current, i_C, for an upper-, middle-, and lower-arm SM is described as:

$$i_{C\,U1} = \frac{1}{2}\left[1 - M\cos(\omega t)\right] i_{U1} \tag{5.15a}$$

$$i_{C\,M1} = \frac{1}{2} M\sqrt{2(1-\cos\sigma)}\cos(\omega t + \alpha)\, i_{M1} \tag{5.15b}$$

$$i_{C\,L1} = \frac{1}{2}\left[1 + M\cos(\omega t + \sigma)\right] i_{L1} \tag{5.15c}$$

By integrating (5.15), the capacitor voltage fluctuation of SMs in the three arms is:

$$\Delta v_{C\,U1} = \frac{1}{C}\int_0^t i_{C\,U1}\, dt$$
$$= \frac{I_o}{4\omega C}\left[\sqrt{4 + \cos^2\varphi\,(M^4 - 4M^2)}\,\sin(\omega t + \beta) - M\sin(2\omega t - \varphi)\right] \tag{5.16a}$$

$$\Delta v_{C\,M1} = \frac{1}{C}\int_0^t i_{C\,M1}\, dt = \left[\frac{M^2 I_o\cos\varphi}{4\omega C}\sqrt{2(1-\cos\sigma)}\right]\sin(\omega t + \alpha) \tag{5.16b}$$

$$\Delta v_{C\,L1} = \frac{1}{C}\int_0^t i_{C\,L1}\, dt$$
$$= \frac{I_o}{4\omega C}\left[-\sqrt{4 + \cos^2\varphi\,(M^4 - 4M^2)}\,\sin(\omega t + \beta) - M\sin(2(\omega t + \sigma) - \varphi)\right] \tag{5.16c}$$

where β is given as:

$$\beta = \tan^{-1}\frac{2\tan\varphi}{M^2 - 2} \tag{5.17}$$

D. SM capacitance design

From (5.16), the capacitor voltage ripple for the upper- and lower-arm SMs pulsate due to both the first- and second-frequency harmonics. Whereas, the middle-arm SM capacitor voltage ripple pulsates at the fundamental frequency. Therefore, the middle-arm SM capacitance design is different compared to that of the upper- and lower-arm SMs, for the same voltage-ripple profile.

Figs. 5.13 and 5.14 investigate the response of capacitor voltage ripple with operating parameters variation, where the normalized SM capacitor voltage ripple is observed in three-dimensional relationships, for different-arm SMs. The influence of both the load current and power factor variation on capacitor voltage ripple is shown in Fig. 5.13a for both the upper- and lower-arm SMs, while shown in Fig. 5.13b for the middle-arm SMs. Although the voltage ripple is directly proportional to the load current, there is a remarkable disparity in the correspondent SM voltage ripple variation, where the increase of the middle-arm SM voltage ripple due to the load current increase is significantly lower than that of both the upper- and lower-arm SMs. In addition, while the middle-arm SM voltage ripple is proportional to the power factor, both the upper- and lower-arm SM voltage ripple are inversely proportional. To quantify the voltage ripple diversity, the maximum voltage ripple ratio between the upper- and lower-arm SMs and the middle-arm SMs, is 3.4.

In a similar way, Fig. 5.14 shows the voltage ripple profile in response to both operating frequency and modulation index variation. Fig. 5.14a shows that the voltage ripple of both the upper- and lower-arm SMs is slightly inversely proportional to the modulation index, but significantly inversely proportional to the operating frequency. On the other hand, the middle-arm SM voltage ripple, shown in Fig. 5.14b, is slightly increasing with either increased modulation index or operating frequency. The ratio between the maximum recorded voltage ripple in Fig. 14a to Fig. 14b is 4.5.

It is worth mentioning that the results in Figs. 5.13 and 5.14 assume the H9A-MMC feeds an asymmetrical machine, where σ is 30°. Unlike the upper and lower arms, the middle-arm SM capacitor voltage ripple depends on the phase angle σ. According to (5.16b), the middle-arm SM capacitor voltage ripple is doubled when the H9A-MMC feeds a symmetrical six-phase machine, compared to an asymmetrical one. Thus, the middle-arm SM capacitance can be reduced to quarter and half the upper- and lower-arm SM capacitance, for asymmetrical and symmetrical machines, respectively.

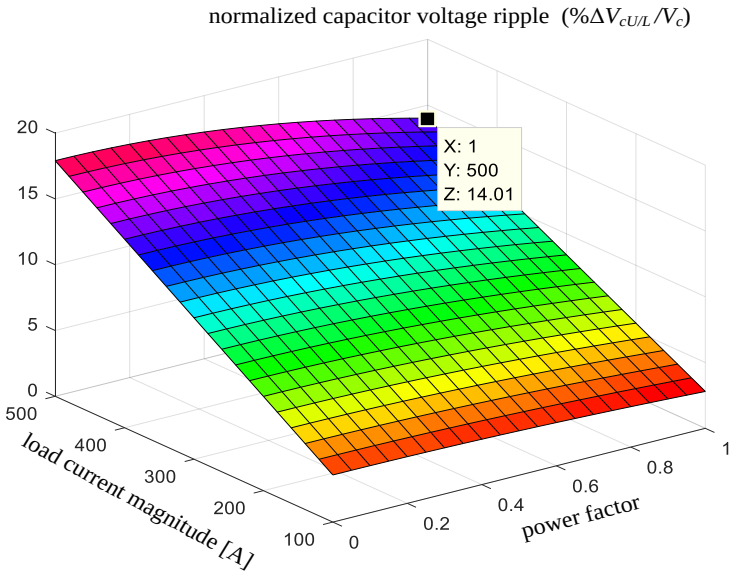

(a)

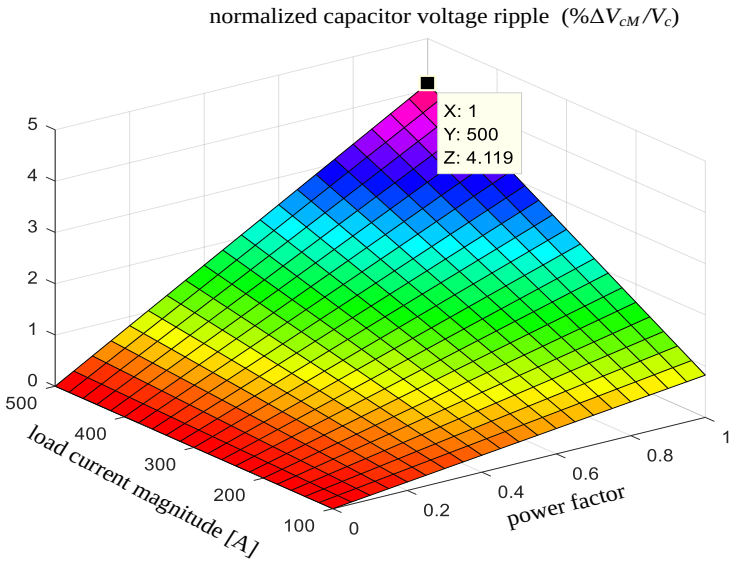

(b)

Fig. 5.13 Normalized peak-to-peak capacitor voltage ripple of H9A-MMC for various operating conditions of load current and power factor, for: (a) upper- and lower-arm SMs and (b) middle-arm SM. (M=1, f=50 Hz, C=5 mF, σ =30°, and V_c=2 kV)

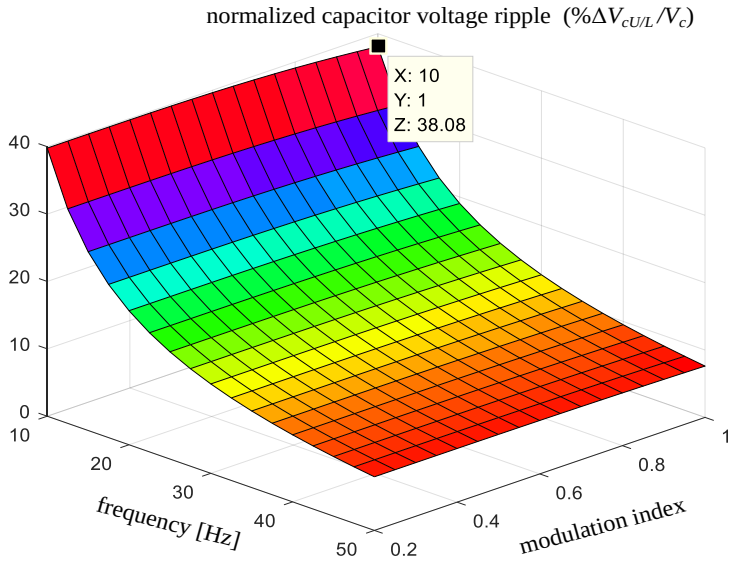

(a)

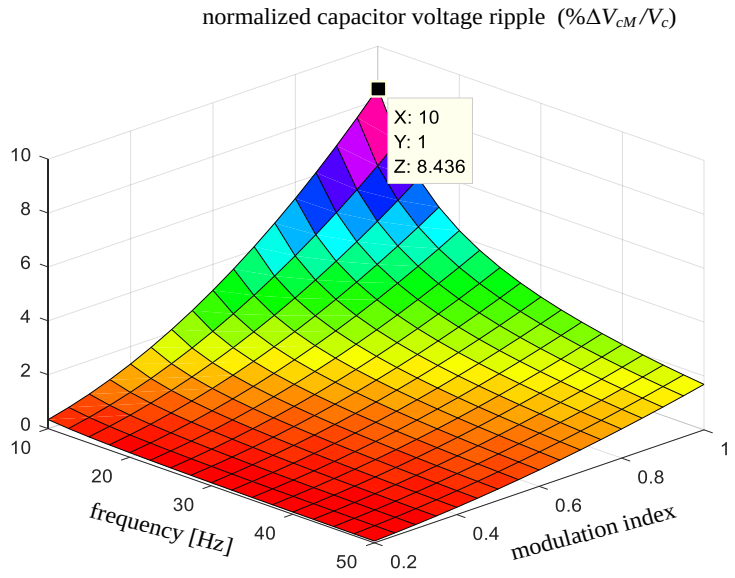

(b)

Fig. 5.14 Normalized peak-to-peak capacitor voltage ripple of H9A-MMC for various operating conditions of frequency and modulation index, for: (a) upper- and lower-arm SMs and (b) middle-arm SM. (I_o=250 A, φ=35°, C=5 mF, σ=30°, and V_c=2 kV)

5.5.2 H9A-MMC Control

H9A-MMC control is similar to that of the 9A-MMC. Both the upper- and lower-arm reference voltages, as given by (5.10), are utilized to determine the necessary number of HB-SMs to be inserted in the upper and lower arms. The number of FB-SMs

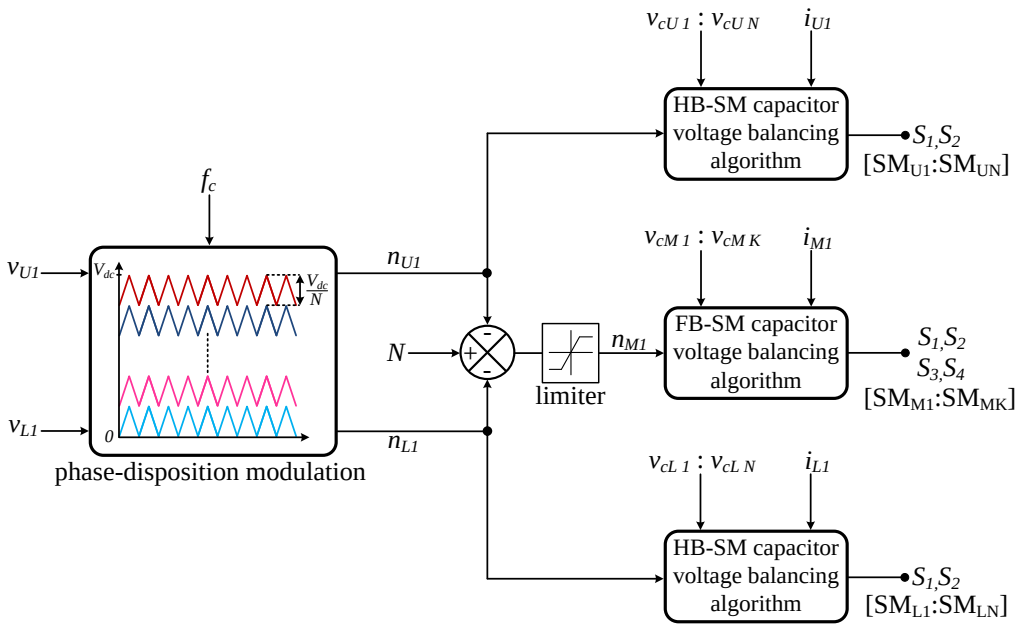

Fig. 5.15 A schematic diagram for the modulation and control of one leg of the H9A-MMC.

to be inserted in the middle arm is calculated as $n_{M1} = N - n_{U1} - n_{L1}$, where a limiter with a bandwidth of either $\pm 0.3N$ or $\pm 0.5N$ is utilized for the asymmetrical and symmetrical operation mode of the H9A-MMC, respectively, as shown in Fig. 5.15. The positive sign of n_{M1} indicates operating the middle-arm FB-SMs under positive voltage state (that is, positive SM output voltage), while the negative sign indicates a negative output voltage state. It should be noted that, although the middle-arm current is unidirectional, the FB-SM capacitors can be charged and discharged by changing the arm-current direction through the capacitors when inserted in the conduction path.

5.5.3 Verification

The performance of the proposed H9A-MMC is examined using both simulation and experimentation, with the parameters listed in Table 5.7.

A. Verification using RL load

A 3.2 MW MATLAB/SIMULINK simulation model is used to verify the features of the proposed H9A-MMC while feeding a six-phase *RL* load (R=15 Ω, L=30 mH). The simulation results are shown in Figs. 5.16 and 5.17 for both asymmetrical and

symmetrical modulation of the H9A-MMC, respectively. The number of HB-SMs in both the upper and lower arms is 10, while the number of FB-SMs in the middle arm is 3 and 5 for the asymmetrical and symmetrical modulation, respectively.

Table 5.7: Parameters for H9A-MMC verification

	Simulation	Experiment
Number of SMs per arm (N)	10	3
Rated active power	3.2 MW	4 kW
Input dc voltage (V_{dc})	10 kV	300 V
Nominal SM capacitor voltage (V_c)	1 kV	100 V
Rated line voltage	6 kV	180 V
Rated current magnitude (I_o)	250 A	9 A
Fundamental output frequency (f_o)	50 Hz	50 Hz
Carrier frequency (f_c)	2 kHz	2 kHz
Arm inductance (L_{arm})	5 mH	2.8 mH
SM capacitance (C)	6 mF	2.2 mF

In Figs. 5.16 and 5.17, the six-phase line voltages and load currents are high quality sinusoidal waveform with 30° and 60° phase shift between the abc and xyz three-phase sets, respectively. Both the upper- and lower-arm voltages transit between 0 to 10 kV through 11 voltage levels. Whereas, the middle-arm voltage is bidirectional and pulsates with ±3 kV and ±5 kV amplitude, for the asymmetrical and symmetrical cases, respectively. Both the upper- and lower-arm currents show a good sinusoidal profile, since the second-order harmonic is eliminated using a parallel-resonant filter. The middle-arm current exhibits almost a dc component with a series of odd-order harmonics due to the SM capacitor voltage fluctuations, that clearly appear in the dc input current.

Investigating the SM capacitor voltage, both the upper- and lower-arm SMs pulsate due to the first- and second- frequency harmonics, with ±5% voltage ripple, for both the asymmetrical and symmetrical cases. The middle-arm SM capacitor voltage pulsates with the fundamental frequency, with ±1.4% and ±2.8% voltage ripple for the asymmetrical and symmetrical cases, respectively.

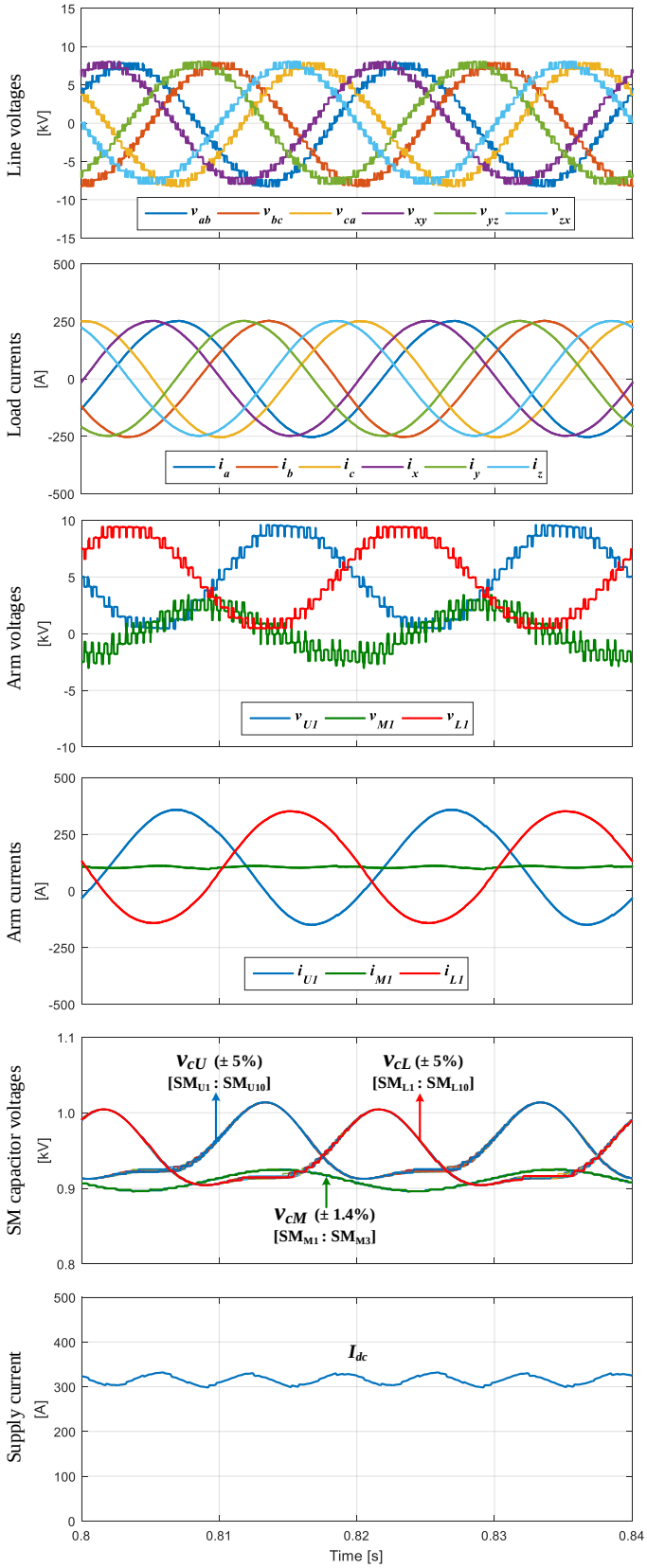

Fig. 5.16 Simulation results of the H9A-MMC supplying six-phase *RL* load with asymmetrical modulation.

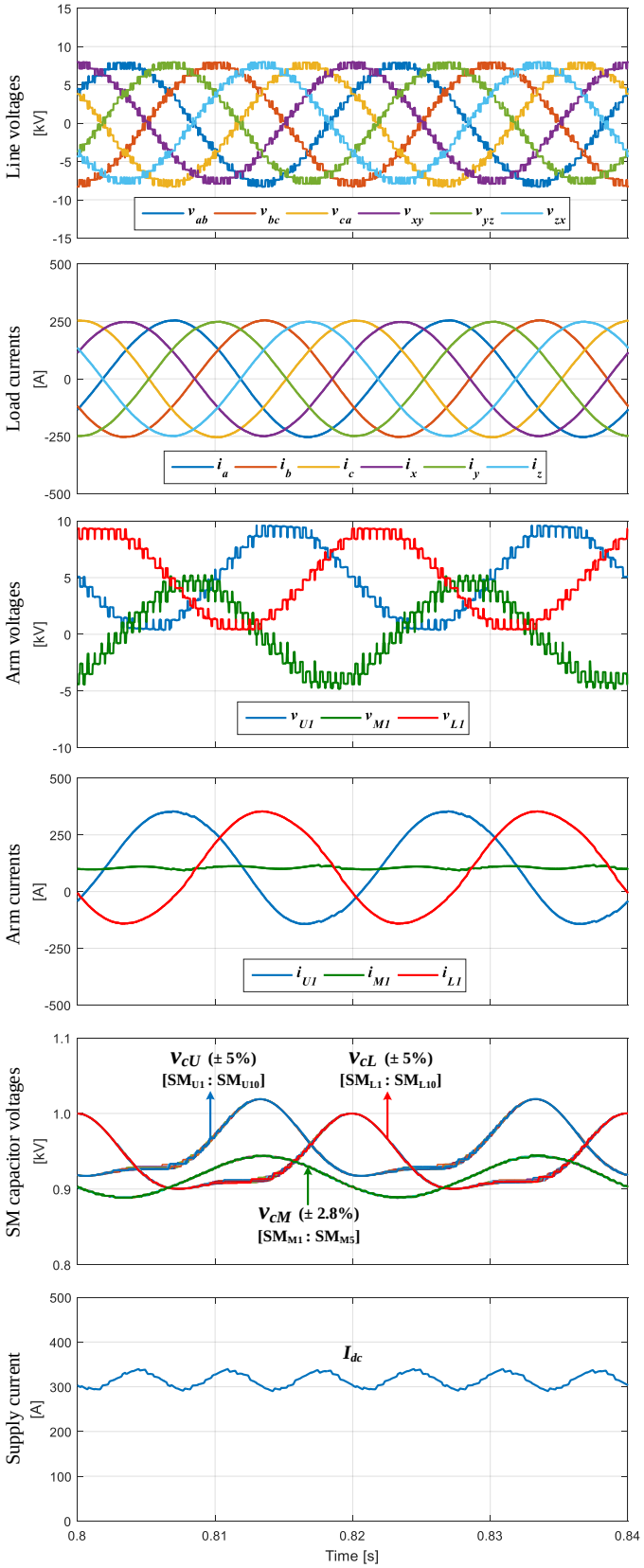

Fig. 5.17 Simulation results of the H9A-MMC supplying six-phase *RL* load with symmetrical modulation.

It is worth mentioning that the results in Figs. 5.16 and 5.17 are obtained when the SM capacitance is 6 mF in all arms. To achieve the same voltage ripple profile across the different-arm SM capacitors, the middle-arm SM capacitance can be reduced to 1.5 and 3 mF, for the asymmetrical and symmetrical cases, respectively.

B. Verification using six-phase machine

The performance of the H9A-MMC is examined when feeding a symmetrical six-phase machine, through both simulation and experimentation at the same operating conditions. A scaled-down laboratory converter prototype feeds a symmetrical six-phase machine constructed by rewinding the stator of an existing three-phase induction machine with two identical three-phase single layer windings shifted in space by 60°. The constructed six-phase machine has half the number of turns per coil and same conductor cross sectional area, compared to the three-phase machine, to maintain the same copper volume. The three-phase machine is rated at 4 kW, 415 V (line-to-line), 50 Hz, 7.5 A, 1450 RPM with two pole pairs. After rewinding, the rated voltage is halved, while other rated values are maintained. The number of HB-SMs in the upper and lower arms is 3, while the number of FB-SMs in the middle arms is 2. The control algorithm is implemented using TMS320F28335 Texas Instruments DSPs.

Both simulation and experimental results are presented in Figs. 5.18 and 5.19, respectively, at the same scale to allow one-to-one comparison. In both figures, two line voltages of each three-phase set are shown to traverse with 7 voltage levels, while the machine currents i_a and i_x are sinusoidal. Both the upper- and lower-arm voltages step between 0 and 300 V, while the middle-arm voltage is bidirectional, alternating between ±200 V. The upper- and lower-arm currents show a sinusoidal profile, however, distorted with low-order harmonics since the circulating current has not been controlled to suppress its inherited harmonics. Thus, both the second- and third-order harmonics simultaneously affect the arm-current waveforms, as clearly appear in the fluctuation of the middle-arm current, with 23% and 8% amplitudes, respectively. These harmonics appear further enlarged in the supply current waveform since their instantaneous value is tripled. The capacitor voltage of the

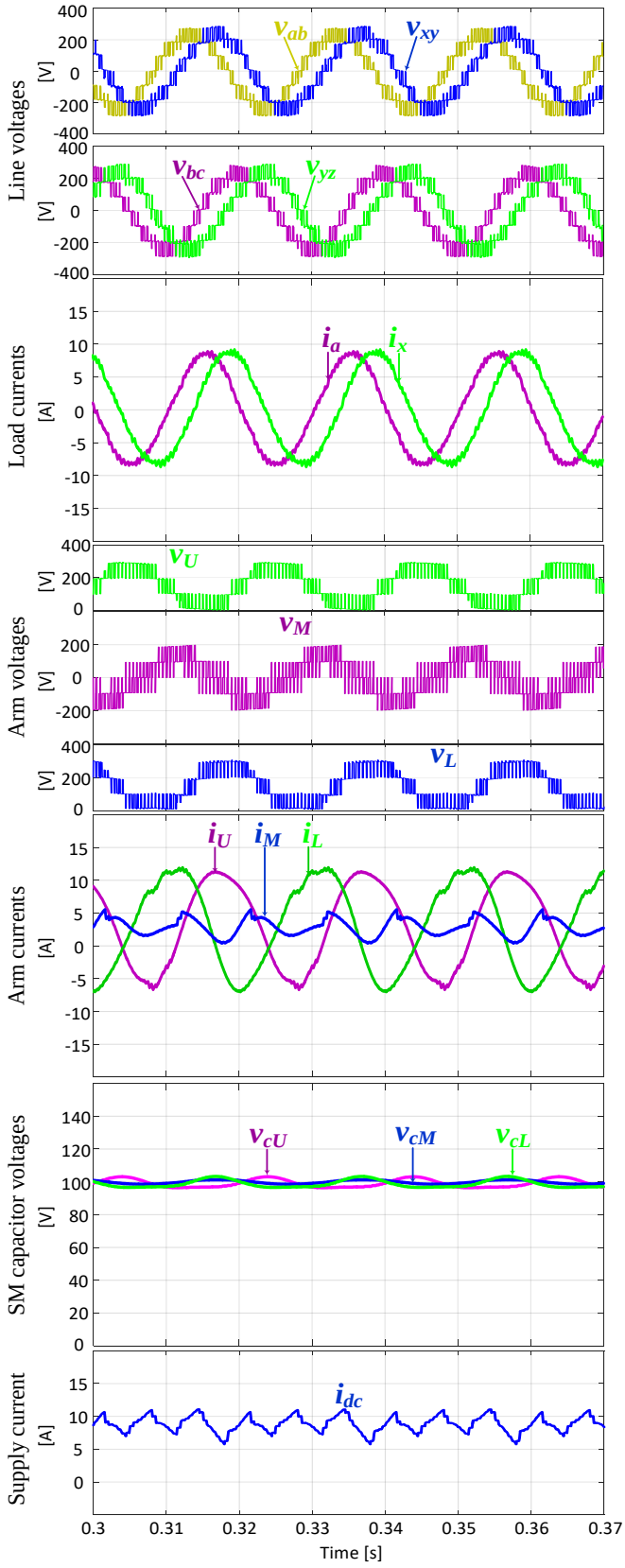

Fig. 5.18 Simulation results of the H9A-MMC supplying a symmetrical six-phase machine.

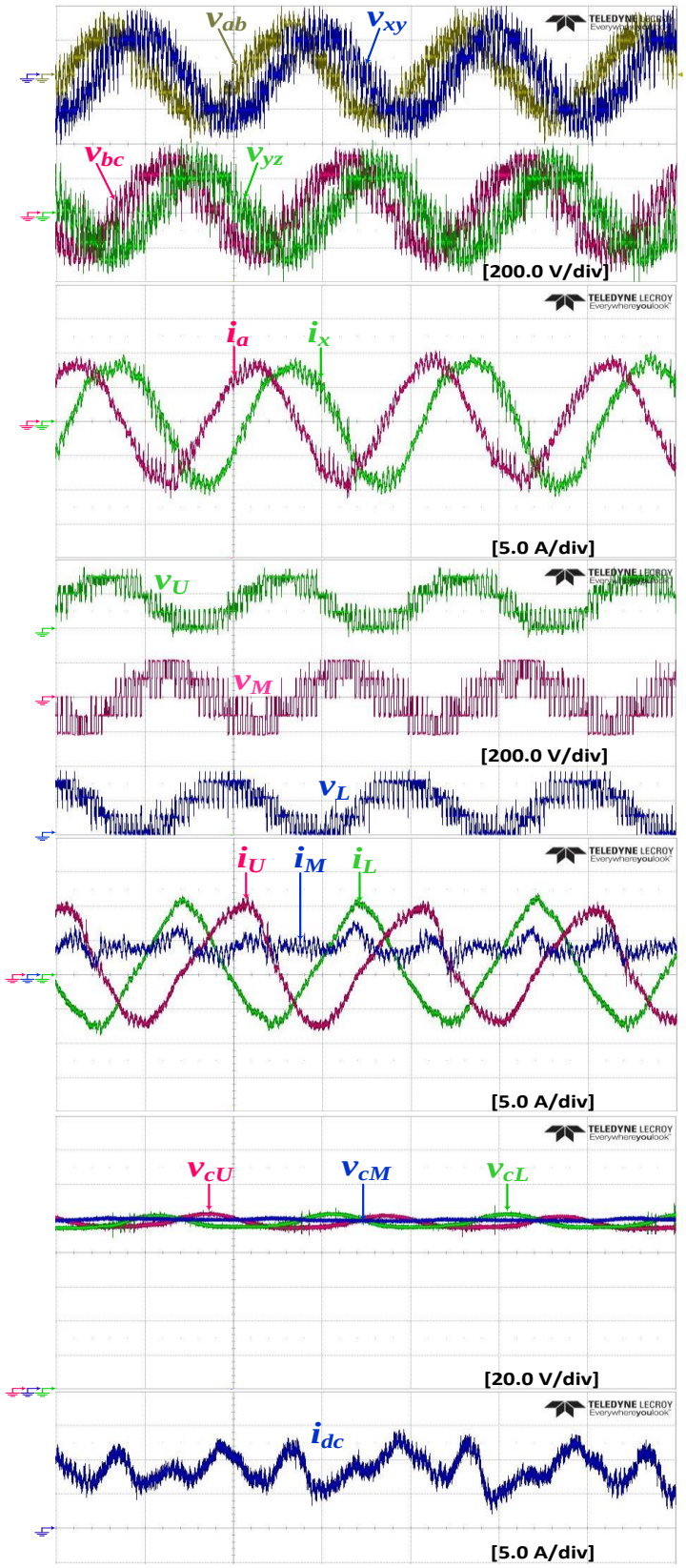

Fig. 5.19 Experimental results of the H9A-MMC supplying a symmetrical six-phase machine (time scale: 10 ms/div).

upper- and lower-arm SMs has ±3% voltage ripple, while the middle-arm SM capacitor voltage ripple is ±0.7%, where the capacitance of all SMs is 2.2 mF.

5.5.4 Assessment

Promoted by the inclusion of FB-SMs, the H9A-MMC achieves the same voltage utilization as the standard 12A-MMC, however with a reduced component count. Table 5.8 assesses the number of components employed by the H9A-MMC, for asymmetrical and symmetrical operation, in addition to IGBTs rating and reactive elements design, in comparison to the 12A-MMC. While the IGBT rated voltage is identical for different SMs in both the 12A-MMC and H9A-MMC, the rated current is doubled for both the upper- and lower-arm IGBTs, and is reduced by 40% for the middle-arm IGBTs of the H9A-MMC, compared to the 12A-MMC.

Table 5.8: Component count and rating of H9A-MMC, compared to the 12A-MMC

	12A-MMC	**H9A-MMC**	
		$\sigma = 30°$	$\sigma = 60°$
DC link voltage	V_{dc}	V_{dc}	
Maximum AC voltage	$½\ V_{dc}$	$½\ V_{dc}$	
Number of SMs	$12N$ HB-SMs	$6N$ HB-SMs and $0.9N$ FB-SMs	$6N$ HB-SMs and $1.5N$ FB-SMs
Number of IGBTs	$24N$	$15.6N$	$18N$
Number of arm inductors	12	6	
Number of SM capacitors	$12N$	$6.9N$	$7.5N$
IGBT rated voltage	V_{dc}/N	V_{dc}/N	
IGBT rated current	$⅙I_{dc} + ½I_o$	$⅓I_{dc} + I_o$ for upper- and lower-arm IGBTs and $⅓I_{dc}$ for middle-arm IGBTs	
Combined power rating	$12V_{dc}I_o + 4V_{dc}I_{dc}$	$12V_{dc}I_o + 5.2V_{dc}I_{dc}$	$12V_{dc}I_o + 6V_{dc}I_{dc}$
SM capacitance	C	$2C$ for upper- and lower-arm SMs	
		$0.5C$ for middle-arm SMs	C for middle-arm SMs
Total capacitive stored energy	$12N\ [½\ C\ (V_{dc}/N)^2]$	$12.45N\ [½\ C\ (V_{dc}/N)^2]$	$12.75N\ [½\ C\ (V_{dc}/N)^2]$
Arm Inductance	L	L	
Total reactive elements	$12NC + 12L$	$12.45NC + 6L$	$13.5NC + 6L$

Since the upper- and lower-arm currents of the H9A-MMC topology are twice the arm currents of a standard MMC, the first-frequency ripple component of the H9A-MMC is twice that of a standard MMC. Therefore, the SM capacitance of both the upper- and lower-arm SMs are doubled to maintain the same voltage ripple. Whilst, the middle-arm SM capacitance is a quarter and a half the upper-/lower-arm SM capacitance, for the asymmetrical and symmetrical designs of the H9A-MMC, respectively.

Fig. 5.20 shows a graphical assessment of the H9A-MMC in comparison to the 12A-MMC, where the latter's parameters are set as 1 p.u., and used as reference for the former's parameters. While the number of arm inductors is reduced by 50%, the number of SM capacitors is reduced by 42.5% and 37.5% for asymmetrical and symmetrical designs of the proposed topology, respectively. However, the sum of the total employed inductance and capacitance is almost the same for both the 12A-MMC and the H9A-MMC, while the total capacitive stored energy is slightly increased by 3.8% and 6.3% for the asymmetrical and symmetrical designs of the H9A-MMC, respectively. The number of IGBTs is reduced by 35% and 25%; nonetheless, the combined power rating of the IGBTs is increased by 8.6% and 14.3%, where the values denote for the asymmetrical and symmetrical modes of the H9A-MMC, respectively.

To assess the size of the H9A-MMC, compared to the 12A-MMC, the 3.2 MW system investigated in the simulation study is selected as the performance index. That is, the 5SNG 0450R170300 phase-leg IGBT module with 1.7 kV, 450 A [148] is selected for both the upper- and lower-arm SMs of the H9A-MMC, while the 5SNG 0225R170300 phase-leg IGBT module with 1.7 kV, 225 A [149] is selected for the middle-arm SMs of the H9A-MMC and for the 12A-MMC's SMs as well, where both IGBT modules are from ABB. Although the current rating is doubled, the size of both IGBT modules is the same, and is calculated as 0.1628 L. To assess the SM capacitors size, according to EPOCS power capacitors [150], [151], the volume of 6, 3, and 1.5 mF capacitors are 19, 11.56, and 2.88 L, respectively, all rated at 1.1 kV. Accordingly, the total capacitor size of the 12A-MMC (incorporating $12N$ capacitors each 3 mF) is 1387.2 L. Whereas, the total capacitor size of the H9A-MMC (incorporating $6N$ capacitors each with 6 mF in addition to either $0.9N$

capacitors with 1.5 mF or 1.5*N* capacitors with 3 mF) is 1166 and 1313.4 L, for asymmetrical and symmetrical H9A-MMCs, respectively. That is, the H9A-MMC achieves 16% and 6% size reduction for asymmetrical and symmetrical operation, respectively. It should be noted that this is only a comparison for the size of the main SM components (capacitors and IGBTs), rather than a comparison of the volume of real SM enclosures (in which there are more components and cooling structures). Nevertheless, an additional decrease in the whole system size is expected, due to the reduction in the number of gate-drive circuits and both voltage and current transducers.

To assess the efficiency of the H9A-MMC, the power loss calculation method in [107] is adopted, with the IGBTs parameters as given in their datasheets. While the efficiency of the 12A-MMC is 97.9%, the efficiency of the H9A-MMC is 97.4% and 97.3% for the asymmetrical and symmetrical cases, respectively. Although these efficiencies are case specific, a general deduction can be drawn that the H9A-MMC's efficiency is lower but does not deviate significantly from that of the 12A-MMC.

The economic feasibility of the H9A-MMC is examined by performing a cost analysis for the main employed components. According to the mainstream suppliers in the electronics market, the H9A-MMC achieves 17% and 9% cost reduction when designed to drive an asymmetrical or symmetrical six-phase machine, respectively, as compared to the conventional 12A-MMC.

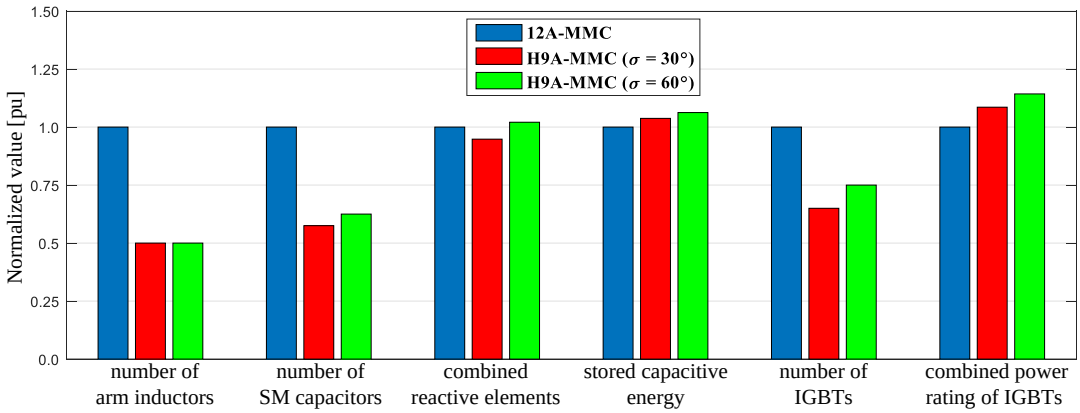

Fig. 5.20 Graphical assessment of the proposed H9A-MMC in comparison to the 12A-MMC.

5.6 DHB-Assisted MMC-Based Six-Phase Machine Drives

The power decoupling approach, addressed in Chapter 4, can be readily extended to six-phase MMC-based machine drives to compensate the SM capacitor voltage ripple at low operating frequencies. The generalized DHB-assisted configuration can be applied to both the 12A-MMC and 8A-MMC, since they inherit the standard MMC phase-leg structure (two arms per phase leg). That is, the DM ripple power component can be bi-directionally transferred between each pair of upper and lower arm in the same phase-leg, through a DHB balancer. For a 12A-MMC supplying a symmetrical six-phase machine with isolated neutral points, an alternative placement of the DHB balancers relative to the MMC SMs is offered, where the DHB balancers can interface adjacent-arm SMs of phase-legs feeding two machine windings with spatial phase opposition, as shown in Fig. 5.21.

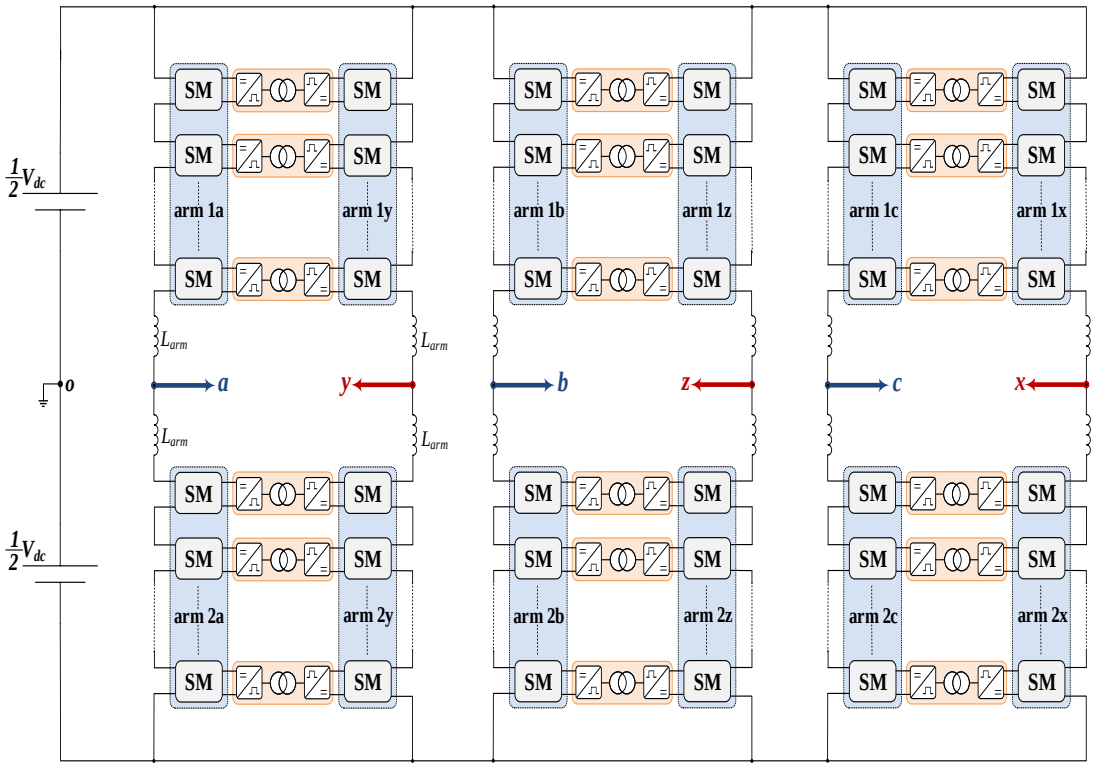

Fig. 5.21 Circuit diagram of DHB-assisted 12A-MMC for symmetrical six-phase machine with isolated neutral points.

The CM and DM power decoupling method, based on symmetrical alternation of three-phase components, can be applied to the 12A-MMC, 9A-MMC, and H9A-MMC. Since the 12A-MMC is a dual three-phase topology, each set of three SMs at the same level, with a common three-phase winding set, can be interfaced through a magnetic chain link with two/three DHB balancers. Likewise, in the 9A-MMC and H9A-MMC, each set of three adjacent-arm SMs in the upper, middle, and lower arms can be magnetically coupled through a chain of two/three DHB balancers.

5.7 Summary

In this chapter, MMC application for multiphase machines has been addressed by presenting four MMC-based topologies for dual three-phase machine drives, namely the 12A-MMC, 8A-MMC, 9A-MMC, and H9A-MMC. The 12A-MMC is the off-the-shelf six-phase MMC topology, being comprised of two standard three-phase MMCs with a common dc-link voltage. Nevertheless, the 12A-MMC employs a significant number of both active and passive components, which increases the size and cost of the six-phase drive system. Thus, reduced MMC structures with lower component count have been investigated. Both the 8A-MMC and 9A-MMC achieves a 33% and 25% reduction in the number of employed components, respectively, compared to the 12A-MMC, however, at the expense of reduced dc-link voltage utilization. The H9A-MMC is an advanced version of the 9A-MMC, which achieves the same performance as the 12A-MMC while employing at most the same number of IGBTs and a lower number of SM capacitors, compared to the 9A-MMC. The four topologies have been studied and quantitatively assessed, while their performance has been verified.

Chapter 6

Conclusion

This chapter summarizes the accomplishments and general conclusions acquired by the thesis in addition to the main research contributions. At the end of this chapter, suggestions for conceived future research are highlighted.

6.1 Summary and Contribution

The main objective of this thesis is to investigate MMC application to MV drives for three-phase and multiphase machines. Chapter 1 highlighted the rising demand of high-power applications employing adjustable-speed drives as the prime driving force when using the MV grid as the main ac power supply. High-power converters for machine drives application were overviewed with emphasis on multilevel VSIs as the prominent contenders fulfilling the motor-side requirements at the MV level. The market interest in multilevel converter-based MV drives was presented, showing that the MMC is a promising candidate for high-power machine drives due to its unlimited extendibility to any voltage/power level, compared to its counterparts.

Chapter 2 provided thesis background through a comprehensive overview of the MMC including its basic structure, operating principle, modulation techniques, circuit analysis, and control methods. MMC application as an MV machine drive was studied, detailing the drive system configurations and their associated control algorithms. The challenge of MMC-fed adjustable-speed drives at low operating frequencies was highlighted, where simulation results assessed MMC performance at both rated and reduced frequencies.

Chapter 3 gave an insight to the problem to be solved by analysing the MMC's arm power and SM capacitor voltage ripple, categorizing their main frequency components. The main approaches introduced in the literature to extend MMC operation to low frequencies were critically reviewed and assessed. Some of the

approaches achieve satisfactory performance at low operating frequencies, but with unavoidable trade-offs. Further, their performance when supplying machine drives with scores of megawatts at the higher limit of the MV range, is problematic.

Chapter 4 represents the major contribution of the thesis, proposing a novel power decoupling scheme for MMC-fed drives for reliable low frequency operation. The concept behind the proposed approach is first illustrated, then applied to the MMC in four different configurations. Mathematical derivations describing the performance of the proposed MMC configurations with power decoupling were provided. Simulation and experimental verification confirmed the effectiveness of the proposed concept. Several assessments were undertaken to quantify the features, advantages, and shortcomings of the proposed approach.

Chapter 5 addressed MMC application for MV multiphase drives, presenting reduced MMC structures for six-phase machines to alleviate the six-phase drive complexity, size, and cost. Starting from the readily established dual three-phase MMC, reduced six-phase MMC topologies were developed and their performance was assessed. To avoid performance trade-offs commonly associated with converters with reduced component count, a novel six-phase MMC-based converter was proposed, without any performance compromise, and was verified through simulation and experimentation.

The contributions of this thesis are summarized as follows:

- Reviewing the state-of-the-art multilevel converter topologies for MV machine drives application, quantifying their advantages and shortcomings in the light of industrial MV drives market interest.
- Mathematically investigating the MMC challenge as an MV adjustable-speed drive by categorizing the main frequency arm power components standing behind the large voltage fluctuations across the SM capacitors.
- Reviewing the state-of-the-art MMC topologies and control approaches to extend MMC operation to low frequencies with limited SM capacitor voltage ripple.
- Proposing an MMC ripple power decoupling approach for SM capacitor voltage ripple compensation as a comprehensive solution for MMC low-

frequency operation. The approach offers a significant reduction in the SM capacitance since the voltage fluctuations across the capacitors are reduced to a very narrow band, therefore reducing the energy stored in the converter system. Also, it eliminates the problems of capacitor voltage fluctuations in an independent operating frequency scheme. Compared to the mainstream HF circulating current injection methods, the proposed approach does not affect the arm current or the CM voltage.

- The proposed power decoupling approach is applied to the MMC topology in four different arrangements applicable to several types of machine winding layouts. The generalized *3N* DHB-assisted MMC decouples the fundamental ripple power in the MMC arms, resulting is SM capacitor voltage alternating at twice the fundamental frequency with a diminutive voltage ripple. The *3N* DHB-assisted dual MMC inherits the same performance as the generalized configuration, with the advantages of operating at half the dc-link voltage, providing lower CM voltage at the machine terminals, and offering dc-fault ride-through capability. The *4N* and *6N* DHB-assisted MMCs decouple both the fundamental and second-order ripple power in the MMC arms, resulting in a constant SM capacitor voltage with only switching-frequency ripple.
- Experimental validation of the proposed power decoupling approach with different DHB balancers allocation and undertaking assessments to quantify the pros and cons of each configuration.
- Reviewing the state-of-the-art MMC configurations with topological reduction for six-phase machine drive applications.
- Proposing a novel six-phase MMC topology with a reduced structure, namely the H9A-MMC, with a combination of HB- and FB-SMs. Unlike its predecessors with reduced structure, the H9A-MMC has the same dc-link voltage utilization as the standard six-phase MMC, with a further reduced component-count. This results in a reduction in the overall size and cost of the MMC-based six-phase drive system without compromising neither the delivered power nor the efficiency. The performance of the H9A-MMC was experimentally verified.

6.2 Future Research

This thesis proposed a class of advanced MMC designs that generally allows for reliable operation of MV high-power variable-speed drives, in addition to a feasible and more-economic implementation of MV six-phase machine drives. The following includes planned and recommended future research:

- Investigating the HF transformer design, involved in the DHB balancer, in a detailed study with the focus on core losses, losses arising from parasitic elements, and switching frequency optimization.
- Studying the several schemes proposed in the literature to realize ZCS for DAB converters for switching losses reduction, to determine which approach is the most effective and easily implemented for the DHB balancers associated with MMC ripple power decoupling.
- Examining the performance of DFB-assisted MMC for variable-speed machine drives in terms of power loss and cost, in comparison to the proposed DHB-assisted MMC.
- Investigating the design of a three-port DHB dc-dc converter with a three-winding HF transformer as an alternative implementation of the *6N* DHB-assisted MMC for decoupling CM and DM ripple power. This can achieve a 67% reduction in the employed magnetic cores and a 50% reduction in the number of DHB switching devices, compared to the *6N* DHB-assisted MMC.
- Extending the *3N* DHB-assisted dual MMC for dc-dc MV applications, since it is able to produce bipolar dc voltages at the output terminals with dc-fault ride-through capability. With the desirable characteristics inherited from both the MMC and DHB, the topology has potential for secure and flexible bidirectional dc power flow control in breaker-less MVDC applications.
- Investigating the possibility of developing additional reduced MMC topologies for multiphase machine drive applications.

References

[1] R. D. Klug and N. Klaassen, "High power medium voltage drives—innovations, portfolio, trends," *2005 European Conference on Power Electronics and Applications*, Dresden, 11-14 September 2005, pp. 10.

[2] B. Wu and M. Narimani, "High-Power Converters and AC Drives," 2nd ed., *IEEE Press*, John Wiley & Sons, Inc., Hoboken, New Jersey, 2017.

[3] S. Kouro, J. Rodriguez, B. Wu, S. Bernet and M. Perez, "Powering the Future of Industry: High-Power Adjustable Speed Drive Topologies," *IEEE Ind. Appl. Magazine*, vol. 18, no. 4, pp. 26-39, July-Aug. 2012.

[4] B. K. Bose, "Power Electronics and Motor Drives: Advances and Trends", *Academic Press*, 2006.

[5] P.K. Steimer, H.E. Gruning, J. Werninger, and S. Linder, "IGCT - a new emerging technology for high power low cost inverters," *IEEE Ind. Appl. Magazine*, vol. 5, no. 4, pp. 12–18, 1999.

[6] S. Wei, N. Zargari, Bin Wu, and S. Rizzo, "Comparison and Mitigation of Common Mode Voltage in Power Converter Topologies," *IEEE IAS 2004*, pp. 1852-1857.

[7] H. Abu-Rub, J. Holtz, J. Rodriguez and G. Baoming, "Medium-Voltage Multilevel Converters—State of the Art, Challenges, and Requirements in Industrial Applications," *IEEE Trans. Ind. Electron.*, vol. 57, no. 8, pp. 2581-2596, Aug. 2010.

[8] J. Rodriguez, J.-S. Lai, and F. Z. Peng, "Multilevel inverters: A survey of topologies, controls, and applications," *IEEE Trans. Ind. Electron.*, vol. 49, no. 4, pp. 724–738, Aug. 2002.

[9] S. Kouro *et al.*, "Recent Advances and Industrial Applications of Multilevel Converters," *IEEE Trans. Ind. Electron.*, vol. 57, no. 8, pp. 2553-2580, Aug. 2010.

[10] A. Lesnicar and R. Marquardt, "An innovative modular multilevel converter topology suitable for a wide power range," *2003 IEEE Bologna Power Tech Conference Proceedings*, Bologna, Italy, 2003, vol. 3, pp. 6.

[11] M. Saeedifard and R. Iravani, "Dynamic performance of a modular multilevel back-to-back HVDC system," *IEEE Trans. Power Del.*, vol. 25, no. 4, pp. 2903-2912, Oct. 2010.

[12] A. Antonopoulos, L. Ängquist, S. Norrga, K. Ilves, L. Harnefors, H.-P. Nee, "Modular multilevel converter AC motor drives with constant torque from zero to nominal speed," *IEEE Trans. Ind. Appl.*, vol. 50, no. 3, pp. 1982-1993, May/Jun. 2014.

[13] Siemens, "SINAMICS PERFECT HARMONY GH150" [Online]. Available: https://w3.siemens.com/drives/global/en/converter/mv-drives/pages/sinamics-gh150.aspx

[14] A. J. Korn, M. Winkelnkemper and P. Steimer, "Low output frequency operation of the Modular Multi-Level Converter," *2010 IEEE Energy Conversion Congress and Exposition*, Atlanta, GA, 2010, pp. 3993-3997.

[15] R. Baker and L. Bannister, "Electric power converter," US Patent 3,867,643, Feb. 1975.

[16] A. Nabae, I. Takahashi, and H. Akagi, "A New Neutral-point Clamped PWM inverter," *IEEE Trans. Ind. Appl.*, vol. IA-17, pp. 518-523, Sept./Oct. 1981.

[17] R. H. Baker, "Bridge Converter Circuit," U.S. Patent 4 270 163, May 1981.

[18] P. W. Hammond, "Medium Voltage PWM Drive and Method," U.S. Patent 5 625 545, Apr. 1977.

[19] F. Z. Peng and J. S. Lai, "Multilevel Cascade Voltage-source Inverter with Separate DC source," U.S. Patent 5 642 275, June 24, 1997.

[20] P. W. Hammond, "Four-quadrant AC-AC Drive and Method," U.S. Patent 6 166 513, Dec. 2000.

[21] M. F. Aiello, P. W. Hammond, and M. Rastogi, "Modular Multilevel Adjustable Supply with Series Connected Active Inputs," U.S. Patent 6 236 580, May 2001.

[22] M. F. Aiello, P. W. Hammond, and M. Rastogi, "Modular Multi-Level Adjustable Supply with Parallel Connected Active Inputs," U.S. Patent 6 301 130, Oct. 2001.

[23] J. P. Lavieville, P. Carrere, and T. Meynard, "Electronic Circuit for Converting Electrical Energy and a Power Supply Installation Making Use Thereof," U.S. Patent 5 668 711, Sept. 1997.

[24] T. Meynard, J.-P. Lavieville, P. Carrere, J. Gonzalez, and O. Bethoux, “Electronic Circuit for Converting Electrical Energy,” U.S. Patent 5 706 188, Jan. 1998.
[25] E. Cengelci, S. U. Sulistijo, B. O. Woo, P. Enjeti, R. Teoderescu and F. Blaabjerg, “A new medium-voltage PWM inverter topology for adjustable-speed drives,” *IEEE Trans. Ind. Appl*., vol. 35, no. 3, pp. 628-637, May-June 1999.
[26] F. Z. Peng, J. S. Lai, J. W. McKeever, J. VanCoevering, “A Multilevel Voltage-Source Inverter with Separate DC Sources for Static VAR Generation,” *IEEE Trans. Ind. Appl*., vol. 32, no. 5, Sept. 1996, pp. 1130-1138.
[27] L. M. Tolbert, F. Z. Peng, T. G. Habetler, “A Multilevel Converter-Based Universal Power Conditioner,” *IEEE Trans. Ind. Appl*., vol. 36, no. 2, Mar./Apr. 2000, pp. 596-603.
[28] G. P. Adam, O. Anaya-Lara, G. M. Burt, S. J. Finney, and B. W. Williams, “Comparison between Two VSC-HVDC transmission technologies: Modular and neutral point clamped multilevel converter,” *35th Annual Conference of IEEE Industrial Electronics (IECON)*, Nov. 2009.
[29] L. M. Tolbert and F. Z. Peng, “Multilevel converters as a utility interface for renewable energy systems,” *2000 Power Engineering Society Summer Meeting*, Seattle, WA, 2000, vol. 2, pp. 1271-1274.
[30] L. M. Tolbert, F. Z. Peng, and T. G. Habetler “Multilevel Converters for Large Electric Drives,” *IEEE Trans. Ind. Appl.*, vol. 35, no. 1, Jan/Feb. 1999, pp. 36-44.
[31] S. Du, A. Dekka, B. Wu, N. Zargari, “Modular Multilevel Converters: Analysis, Control, and Applications,” *IEEE Press*, Wiley, 2018.
[32] Q. Tu, Z. Xu, H. Huang, J. Zhang, “Parameter design principle of the arm inductor in modular multilevel converter based HVDC,” *2010 International Conference on Power System Technology (POWERCON)*, pp.1-6, 2010.
[33] Q. Tu, Z. Xu, and L. Xu, “Reduced switching-frequency modulation and circulating current suppression for modular multilevel PWM converters,” *IEEE Trans. Power Del*., Vol. 26, No. 3, pp. 2009-2017, Jul. 2011.
[34] Z. Li, P. Wang, Z. Chu, H. Zhu, Y. Luo, and Y. Li, “An inner current suppressing method for modular multilevel converters,” *IEEE Trans. Power Electron*., Vol. 28, No. 11, pp. 4873-4879, Nov. 2013.
[35] B. Jacobson, P. Karlsson, G. Asplund, L. Harbefors, and T. Jonsson, “VSC-HVDC transmission with cascaded two-level converters,” in *Proc. CIGRE2010*, Paris, France, 2010, pp. B4–B110.
[36] B. Popadic, B. Dumnic, D. Milicevic, V. Katic and Z. Corba, "Tuning methods for PI controller - Comparison on a highly modular drive," *2013 4th International Youth Conference on Energy (IYCE)*, Sio¿fok, 2013, pp. 1-6.
[37] H. Khalfalla, S. Ethni, M. Al-Greer, V. Pickert, M. Armstrong and V. T. Phan, "An adaptive proportional resonant controller for single phase PV grid connected inverter based on band-pass filter technique," *2017 11th IEEE International Conference on Compatibility, Power Electronics and Power Engineering (CPE-POWERENG)*, Cadiz, 2017, pp. 436-441.
[38] Benshaw, “M2l 3000 series medium voltage motor drive”, [Online]. Available: https://www.benshaw.com/sites/default/files/downloads/brochures/benshaw-m2l-3000 brochure.pdf
[39] Siemens, “SINAMICS SM120”, [Online]. Available: http://www.industry.siemens.com/drives/global/en/converter/mv-drives/sinamics-sm120-cm/
[40] B. Wu, Y. Lang, N. Zargari, and S. Kouro, “Power Conversion and Control of Wind Energy Systems,” 1st ed., *ser. IEEE Press Series on Power Engineering*. Hoboken, NJ: John Wiley & Sons, Inc., Jul 2011.
[41] A. Yazdani and R. Iravani, “Voltage-Sourced Converters in Power Systems,” Hoboken, NJ: John Wiley & Sons, Inc., Jan 2010.
[42] P. Vas, “Sensorless Vector and Direct Torque Control,” *Oxford Science Publications*, 1998.

[43] D. Novotny and T. Lipo, "Vector Control and Dynamics of AC-Drivers," *Oxford Science Publications*, 1996.
[44] Guo XQ, Wu WY, and Gu HR, "Phase locked loop and synchronization methods for grid interfaced converters: a review," Przegląd Elektrotechniczny (Electrical Review), Vol. 87, No. 4, Jan 2011, pp. 182-187.
[45] M. P. Kazmierkowski and L. Malesani, "Current control techniques for three-phase voltage-source PWM converters: a survey," *IEEE Trans. Ind. Electron.*, vol. 45, no. 5, pp. 691-703, Oct. 1998.
[46] S. Debnath, J. Qin and M. Saeedifard, "Control and Stability Analysis of Modular Multilevel Converter under Low-Frequency Operation," *IEEE Trans. Ind. Electron*, vol. 62, no. 9, pp. 5329-5339, Sept. 2015.
[47] J. Kolb, F. Kammerer, M. Gommeringer, and M. Braun, "Cascaded control system of the modular multilevel converter for feeding variable-speed drives," *IEEE Trans. Power Electron.*, vol. 30, no. 1, pp. 349–357, Jan. 2015.
[48] M. Spichartz, V. Staudt, A. Steimel, "Modular multilevel converter for propulsion system of electric ships," *IEEE Electric Ship Technologies Symposium (ESTS)*, 2013, pp. 237–242.
[49] J. Jung, H. Lee, and S. Sul, "Control of the modular multilevel converter for variable-speed drives," in *Proc. IEEE International Conference on Power Electronics, Drives and Energy Systems*, 16-19, Bengaluru, India, Dec. 2012, pp. 1–6.
[50] K. Wang, Y. Li, Z. Zheng, and L. Xu, "Voltage balancing and fluctuation-suppression method of floating capacitors in a new modular multilevel converter," *IEEE Trans. Ind. Electron.*, vol. 60, no. 5, pp. 1943–1954, May 2013.
[51] M. Hagiwara, I. Hasegawa and H. Akagi, "Start-Up and Low-Speed Operation of an Electric Motor Driven by a Modular Multilevel Cascade Inverter," *IEEE Trans. Ind. Appl.*, vol. 49, no. 4, pp. 1556-1565, July-Aug. 2013.
[52] Fei Wang, "Motor shaft voltages and bearing currents and their reduction in multilevel medium-voltage PWM voltage-source-inverter drive applications," *IEEE Trans. Ind. Appl.*, vol. 36, no. 5, pp. 1336-1341, Sept.-Oct. 2000.
[53] Y. Okazaki, H. Matsui, M. Hagiwara, *et al.*, "Research trends of modular multilevel cascade inverter (MMCI-DSCC)-based medium-voltage motor drives in a low-speed range," 2014 *Int. Power Electronics Conf*., Hiroshima, Japan, August 2014, pp. 1586–1593.
[54] Y. Okazaki, M. Hagiwara, and H. Akagi, "A speed-sensorless start-up method of an induction motor driven by a modular multilevel cascade inverter (MMCI-DSCC)," *IEEE Trans. Ind. Appl*., vol. 50, no. 4, pp. 2671–2680, Jul./Aug. 2014.
[55] J. Jung, H. Lee, and S.-K. Sul, "Control strategy for improved dynamic performance of variable-speed drives with modular multilevel converter," *IEEE J. Emerg. Sel. Top. Power Electron*., vol. 3, no. 2, pp. 371–380, Jun. 2015.
[56] S. Song, J. Liu, S. Ouyang and X. Chen, "An improved high-frequency common-mode voltage injection method in modular multilevel converter in motor drive application," *2018 IEEE Applied Power Electronics Conference and Exposition (APEC)*, San Antonio, TX, 2018, pp. 2496-2500.
[57] Z. Wang, J. Chen, K. Liao, J. Xiong and K. Zhang, "Review on low-frequency ripple suppression methods for MMCs for medium-voltage drive applications," *IET Power Electronics*, vol. 11, no. 15, pp. 2403-2414, 18 12 2018.
[58] A. Antonopoulos, L. Ängquist, L. Harnefors and H. P. Nee, "Optimal Selection of the Average Capacitor Voltage for Variable-Speed Drives with Modular Multilevel Converters," *IEEE Trans. Power Electron.*, vol. 30, no. 1, pp. 227-234, Jan. 2015.
[59] B. Tai, C. Gao, X. Liu, Z. Chen, "A Novel Flexible Capacitor Voltage Control Strategy for Variable-Speed Drives with Modular Multilevel Converters," *IEEE Trans. Power Electron.*, vol. 32, no. 1, pp. 128-141, Jan. 2017.

[60] B. Li *et al*., "An Improved Circulating Current Injection Method for Modular Multilevel Converters in Variable-Speed Drives," *IEEE Trans. Ind. Electron.*, vol. 63, no. 11, pp. 7215-7225, Nov. 2016.

[61] S. Du, B. Wu, K. Tian, N. R. Zargari and Z. Cheng, "An Active Cross-Connected Modular Multilevel Converter (AC-MMC) for a Medium-Voltage Motor Drive," *IEEE Trans. Ind. Electron*, vol. 63, no. 8, pp. 4707-4717, Aug. 2016.

[62] S. Du, B. Wu, N. R. Zargari and Z. Cheng, "A Flying-Capacitor Modular Multilevel Converter for Medium-Voltage Motor Drive," *IEEE Trans. Power Electron.*, vol. 32, no. 3, pp. 2081-2089, March 2017.

[63] S. Du, B. Wu and N. R. Zargari, "A Star-Channel Modular Multilevel Converter for Zero/Low-Fundamental-Frequency Operation Without Injecting Common-Mode Voltage," *IEEE Trans. Power Electron.*, vol. 33, no. 4, pp. 2857-2865, April 2018.

[64] S. Du, B. Wu and N. R. Zargari, "A Delta-Channel Modular Multilevel Converter for Zero/Low-Fundamental-Frequency Operation," *IEEE Trans. Ind. Electron.*, vol. 66, no. 3, pp. 2227-2235, March 2019.

[65] M. Vasiladiotis, N. Cherix, and A. Rufer, "Accurate capacitor voltage ripple estimation and current control considerations for grid-connected modular multilevel converters," *IEEE Trans. Power Electron.*, vol. 29, no. 9, pp. 4568–4579, Sep. 2014.

[66] L. He, K. Zhang, J. Xiong, S. Fan and Y. Xue, "Low-Frequency Ripple Suppression for Medium-Voltage Drives Using Modular Multilevel Converter with Full-Bridge Submodules," *IEEE J. Emerg. Sel. Top. Power Electron.*, vol. 4, no. 2, pp. 657-667, June 2016.

[67] B. Li, S. Zhou, D. Xu, S. J. Finney and B. W. Williams, "A Hybrid Modular Multilevel Converter for Medium-Voltage Variable-Speed Motor Drives," *IEEE Trans. Power Electron.*, vol. 32, no. 6, pp. 4619-4630, June 2017.

[68] S. Zhou, B. Li, M. Guan, X. Zhang, Z. Xu and D. Xu, "Capacitance Reduction of the Hybrid Modular Multilevel Converter by Decreasing Average Capacitor Voltage in Variable-Speed Drives," *IEEE Trans. Power Electron.*, vol. 34, no. 2, pp. 1580-1594, Feb. 2019.

[69] S. Sau, S. Karmakar and B. G. Fernandes, "Reduction of capacitor ripple voltage and current in Modular Multilevel Converter based variable speed drives," *2017 IEEE 3rd International Future Energy Electronics Conference and ECCE Asia (IFEEC 2017 - ECCE Asia)*, Kaohsiung, 2017, pp. 1451-1456.

[70] Q. Lei, Y. Liu and Y. Si, "Extreme high power density T-modular-multilevel-converter for medium voltage motor drive," *IECON 2017 - 43rd Annual Conference of the IEEE Industrial Electronics Society*, Beijing, 2017, pp. 1133-1139.

[71] Y. S. Kumar and G. Poddar, "Control of Medium-Voltage AC Motor Drive for Wide Speed Range Using Modular Multilevel Converter," *IEEE Trans. Ind. Electron.*, vol. 64, no. 4, pp. 2742-2749, April 2017.

[72] Y. S. Kumar and G. Poddar, "Medium-Voltage Vector Control Induction Motor Drive at Zero Frequency Using Modular Multilevel Converter," *IEEE Trans. Ind. Electron.*, vol. 65, no. 1, pp. 125-132, Jan. 2018.

[73] M. Guan, B. Li, S. Zhou, Z. Xu and D. Xu, "Back-to-back hybrid modular multilevel converters for ac motor drive," *IECON 2017 - 43rd Annual Conference of the IEEE Industrial Electronics Society*, Beijing, 2017, pp. 1822-1827.

[74] G. P. Adam, S. J. Finney, A. M. Massoud and B. W. Williams, "Capacitor Balance Issues of the Diode-Clamped Multilevel Inverter Operated in a Quasi Two-State Mode," *IEEE Trans. Ind. Electron*, vol. 55, no. 8, pp. 3088-3099, Aug. 2008.

[75] I. A. Gowaid, G. P. Adam, A. M. Massoud, S. Ahmed, D. Holliday and B. W. Williams, "Quasi Two-Level Operation of Modular Multilevel Converter for Use in a High-Power DC Transformer with DC Fault Isolation Capability," *IEEE Trans. Power Electron.*, vol. 30, no. 1, pp. 108-123, Jan. 2015.

[76] A. Mertens and J. Kucka, "Quasi Two-Level PWM Operation of an MMC Phase Leg with Reduced Module Capacitance," *IEEE Trans. Power Electron.*, vol. 31, no. 10, pp. 6765-6769, Oct. 2016.

[77] J. Kucka and A. Mertens, "Control for Quasi Two-Level PWM Operation of Modular Multilevel Converter," *2016 IEEE 25th International Symposium on Industrial Electronics (ISIE)*, Santa Clara, CA, 2016, pp. 448-453.

[78] J. Kucka and A. Mertens, "Improved Current Control of a Quasi-Two-Level PWM-Operated Modular Multilevel Converter," *2018 IEEE Energy Conversion Congress and Exposition (ECCE)*, Portland, OR, 2018, pp. 2948-2955.

[79] J. Kucka and A. Mertens, "Common-Mode Voltage Injection Techniques for Quasi Two-Level PWM-Operated Modular Multilevel Converters," *2018 International Power Electronics Conference (IPEC-Niigata 2018 -ECCE Asia)*, Niigata, 2018, pp. 1904-1911.

[80] C. Wang, K. Wang, Z. Zheng and Y. Li, "A New Control Strategy for Modular Multilevel Converter Operating in Quasi Two-Level PWM Mode," *2018 International Power Electronics Conference (IPEC-Niigata 2018 -ECCE Asia)*, Niigata, 2018, pp. 2386-2392.

[81] R. W. A. A. De Doncker, D. M. Divan and M. H. Kheraluwala, "A three-phase soft-switched high-power-density DC/DC converter for high-power applications," *IEEE Trans. Ind. Appl.*, vol. 27, no. 1, pp. 63-73, Jan/Feb 1991.

[82] S. Inoue and H. Akagi, "A bidirectional isolated DC–DC converter as a core circuit of the next-generation medium-voltage power conversion system," *IEEE Trans. Power Electron.*, vol. 22, no. 2, pp. 535–542, Mar. 2007.

[83] M. H. Kheraluwala and R. W. Gascoigne, "Performance characterization of a high-power dual active bridge dc-to-dc converter," *IEEE Trans. Ind. Appl.*, vol. 28, no. 6, pp. 1294–1301, Nov./Dec. 1992.

[84] F. Z. Peng, H. Li, G.-J. Su, and J. S. Lawler, "A new ZVS bidirectional dc–dc converter for fuel cell and battery application," *IEEE Trans. Power Electron.*, vol. 19, no. 1, pp. 54–65, Jan. 2004.

[85] E. R. Ronan, S. D. Sudhoff, S. F. Glover and D. L. Galloway, "A power electronic-based distribution transformer," *IEEE Trans. Power Del.*, vol.17, no.2, pp.537-543, Apr. 2000.

[86] A. Zafeiropoulos, A. Antonopoulos and J. R. Svensson, "An MMC-based topology using DHB power channels for load balancing in 50 Hz railway applications," *2017 IEEE Energy Conversion Congress and Exposition (ECCE)*, Cincinnati, OH, 2017, pp. 83-90.

[87] A. Somani, R. Gupta, K. Mohapatra, and N. Mohan, "On the causes of circulating currents in PWM drives with open-end winding ac machines," *IEEE Trans. Ind. Electron*., vol. 60, no. 9, pp. 3670-3678, Sep. 2013.

[88] M. R. Baiju, K. K. Mohapatra, R. S. Kanchan, and K. Gopakumar, "A dual two-level inverter scheme with common mode voltage elimination for an induction motor drive," *IEEE Trans. Power Electron*., vol. 19, no. 3, pp. 794–805, May 2004.

[89] N. Bodo, M. Jones, and E. Levi, "A Space vector PWM with common mode elimination for open-end winding five-phase drives with a single dc supply," *IEEE Trans. Ind. Electron*., vol. 61, no. 5, pp. 2197- 2207, May 2014.

[90] P. Rajeevan, K. Sivakumar, K. Gopakumar, C. Patel, and H. Abu-Rub, "A nine-level inverter topology for medium-voltage induction motor drive with open-end stator winding," *IEEE Trans. Ind. Electron*., vol. 60, no. 9, pp. 3627-3636, Sep. 2013.

[91] M. Darijevic, M. Jones, and E. Levi, "An open-end winding four-level five-phase Drive," *IEEE Trans. Ind. Electron*., vol. 63, no. 1, pp. 538-549, Jan. 2016.

[92] H. Stemmler and P. Guggenbach, "Configurations of high-power voltage source inverter drives," in *Proc. 5th Eur. Conf. Power Electron. Appl.*, 1993, vol. 5, pp. 7–14.

[93] K. Corzine, M. Wielebski, F. Peng, and J. Wang, "Control of cascaded multilevel inverters," *IEEE Trans. Power Electron.*, vol. 19, no. 3, pp. 732–738, May 2004.

[94] V. Somasekhar, K. Gopakumar, M. R. Baiju, K. Mohapatra, and L. Umanand, "A multilevel inverter system for an induction motor with open-end windings," *IEEE Trans. Ind. Electron.*, vol. 52, no. 3, pp. 824– 836, Jun. 2005.

[95] R. S. Kanchan, P. N. Tekwani, and K. Gopakumar, "Three-level inverter scheme with common mode voltage elimination and dc link capacitor voltage balancing for an open-end winding induction motor drive," *IEEE Trans. Power Electron.*, vol. 21, no. 6, pp. 1676–1683, Nov. 2006.

[96] G. Mondal, K. Gopakumar, P. N. Tekwani, and E. Levi, "A reduced-switch count five-level inverter with common-mode voltage elimination for an open-end winding induction motor drive," *IEEE Trans. Ind. Electron.*, vol. 54, no. 4, pp. 2344–2351, Aug. 2007.

[97] A. Edpuganti and A. K. Rathore, "Optimal Pulse-Width Modulation for Common-Mode Voltage Elimination Scheme of Medium-Voltage Modular Multilevel Converter-Fed Open-End Stator Winding Induction Motor Drives," *IEEE Trans. Ind. Electron.*, vol. 64, no. 1, pp. 848-856, Jan. 2017.

[98] M. Leibl, G. Ortiz and J. W. Kolar, "Design and Experimental Analysis of a Medium-Frequency Transformer for Solid-State Transformer Applications," *IEEE J. Emerg. Sel. Topics Power Electron.*, vol. 5, no. 1, pp. 110-123, March 2017.

[99] G. Ortiz, H. Uemura, D. Bortis, J. W. Kolar and O. Apeldoorn, "Modeling of Soft-Switching Losses of IGBTs in High-Power High-Efficiency Dual-Active-Bridge DC/DC Converters," *IEEE Trans. Electron. Devices*, vol. 60, no. 2, pp. 587-597, Feb. 2013.

[100] G. Ortiz, M. G. Leibl, J. E. Huber and J. W. Kolar, "Design and Experimental Testing of a Resonant DC–DC Converter for Solid-State Transformers," *IEEE Trans. Power Electron.*, vol. 32, no. 10, pp. 7534-7542, Oct. 2017.

[101] G. Ortiz, M. Leibl, J. W. Kolar and O. Apeldoorn, "Medium frequency transformers for solid-state-transformer applications — Design and experimental verification," *2013 IEEE 10th International Conference on Power Electronics and Drive Systems (PEDS)*, Kitakyushu, 2013, pp. 1285-1290.

[102] G. Ortiz, J. Biela, D. Bortis and J. W. Kolar, "1 Megawatt, 20 kHz, isolated, bidirectional 12kV to 1.2kV DC-DC converter for renewable energy applications," *The 2010 International Power Electronics Conference - ECCE ASIA -*, Sapporo, 2010, pp. 3212-3219.

[103] ABB HiPak 5SNA 1200G450350. [Online]. Available: https://library.e.abb.com/public/afe3c7e548fe45ff8e4506203449f363/5SNA%201200G450350_5SYA%201415-04%2003-2016.pdf.

[104] ABB HiPak 5SNA 0650J450300. [Online]. Available: https://library.e.abb.com/public/3292e84562f947b1aea83bdb9c408df8/5SNA%200650J450300_5SYA%201598-05%2005-2016.pdf.

[105] EPOCS Product Brief 2009, Power Capacitors [Online]. Available: http://www.rollay.com.cn/ImgUpload/Articleimage/201007091740522.pdf.

[106] ETHZ MegaCube project. [Online]. Available: https://www.pes.ee.ethz.ch/uploads/tx_ethpublications/01_MegaCube_Trafo_Digest_APEC2013.pdf.

[107] D. Graovac and M. Pürschel, "IGBT power losses calculation using the datasheet parameters," [Online]. Available: http://application-notes.digchip.com/070/70-41484.pdf.

[108] E. Levi, "Advances in Converter Control and Innovative Exploitation of Additional Degrees of Freedom for Multiphase Machines," *IEEE Trans. Ind. Electron*., vol. 63, no. 1, pp. 433-448, Jan. 2016.

[109] F. Barrero and M. J. Duran, "Recent advances in the design, modeling and control of multiphase machines—Part 1," *IEEE Trans. Ind. Electron*., vol. 63, no. 1, pp. 449–458, Jan. 2016.

[110] M. J. Duran and F. Barrero, “Recent advances in the design, modeling and control of multiphase machines—Part 2,” *IEEE Trans. Ind. Electron*., vol. 63, no. 1, pp. 459–468, Jan. 2016.

[111] E. Levi, F. Barrero and M. J. Duran, “Multiphase machines and drives - Revisited,” *IEEE Trans. Ind. Electron*., vol. 63, no. 1, pp. 429-432, Jan. 2016.

[112] P. T. Norton and P. E. Thompson, “The naval electric ship of today and tomorrow,” in *Proc. 3rd All Electric Ship Symp.*, Paris, France, Oct. 2000, pp. 80–86.

[113] I. Gonzalez-Prieto, M. Duran, J. Aciego, C. Martin, and F. Barrero, “Model predictive control of six-phase induction motor drives using virtual voltage vectors,” *IEEE Trans. Ind. Electron*., vol. 65, no. 1, pp. 27–37, Jan. 2018.

[114] Y. Hu, Z. Q. Zhu, and M. Odavic, “Comparison of two-individual current control and vector space decomposition control for dual three-phase PMSM,” *IEEE Trans. Ind. Appl*., vol. 53, no. 5, pp. 4483–4492, Sep./Oct. 2017.

[115] F. Baneira, J. Doval-Gandoy, A. Yepes, O. Lopez, and D. Perez-Estevez, “Control strategy for multiphase drives with minimum losses in the full torque operation range under single open-phase fault,” *IEEE Trans. Power Electron*., vol. 32, no. 8, pp. 6275–6285, Aug. 2017.

[116] M. J. Duran, E. Levi, and F. Barrero, “Multiphase electric drives: Introduction,” in *Wiley Encyclopedia of Electrical and Electronics Engineering*. Hoboken, NJ, USA: Wiley, 2017.

[117] E. Levi, R. Bojoi, F. Profumo, H. A. Toliyat, and S. Williamson, “Multiphase induction motor drives – A technology status review,” *IET Electr. Power Appl.*, vol. 1, no. 4, pp. 489–516, Jul. 2007.

[118] W. Cao, B. C. Mecrow, G. J. Atkinson, J. W. Bennett, and D. J. Atkinson, “Overview of electric motor technologies used for more electric aircraft (MEA),” *IEEE Trans. Ind. Electron.*, vol. 59, no. 9, pp. 3523–3531, Sep. 2012

[119] D. Hadiouche, H. Razik, and A. Rezzoug, “On the modeling and design of dual-stator windings to minimize circulating harmonic currents for vsi fed ac machines,” *IEEE Trans. on Ind. Appl.*, vol. 40, pp. 506–515, Mar. 2004.

[120] R. H. Nelson and P. C. Krause, “Induction machine analysis for arbitrary displacement between multiple winding sets,” *IEEE Trans. Power App. Syst.*, vol. PAS-93, pp. 841–848, May/June 1974

[121] W. N. W. A. Munim, M. Duran, H. S. Che, M. Bermudez, I. Gonzalez-Prieto, and N. A. Rahim, “A unified analysis of the fault tolerance capability in six-phase induction motor drive,” *IEEE Trans. Power Electron*., vol. 32, no. 10, pp. 7824–7836, 2016.

[122] A. Pantea, A. Yazidi, F. Betin, M. Taherzadeh, S. Carrière, H. Henao, and G. Capolino, “Six-phase induction machine model for electrical fault simulation using circuit-oriented method,” *IEEE Trans. Ind. Electron*., vol. 63, no. 1, pp. 494-503, Jan. 2016.

[123] I. Gonzalez-Prieto, M. J. Duran, J. J. Aciego, C. Martin and F. Barrero, “Model Predictive Control of Six-Phase Induction Motor Drives Using Virtual Voltage Vectors,” *IEEE Trans. Ind. Electron*., vol. 65, no. 1, pp. 27-37, Jan. 2018.

[124] A. C. N. Maia, C. B. Jacobina, N. B. de Freitas and I. R. F. M. P. da Silva, “Open-End Multilevel Six-Phase Machine Drive System with Five Three-Leg Converters,” *IEEE Trans. Ind. Appl.*, vol. 53, no. 3, pp. 2271-2281, May-June 2017.

[125] E. Ariff, O. Dordevic, and M. Jones, “A space vector PWM technique for a three-level symmetrical six phase drive,” *IEEE Trans. Ind. Electron*., vol. 64, no. 11, pp. 8396-8405, Nov. 2017.

[126] M. S. Diab, A. A. Elserougi, A. S. Abdel-Khalik, A. M. Massoud and S. Ahmed, “A Nine-Switch-Converter-Based Integrated Motor Drive and Battery Charger System for EVs Using Symmetrical Six-Phase Machines,” *IEEE Trans. Ind. Electron.*, vol. 63, no. 9, pp. 5326-5335, Sept. 2016.

[127] A. S. Abdel-Khalik, A. M. Massoud and S. Ahmed, "Effect of DC-Link Voltage Limitation on Postfault Steady-State Performance of Asymmetrical Six-Phase Induction Machines," *IEEE Trans. Ind. Electron*., vol. 65, no. 9, pp. 6890-6900, Sept. 2018.

[128] A. Iqbal, S. Moinuddin, M. R. Khan, S.M. Ahmed, and H. AbuRub, "A novel three-phase to five-phase transformation using a special transformer connection," *IEEE Trans. Power Delivery*, vol. 25, no. 3, pp. 1637-1644, 2010.

[129] Xusheng Chen, "Three-phase/six-phase conversion autotransformers," *IEEE Trans. Power Delivery*, vol. 18, no. 4, pp. 1554-1561, Oct. 2003.

[130] S. Moinoddin, A. Iqbal, H. Abu-Rub, M.R. Khan, and S.M. Ahmed, "Three-phase to seven-phase power converting transformer," *IEEE Trans. Energy Conver*., vol. 27, no. 3, pp. 757-766, 2012.

[131] R. O. C. Lyra and T. A. Lipo, "Torque density improvement in a six-phase induction motor for space vector PWM control," in *Conf. Rec. IEEE-IAS Annu. Meeting*, 2001, pp. 1779–1786.

[132] D. Novotny and T. A. Lipo, "Vector Control and Dynamics of AC Drives," Oxford, U.K.: Clarendon, 2000.

[133] R. Bojoi, M. Lazzari, F. Profumo and A. Tenconi, "Digital field-oriented control for dual three-phase induction motor drives," *IEEE Trans. Ind. Appl.*, vol. 39, no. 3, pp. 752-760, May-June 2003.

[134] M. I. Daoud, A. Massoud, A. Abdel-Khalik and S. Ahmed, "An asymmetrical six-phase induction machine-based flywheel energy storage system using modular multilevel converters," *2016 19th International Conference on Electrical Machines and Systems (ICEMS)*, Chiba, 2016, pp. 1-6.

[135] M. S. Diab, B. W. Williams, D. Holliday, A. M. Massoud and S. Ahmed, "A modular multilevel converter with isolated energy-balancing modules for MV drives incorporating symmetrical six-phase machines," *2017 IEEE Energy Conversion Congress and Exposition (ECCE)*, Cincinnati, OH, USA, 2017, pp. 2715-2722.

[136] H. W. V. D. Broeck and J. D. V. Wyk, "A comparative investigation of a three-phase induction machine drive with a component minimized voltage-fed inverter under different control options," *IEEE Trans. Ind. Appl*., vol. IA-20, no. 2, pp. 309–320, Mar. 1984.

[137] R. Wang, J. Zhao, and Y. Liu, "A comprehensive investigation of four-switch three-phase voltage source inverter based on double fourier integral analysis," *IEEE Trans. Power Electron.*, vol. 26, no. 10, pp. 2774–2787, Oct. 2011.

[138] G.-T. Kim and T. A. Lipo, "Vsi-pwm rectifier/inverter system with a reduced switch count," in *Proc. IEEE-IAS Annu. Meeting*, 1995, pp. 2327–2332.

[139] R. L. A. Ribeiro, C. B. Jacobina, E. R. C. da Silva, and A. M. N. Lima, "ac/ac converter with four switch three phase structures," in *Proc. IEEE PESC*, 1996, pp. 134–139.

[140] C. B. Jacobina, I. S. de Freitas, C. R. da Silva, M. B. de Rossiter Correa and E. R. C. da Silva, "Reduced Switch-Count Six-Phase AC Motor Drive Systems Without Input Reactor," *IEEE Trans. Ind. Electron.*, vol. 55, no. 5, pp. 2024-2032, May 2008.

[141] C. B. Jacobina, I. S. de Freitas, E. R. C. da Silva, A. M. N. Lima, and R. L. A. Ribeiro, "Reduced switch count DC-link AC–AC five-leg converter," *IEEE Trans. Power Electron*., vol. 21, no. 5, pp. 1301–1310, Sep. 2006.

[142] T. Kominami and Y. Fujimoto, "A novel nine-switch inverter for independent control of two three-phase loads," in *Proc. IEEE Ind. Appl. Conf.*, New Orleans, LA, USA, 2007, pp. 2346–2350.

[143] M. Jones, S. N. Vukosavic, D. Dujic, E. Levi, and P. Wright, "Five-leg inverter PWM technique for reduced switch count two-motor constant power applications," *IET Electr. Power Appl.*, vol. 2, no. 5, pp. 275–287, Sep. 2008.

[144] M. S. Diab, A. Elserougi, A. Massoud, A. Abdel-khalik, and S. Ahmed, "A four-switch three-phase SEPIC-based inverter," *IEEE Trans. Power Electron.*, vol. 30, no. 9, pp. 4891–4905, Sep. 2015.

[145] A. Elserougi, I. Abdelsalam, A. Massoud, and S. Ahmed, "Four-Arm Three-Phase Modular Multilevel Converter (4A-TPMMC)," *Journal of Electric Power Components and Systems*, 45:17, 1951-1961,

[146] A. A. Elserougi, A. S. Abdel-Khalik, A. M. Massoud and S. Ahmed, "A nine-arm modular multilevel converter (9A-MMC) for six-phase medium voltage motor drives," Industrial Electronics Society, *IECON 2015-41st Annual Conference of the IEEE*, vol., no., pp.1735-1740, 9-12 Nov. 2015.

[147] T. Kominami and Y. Fujimoto, "A novel nine-switch inverter for independent control of two three-phase loads," in *Proc. IEEE Ind. Appl. Soc. Annu. Conf. (IAS)*, 2007, pp. 2346–2350.

[148] *ABB LoPak 5SNG 0450R170300*, [online] Available: https://library.e.abb.com/public/a526a0fcfab646a19418fd64b88d1b00/5SNG%200450R170300%205SYA%20145101%20201705%20preliminary.pdf.

[149] *ABB LoPak* 5SNG 0225R170300, [online] Available: https://library.e.abb.com/public/a40ce97a08574633b387b60bd3a3431d/5SNG%200225R170300%205SYA%20145300%20201705%20preliminary.pdf.

[150] *EPOCS Product Brief 2009. Power Capacitors*, (2009), [online] Available:http://www.rollay.com.cn/ImgUpload/Articleimage/20100701740522.pdf.

[151] *EPOCS Product Brief 2016. Power Capacitors*, (2016), [online] Available: https://en.tdk.eu/inf/20/50/ds/B2562_.pdf.

Appendix A

Experimental Rig

This appendix presents the experimental prototype structure, detailing the employed hardware components and DSP software environment.

A.1 Hardware Structure

The experimental test rig can be divided into three functional sub-groups:

- Power circuitry
- Control circuitry
- Recording devices

A photograph for the overall experimental setup is shown in Fig. A.1, where employed components are labelled and defined as listed in Table A.1.

Table A.1: Components of experimental setup

Component Number	Power Circuitry (P)	Control Circuitry (C)	Recording devices (R)
1	DC power supply	Digital Signal Processor	Digital oscilloscope
2	DC link capacitor	Voltage transducer circuit	Differential voltage probe
3	MMC arm with 3 SMs	Current transducer circuit	Current probe
4	Arm inductor	Gate drive circuit	CAN bus module
5	SM capacitor	Dead time generator circuit	
6	Filtering capacitor	Biasing DC supply	
7	DHB converter		
8	Resistive Load		
9	Inductive Load		
10	Induction machine		

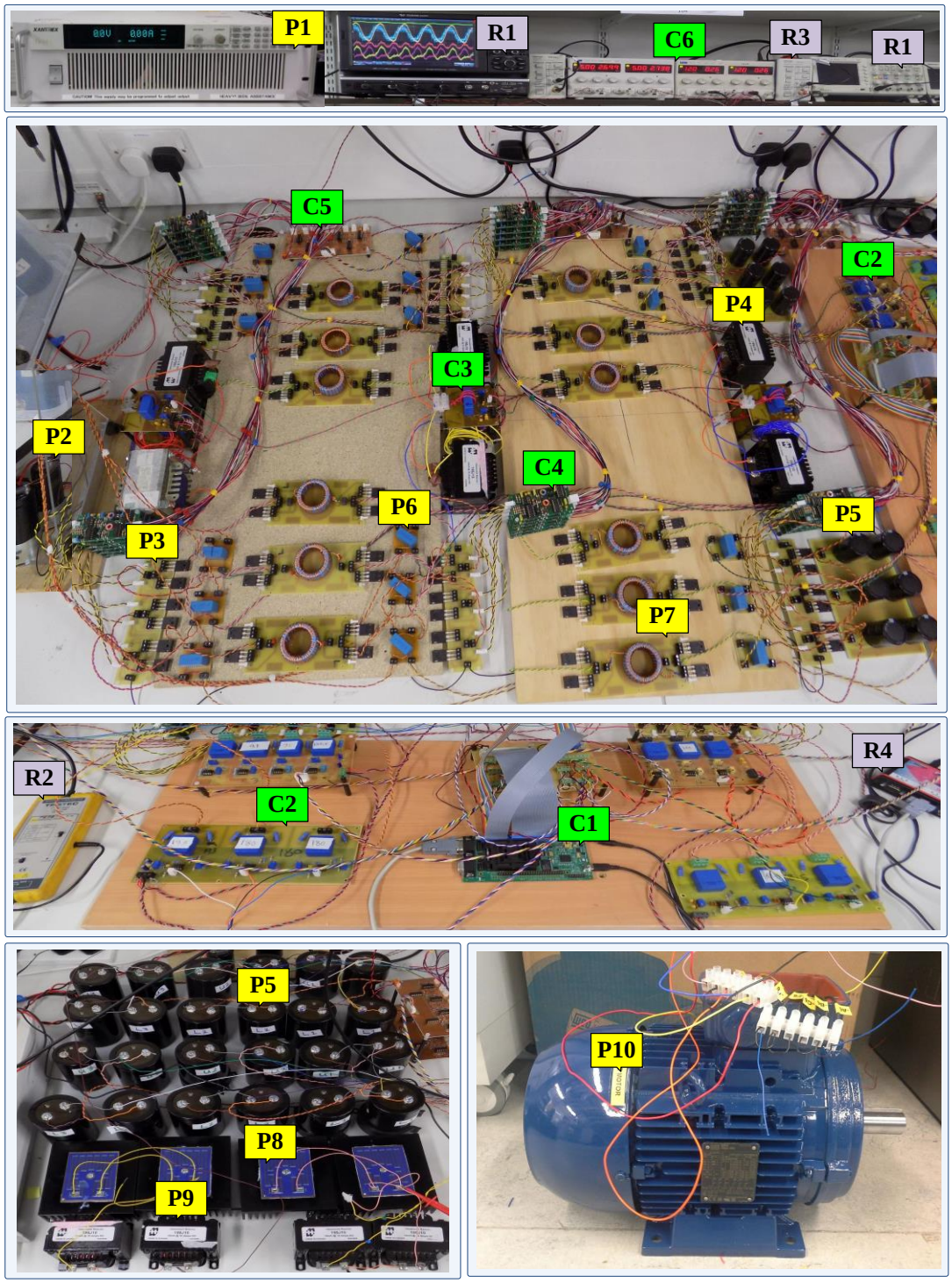

Fig. A.1 Experimental setup.

A1.1 Power Circuitry

The main components comprising the setup power circuits are briefed in this subsection.

A. MMC arm

Each MMC arm is comprised by 3 SMs. The switching devices are STGW38IH130D IGBTs manufactured by ST MICROELECTRONICS, and are rated at 1.3 kV and 63 A, with 250 W power dissipation. HB-SMs (Fig. A.2a) are used to verify the DHB-assisted MMC's performance, while FB-SMs (Fig. A.2b) are used for the H9A-MMC topology.

B. DHB converter

The DHB converter is comprised by 4 IGBTs, with the same parameters as those used in MMC SMs, and an HF transformer. The DHB circuit is shown in Fig. A.3. The HF transformer uses a nano-crystalline core which is favorable for HF operation due to its high core permeability, high magnetizing inductance, low losses, and near square hysteresis loop. The selected transformer core is MAGNETEC GmbH M-011-04 YM. The core has a relative permeability of 30000 at 10 kHz, while the core cross-sectional area is 0.73 cm^2. Core dimensions and other specifications are outlined in the datasheet shown in Fig. A.4, while transformer parameters are listed in Table A.2.

Table A.2: HF transformer parameters

Power rating	1.5 kVA
Primary side voltage	200 V
Secondary side voltage	200 V
Primary turns	30
Secondary turns	30
Turns ratio	1
Leakage inductance	14.63 μH
Parasitic winding resistance	0.7 Ω

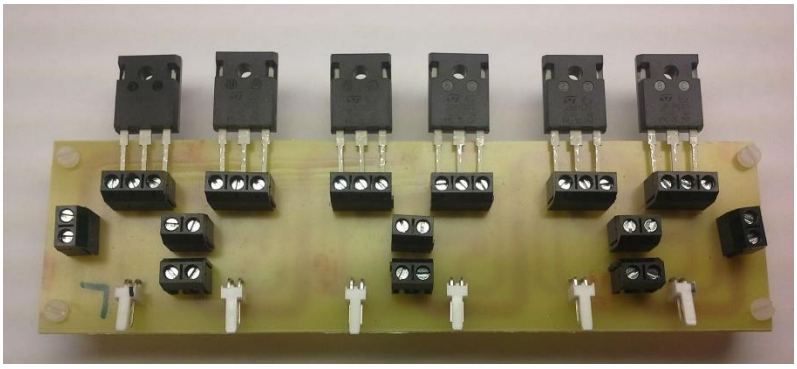

(a)

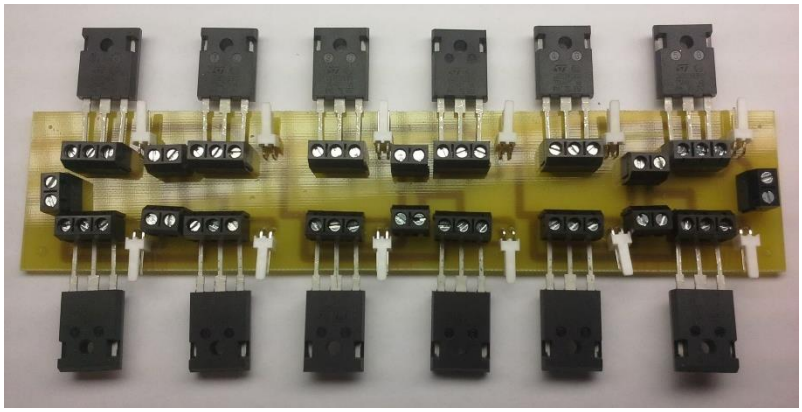

(b)

Fig. A.2 MMC arm with 3 SMs using: (a) HF-SMs and (b) FB-SMs.

Fig. A.3 DHB converter circuit with nano-crystalline core-based HF transformer.

FORM Identifier: F 108 Revision: 04 Page: 1/1	Product specification for inductive components	MAGNETEC GmbH Industriestrasse 7 D-63505 Langenselbold

☐

Client:	MAGNETEC GmbH	Magnetec P/N:	M-011	Magnetec A/N:	12023
Client's P/N:	/	PS Index:	04	PS Revision:	05
Subject:	EMC WANDLER			Type:	E

1. Mechanical Outline

Nominal core dimensions:

50 x 40 x 20

Finished product dimensions:

OD ≤ 52,3
ID ≥ 37,1
H ≤ 22,3

[dimensions] = mm

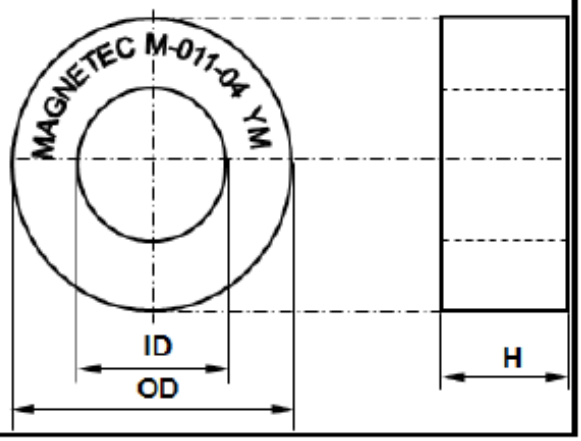

2. Core data (nominal values)

Core material:	NANOPERM®	L_{Fe} = 14,08 cm	A_{Fe} = 0,73 cm²
Permeability level		@ frequency	@ H peak
	30 000	10 kHz	3,0 mA/cm

3. Inspection values

	Measured value	Measurement limits	Frequency	leff x N [mA x turn]
	AL [µH]	12,6 - 28,4	10 kHz	30
	AL [µH]	6,3 - NA	100 kHz	30

4. Core finishing

Type:	Epoxy coated
Marking:	MAGNETEC M-011-04 YM (YM = Year/Month), acc. to IEC 60062 6.1.1
Packaging:	15 pcs. per layer; 4 layers per carton box ; PU = 60 pcs.

5. Comments:

Index / Revision	Alteration	Date
03 / 00	Sample	03.11.1999
04 / 00	Product Specification	30.03.2001
04 / 01	PU = 15 pcs.; AL = 13,6 - 28,4 µH	09.07.2001
04 / 02	PU = 45 pcs.	20.11.2002
04 / 03	PU = 60 pcs.; AL = 12,6 - 28,4 µH	29.07.2004
04 / 04	New format	20.06.2007
04 / 05	Define 100kHz lower limit	26.08.2014

Created:	Z. Palánki 26.08.2014	Approved (Techn):	F. Zámborszky 04.09.2014	Approved (Quality):	J. Gulyás 04.09.2014	Released:	T. Trupp 05.09.2014

Fig. A.4 Datasheet of the employed nano-crystalline core.

A1.2 Control Circuitry

Control circuits are mainly powered by +5 V and ±15 V biasing dc supplies. They consist of a digital signal processor (DSP) acting as the main system controller, voltage and current transducer circuits, dead time generator circuits, and gate drive circuits.

A. DSP

The DSP is the main system controller, reading the actual voltage and current signals from the measurement devices. The analogue signals are sampled and converted to digitally coded numbers using the embedded analogue to digital conversion. Based on the feedback signals, the DSP controls the overall system operation according to the loaded flash memory program. Thus, the controller must have some features as fast calculating processor, sufficient storage memory, compatible and fast analogue to digital converters, and easy programming packages. For these reasons, Texas Instrument TMS320F28335 floating point DSP is used, with the main task is to generate the PWM signals for gate drive circuits that operate the switching devices of the power converters. The DSP output port is compatible with the gate drive input voltages and currents; thus the TMS320F28335 DSP does not require additional interfacing circuits. The measurement transducers are designed to have voltages and currents within DSP read range. The DSP support real-time monitoring and control by sending the data to addressed memory in the RAM and display it by Code Composer Studio V.3.3 software. One of the most important features of the TMS320F28335 DSP is that it can be programmed either by C, C++ coding or MATLAB SIMULINK. This eases the programming process when high level programming is required. In this thesis, three synchronized TMS320F28335 DSPs are used in parallel to control the experimental setup. Thesis control algorithms are coded using MATLAB SIMULINK graphical programing. The TMS320F28335 DSP has the following main features**:**

- High-Performance Static CMOS Technology
- High-Performance 32-Bit CPU
    - IEEE-754 Single-Precision Floating-Point Unit (FPU)

- Harvard Bus Architecture
- 150 MHz (6.67 ns Cycle Time)
- Code-Efficient (in C/C++ and Assembly)
- Fast Interrupt Response and Processing

- Memory
  - 256K data flash
  - 34K on-Chip SARAM
  - 8K x 16 Boot ROM
  - 16K instruction cache
- Clock and System Control
  - Dynamic PLL Ratio Changes Supported
  - On-Chip Oscillator
  - Watchdog Timer Module
- 128-Bit Security Key/Lock
  - Protects Flash/OTP/RAM Blocks
  - Prevents Firmware Reverse Engineering
- Enhanced Control Peripherals
  - Up to 18 PWM Outputs
  - Up to 6 HRPWM Outputs with 150 ps MEP Resolution
  - Up to 6 Event Capture Inputs
  - Up to 2 Quadrature Encoder Interfaces
  - Up to 8 x 32-Bit Timers (6 for eCAPs and 2 for eQEPs)
- Three 32-Bit CPU Timers
- Serial Port Peripherals
  - Up to 2 CAN Modules
  - Up to 3 SCI (UART) Modules
  - Up to 2 McBSP Modules (Configurable as SPI)
  - One SPI Module
  - One Inter-Integrated-Circuit (I2C) Bus
- Analogue to Digital Converters (ADC)
  - 12-Bit ADC, 16 Channels
  - 80 ns Conversion Rate

- 2 x 8 Channel Input Multiplexer

- Digital Inputs and Outputs
  - Up to 88 Individually Programmable, Multiplexed GPIO Pins With Input Filtering
- Emulation Features
  - Analysis and Breakpoint Functions
  - Real-Time Debug via Hardware
- Development Support Includes
  - ANSI C/C++ Compiler/Assembler/Linker
  - Code Composer Studio IDE
  - Digital Motor Control and Digital Power Software Libraries
- Temperature Options:
  - –40°C to 125°C

B. Voltage and current transducer circuits

The following transducer circuit designs serve for measuring MMC SM capacitor voltages and arm currents necessary for capacitor voltage balancing, DHB converter power flow control, and circulating current control.

1) Voltage transducer circuit

This circuit is used for MMC SM capacitor voltage measurement, feeding the measured signal to the DSP ADC module. The circuit scales the input voltage and adds a dc-bias to maintain the output voltage compatible with ADC signal level. The circuit implements a Hall effect sensing device LEM (LV 25-P) with voltage sensing range of 0–500V, with high frequency bandwidth, for dc and ac voltage measurements. A schematic diagram for the voltage transducer circuit is shown in Fig. A.5.

2) Current transducer circuit

MMC arm currents are measured and sent to the DSP for capacitor voltage balancing. A Hall effect current sensing LEM (LA 55-P) is used, which has high accuracy and optimized response time. The Hall effect sensor fully isolates the sensed signals from the real current signals. The sensing range is 0–50 A and the

frequency range is from dc to 100 kHz. The transducer output voltage is level-shifted and scaled using signal conditioning circuit. The schematic diagram of the current sensing signal conditioning circuit is shown in Fig. A.6. A photograph for the printed circuit board for both voltage and current transducer circuits is shown in Fig. A.7.

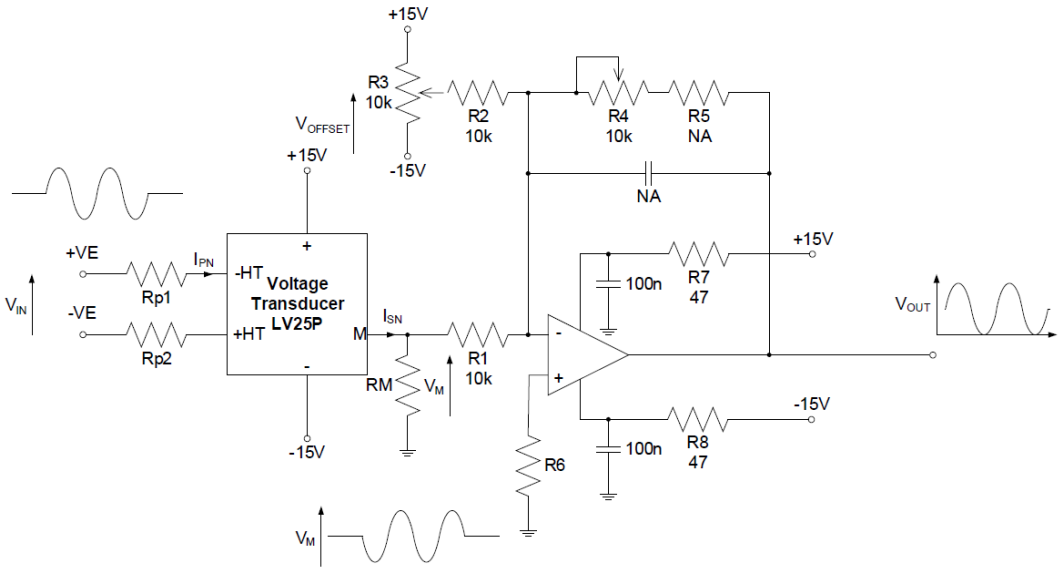

Fig. A.5 Schematic diagram of voltage transducer circuit.

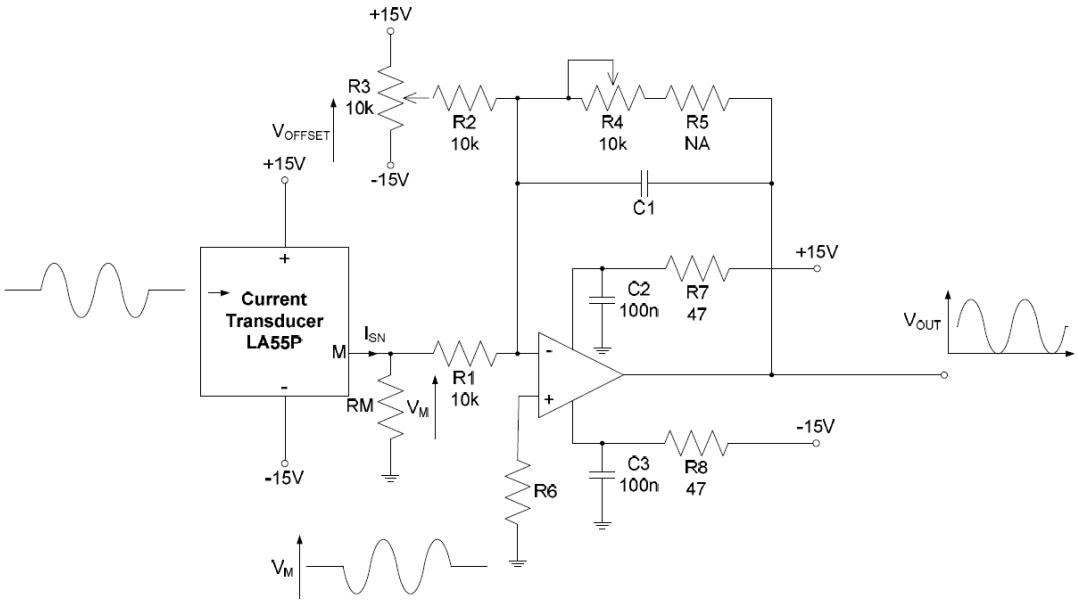

Fig. A.6 Schematic diagram of current transducer circuit.

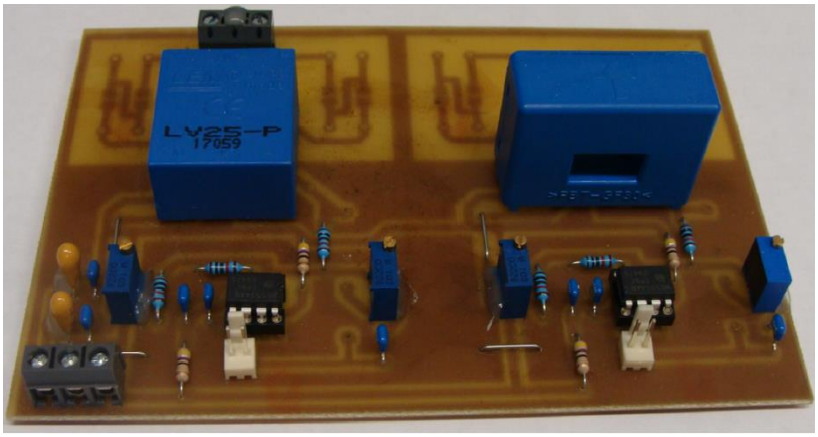

Fig. A.7 Voltage (left) and current (right) transducer circuits.

C. Gate drive circuits

The gate drive circuit implemented in the experimental rig is shown in Fig. A.8, with the circuit diagram depicted in Fig. A.9. The main functions of this circuit are:

- Step up the 3.3 V TTL PWM signals from the DSP to the 15 V CMOS level for IGBT gate signals.
- Provide galvanic isolation between the common-grounded PWM DSP signals and the IGBT common points.
- Source enough current for the IGBTs to be switched on. The maximum current that can be drawn from the DSP is in the range of mille-amperes, while the IGBT gate terminal may require a large instantaneous spike of current to enable fast charging of the gate capacitance, and hence the IGBT turn on.

The first and second functions are realised using two HF transformers in the gate drive circuit. The first transformer magnetically isolates the PWM signal, boosting it from 3.3 V to 15 V. The voltage boost is performed by 'NANDing' the PWM signal with an HF clock signal (produced from an on-chip oscillator), inverting, passing through the first transformer with 1:3 step up turns ratio, and finally rectifying it to restore the original PWM signal at 15 V. Likewise, the second transformer steps up the 3.3 V supply voltage from the DSP to 15 V to bias the necessary chips on the transformer high voltage side. IGBT gate drive current is drawn through the latter transformer. Due to the magnetic isolation offered by the gate drive circuit, only one 5 V supply is needed for all IGBTs. However, this supply should be capable of withstanding the total switching current of all driven IGBTs. The gate drive circuit specifications are listed in Table A.3.

Table: A.3 Gate drive circuit parameters

Output voltage	15 V
Output current	±3 A
Maximum supply voltage	5 V
Maximum signal frequency	75 kHz
$t_{d\ on}$	60 ns
$t_{d\ off}$	60 ns

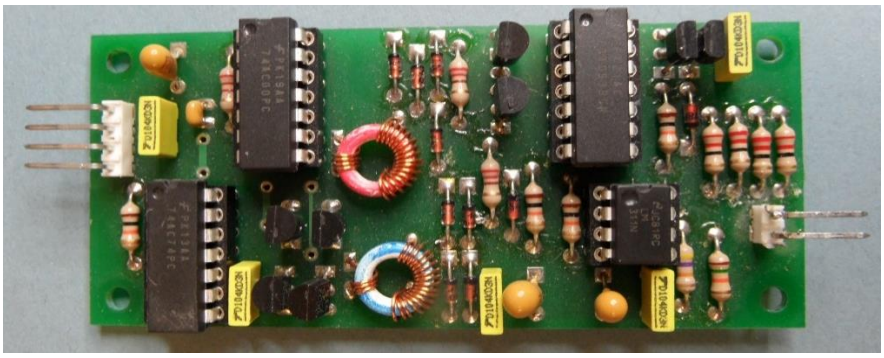

Fig. A.8 Gate drive circuit.

D. Dead time generator circuit

Dead time generation is realized using a hardware approach that avoids any conduction overlap in the PWM switching signals driving two IGBTs in one MMC SM or in each DHB converter side. The dead time is obtained based on the time constant of an *RC* circuit interfaced with NAND gates. The dead time circuit generator is shown in Fig. A.10.

E. Biasing dc supplies

Regulated dc supplies with different grounds are necessary to bias the various control circuits. The necessary supplies are:

- ±15 V for the current and voltage transducer circuits.
- +5 V for the DSP, gate drive circuits, and the dead time generator circuit.

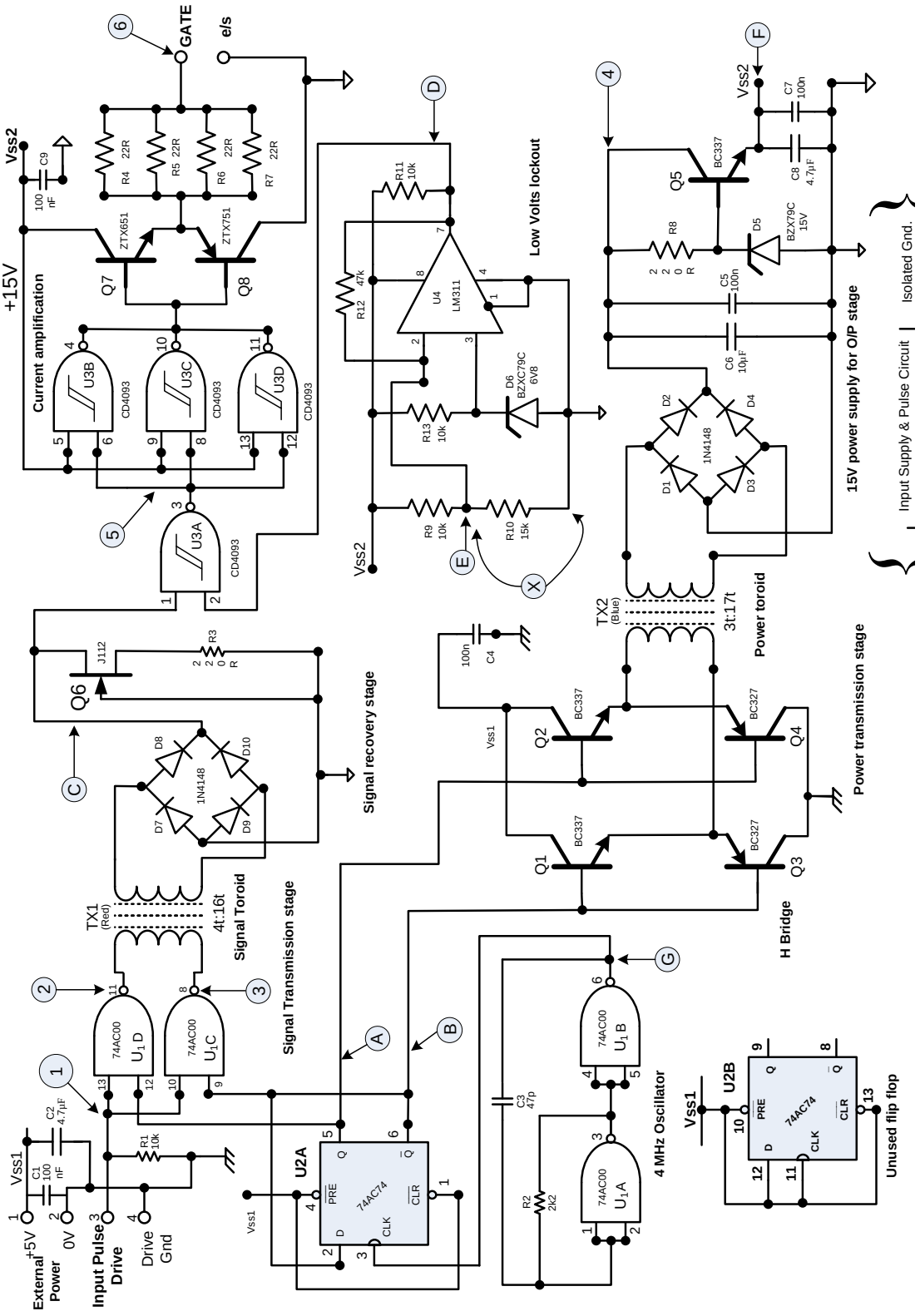

Fig. A.9 Schematic diagram of the gate drive circuit.

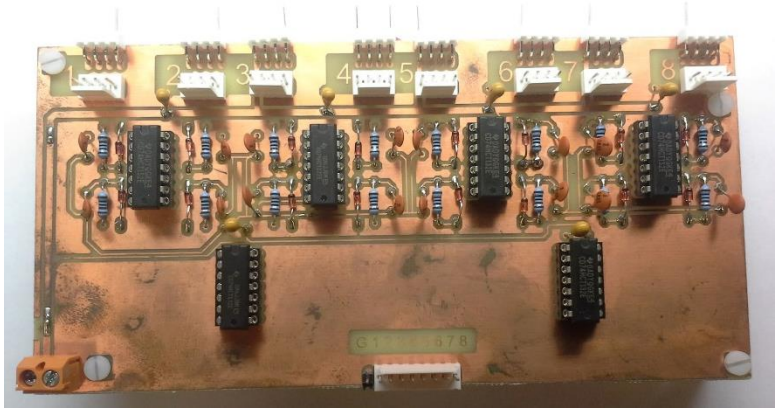

Fig. A.10 Dead time generator circuit

A1.3 Recording Devices

In this subsection, the devices used to monitor and record voltages and currents from the experimental prototype are highlighted.

A. Oscilloscope

A 400 MHz – 4 GHz with 40 GS/s sampling rate four-channel WaveRunner 604 Zi digital oscilloscope from TELEDYNE LECROY is used for measuring and recoding voltages and currents. The oscilloscope is shown in Fig. A.11.

B. Voltage and current probes

In order to record and view voltage and current signals on the oscilloscope, test probes are necessary for signal conditioning and isolation. The oscilloscope demands same-ground signal inputs to its channels. However, several signals at different circuit locations may need to be measured simultaneously. Also, appropriate signal scaling is needed to view high and low voltages. Grounding isolation and signal conditioning are performed by the test probes. A TESTEC TT-SI9002 voltage probe and a Tektronix TCPA300 current probe, both with high frequency precision, are used in the test rig, as shown in Fig. A.12.

C. CAN bus module

The TMS320F28335 DSP supports CAN protocol, thus can be interfaced with CANalayzer modules. All variables inside the running C/MATLAB code can be transferred with CANalyzer Vector-XL to the host computer via CAN communication protocol. The CANalyzer enables real time monitoring, controlling

the system variables and provides data logging excel sheets for more than 32 different signals all running in the background without affecting the processor's main tasks. A photograph for the CAN module is shown in Fig. A.13.

Fig. A.11 Digital oscilloscope.

(a) (b)

Fig. A.12 Test probes for: (a) voltage and (b) current.

Fig. A.13 CANcaseXL device.

A.2 Six-Phase Machine Winding Layout

The H9A-MMC experimental prototype uses a symmetrical six-phase induction machine. The machine is constructed by rewinding the stator of an existing three-phase induction machine with two identical three-phase single layer windings shifted in space by 60°. The constructed six-phase machine has half the number of turns per coil and same conductor cross sectional area, compared to the three-phase machine, to maintain the same copper volume. The three-phase machine is rated at 4 kW, 415 V (line-to-line), 50 Hz, 7.5 A, 1450 RPM. After rewinding, the rated voltage is halved, while other rated values are maintained. The number of slots is 36, while the number of poles is 4 (that is, the pole pitch is 9). The winding layout is shown in Fig. A.14.

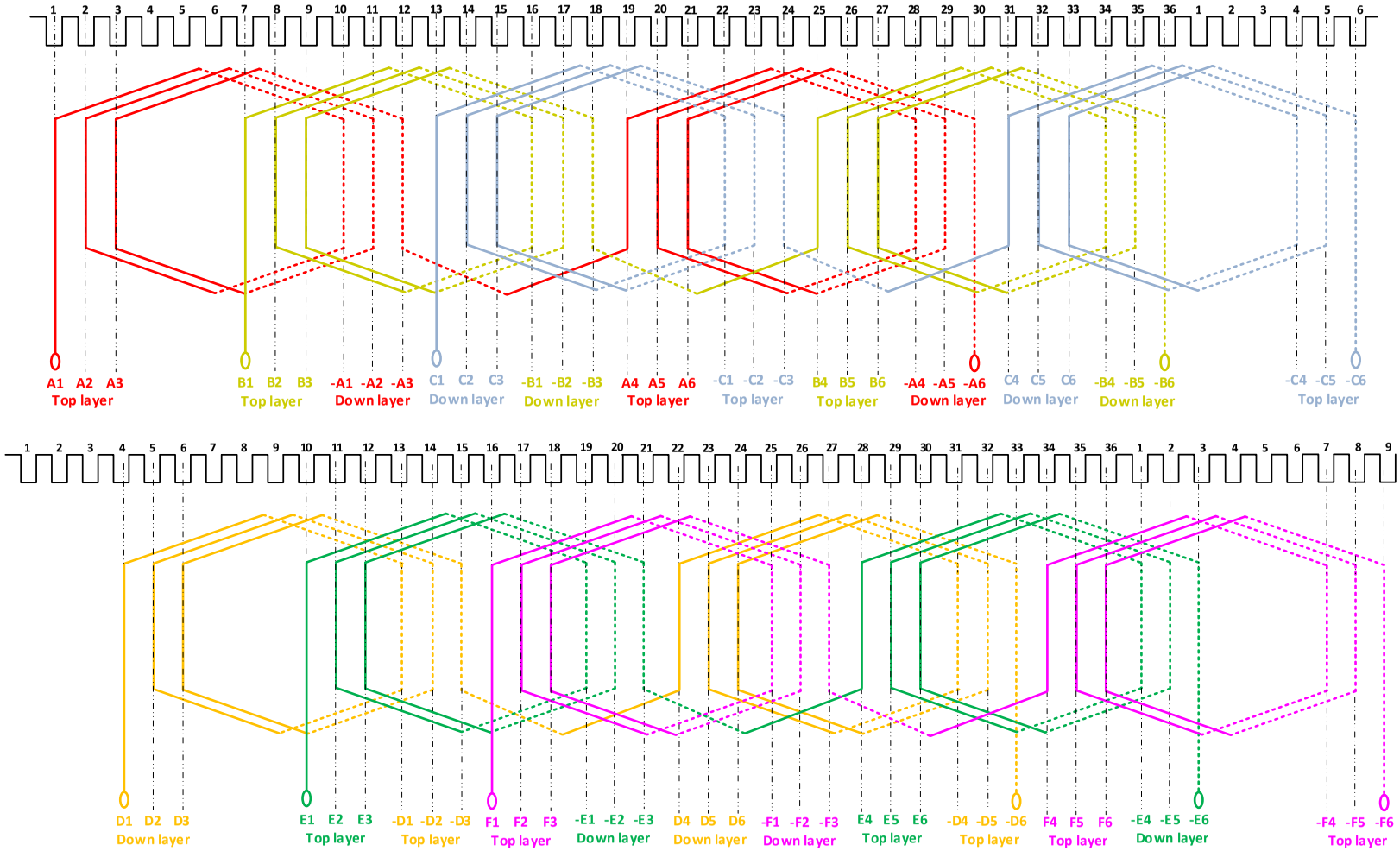

Fig. A.14 Symmetrical six-phase machine winding layout.

A.3 Software Experimental Code

Samples of MATLAM M-file codes used in experimental verification are presented, illustrating the SM capacitor voltage balancing algorithm for the H9A-MMC topology.

A.3.1 Experimental Code for Upper/Lower Arm with 3 HB-SMs

```
function [PWM_signals1, PWM_signals2, PWM_signals3, insert] =
PWM_FCN(ref, car1, car2, car3, Vc1, Vc2, Vc3, Iarm)

Vc=[Vc1 Vc2 Vc3];
N=3;
PWM_signals=ones(3,1);
insert=0;

[Vas Ias]=sort(Vc,'ascend');
[Vds Ids]=sort(Vc,'descend');

    if ref >= car1
    insert=3;
    end

    if ref >= car2 && ref < car1
    insert=2;
    end

    if ref >= car3 && ref < car2
    insert=1;
    end

    if ref < car3
    insert=0;
    end

    if Iarm>0
        for j=1:N
            if j<=insert
                PWM_signals(Ias(j))=1;    %insert
            else
                PWM_signals(Ias(j))=0;    %bypass
            end
        end
    else  %Iarm<0
        for j=1:N
            if j<=insert
                PWM_signals(Ids(j))=1;    %insert
            else
                PWM_signals(Ids(j))=0;    %bypass
            end
        end
    end

    PWM_signals1=PWM_signals(1);
    PWM_signals2=PWM_signals(2);
    PWM_signals3=PWM_signals(3);
end
```

A.3.2 Experimental Code for Middle Arm with 3 FB-SMs

```
function [PWM_signals1, PWM_signals2, PWM_signals3, insert] =
PWM_FCN(ref, car1, car2, car3, Vc1, Vc2, Vc3, Iarm)

Vc=[Vc1 Vc2 Vc3];
N=3;
PWM_signals=ones(3,1);
insert=0;

[Vas Ias]=sort(Vc,'ascend');
[Vds Ids]=sort(Vc,'descend');

    if ref >= car1
    insert=3;
    end

    if ref >= car2 && ref < car1
    insert=2;
    end

    if ref >= car3 && ref < car2
    insert=1;
    end

    if ref < car3
    insert=0;
    end

    if Iarm>0
        for j=1:N
            if j<=insert
                PWM_signals(Ias(j))=1;    %insert
            else
                PWM_signals(Ias(j))=0;    %bypass
            end
        end
    else  %Iarm<0
        for j=1:N
            if j<=insert
                PWM_signals(Ids(j))=1;    %insert
            else
                PWM_signals(Ids(j))=0;    %bypass
            end
        end
    end

    PWM_signals1=PWM_signals(1);
    PWM_signals2=PWM_signals(2);
    PWM_signals3=PWM_signals(3);

end
```

Appendix B

List of Figures and Tables

This appendix summarises the list of figures and tables presented in the thesis.

B.1 List of Figures

B.2 List of Tables

Appendix C

Author's Publications

This appendix summarises the author's accepted and submitted publications related to the PhD work.

C.1 Journal Publications

1. M. S. Diab, A. M. Massoud, S. Ahmed and B. W. Williams, "A Dual Modular Multilevel Converter with High-Frequency Magnetic Links Between Submodules for MV Open-End Stator Winding Machine Drives," *IEEE Transactions on Power Electronics*, vol. 33, no. 6, pp. 5142-5159, June 2018.

   Abstract: This paper presents a dual modular multilevel converter (MMC) topology that utilizes energy exchange between adjacent-arm sub-modules (SMs), operating with out-of-phase modulation. The proposed configuration is applicable to medium-voltage, high-power variable-speed drives incorporating open-end stator winding machines. A novel concept of power decoupling between adjacent-arm SMs in the dual MMC topology is realized through high-frequency transformer-based dc-dc converter modules. This concept offers a significant reduction in the sizing requirement of the SM capacitance and the stored energy in the MMC system, while avoiding the problem of wide voltage fluctuations of SM capacitors, especially at low operating frequencies. The proposed configuration can produce dc voltage, therefore, a machine speed-range from zero speed to the rated speed is possible under the rated torque operating condition. The operating principles of the proposed dual MMC configuration are elaborated and necessary

mathematical analysis is derived. Simulation and experimental results verify the concept of the proposed drive configuration.

2. M. S. Diab, A. Massoud, S. Ahmed and B. W. Williams, "A Modular Multilevel Converter with Ripple-Power Decoupling Channels for Three-Phase MV Adjustable-Speed Drives," *IEEE Transactions on Power Electronics*, July 2018.

Abstract: This paper presents a drive system based on a modular multilevel converter (MMC) with high-frequency magnetic channels between adjacent-arm submodules (SMs), suitable for medium-voltage, high-power three-phase variable-speed machines. The configuration employs chains of dual half-bridge (DHB) modules linking adjacent SMs of three-phase symmetrical arms. The DHB modules are operating as power channels enabling energy exchange to restore the power imbalance among the SM capacitors. This allows arms' ripple-powers to be entirely decoupled through bidirectional power transfer between adjacent-arm SMs, resulting in a near ripple-free SM capacitor voltage profile. Therefore, the MMC common problem of wide voltage fluctuation across SM capacitors is comprehensively solved, independent of the operating frequency. Additionally, a significant reduction in the sizing requirement of SM capacitance is achieved. The configuration is able to drive multi-megawatt machines from standstill to the rated speed at the rated torque operating condition. The operating principle of the proposed MMC configuration is explained and necessary mathematical analysis is derived. Features and viability of the proposed drive system are verified through simulation and experimentation.

3. M. S. Diab, A. Elserougi, A. M. Massoud, S. Ahmed and B. W. Williams, "A Hybrid Nine-Arm Modular Multilevel Converter for Medium-Voltage Six-Phase Machine Drives," *IEEE Transactions on Industrial Electronics*, November 2018.

Abstract: The nine-arm modular multilevel converter (9A-MMC) has been recently proposed as a reduced MMC topology variation for six-phase drive applications, with 25% reduction in the number of employed arms and associated components, compared to a standard dual three-phase MMC, however with a limited output voltage amplitude. This paper proposes a hybrid 9A-MMC comprised of half-bridge submodules (SMs) in both the upper and lower arms, and full-bridge SMs in the middle arms. By employing the negative-voltage state of the full-bridge SMs, the hybrid 9A-MMC avoids the limitations imposed on the dc-link voltage utilization, while achieving further reduction in the component count, compared to a standard 9A-MMC with identical half-bridge SMs. The operating principles of the proposed hybrid 9A-MMC are illustrated with mathematical analysis, while its characteristics are verified through both simulation and experimentation. An assessment of the proposed topology quantifying its employed components is also provided, in comparison to other MMC-based six-phase machine drives.

C.2 Conference Publications

4. M. S. Diab, B. W. Williams, D. Holliday, A. M. Massoud and S. Ahmed, "A Modular Multilevel Converter with Isolated Energy-Balancing Modules for MV Drives Incorporating Symmetrical Six-Phase Machines," *2017 IEEE Energy Conversion Congress and Exposition (ECCE),* Cincinnati, OH, 2017, pp. 2715-2722.

Abstract: A modular multilevel converter (MMC) configuration is presented as a medium-voltage high-power drive for variable-speed applications incorporating symmetrical six-phase machines. The topology employs six standard MMC phase-legs feeding two isolated groups of three-phase machine windings, each with 60° spatial phase-displacement. A novel concept of ripple-power decoupling between adjacent sub-modules (SMs) of MMC phase-legs, while feeding machine windings in a spatial phase-opposition fashion, is realized through isolated dc-dc converter modules. This

concept offers a significant reduction in SM capacitance, while eliminating the problem of SM capacitor wide voltage fluctuations, especially at low operating frequencies. Furthermore, the proposed configuration can efficiently operate at near zero frequency, therefore a machine speed-range from zero speed up to the rated speed is possible under rated torque operating conditions. The proposed MMC configuration is analysed in detail, and its performance is validated using both simulation and experimentation.

5. M. S. Diab, G. P. Adam, B. W. Williams, A. M. Massoud and S. Ahmed, "Quasi Two-Level PWM Operation of a Nine-Arm Modular Multilevel Converter for Six-Phase Medium-Voltage Motor Drives," *2018 IEEE Applied Power Electronics Conference and Exposition (APEC)*, San Antonio, TX, 2018, pp. 1641-1648.

Abstract: This paper proposes a hybrid converter for medium-voltage six-phase machine drive systems that mixes the operation of a traditional two-level voltage-source inverter and the modular multilevel converter (MMC) to enable operation over a wide frequency range. Topologically, the proposed converter consists of nine arms resembling two sets of three-phase MMCs with three common arms, yielding a nine-arm MMC with a 25% reduction in the number of employed arms compared to a traditional dual three-phase MMC. The multilevel property of a standard MMC is emulated in the proposed converter, however on a two-level basis, resulting in a stepped two-level output voltage waveform. The proposed converter has a reduced footprint with advantages of small voltage steps, modular structure, and ease of scalability. Further, it is able to drive high-power six-phase machines within low operating frequencies at the rated torque. The operating principle of the converter is elaborated, and its modulation scheme is discussed. The features of the proposed converter are verified through simulations and experimentally.

6. M. S. Diab, B. W. Williams, A. M. Massoud and S. Ahmed, "A Modular Multilevel Converter with Integrated Shared Capacitor Sub-Module for MV Motor Drives Incorporating Symmetrical Six-Phase Machines," *2018 IEEE 19th Workshop on Control and Modelling for Power Electronics (COMPEL)*, Padua, 2018, pp. 1-6.

Abstract: This paper proposes a new modular multilevel converter (MMC) configuration as a medium-voltage drive for variable-speed applications incorporating symmetrical six-phase machines. The proposed topology employs six MMC phase-legs feeding two isolated groups of three-phase machine windings, each with 60° spatial phase-displacement. A novel concept of sharing one capacitor between each pair of adjacent-arm sub-modules (SMs) of MMC phase-legs, while feeding machine windings in a spatial phase-opposition, is realized through a new integrated SM arrangement. The integrated SM allows the shared capacitor to absorb and release the same energy amount in a consecutive switching scheme, where the capacitor is experiencing both charging and discharging arm currents, one after another. This results in a limited voltage variation across the SM shared capacitor, independent of the operating frequency. Also, the proposed approach allows the MMC to utilize half the number of the SM capacitors, compared to a traditional MMC topology, while further diminishes the SM capacitance requirement, reducing the volume of the MMC system and its stored energy. The proposed configuration can efficiently operate at near zero frequency, therefore a machine speed-range from zero speed to the rated speed is possible under rated torque operating condition. The proposed MMC topology is elucidated in detail, and its effective performance is verified using simulation.

7. M. S. Diab, D. Holiday, A. M. Massoud, S. Ahmed, and B. W. Williams, "A Modular Multilevel Converter with DHB Energy Balancing Channels for Medium-Voltage Adjustable-Speed Drives," *International Conference on Power Electronics, Machines and Drives (PEMD), 2018.*

Abstract: This paper presents a modular multilevel converter (MMC) configuration that utilises energy exchange between submodules (SMs) of upper and lower arms, for energy rebalancing. The configuration is applicable to medium-voltage high-power variable-speed drives with any number of motor phases, where the traditional MMC topology experiences challenging shortcomings. With the out-of-phase alternation of the fundamental ripple power in upper and lower arms, the proposed MMC configuration decouples this ripple power by employing dual half-bridge modules linking opposite SMs in upper and lower arms of the same MMC-leg. This counter-balances arm ripple-power through bidirectional power transfer between opposite SMs, resulting in a reduction in the SM capacitance and the MMC system stored energy. The proposed MMC configuration solves the problem of wide SM capacitor voltage fluctuation, especially at low operating frequencies, where the SM capacitor voltage ripple profile is almost constant, independent of the operating frequency. Therefore, the configuration is able to drive multi-megawatt machines from stand-still to the rated speed, at rated torque. The operation of the proposed converter topology is elucidated in detail, and its effectiveness is verified through simulation and experimentation.

8. M. S. Diab, A. M. Massoud, S. Ahmed, and B. W. Williams, "A Dual Modular Multilevel Converter with Shared Capacitor Sub-Module for MV Open-End Stator Winding Machine Drives," *International Conference on Power Electronics, Machines and Drives (PEMD), 2018.*

Abstract: This paper proposes a new dual modular multilevel converter (MMC) topology as a medium-voltage drive for variable-speed applications incorporating open-end stator winding machines. A novel concept of sharing one capacitor between each two adjacent-arm sub-modules (SMs) of MMC phase-legs, operating with out-of-phase modulation, is realized through new SM arrangement. This concept allows the MMC to utilize half the number of the SM capacitors, compared to a traditional MMC topology. Additionally, the sizing requirement of the shared capacitor is diminished, which

significantly reduces the volume of the drive system and its stored energy. The switching scheme of the shared capacitor between two oppositely modulated SMs eliminates the problem of capacitor wide voltage fluctuations, independent of the operating frequency. Further, the proposed MMC can efficiently operate at near zero frequency, therefore a machine speed-range from zero speed to the rated speed is possible under rated torque operating condition. The proposed MMC topology is elucidated in detail, and its effective performance is verified through simulation.

C.3 Submitted Synopsis

9. M. S. Diab, G. P. Adam, and B. W. Williams, "A Dual-Half-Bridge-Assisted Modular Multilevel DC-DC Converter for MVDC Applications with DC Fault Ride-through Capability," *2019 21st European Conference on Power Electronics and Applications (EPE'19-ECCE Europe)*, Genova, 2019.

Abstract: This synopsis presents a bipolar dc-dc converter configuration based on the modular multilevel converter (MMC), suitable for medium-voltage DC (MVDC) applications. The proposed converter employs two front-to-front MMC phase-legs, with each pair of adjacent-arm submodules (SMs) are coupled through a dual half-bridge (DHB) unit. The DHB units are employed as auxiliary balance branches that assist the MMC arm powers be balanced, resulting in a bounded voltage-ripple profile across the SM capacitors with a diminished capacitance requirement. With the desirable characteristics inherited from both the MMC and DHB, the proposed configuration has a large potential for secure and flexible bidirectional dc power flow control in MVDC applications. Additionally, the proposed converter is suitable for a breaker-less MVDC system since it can realize bidirectional dc fault ride-though operation.